Multi-Scale Modelling of Proto-Zeolitic Solutions

Keith Tobias Butler

Centre for Theoretical and Computational Chemistry
Department of Chemistry
University College London

A thesis for the degree of Doctor of Philosophy

October 2009

I, Keith Tobias Butler, confirm that the work presented in this thesis is my own. Where information has been derived from other sources, I confirm that this has been indicated in the thesis.

October 2009

Abstract

A number of aspects of the pre-nucleation zeolite synthesis solution are considered. Various environmental and structural effects on the ^{29}Si NMR chemical shift of silicon nuclei are investigated, in order to ascertain the necessary computational model for a systematic study of oligomeric silicate species identified or postulated to be present during this phase of zeolite crystal growth. It is demonstrated that, using a model with the oligomer in a fully protonated state and including an implicit representation of the solvent, a reasonably inexpensive model can provide good agreement with experimental results. The systematic study of 59 oligomers reveals several cases for re-assignment of experimentally observed peaks, as well as providing assistance in cases where full assignment has proved impossible from experiment.

The effects of structure directing agents (SDAs), commonly used in zeolite synthesis, are investigated. Using *ab initio* molecular dynamics (AIMD) to simulate the SDA in the presence of water and a specifically designed computer code, it is demonstrated how SDAs lead to the formation of various rings of water in their hydration layer. Furthermore, different properties of the SDAs are shown to induce the formation of different distributions of the various sizes of rings. It is found that certain SDAs result in the formation of clusters of water rings in a network which is isomorphic with some of the zeolite frameworks for which they are know to direct.

Finally a new inter-atomic potential is developed for modelling silicate clusters, in order to allow longer simulations of larger systems than are accessible using AIMD methods. This potential is then used to simulate two cage-like silicate oligomers surrounded by water. In these simulations layers of ordered water, similar to those found at zeolite crystal surfaces, are found. These findings have implications for the understanding of the aggregation of oligomeric species prior to nucleation.

This work was generously supported by the Engineering and Physical Science Research Council.

The final chapter was also made possible by a Junior Research Fellowship from the Thomas Young Centre.

The simulation presented in chapter 4 were performed on the HPCx supercomputer and UCL's Legion supercomputer.

Acknowledgements

I would like to take the opportunity to thank the people who have supported me through my Ph.D. experience. My supervisors Dr. Dewi Lewis, Dr. Ben Slater and Prof. Steve Parker, who have provided me with guidance and advice. I would also like to thank my colleagues, who have made the past three years a more enjoyable experience, in particular Kim Jelfs, Tony Devey, Alan Lobo, Jamieson Christie, Bevan Sharma and Wojtek Grèn.

Thank you to everybody who continued to interact with me during the past months, despite the fact that I have, undoubtedly, talked of little else but my thesis; Cian O'Donovan, Olivia Hegarty, Andrew Smith, Eoghan Daly and Greg Morrissey.

A special mention has to go to those who were not only friends but ensured that I had a roof over my head at all stages during the writing of this thesis; Ewan Russell and Zara Moran. In this regard, and so many others, I owe a special debt to Anne Dennis, thank you.

Finally, most importantly and in no particular order my greatest thanks for so many things to Kate Hartnoll, Jane, Niall and Colin Butler.

Contents

List of Figures

List of Tables

CHAPTER 1

Introduction

The scientific history of zeolites can be traced back as far as 1756 when Cronstedt discovered what has come to be called stilbite [1]. The word zeolite comprises of the Greek words; "zeo" meaning "to boil" and "lithos" meaning "a stone" and was used by Cronstedt, who observed that upon rapid heating the rock produced large amounts of steam due to water which had been adsorbed by the mineral.

Pioneering work in zeolite synthesis and adsorption was started by Barrer in the mid 1930s. By this stage zeolites had already been observed to have many useful properties including ion exchange, adsorption and molecular sieving[1]. Among Barrer's many contributions to zeolite science were the first classification of the known zeolites based on molecular size [2] and the first reported definitive synthesis of a zeolite, mordenite, in 1948 [3].

Although there is a vast body of work in the area of zeolite science today the nucleation and growth of zeolite crystals still remain enigmatic [4]. The problem arises due to the scale on which such events take place. The early stages of the synthesis have been well characterized both experimentally, using NMR [5, 6, 7] and mass spectrometry [8] and also theoretically, in terms of thermodynamics [9, 10] and kinetics [11, 12] . The later stages, involving larger species have also been studied using scattering techniques [13, 14]. The scale on which nucleation takes place however, is intermediate to the scales of these experimental techniques. Although the nucleation event has been tackled using an approach involving multiple techniques [15, 16, 17] the results of these experiments have then been challenged by other investigators [18].

Understanding how nucleation occurs is fundamental to any *a priori* knowledge of the parameters necessary for synthesis of a particular zeolite. Although the task is exceedingly difficult, the rewards of such knowledge make it nonetheless an attrac-

tive proposition. The ability to rationally control the synthesis in order to obtain a specific crystal would allow the synthesis of tailor-made zeolites which, given the many commercial uses of currently existing zeolites, means that the area of investigation of zeolite crystal growth remains a vibrant field more than 60 years after Barrer's pioneering studies.

The investigation of the pre-nucleation stage and how the properties of the system at this stage may influence the nucleation event will be the focus of this thesis. As the individual areas investigated are introduced in detail in the relevant chapters this section shall be used to provide a general overview of the nature and use of zeolites, as well as an introduction to some of the key questions surrounding the formation of zeolites, finally the objectives of the thesis shall also be set forth in this section.

1.1 Natural Zeolites

As alluded to in the previous section the early history of zeolite science was concerned with naturally occurring zeolites. Some of the earliest known zeolites were found in cavities and vugs of basalts, towards the end of the 19th century, however, zeolites were also discovered in sedimentary rocks. Following extensive geological explorations of zeolites the following types of zeolite formation were proposed [19]:

- Crystals resulting from hydrothermal or hot spring activity, involving reactions between solutions and basaltic lava flows.
- Deposits formed from volcanic sediments in closed alkaline and saline lake-systems.
- Similar formations from open fresh-water and ground-water systems acting on volcanic sediments.
- Deposits formed from volcanic minerals in alkaline soils.
- Deposits formed from hydrothermal or low-temperature alterations of marine sediments.
- Formations as the result of low-grade burial metamorphism.

With continued geological exploration more and more natural zeolites have been discovered. To date over 40 types of natural zeolite have been discovered, although the structures of fewer than 30 have been solved [20]. The applications of natural zeolites also continue to receive attention; they have been widely used in such processes as drying, separation of gases and liquids, softening of hard water and treatment of sewage. In addition carefully selected, or modified natural zeolites find use as catalysts or catalyst supports in chemical synthesis.

As abundant natural deposits of zeolites were found in sedimentary rocks near the earth's surface it was concluded that they were formed at temperatures and pressures which were not very high. This finding lead to the development of hydrothermal synthesis procedures (discussed further in section 1.3), which were designed to mimic the conditions under which natural zeolites form.

Although, compared to natural zeolites, synthetic zeolites have many advantages, such as higher purity and uniform pore size, natural zeolites have advantages when large quantities of zeolite are required and purity concerns are not as important. Due to their being found near the earth's surface the costs of extraction are not prohibitively high and natural zeolites still find many applications today, some of the areas of use being agriculture and environmental protection [20].

1.2 Zeolite Structure and Classification

Zeolites are generally defined as aluminosilicate crystals containing pores and cavities of molecular dimenstions (ca. 3 - 15 Å)[4]. Although the chemical composition of zeolites is generally quite restricted (O, Si, Al) it is the wide array of ways in which these elements can be arranged that gives rise to the many exploitable properties of zeolites. In addition, a large number of materials isomorphic to zeolites also exist, for example aluminophosphates (AlPOs) and silicoaluminophosphates (SAPOs). Furthermore the possible properties of zeolites have been expanded by the incorporation of new elements such as Ti, P, Fe, V, Cr and Mn into the aluminosilicate framework [21]. We shall now consider some of the concepts used to classify zeolites.

1.2.1 Framework Types

Zeolites can be categorized according to the structure of the crystal framework. Zeolite framework types are classified by a three letter code, which is assigned to each unique framework type by the International Zeolite Association (IZA). Currently there are 191 different framework types listed on the IZA website (www.iza-structure.org/databases). It is important to state that this three letter code refers to framework type only, not to a specific material. For example the materials amicite and garronite are both examples of GIS framework type zeolites. We shall now examine some of the common structural units which can be used to build zeolite structures.

1.2.2 Basic Building Units: The Tetrahedron.

All zeolite frameworks are built up from a pattern of basic building units (BBUs). These BBUs are tetrahedral, of TO_4 composition where T is usually silicon or aluminium, but can be many atoms which have low electronegativity (P^V, Zn^{II} etc.)

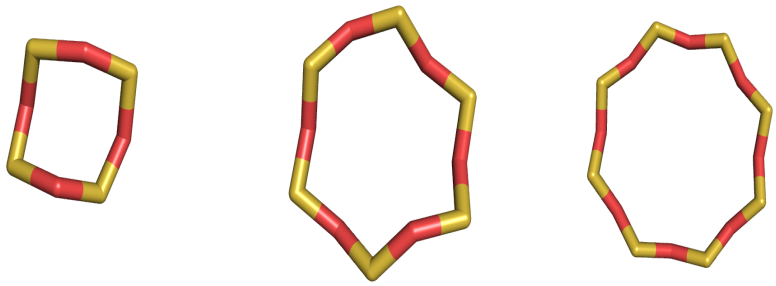

Figure 1.1: Examples of some common ring types found in zeolites. Yellow : T-atom, Red: bridging oxygen. From left to right the 4 ring, 6 ring and 8 ring. The number refers to the number of T-atoms in the ring.

and the corners of the tetrahedron are O^{2-} atoms. These tetrahedra are linked together by the apical Os to form the crystal structure, each O being shared by two Ts, thus the chemical composition of the overall crystal has the stoiciometric formula TO_2.

1.2.3 Composite Building Units

More complex composite building units (CBUs) can be formed by linking together the BBUs. The simplest form of CBU is a ring, a ring containing n BBUs is referred to as an n ring, some common examples are shown in figure 1.1. The most common rings in zeolite structures are 4, 5, 6, 8, 10 and 12 rings [22], however structures with rings of order up to 20 are known [23]. Structures containing 3, 7 or 9 rings are extremely rare [24].

The next level of complexity in CBUs is obtained by linking together rings to form larger CBUs. Cages are an example of these more complex CBUs. Some examples of CBUs are shown in figure 1.2.

Cages are usually considered to be polyhedra whose largest ring is small enough to restrict the passage of molecules larger than water, this limit is commonly set at 6 rings [22]. The CAN cage in figure 1.2 is referred to as a $[4^6 6^5]$ polyhedron, the SOD cage is referred to as a $[4^6 6^8]$ polyhedron. In the $[m^n]$ notation n refers to the number of rings of order m in the polyhedron. The structures in figure 1.2 show only the tetrahedral centres, i.e. the oxygens are not explicitly depicted, this is common practice when graphically representing zeolite structures.

Another type of composite building unit is the chain. Chains are a 1 dimensional arrangement of rings, two examples built from 4 rings are shown in figure 1.2.

Cavities are a class of CBUs which are similar to cages, but containing rings which are large enough to allow the free passage of molecules in and out of the unit. In figure 1.2 we show the LTA cavity, found in zeolite A, this is a $[4^{12} 6^8 8^6]$ polyhedron. In zeolite A these cavities are linked together by the 8 ring face and, as such, allow the free diffusion of molecules such as water, nitrogen and carbon

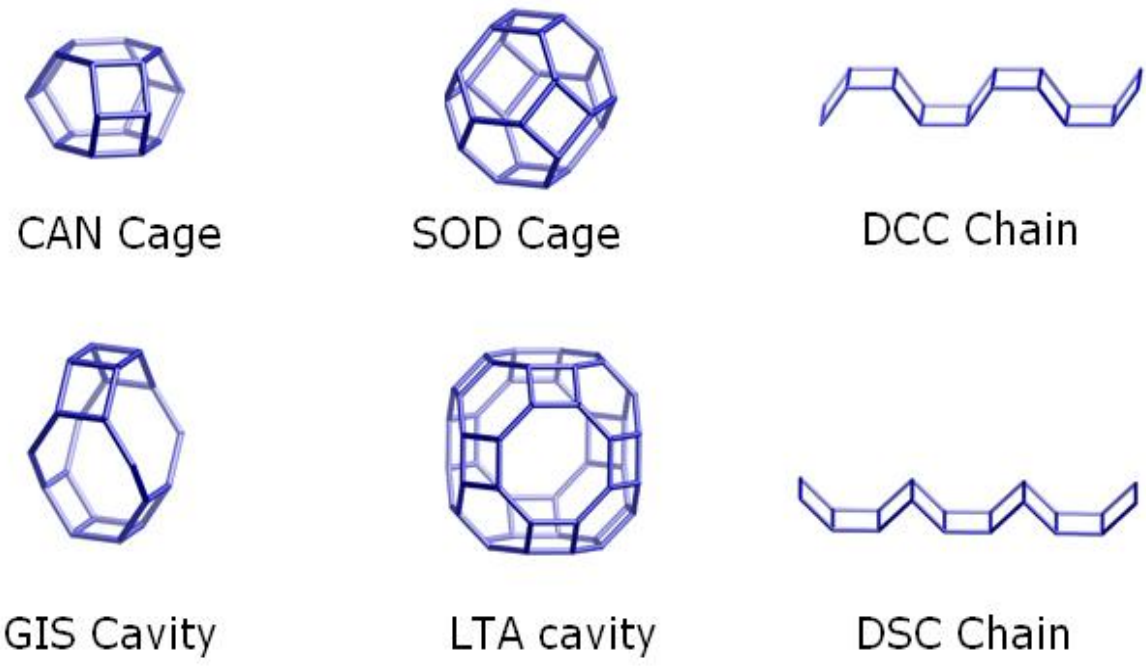

Figure 1.2: Examples of composite builing units found in zeolite. Each vertex represents a T atom, bridging oxygens are not shown.[a]

[a]All images adapted from www.iza-structure.org/databases

dioxide through the zeolite structure.

A channel is a pore which is infinitely extended in one dimension, with a minimum ring size, allowing the diffusion of guest molecules in the zeolite through the pore. In many zeolites there are inter-connected pores running in different directions to form 2 and 3 dimensional networks. The dimension of a channel is quantified by the number of T atoms in the n ring which defines the channel. The most commonly found channel sizes are 8, 10 and 12 ring channels, know as small-, medium- and large- pore zeolites [22]. Materials with 14 and larger ring channels are known as extra large pore zeolites [25].

1.2.4 Secondary Buliding Units

The final class of building unit which we shall introduce here are the so-called secondary building units (SBUs). The concept of SBUs which is most commonly used today dates back to 1967 when Meier proposed the smallest number of topological entities from which all known zeolites may be built [19]. The current set of SBUs is shown in figure 1.3.

Obviously this concept of SBUs is merely a theoretical tool for representing zeolite topologies and can be very useful for imagining possible topologies. However, SBUs have also been proposed to be important species in the mechanism synthesis. This shall be explored further in the section on hydrothermal synthesis (section 1.3).

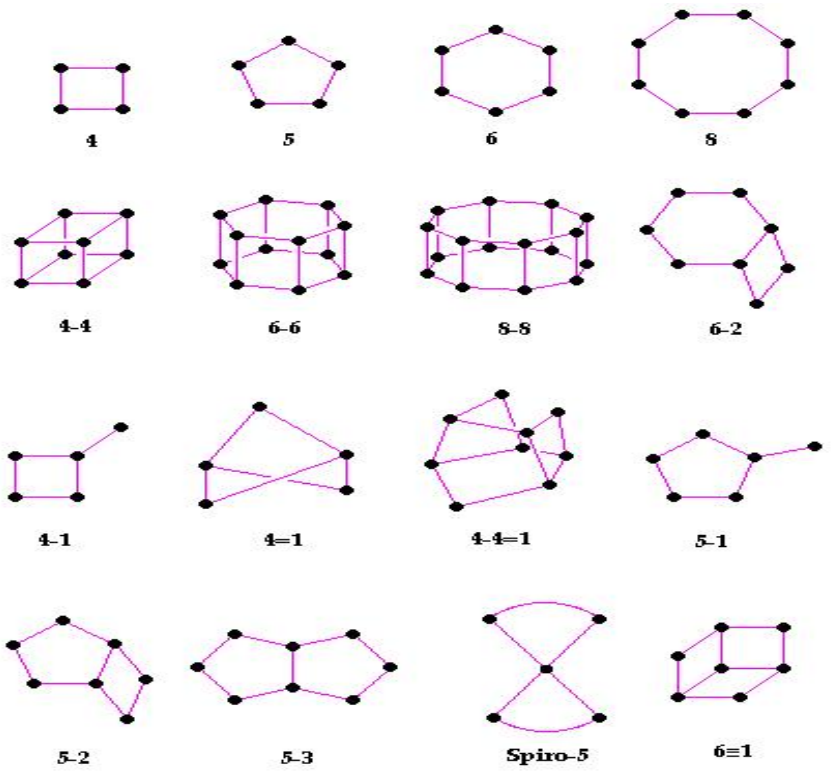

Figure 1.3: The current set of secondary building units, from which all zeolite topologies can be built. Each vertex represents a T-atom site.[a]

[a]Figure adapted from www.ch.ic.uk/chemlib/course/zeolite.

1.3 Hydrothermal Synthesis

The most common approach to synthesizing zeolites is the so called hydrothermal synthesis approach which, as the name suggests, takes place in water at elevated temperatures. A typical synthesis system consists of sources of Si and Al as well as water and an alkaline base reacting in a batch process at temperatures between 80 °C and 200 °C [26]. The evolution of this mixture occurs on a variable timescale, depending on the synthesis, taking from minutes to days [19].

During the synthesis there are several stages: first, during an induction period seed structures are formed, this is the period marked τ in figure 1.4, followed by rapid crystal growth to form the final crystalline zeolitic structure. This s-shaped, or sigmoidal curve is typical of crystal growth processes.

The system during a hydrothermal synthesis consists of liquid, crystalline and amorphous solid phases. As the system is also at high pH the silicates are expected to be at least partially deprotonated. Because of this multi-phase nature and lack of any trustworthy measure of the charge state of the silicates understanding this system is challenging from both an experimental and a modelling point of view. However there have been many studies of these systems since the 1960s, and much has been learnt about the processes involved. The knowledge of what is happening in these systems owes much to increasingly sophisticated spectroscopic techniques, we shall now consider a brief overview of some of the most important studies of

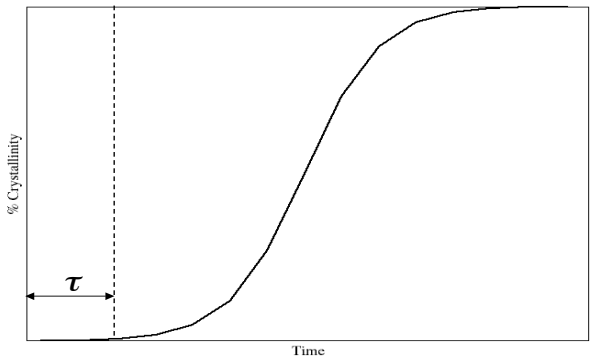

Figure 1.4: The evolution of a system during hydrothermal synthesis. τ represents the nucleation time.

zeolite crystal growth.

1.3.1 Proposed Mechanisms of Zeolite Crystal Growth

Flanigen and Breck produced the first X-ray diffraction (XRD) study of zeolite growth [27]. This resulted in the now familiar sigmodial curve for the rate of crystal growth (figure 1.4) referred to above. The authors proposed a mechanism for crystal growth involving both solid and liquid phases.

At around the same time Barrer put forth the view of crystal growth as proceeding from the association of aluminosilicate polyhedra [28]. He stated that "a plausible process would be the accretion in simple condensation of polygonal or polyhedral anions by condensation polymerization". The units which Barrer proposed as being possible candidates for these polygons and polyhedra include 4 rings, 6 rings and cubes, this gives us the second concept of SBUs. As opposed to the concept presented in section 1.2.4, in which SBUs merely serve as a theoretical tool for defining zeolite topology, Barrer viewed SBUs important intermediates in the process of crystal growth.

Another landmark study in the understanding of the mechanisms of crystal growth was presented by Zhandov [29]. He performed measurements of linear crystal growth rates finding that the crystals grew at a near constant rate over the majority of the synthesis period. Also, by working backwards from the crystal size distribution Zhandov was able to deduce the nucleation profile [30], separating out the contributions of nucleation and growth to the overall growth curve. This lead to a view of the mechanism of crystal growth whereby solid and liquid phases are connected by a solubility equilibrium, with condensation giving rise to simple poly-

hedra (such as 4 rings and 6 rings) and crystal nuclei. He proposed that crystal growth then occurs from solution until complete dissolution of the amorphous solid phase.

The advent of laser-powered instruments in the 1980s lead to an improvement in the understanding of the mechanisms of crystallization. Rozeboom *et al.* [31] used a combination of laser Raman spectroscopy (LRS), XRD and chemical analysis to study the crystallization of zeolites A,X and Y. They found that the condensation of silica and aluminium sources lead to the formation of a large variety of complexes, which they identify as polymeric aluminosilicates which form the nuclei of crystal growth. Dutta *et al.* also performed an number of important studies of the synthesis of zeolites at this time, using a combination of LRS, XRD and nuclear magnetic resonance (NMR) experiments [32, 33]. They found that during the synthesis of zeolite A there was a gel which, though amorphous, contained large numbers of aluminosilicate 4 rings, and that during the synthesis of zeolite Y the same situation pertained, but with large numbers of 6 , rather than 4, rings.

In the 1990s scattering techniques lead to further identification of nanoparticles in synthesis solutions. Studies of the silicate 1 (MFI) synthesis suggested that both nucleation and crystal growth are solution mediated processes, even with an amorphous gel present [34]. X-ray scattering techniques such as small angle x-ray scattering (SAXS), wide angle x-ray scattering (WAXS) and ultra-small angle x-ray scattering (USAXS) demonstrated the role of alkalinity in the formation of colloids in the synthesis of high silica zeolites [34, 35]. Using diffraction techniques, nanometre sized particles, which have been considered to be primary building units for crystal growth have been identified [14, 36, 37]. These particles were found to have different dimensions, depending on the synthesis involved, 2.8 nm in MFI, 2.6 nm in BEA and 1.5 nm in MTW zeolite synthesis. It was, therefore, suggested that each zeolite topology has a unique nano-particle in this stage of its synthesis. In addition to these methods, extended X-ray absorption fine structure (EXAFS) and X-ray absorption near edge structure (XANES) spectroscopies showed that the local structure of the amorphous phases in the synthesis solution resembles the structure of a zeolite [38].

Another series of experiments on MFI [15, 16, 17, 39, 40] revealed a unique particle believed to be building unit of the final zeolite. This work also revealed the existence of clusters with dimensions of 1.3 x 4.0 x 4.0 nm, which were termed "nanoslabs". It was postulated that these nanoslabs were formed by the aggregation of the primary units, with the slabs then self-assembling to form the final crystal structure, the proposed mechanism from this work is depicted in figure 1.5. This mechanism has received significant criticism, due to possible over-interpretation of the NMR spectrum [18, 41], the specifics of this debate are dealt with in greater detail in the introduction to chapter 3.

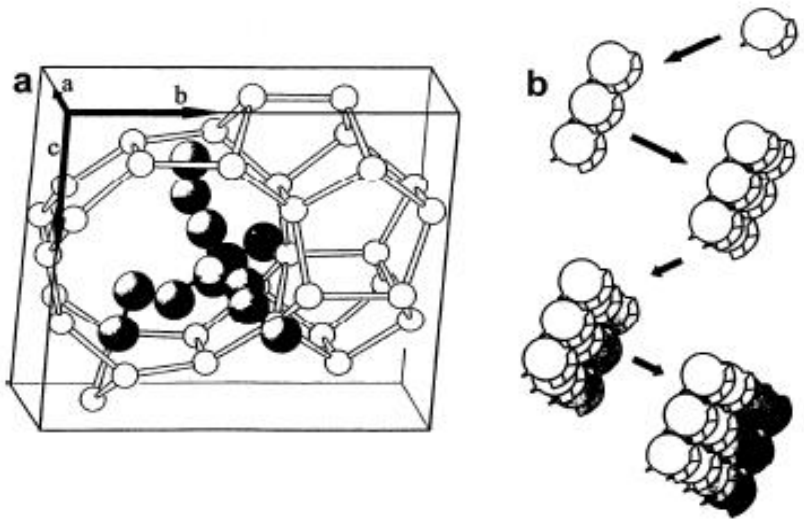

Figure 1.5: The "nanoslab" hypothesis of zeolite growth. a) The precursor unit containing one TPA cation. b) Schematic representation of the formation of the nanoslab by aggregation of the precursor units.[a]

[a]Figure adapted from reference [17]

1.3.2 NMR for Studying Pre-Nucleation Solutions

For particles smaller than 2.8 nm ^{29}Si NMR has been the primary tool for identification of the structure [5, 42, 43, 44, 45]. For more than 30 years 2-dimensional NMR has been used to identify such species in the pre-nucleation solution phase. In the early 1980s Si-Si homonuclear decoupling in conjunction with computer simulation was used to identify 18 silicate species in solution [43], using correlation spectroscopy (COSY) 22 species were identified based on chemical shifts and connectivity data [45].

NMR has been the primary tool in the search for SBUs (as proposed by Breck[26] and Barrer[28]) in the pre-nucleation solution. The idea that one may identify these discreet units which would lead, through a series of simple mechanistic steps, to the final crystal product is an appealing one, as it would allow for rational control of a synthesis by controlling the species formed at the earliest stages of the synthesis (τ in figure 1.4).

The proving (or indeed disproving) of the existence of pre-organized units in the pre-nucleation solution is an important question, and may be addressed by the use of *ex-situ* NMR experiments in which the reaction is stopped at various stages, the liquid and solid phases separated and the liquid phase investigated to determine the kind of species present. The concept of synthesis proceeding via SBUs is flourishing in aluminophosphate chemistry[46, 47, 48]. In zeolite synthesis solutions in contrast, as noted by Kinrade and Knight, the SBUs of Barrer are characterized by their "almost complete absence" in the synthesis media. However there is also the possibility that the species in solution may be considered as pre-

nucleation building units (PNBUs)[49]. These are structures which, although not possessing the property of the SBUs that they are found in the final crystal, are nonetheless very closely related to the SBUs. The existence of such PNBUs,related by isomeization to SBUs, has been demonstrated for alumino- and gallo- phosphate syntheses [46, 49]. In this picture nucleation is considered as a two step process; the PNBUs first join together, followed by a clipping together of the resultant network to form a larger crystallite structure[46]. Such a process has been demonstrated by NMR experiments to take place in aluminophosphate syntheses, and attempts to explore its possibility in zeolite synthesis solutions continues to be one of the major areas of ^{29}Si NMR investigations of pre-nucleation zeolite solutions[5, 44, 50].

NMR spectroscopy has also been used to investigate the effects of organic cations in the synthesis solution [6, 7], the effects of different sized cations tetraalkyl ammonium (TAA) cations were investigated. The authors found that the presence of organic cations favours the formation of cage type species, such as the double 3 ring and double 4 ring (structures 6M and 8D in figure 1.6).

As the experimental techniques become ever more powerful, more and more oligomers have been identified in these solutions. Figure 1.6 from [44] shows the structure of 52 unique oligomers identified in a recent study. The ever increasing complexity of such spectra has meant the theoretical modelling has become increasingly important [51, 52], one of the primary aims of chapter 3 of this thesis is to establish a robust, yet computationally inexpensive protocol for calculations of ^{29}Si NMR shifts, in order to aid interpretation of experimental spectra, and to produce a library of calculated NMR shifts for previously identified, or proposed structures.

1.3.3 Templates

One of the threads which has linked much of the effort in zeolite science over the past two decades has been in converting the knowledge that zeolite synthesis employs relatively weak, non-covalent intermolecular interactions into criteria for finding templates for designing a specific zeolite. In general, organic cations, commonly used as templates for zeolite syntheses, tend to organise water molecules in their vicinity (this is dealt with in greater detail in section 1.3.4). Upon addition of a silicate source to a solution with hydrophobically hydrated cations the negatively charged silicate species condense and polymerize at the surface of a single organic cation. The geometry of the cation can, therefore, be transferred into the geometry of the zeolite framework, although the mechanism for such this association remains somewhat unclear. Three modes of action of templates can be distinguished. The first is merely a space filling action, whereby the geometry of the cation alone determines the final crystal structure; this is illustrated by the fact that 22 different organic cations can be used to synthesize the ZSM-5 framework. The second mode of action is as a structure directing agent (SDA), in this situation a specific SDA is required

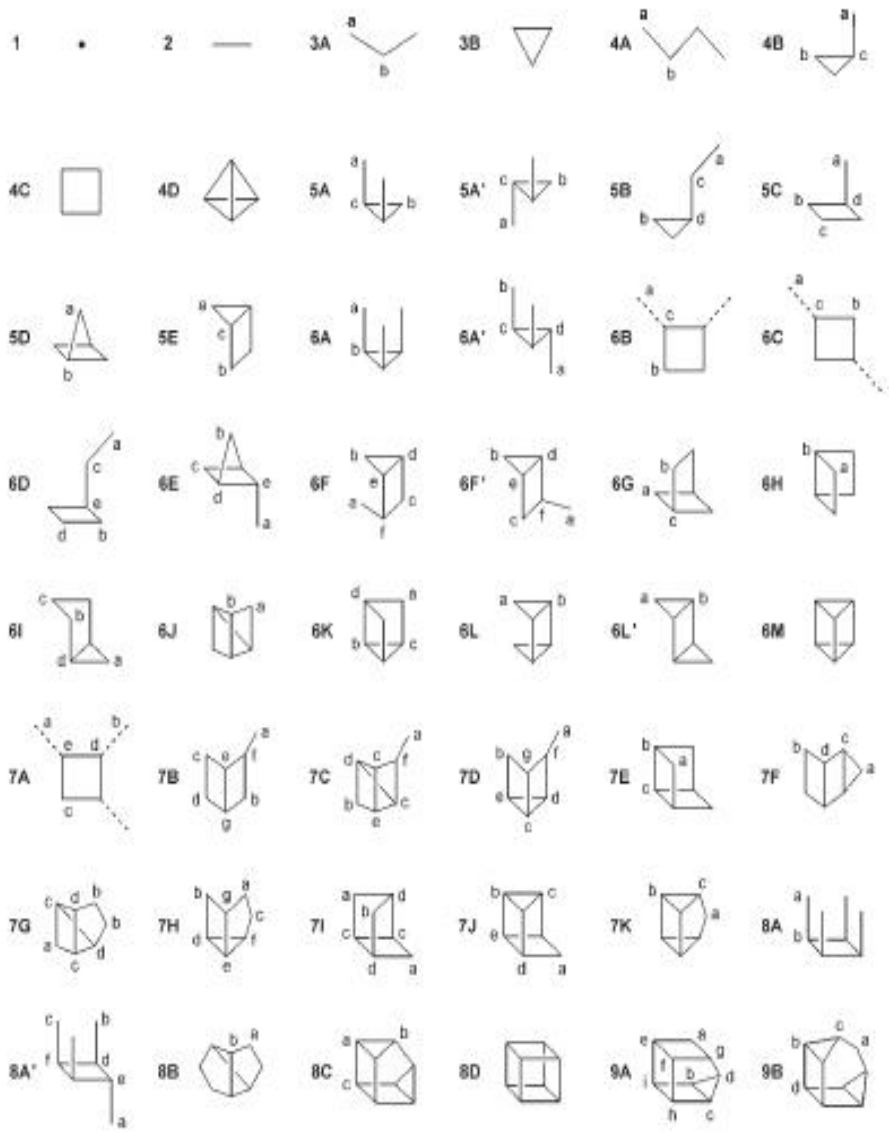

Figure 1.6: 52 unique silicate oligomers identified from a COSY NMR study of pre-nucleation zeolite synthesis solutions [44]. Each solid line represents a Si-O-Si linkage, dashed lines represent attached $OSi(OH)_3$ units, whose abslute conformation could not be determined.[a]

[a]Figure adapted from reference [44].

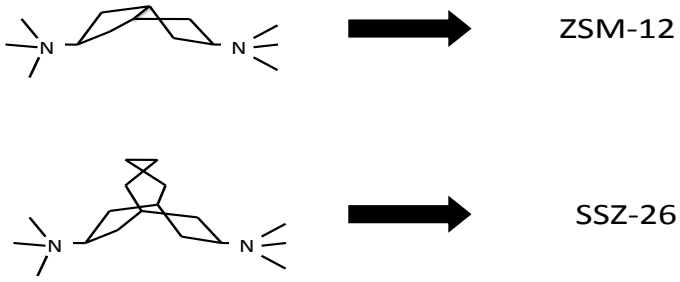

Figure 1.7: Different diquats used in reference [53] as structure directing agents for different crystal structures.

to synthesize a particular structure. An example of this is the synthesis of high silica SSZ-26 using the N,N,N,N',N',N'-8,11-[4.3.3.0] dodecane diammonium cation [53], this cation is an example of an important class of templates; the diquaternary ammoniums, commonly referred to as diquats. The final mode of action of templates is templating proper, this involves crystallization of the final product in the presence of the organic cation, with the guest organic compound being present in the resultant pore network.

An example of the rational use of templates to arrive at different structures is that of the syntheses of ZSM-12 and SSZ-26 using different diquats. Using the linear diquat the (the upper structure in figure 1.7) Zones *et al.* synthesized ZSM-12, which has no intersecting pores. In order to achieve the synthesis of a structure with intersecting pores, SSZ-26, another ring was added to the diquat (giving the lower structure in figure 1.7), thus breaking the symmetry about the axis of the template. As mentioned the exact mechanisms via which templates achieve their effects remain unclear, however a theory based on water structure is explored further in section 1.3.4 and chapter 4, and some important results from molecular modelling of template/silica interactions are reviewed in section 1.4.1.

1.3.4 Templates, Water and Zeolite Crystal Growth

As mentioned previously there have been many proposed mechanisms for zeolite growth which evoke the concept of crystal nuclei formed by the aggregation of SBUs [15, 16, 17, 28, 39, 40]. It has also been proposed that certain SBUs are stabilized by the presence of cations in the solution, so for example certain cage type oligomers have been proposed to be stabilized by the presence of Na^+ [54].

The idea that the cation in the synthesis gel is responsible for the formation of

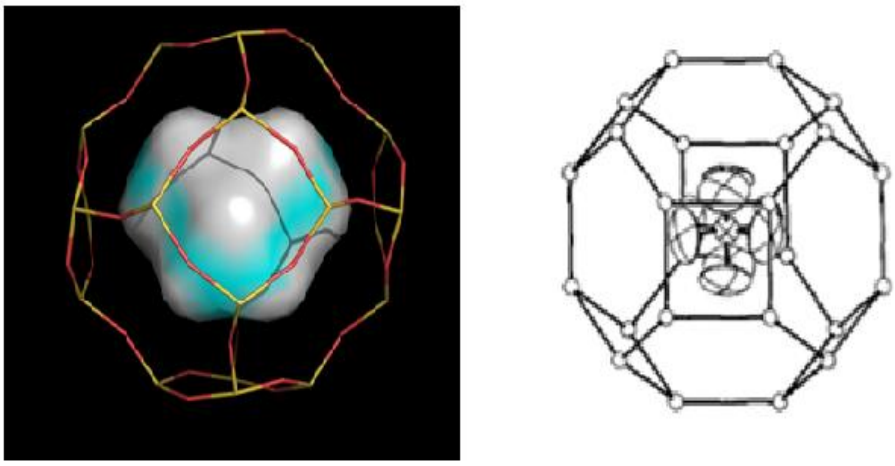

Figure 1.8: The structures of TMA encapsulated in a SOD zeolite cage (left), red: oxygen, yellow: silicon and TMA hydrate, vertices of the polyhedron indicate oxygen sites[a].

[a]The picture of TMA hydrate is adapted from reference[59]

nuclei leads to an obvious next step of altering the cation in order to form different nuclei. The first use of an organic cation was by Barrer and Denny [55], who introduced tetramethyl ammonium (TMA) into the synthesis. Subsequently a number of syntheses were reported using TMA [56, 57]. These studies revealed how the use TMA as a source of cations resulted in the synthesis of TMA-sodalite, but formation of structures which contain different structural building blocks required the presence of other cations. For example zeolite A, which has D4Rs as well as sodalite cages, does not form with TMA^+ alone but requires the presence of Na^+ cations in the synthesis.

After the use of TMA other quaternary ammonium ions were also introduced in the synthesis of zeolites. Primarily tetraalkyl ammoniums (TAAs) were used, including tetraethyl ammonium (TEA),tetrapropyl ammonium (TPA), tetrabutyl ammonium (TBA) and tetrapentyl ammonium (TPeA) [54]. The introduction of these cations, which are markedly more hydrophobic than TMA, had two major impacts on the types of structure produced. Firstly, a higher silicon/aluminium ratio in the final crystal became accessible for already synthesised zeolites, secondly many other structures were reported[54]. Another class of quaternary ammonium ions, which were introduced around this time, were large bulky cations such as DDO (1,4-dimethyl-1, 4diazoniabicyclo[2,2,2] octane) used to make ZK-5 [58].

As mentioned above, a number of roles for the cation, or template molecule have been proposed and refuted. Clearly the presence of a particular cation plays many roles in the synthesis, from space filling, to direction of different structures, to affecting the gel chemistry of the system itself [54]. One of the theories regarding the structure directing effect of templates is based on the interesting observation of isomorphicity between zeolite structures and clathrate hydrates. Wiebcke [60] published a communication highlighting this isomorphicity between a number of

TMA hydrates and zeolites in which TMA is also present. At the same time Mootz [59] published a study of different clathrate hydrates of TMA, with the striking example of one particular hydrate which is exactly isomorphic with a sodalite cage (figure 1.8), which, as stated earlier, is the only zeolite accessible when TMA is the only cation present during synthesis. Chang and Bell at this time published a landmark paper in which they studied the formation of ZSM-5 using XRD and Fourier transform NMR (FT-NMR) measurements [61]. This investigation revealed the formation of channel intersections about the TPA cation prior to the formation of a crystal structure: these intersections were said to be clathrate-like structures. Drawing upon this information and also theories of hydrophobic hydration, based on measurements of entropies of solution and other measurements [56], they proposed an interesting mechanism for the role of the TPA. In this picture the TPA first formed a clathrate-like hydration layer with the solvent water molecules, this is then followed by dynamic replacement of the water molecules by silicates which take on this structure and begin to form the channel intersections observed. This hypothesis was used to explain the aforementioned exemplary isomorphism between zeolites and clathrate hydrates.

Experimental work by Burkett and Davis [62, 63] cast further light on the mechanisms of organic-inorganic composite formation. In their study of a series of TAAs they were able to show, using cross-polarization NMR, that inorganic-organic composites were extant in the synthesis gel prior to crystallization. They also showed that increasing the length of the alkyl chain led to an increased propensity for the formation of these composites. This is interpreted as due to the fact that the increased chain length leads to increased hydrophobicity and thus the formation of hydrates can be seen as due to favourable hydrophobic interactions between cation and silicate. They further proposed that the exchange of water for silicate results in the release of a water molecule from an ordered hydration layer to the bulk solution, in which its degrees of freedom are increased, thus invoking entropy as a driving force for association. It is also noted in this study that when the alkyl chain is too long to form a zeolite under these conditions, as in the case of TBA, the cation tends to agglomerate which is used to explain the fact that TBA needs higher temperature to act as a template in synthesising ZSM-5. This study is very important in a number of respects: primarily it embellishes the work of Chang and Bell by proposing a mechanism proper (depicted in figure 1.9) for association between silicate and template and secondly it also demonstrated how cations could have a structure directing effect which is not based solely on geometrical filling of pores.

There have been numerous studies of monolayer hydration of templates in zeolite crystals [64]. Although due to the close packing of zeolite crystals and organic components which occurs more often than not it is difficult to observe water positions in final crystals. N-propylamine is one template molecule whose hydration behaviour

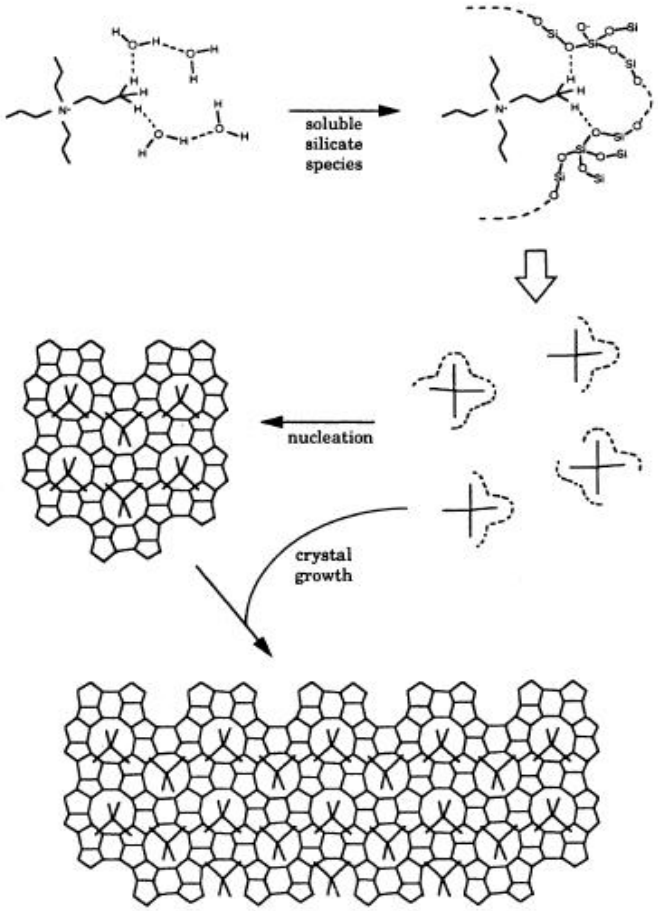

Figure 1.9: Mechanism for the structure directing effect of TPA in ZSM-5 synthesis. In the first step silicate species displace hydration layer water molecules around the TPA, followed by the formation of organic/inorganic composite precursor units, which then aggregate during nucleation and attach to the crystal during crystal growth.[a]

[a]Picture adapted from [62]

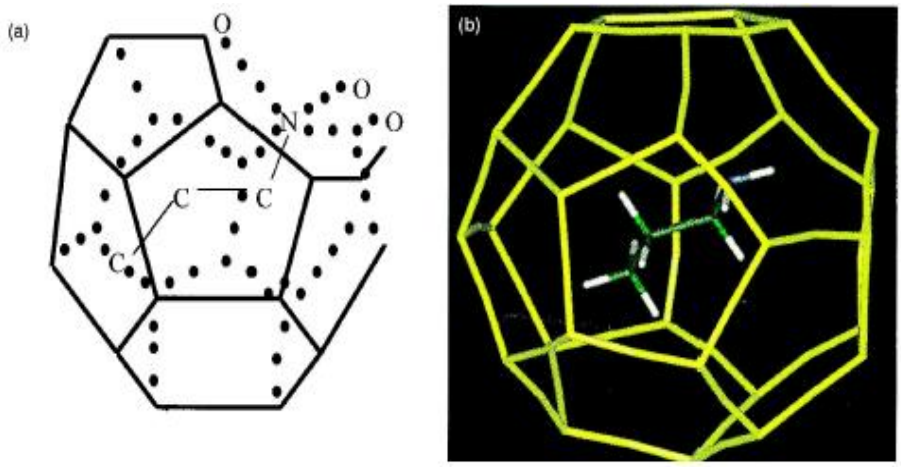

Figure 1.10: The structures of n-propylamine encapsulated in the MTN framework (left) and the simulated hydration layer of n-propylamine from reference [64] (right).[a]

[a]Picture adapted from reference [64].

has been extensively studied [65], and a striking similarity between the $[5^{12}6^4]$ hydration layer of n-propylamine and the MTN framework which it synthesises is evident. Cox *et al.* [64]carried out simulated annealing Monte Carlo simulations of water in the hydration layer of n-propylamine and found that the preferred configuration of the water molecules was indeed that of the MTN frame work (figure 1.10), thus adding strength to the argument for the mechanism proposed by Chang and Bell [61] and Burkett and Davis[62, 63].

In chapter 4 of this thesis the hydration layers of some common templates used in zeolite synthesis are modelled using *ab initio* molecular dynamics methods. The results of these simulations are then analyzed in order to search for possible correlations between the structure of the hydration layer and the zeolite crystals for which these template molecules are used in synthesis. Chapter 5 then investigates the existence of hydration layers of some common cage type silicates. The existence of such hydration layers is important to establish if hydrophobic interactions are to be invoked as driving forces for oligomer aggregation.

1.4 Theoretical Studies of Pre-Nucleation Zeolite Solutions

In studying zeolite synthesis, molecular modelling has provided insights into many aspects of process which affect the final crystal product. Some of the major areas which have been investigated are the determination of the role played by templates in determining the final structure and detailed investigations of the formation of small oligomeric species in the pre-nucleation solution. We shall now consider some of the most important modelling studies of zeolite synthesis solutions.

1.4.1 Zeolite/Template Pairs

Molecular modelling offers the advantage, over experimental techniques, that the energy of interaction between a zeolite structure and the template molecule may be investigated. However, experimental techniques, in particular X-ray diffraction, provide important information regarding the location of template within a zeolite framework, which allows validation of modelling procedures. Moini *et al.* [66] demonstrated the excellent space-filling properties of a di-benzylmethylammonium templates in the channel systems of the EU-1 zeolite. This was achieved by geometry optimizing the template molecules using molecular mechanics methods (see section 2.2) followed by docking the templates "by eye" in the zeolite channels. Using Monte Carlo (MC) techniques, which make random geometry changes, which are then accepted or rejected based on the relative energy of the resultant geometry, this kind of approach has been improved. This approach has shown convincing evidence

for a match between the non-bonded energy between the template and the zeolite structure and the efficiency of a given template for directing for a crystal structure. Stevens *et al.* demonstrated how a template which directs for a number of different structures has a similar binding energy to all of these structures [67].

De novo methods, which build a template for a given zeolite structure have also been developed. These methods take a zeolite structure and then grow a template within the structure from a library of molecular fragments, using a MC approach [68], this has resulted in the successful determination of a new template for DAF-5 [69]. A recent study using a variety of different modelling techniques has demonstrated the role played by TPA in the early stages of the synthesis of MFI [70], finding that the presence of the TPA cation within a zeolite precursor unit is crucial for preventing the collapse of this unit in the solution.

1.4.2 Silicate Clusters in Solution

As stated previously the synthesis of zeolites generally proceeds through a hydrothemal process. The first attempts to model such processes were made in the mid-1980s [71]. These studies involved simulations of small silicate clusters (monomers and dimers) in the presence of water and used a Born-Mayer Huggins (BMH, these are explained more fully in chapter 5) type potential to represent silicate interactions and Rahman-Stillinger-Lemberg (RSL2) potentials for the water. These studies showed that, by a modification of the BMH potential, it was possible to obtain reasonable descriptions of the silicate species, demonstrated by the deprotonation energy of the monomer, which was in agreement with quantum mechanical calculations. The simulations also proved capable of capturing attractive interactions between clusters, although no actual chemical reaction proper was observed.

The first instance of successful modelling of the reaction process was achieved by Feuston and Garofalini in 1990 [72, 73]. These simulations, once again, employed the BMH potential for silica and the RSL2 potential for water but also incorporated three body terms to control bond angles and lengths (see section 2.2). The simulations treated the O-O interactions for silica and water susbsystems the same way. For temperatures of over 1500 K the simulations showed the onset of condensation of monomers to form species with up to six silicon atoms. The simulations also revealed pathways of oligiomerization involving ionized monomers and pentacoordinate silicon intermediates. This scheme was subsequently extended longer simulation times of 120 ps showing the onset of ring closure reactions of the chains formed previously with activation enthalpies for condensation of $\sim$ 12 kcal mol^{-1} which agreed well with experimental values of $\sim$ 15 kcal mol^{-1}. Other studies utilizing this methodology included the investigation of the concentration of H^+ on the condensation reaction, revealing the effect of acid catalyziation of such reactions [74].

Pereira *et al.* have used non-reactive empirical potentials to study the stability of small silica clusters and solutions of water, ethanol, TMOS and TEOS [75, 76] and have shown that the potentials implemented in the DISCOVER[77] and DLPOLY [78] packages can provide a good description of these systems under the sol-gel conditions tyical of zeolite synthesis. These studies showed good agreement with the variation of experimental densities with temperature and pressure. In addition experimental radial distribution functions and enthalpies of vapourization were found to be well described. By close inspection of the radial distribution functions they concluded that condensation reactions between dimers to form more complex clusters were favoured over all other reactions.

In addition to empirical potential models, *ab initio* calculations have also been widely used in the study of pre-nucleation silicate clusters, such as those studies mentioned in the previous section [79, 80, 81] and studies mentioned in the section on the calculation of NMR properties of silicate species (see section 3.1). Silicate clusters were also employed as model systems for the calculation of properties of bulk zeolites [82]. A comprehensive review of the use of *ab initio* methods for the study of zeolite crystals and clusters up to the mid-1990s is available [83].

Subsequently static *ab initio* methods have been used to study the acid catalyzed dimerization of silicic acid [84], giving an activation energy of 12 - 15 kcal mol^{-1}, in agreement with the empirical potential model mentioned above. They have also been used to study the energetics and conformations of both simple [85] and complex [86] silica-based clusters. Mora-Fonz *et al.* studied the relative energies of cyclization and chain growth reactions using DFT methods with implicit solvation models [9], highlighting specifically the pH dependance of the energies of polymerization and cyclization. Improved models for calculation of free energies of cyclizations and polymerizations were also proposed by Mora-Fonz *et al.* [10] who showed that an explicit representation of the surrounding environment leads to free energies which agree with experiment to within "chemical accuracy". However such representations of the surrounding media become prohibitively expensive as the size of the system increases.

Ab initio methods have also been used to study the energy barriers of silica condensation in the formation of various clusters. The first DFT study carried out considered the solvent effects with the implicit COSMO model [12] and showed how an anionic pathway was preferred to a neutral pathway kinetically. This study also demonstrated, as in the earlier study of Feuston and Garofalini [72], that the condensation tends to proceed via a penta-coordinated silicon intermediate. The activation energies calculated in this study were somewhat higher than experimental values, a discrepancy which the authors ascribe to the lack of explicit representation of the solvent in the simulation. A subsequent study of the same systems employing a hybrid implicit/explicit model of solvation [87] revealed, once again, this to be an

important consideration. This study showed how the presence of excess water had a marked effect on the simulations, stabilizing both transition states and stable intermediate penta-coordinate species. An even fuller consideration of the surrounding solvent was achieved by the used of Car-Parrinello molecular dynamics (CPMD) in conjunction with a constrained molecular dynamics scheme, employing periodic boundary conditions [11]. Lower barriers than previously calculated were now found. Also, importantly, it was demonstrated that the formation of three silicon ring is favourable over any further chain growth.

The goal of this thesis is to further the existing modelling work which has been done to investigate the pre-nucleation phase of zeolite synthesis. The results presented within address both areas mentioned above, i.e. the role of templates and the modelling of silicate clusters. To achieve this we have performed simulations at a number of levels, from *ab initio* to molecular mechanics simulations. The outline of the chapters shall now be briefly presented.

1.5 The Current Study

In chapter 3 theoretical methods for assisting and understanding ^{29}Si NMR spectra of pre-nucleation solutions are presented, the specific aims are to:

- Develop a rigorous yet accessible methodology for modelling ^{29}Si NMR chemical shifts of pre-nucleation species.
- Investigate the electronic structure origins of empirically observed trends in ^{29}Si NMR.
- Use this information to assign previously unassignable signals.
- Test the validity of more tenuous experimental assignments.

In chapter 4 The role of templates in structuring solution water is investigated. The specific aims of this section are to:

- Develop a methodology for *ab initio* molecular dynamics of template molecules in solution.
- Investigate the degree of structure in the hydration layers of such species using measures such as are accessible experimentally.
- Search for zeo-morphic structures in the hydration layers of water.

Finally chapter 5 deals with the structure of water in the vicinity of silicate species, the specific aims being to:

- Develop a new inter-atomic potential for the accurate modelling of silicate clusters.
- Use this potential to investigate the existence of hydration layers in the vicinity of some key species.

The current introduction has been necessarily brief, however specific areas are presented in greater detail in the relevant chapters. More detailed accounts of the subjects touched upon are also available in the many excellent reviews of the area of zeolite science which exist [4, 54].

CHAPTER 2

Methods

The past three decades have seen a dramatic expansion of the use of computational methods for tackling many important questions in all fields of the physical sciences (and indeed beyond).The application of computational methods to the modelling of zeolites has been no exception to this general trend. The availability of increasingly sophisticated tools as well as the continued rapid development of computing hardware means that this trend can only be expected to continue.

The methods of computational chemistry allow calculation and prediction of a wide array of interesting properties of chemical systems and many excellent texts outlining the methods and their applications exist [88, 89, 90]. This chapter will describe only those methods relevant to the calculations presented in the rest of this thesis. Broadly the areas considered are:

- Calculating Energy
- Accounting for the Environment
- Minimizing Energy
- Thermochemistry
- Molecular Dynamics
- Theoretical NMR
- Interpreting Electronic Structure

In atomistic simulations there are very broadly two approaches to calculating the energy of a system. One can consider the energy using the methods of quantum mechanics, or choose to ignore the electronic structure of the system and calculate

the energy using what are known as molecular mechanics methods. Within each paradigm there exist many different methods and indeed there are methods which combine elements of both approaches. In this section a number of these approaches shall be considered.

2.1 *Ab Initio* Methods

Ab initio is a Latin term meaning from the beginning. A calculation is said to be *ab initio* (or "from first principles") if it relies on basic and established laws of nature without additional assumptions or special models, setting these methods apart from so called empirical methods, which rely on experimentally determined parameters to calculate the properties of the system being studied.

For example, an *ab initio* calculation of the properties of liquid water might start with the properties of the constituent hydrogen and oxygen atoms and the laws of quantum mechanics. From these basics, the properties of isolated individual water molecules would be derived, followed by computations of the interactions of larger and larger groups of water molecules, until the bulk properties of water are determined. In contrast a "classical mechanics" or empirical calculation might treat the water as a series of point charges connected and interacting through a series of potentials which have been parameterized to fit to experimental data, these methods will be treated in more detail in a subsequent section (2.2).

The essential question at the heart of choosing between *ab initio* and empirical methods, as with most decisions in computational chemistry, is that of how much accuracy is required and how large are the computational resources available for tackling the problem. This is referred to as "scaling" and is demonstrated in figure 2.1. The important factors when estimating how a problem will scale are the order with which it scales O, and the prefactor with which it scales P, both with respect to the number of particles in the system. Empirical models typically scale to the order of 1 (i.e. the CPU time needed for N particles is proportional to N), whereas *ab initio* models typically scale with higher orders of $O = 2$ up to $O = 8$ for some of the highest level methods.

While empirical models have enjoyed enormous success in modelling chemical systems, a number of drawbacks exist which necessitate the use of more expensive *ab initio* models. While empirical models are designed to behave well for the set of data used to derive the parameters (the training set) this is absolutely no guarantee that the model will behave well beyond this training set. Among the systems where empirical models can have difficulties are systems where there are many types of chemical interaction, requiring many model potentials to describe them and systems where the bonding pattern changes. An example of this is the fact that, in general, empirical models cannot model chemical reactions, although some recent models

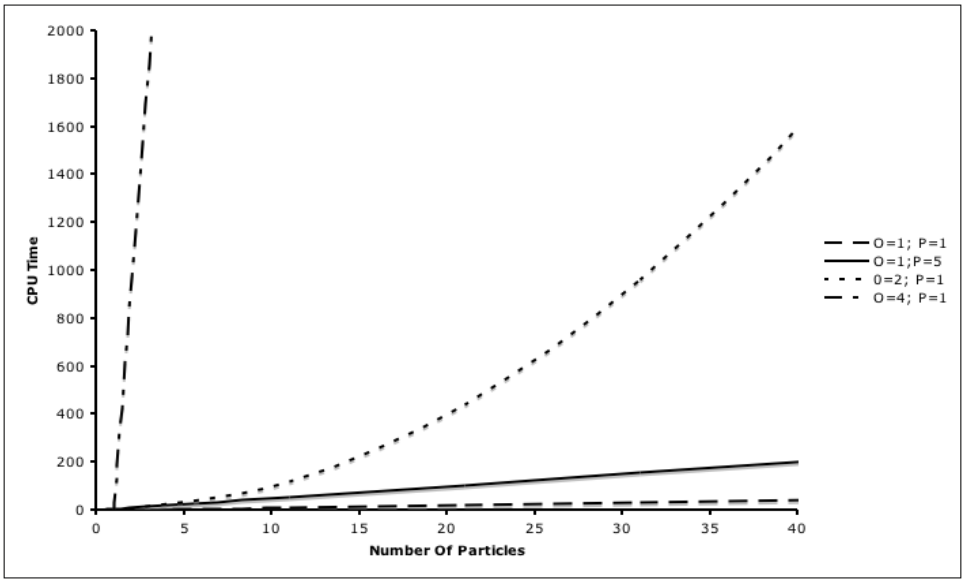

Figure 2.1: CPU time versus number of particles for a series of orders O and prefactors P; Time = PN^O.

have claimed to overcome this barrier [91, 92].

Ab initio methods are also often referred to as "Electronic Structure Methods" as they rely on solving the electronic state of the system, that pertaining to the electrons, to calculate various properties of the system. Electronic structure methods apply the laws of quantum mechanics[93, 94] to obtain properties of chemical species. The basis of these methods is to attempt to solve the Schrödinger equation:

$$H\Psi(r,t) = \frac{ih}{2\pi}\frac{\partial\Psi(r,t)}{\partial t} \tag{2.1}$$

where H is the Hamiltonian operator of the system, which is represented by the wave function Ψ, and which has a probability distribution $|\Psi|^2$, this is the probability that the system will be in a given state. If we consider that the system's potential energy, V, is time independent, we obtain the time-independent Schrödinger equation:

$$H\Psi = E\Psi \tag{2.2}$$

in which the energy E is the eigenvalue of the Hamiltonian operator. To aid the calculation of these eigenvalues the system's Hamiltonian can be split up into different contributions:

$$H = T^e(r) + T^n(R) + V^{n-e} + V^e(r) + V^n(R) \tag{2.3}$$

where the superscripts n and e refer to the nucleus and electrons respectively, V is potential energy, T is kinetic energy and R and r refer to nuclear and electron position respectively. A number of approximations are necessary if we are to solve the Schrödinger equation. The first important approximation which is made is the Born-Oppenheimer (BO) approximation which states that, given that electrons are much lighter than the nucleus and therefore move much more rapidly, the motions

of the nucleus and electrons can be decoupled. The electrons are assumed to be always equilibrated and thus forces on the nuclei arise only as a result of atomic positions. Therefore the electronic structure part of the problem is reduced to that of solving the time-independent Schrödinger equation, with the electrons assumed to be in the ground state. This removes the second term from the above equation (2.3), yielding the electronic Hamiltonian, H^e.

The next approximation relates to the wave function and is called the "Linear Combination of Atomic Orbitals" (LCAO) approximation. Essentially we assume that the total wave function Ψ, can be represented by a summation of smaller functions called basis functions ϕ :

$$\Psi = \sum_i c_i \phi_i \tag{2.4}$$

where ϕ_i are the atomic orbitals and c_i is a factor weighting their overall contribution to the molecular orbital (MO), Ψ. The choice of the set of basis functions, called the basis set, to be used in a calculation is of crucial importance in electronic structure calculations. This relates to both the form of the basis functions and also to the number of functions to be used. The minimum number of basis functions to be used is that which can accommodate all the electrons of the system, however for more accurate and sophisticated calculations basis functions representing unoccupied orbitals must be employed, once again which basis set to use comes down to a question of accuracy versus computational resources available. A more detailed discussion of basis sets is presented in section 2.1.5.

2.1.1 Hartree-Fock[88]

[1]To solve the Schrödinger equation we have to obtain the set of constants c_i, using the variational principle, which states that the calculated energy will always be higher than exact solution. The Hartree-Fock method uses the variational principle to obtain the constants, c_i which allows us to solve the Roothan matrix equation,

$$\mathbf{FC} = \mathbf{SC}\epsilon \tag{2.5}$$

$$det|\mathbf{F} - \epsilon_a \mathbf{S}| = 0 \tag{2.6}$$

where $\mathbf{F}$ is the Fock matrix, $\mathbf{C}$ is the matrix of constants c_i, ϵ_a is the matrix of the energy levels of the system and S is the matrix of the overlap orbitals.

The Fock matrix elements are given by

$$F_{\mu\nu} = \int \phi_\mu(1) f_j(1) \phi_\nu(1) d\nu_i \tag{2.7}$$

[1]Please note that, for simplicity, this discussion is limited to the closed shell case where all orbitals are either fully occupied, or not occupied.

where f is the Fock operator, an effective one electron operator for an electron in a poly-electronic system. The Fock operator can be written as

$$f(1) = \mathcal{H}^{core}(1) + \sum_{j=1}^{N/2}\{2\mathcal{J}_j(1) - \mathcal{K}_j(1)\} \tag{2.8}$$

in which $\mathcal{H}^{core}$ is the core Hamiltonian,

$$\mathcal{H}^{core} = -\frac{1}{2}\nabla^2 - \sum_{A=1}^{M}\frac{Z_A}{r_{1A}} \tag{2.9}$$

$$\tag{2.10}$$

Which takes into account the kinetic energy through ∇^2 and a potential energy through Z_A/r_{1A} in which Z_A is the nucleus charge, r_{1A} is the electron nucleus separation and M is the number of nuclei in the system.

$\mathcal{J}_j$ is the Coulomb operator and $\mathcal{K}_j$ is the exchange operator. The contributions from these terms may be calculated from,

$$\mathcal{J}_j(1) = \int \chi_j(1)\frac{1}{r_{12}}\chi_j(2)d\nu_i \tag{2.11}$$

$$\mathcal{K}_j(1)\chi_j(1) = \left[\int \chi_j(2)\frac{1}{r_{12}}\chi_i(2)\right]\chi_j(2)d\nu_i \tag{2.12}$$

where r_{12} is the electron electron separation. The exchange operator cancels out exactly the self-interaction terms which arise as a result of the mean field approximation in the Coulomb term. Using these terms the Fock matrix elements are calculated as,

$$F_{\mu\nu} = \int \phi_\mu(1)\mathcal{H}^{core}(1)\phi_\nu(1)d\nu_i + \sum_{j=1}^{N/2}\int \phi_\mu(1)[2\mathcal{J}_j(1) - \mathcal{K}_j(1)]\phi_\nu(1)d\nu_i \tag{2.13}$$

The Hartree-Fock method utilizes a Self-Consistent Field (SCF) procedure to solve the variational principle equations. In the SCF procedure (schematized in figure 2.3)the first calculation involves an educated guess of the values of c_i, which are then used for a calculation of the Fock matrix. The resulting Fock matrix is then used to generate a new better set of coefficients, and the process is repeated until the difference between the new and the old Fock matrices is below a certain threshold value, called the convergence criterion.The choice of convergence value is another important consideration when setting up a calculation.

2.1.2 Post Hartree-Fock Methods[94]

The Hartree-Fock method suffers from the fact that it approximates the many-electron problem as a one-electron problem and implies that each electron sees the other electrons as a mean-field. Many attempts have been made to include electron correlation effects in electronic structure calculations.

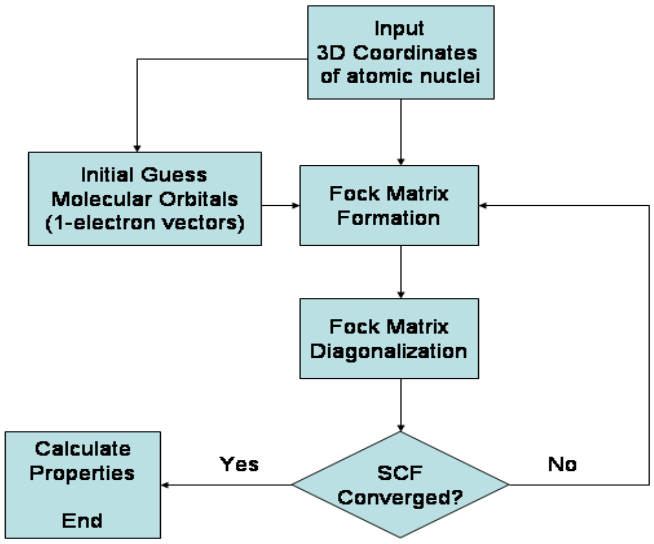

Figure 2.2: A Schematic Representation of The Hartree-Fock SCF Procedure.

The Configuration Interaction (CI) method takes into account mixing of possible electronic states of the molecule in the form,

$$\Psi = b_0\Psi_0 + \sum_s b_s\Psi_s \tag{2.14}$$

where $b_0\Psi_0$ is the Hartree-Fock expression and the second term on the RHS takes into account substitutions of virtual or excited states for occupied orbitals.

Another approach is the Møller-Plesset theory (MP)[95]. MP uses a perturbation on Hartree-Fock theory, removing the error that is introduced when the two electron integrals are replaced by a one-electron potential, by restoring the two electron integrals. Perturbation theory makes use of expanding the equation in a Taylor series with respect to the Lagrange multiplier λ. The new Hamiltonian is

$$H = H_0 + \lambda V \tag{2.15}$$

where H_0 is the Hartree-Fock Hamiltonian. Expanding up to the first order gives the Hartree-Fock solution. Including second order corrections leads to MP2; MP3 and MP4 are also commonly used methods. The MP series often does not converge, because in going from MP2 to MP3 and on to MP4, one does not necessarily achieve a better approximation to the ground state wave function. This is because perturbation theory is not variational, thus a calculated energy is not necessarily an upper bound to the true ground state energy. Post Hartree Fock methods, however, are often simply not practical for calculations. For a system of N atoms MP2 and MP4 scale as N^5 and N^7 respectively while CI methods CISD and CISD(T) scale as N^6 and N^8 respectively. Compared to N^4 scaling for Hartree-Fock calculations [96].

2.1.3 Density Functional Theory (DFT)[97]

The central focus of DFT is the electron density, ρ and not the wave function as in Hartree-Fock methods. It is called a functional theory as the energy is a function of the density, $E[\rho]$, which in turn is a function of the position, $\rho(r)$. A functional is a function of a function. The attraction of DFT is that it provides 'better' results than Hartree-Fock, in many cases comparable with the MP methods, whilst scaling as N^4.

The basis for DFT is the *Reductio ad absurdum*[2] proof of Hohenberg and Kohn[98] that the ground state electronic energy is completely defined by the electron density, ρ. The foundation for the use of DFT methods in chemistry is the introduction of orbitals as suggested by Kohn and Sham (KS)[99]. Within these DFT formalisms the energy is split up as follows:

$$E_{DFT}[\rho] = T_s[\rho] + E_{ne}[\rho] + J[\rho] + E_{xc}[\rho] \tag{2.16}$$

with $T_s[\rho]$ the electron kinetic energy, $E_{ne}[\rho]$ the potential nuclear-electron interaction energy and $J[\rho]$ the potential electron-electron interaction energy. The final term $E_{xc}[\rho]$ is the exchange-correlation energy which is calculated with an exchange-correlation functional. The choice of this last functional is where different DFT methods diverge, it is crucial to the success of the method and will be dealt with in the following section.

The molecular orbitals Φ_i, the electron density and finally the total energy are solved using the Kohn-Sham equations,

$$\{-\frac{-\nabla^2}{2} - V_n + V_e + V_{xc}\}\Phi_i = \epsilon_i \Phi_i \tag{2.17}$$

which can be cast as a Roothan type equation,

$$\mathbf{HC} = \epsilon \mathbf{SC} \tag{2.18}$$

which in turn allows for an iterative solution in the spirit of a Hartree-Fock SCF calculation.

2.1.3.1 Exchange and Correlation Energy, $E_{xc}[\rho]$

The exchange and correlation energy, E_{xc}, is defined as the difference between the exact energy and the energy numerically calculated from all other contributions. In practice it is necessary to make approximations to this term. It can be considered by coupling a system of fully and non-interacting electrons, through a variable λ, where $\lambda = 0$ corresponds to a non-interacting system and $\lambda = 1$ corresponds to a fully interacting, *physical* system. This leads to the expression [100]:

$$E_{xc} = \frac{1}{2} \int d\vec{r}\vec{r} n(\vec{r}) \int d\vec{r'}\vec{r'} \frac{1}{|\vec{r} - \vec{r'}|} n_{xc}(\vec{r}, \vec{r'} - \vec{r}) \tag{2.19}$$

[2]Reductio ad absurdum: the premise that something impossible is actually true, and then proving it is ludicrous.

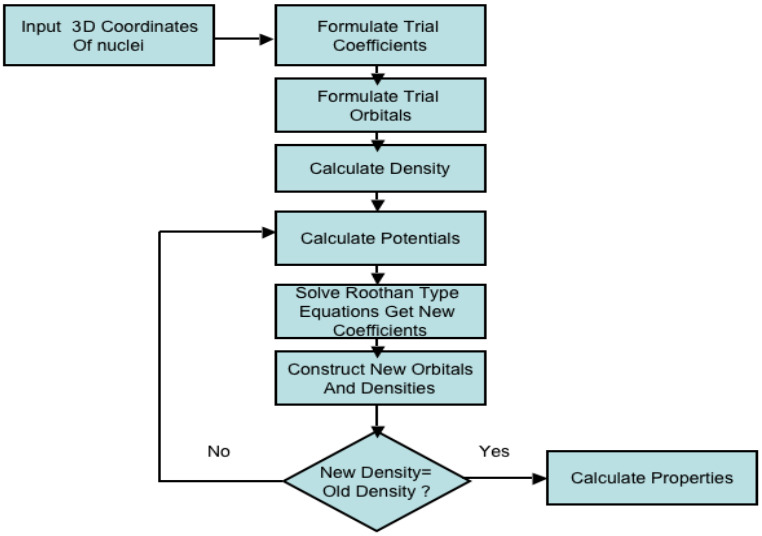

Figure 2.3: A Schematic Representation of The DFT SCF Procedure.

where;

$$n_{xc}(\vec{r}, \vec{r'} - \vec{r}) = n(\vec{r'}) \int_0^1 d\lambda (g(\vec{r}, \vec{r'}, \lambda) - 1) \tag{2.20}$$

where $g(\vec{r}, \vec{r'}, \lambda)$ is called the pair-correlation function and n_{xc} is the exchange-correlation hole, i.e. the effect that an electron present at one point $\vec{r}$ has on finding another electron at the point $\vec{r'}$. E_{xc} can be viewed as resulting from the interaction between an electron and its exchange-correlation hole. We consider now some methods which have been used to calculate E_{xc}.

Local Density/Local Spin Density (LD/LSD) Approximations

The LD approximation has two components. The first is an exchange component, given by the Dirac formula;

$$\epsilon_x^{Dirac} = -\frac{3}{4}\left(\frac{3}{\pi}\right)^{1/3} n^{1/3} = \frac{0.458}{r_s} a.u. \tag{2.21}$$

which is derived from the exchange energy density in a homogeneous electron gas, with $r_s = (3/4\pi n)^{1/3}$ and is a measure of average interelectronic distance. The correlation component, ϵ_c, is more complex and is commonly based upon the results of Quantum Monte Carlo (QMC) calculations for homogenous electron gases of varying density[101].

The electron density in solids and molecules is generally quite close to a superposition of atomic densities, which is far from uniform, and may even involve a cusp at the nuclei. This lead to an initial skepticism as to the usefulness of these approximations, however it has been shown by application that they generally lead to a correct prediction of trends in properties such as structures, bond lengths and vibrational frequencies[97].

For systems with increasingly larger and smother density the L(S)DA performs increasingly better. If, however, a system has substantial gradients in the density it becomes increasingly less accurate, a failing which is addressed by the use of the generalized gradient approximation, dealt with in the next section.

Generalized Gradient Approximations (GGA)

One of the earliest alternatives to calculating E_{xc} using the L(S)D formalism was the GGA method. In this formalism the second order approximation to E_{xc} is written

$$E_{xc}^{GGA}(n) = \int d\vec{r}\epsilon_{xc}(n, |\nabla n|, \nabla^2 n) \tag{2.22}$$

In the development of GGA functionals, two opposing views of how best to proceed with the improvement of exchange-correlation functionals developed. The first was that the search for a functional is extremely difficult and that the most fruitful path would be to develop functional forms with parameters adjustable to fit experimental data. Such a pragmatic approach has been extremely popular, as evidenced by the propensity for the use of parameterized models, such as BLYP[102, 103] and PBE[104]. The second approach consists in building upon the positive elements of the LSD approximation, as exemplified by the PBE[104] functional.

GGA generally leads to improved bond angles,lengths and energies as compared to LSD. Particularly in the case of hydrogen and other weak bonding interactions between closed shell systems. They do however still suffer from some of the deficiencies of LSD such as the self interaction problem.

Hybrid Methods

One of the most popular recent developments in DFT has been to incorporate a fraction of HF exchange, which is calculated exactly:

$$E_{xc}^{Hybrid} = \alpha E_x^{HF} + E_c \tag{2.23}$$

where α can be chosen to satisfy certain criteria. The huge popularity of the B3LYP[103, 105] functional is a testament to the versatility and applicability of hybrid methods. The major criticism of hybrid DFT methods is that the percentage of HF exchange used is obtained by fitting to experimental data, as such may be considered not to be strictly *ab initio*. So for example, B3LYP which was parameterized based on heats of formation and so works well for energies but not necessarily well for other properties such as nuclear shielding constants.

2.1.3.2 Challenges in DFT

All DFT functionals have problems reproducing physical and intermolecular interactions, such as the van der Waals force. The reason for this is the incorrect asymptotical behaviour of the DFT interaction energy between multiple closed shell systems. DFT is a local or short-range potential, whereas intermolecular interactions are long-range. Corrections have been proposed to enhance the ability of DFT

to model dispersion forces such as the DFT:MP2 hybrid approach[106]. Improvements for modelling dispersion have also been proposed by the group of Lundqvist and Langreth [107]; these corrections are based on a double local density approximation. Yet another method for improved modeling of dispersion is the use of a damped dispersion function[108],

$$E_{tot} = E_{DFT} + E_{Disp} \tag{2.24}$$

with E_{Disp} given by a dispersion function which is dampened to remove unrealistic behavior at small distances.

The problem of self interaction (SI) arises in DFT due to the incomplete cancellation of electron-electron interaction arising from the Coulomb electron-electron repulsion term[109]. Molecular orbital theory methods such as Hartree Fock are inherently SI free as the exchange operator cancels out exactly the electron-electron terms arising from the Coulomb operator. However, since DFT uses approximate exchange-correlation functionals the canceling of self interaction terms is in no way guaranteed. This can be a serious problem for DFT, although some solutions have been proposed and implemented [110].

2.1.4 Semi Empirical Theory

The most expensive part of an *ab initio* calculation is the calculation of the integrals during the SCF procedure. In order to address this situation semi-empirical methods have been developed since the 1960s. These methods consist of simplifying and parameterizing these integrals in order to reduce computational cost. These methods ignore the overlap integrals in the secular equation. Thus rather than solve

$$|\mathbf{H} - E\mathbf{S}| = 0, \tag{2.25}$$

we now have the expression

$$|\mathbf{H} - E\mathbf{I}| = 0, \tag{2.26}$$

since ignoring overlap integrals reduces the overlap matrix $\mathbf{S}$ to a unitary matrix. In these equations $\mathbf{H}$ is the secular determinant, and E is any one of the set of eigenvalues. This allows for larger systems to be studied. Semi-empircal methods still maintain much of the accuracy of quantum theory, yet are fast enough to allow more systems of chemical interest to be accesed.

The next approximation which is made in semi-empirical theories is to neglect differential overlap (NDO) between different orbitals in the calculation of the Fock matrix elements, so that

$$\phi_\mu \phi_\nu d\nu = 0, \forall \mu \neq \nu. \tag{2.27}$$

If the orbitals are located on the same atom, this is called monatomic overlap, if they are located on different atoms it is called diatomic overlap, this gives rise to many of the common acronyms in semi-empirical theory.

One of the earliest implementations of semi-empirical theory was by Pople *et al.* [111] who employed a complete neglect of differential overlap (CNDO) method. In order to correct for the fact that CNDO makes no allowance for interactions between electrons with the same spin, Pople *et al.*improved the model with intermediate neglect of differential overlap (INDO)[112] and also neglect of differential diatomic overlap only (NDDO)[111].

The next step for semi-empirical theories came not through a major change in the model, but rather through a re-parameterization of the integrals based upon more experimental data, resulting in the modified INDO or (MINDO) [113] and modified NDDO (MNDO)[114] models.

The AM1, which is employed for the calculations in this thesis, is based on MNDO, but introduces Gaussian functions placed both on and between nuclei in order to modify core-core interactions.

2.1.5 Basis Sets

It would be negligent when introducing *ab initio* methods to overlook an explanation of basis sets which, after the choice of method, are the most important factor in setting up a calculation and a continual source of controversy and debate.

As stated earlier, basis sets are sets of basis functions which are combined to give a wave function. There exist two major types of basis sets; plane wave basis sets and atom centred basis sets. We will concentrate primarily on the latter as they are more commonly used in liquid and gas phase calculations. Atom centred basis sets are comprised of atomic functions representing the electron population at a given distance from the nucleus and can be thought of as being atomic orbitals. There are a number of different types of atom centred basis functions available. One obvious choice are Slater type orbitals (STOs) which are of the form:

$$R(r) = Nr^{n-1}e^{-\zeta r} \tag{2.28}$$

where n is the principal quantum number, N is a normalization constant, r is the distance from the nucleus and ζ is a constant related to the atomic charge of the nucleus. Unfortunately STOs are often impractical for quantum chemical calculations as some of the integrals are difficult to compute and must be obtained numerically.

By far the most popular type of basis sets used in quantum chemistry are those based on Gaussian functions, Gaussian type orbitals (GTOs), these have the form:

$$R(r) = x^a y^b z^c e^{-\alpha r^2} \tag{2.29}$$

α determines the spread of the function, r is the distance from the nucleus, x, y, z are cartesian variables and a, b, c determine the order of the function. If $a+b+c = 0$

then the function is zeroth order, and one such function exists. If $a + b + c = 1$ the function is first order and three such functions exist. Zeroth order functions are equivalent to s orbitals, first order functions to p_x, p_y and p_z orbitals and so on up the orders.

As also stated earlier, it is common, in practice, to expand basis sets beyond occupied orbitals to improve the accuracy of *ab initio* calculations. The basis set can be expanded in a number of ways. One way is to split each of the functions in the basis set. If the functions are split once this is known as a double zeta basis set; basis sets up to quadruple zeta are commonly used. An alternative approach, which is highly popular, is to split only the basis sets used for valance electrons, the rationale being that the chemical properties of interest are affected by the valance, rather than the core, electrons. This approach is known as the split valance approach and is so popular that it has its own notation, exemplified by the label 3-21G, which means that core electrons are teated with 3 functions, whilst valance electrons are treated with functions split into two contracted and one valence Gaussian. Popular examples of this type of basis set are 3-21G, 4-31G and 6-31G.

Simply increasing the number of basis functions may not necessarily improve the model and there are other factors which must be considered when issues such as orbital mixing are involved. For example, in an isolated hydrogen atom the electron cloud is spherical. However as the atom approaches another hydrogen atom this becomes distorted and the cloud takes on some p orbital character or is said to be sp hybridized. In order to account for this we introduce what are called polarization functions, which have higher angular quantum numbers. Thus the polarization function for a hydrogen atom corresponds to a p orbital function, and to a d orbital function for first and second row atoms. The use of polarization functions is denoted by an asterix. Hence the 6-31G basis with added polarization is denoted 6-31G*.

A final complication which we will consider is that of species with lone pairs of electrons. These lone pairs reside far away from the nucleus and are poorly represented by Gaussian functions, as they decay quickly when moving away from the nucleus. The solution is to add highly diffuse functions. These are denoted by a +, so the 6-31G* basis set with added diffuse functions for heavy atoms is denoted 6-31+G*.

When modelling periodic systems, basis sets of the plane wave form are usually chosen. The general form of such basis sets is:

$$\psi(r) = \sum_G c_G exp(i(k + G)r) \tag{2.30}$$

Where G are the reciprocal space lattice vectors, k is a wave-vector and c_G are constants to be optimized during the SCF procedure. In this case the basis function is continuous and not centred on the atom as with Gaussian type basis sets.

2.1.6 Pseudopotentials[115]

A common simplification employed in plane-wave basis set calculations and atom-centred basis set calculations of large atoms is to consider the core electrons as an effective potential combined with the nucleus, thus reducing the number of integrals to be calculated and simplifying the calculation, hopefully without affecting the properties of interest. The interaction of the valance electrons with the ionic core is represented by means of the pseudopotential, which is a potential constructed in such a way that: Kohn-Sham eigenvalues for valance electrons are unchanged; valance wave functions are as smooth as possible and states of lowest energy are valance, not core, states. Furthermore pseudopotentials must reproduce scattering properties of the actual potential, not only at energies of atomic valance states, but over a range of typically 10-20 eV. This can be achieved by satisfying the condition

$$\int_{|r|<R} |\psi_{PP}(\mathbf{r})|^2 d\mathbf{r} = \int_{|r|<R} |\psi_{AE}(\mathbf{r})|^2 d\mathbf{r} \tag{2.31}$$

where $\psi_{PP}(\mathbf{r})$ is the pseudopotential wave function and $\psi_{AE}(\mathbf{r})$ is the all-electron wave function and where $R > r_{core}$; called the condition of norm conservation. Pseudopotentials are separated into local and non-local parts, which improves efficiency by reducing the number of integrals which must be calculated. Pseudopotentials are constructed from DFT calculations on free atoms.

The pseudopotentials implemented in the cp2k package (which is used for the calculations herein) are the Goedecker, Teter and Hutter (GTH) potentials, which depend on only 4 parameters which have been optimized with respect to atomic all-electron wave functions from fully relativistic DFT calculations. The emphasis in the construction of these pseudopotentials is on accuracy. Hence they may be considered 'hard' pseudopotentials which are computationally demanding for plane wave methods. However as the gaussian and plane wave method (which is used by cp2k) computes the kinetic energy and short range pseudopotential terms analytically from Gaussian basis, it is less sensitive to the expense incurred due to hardness.

2.1.7 Gaussian and Plane Wave (GPW) Method[116]

The GPW method utilizes both types of basis set mentioned previously as representations of the electron density, allowing for efficient treatment of electrostatic interactions. The density $n(\mathbf{r})$ is represented by an expansion of atom centered Gaussian functions and plane waves. The Kohn-Sham energy expression within the GPW method is

$$E[n] \quad = E^T[n] + E^V[n] + E^H[n] + E^{XC}[n] + E^{II} \tag{2.32}$$

$$
\begin{aligned}
&= \sum_{\mu\nu} P^{\mu\nu} \langle \varphi_\mu(\mathbf{r}) | -\tfrac{1}{2}\nabla^2 | \varphi_\nu(\mathbf{r}) \rangle \\
&+ \sum_{\mu\nu} P^{\mu\nu} \langle \varphi_\mu(\mathbf{r}) | V_{loc}^{PP}(\mathbf{r}) | \varphi_\nu(\mathbf{r}) \rangle \\
&+ \sum_{\mu\nu} P^{\mu\nu} \langle \varphi_\mu(\mathbf{r}) | V_{nl}^{PP}(\mathbf{r}, \mathbf{r}') | \varphi_\nu(\mathbf{r}') \rangle \\
&+ 2\pi\Omega \sum_G \frac{\tilde{n}^*(\mathbf{G})\tilde{n}(\mathbf{G})}{G^2} + \int e^{XC} \mathbf{r} d\mathbf{r} \\
&+ \tfrac{1}{2} \sum_{i \neq j} \frac{Z_I Z_J}{\mathbf{R}_I - \mathbf{R}_J}
\end{aligned}
$$

The terms on the right hand side of the first line are respectively: electronic kinetic energy; electronic interaction with ionic cores; electronic Hartree energy; the exchange-correlation energy; and the interaction energies between ionic cores. The electronic interaction with the ionic cores is split into a local and non-local part, described by norm-conserving pseudopotentials (see previous section), $V_{loc}^{PP}(\mathbf{r})$ and $V_{nl}^{PP}(\mathbf{r}, \mathbf{r}')$, respectively.

The terms contributing to electrostatic energy are treated simultaneously with Quickstep using the Ewald sum method [117], with the long range part treated in reciprocal space and the short range part treated in real space.

The exchange and correlation energy term (E^{XC}) is treated in quickstep by gradient approximations (GGA) and meta-GGAs such as BLYP [102, 103], PBE [104], HCTH [118], etc. In the simulations presented in this thesis the BLYP functional is employed.

2.1.8 Thermochemistry[119]

The total energy value which is obtained from any *ab initio* method, E_{eq}, is the sum of electronic and nuclear-nuclear repulsion energies at 0K, for molecules isolated and in vacuum.

$$E_{eq} = E_{el} + E_{n-n} \tag{2.33}$$

This restricts the "chemical space" to which such methods can be applied, and excludes the vast majority of chemical systems of interest for study. Although these values can be considered a reasonable approximation, it is desirable to have methods which can be used to convert these results into "useful" (physical) results. In a later section (2.5) methods for simulating the system in environments other than *in vacuo* will be explored, this section will deal specifically with methods to derive thermochemical data from 0K calculations.By using statistical mechanics to incorporate vibrational, rotational and translational energies, through partition functions, thermodynamic quantities can be calculated for the systems which have been modeled.

The vibrational contribution to the internal energy is calculated from the zero kelvin potential energy surface. By applying the harmonic oscillator approximation, the vibrational frequencies of the normal modes of vibration can be calculated, and hence vibrational, rotational and translational partition functions, energies,

entropies and heat capacities can be calculated. We begin by considering the vibrational contribution. There are two sources of vibrational energy in a system, the first corresponds to zero point energy and the second to additional vibrational contributions as temperature increases from zero to T kelvin. i.e.

$$E_{vib} = ZPE + E_{vib}(0 \rightarrow T) \tag{2.34}$$

At a temperature of greater than zero kelvin, a molecule will rotate and translate also. By assuming equipartition of energy, energies for rotation and translation E_{rot} and E_{tr} are calculated.

The internal energy at temperature, T, is :

$$U = E_{eq} + [E_{vib} + E_{rot} + E_{tr}] \tag{2.35}$$

or partitioning the vibrational energy

$$U = E_{eq} + [ZPE + E_{vib}(0 \rightarrow T) + E_{rot} + E_{tr}] \tag{2.36}$$

Assumption of ideal gas behaviour leads to an expression for enthalpy:

$$H = U + pV = U + RT \tag{2.37}$$

Thus the Gibbs free energy may be calculated.

$$G = H - TS \tag{2.38}$$

2.2 Molecular Mechanics[90]

As discussed in the section on *ab initio* modelling, a major drawback of modelling techniques is that they become prohibitavily expensive as the system size increases or as the desired length of the simulation(in the case of Molecular Dynamics) increases. In such scenarios, where *ab initio* methods prove impossible, a common alternative is to use Force Field models or Molecular Mechanics (MM). MM models achieve their improved effeciancy by ignoring the contribution of electron motions [3], and thus consider the potential energy of the system as a function of only the nuclear co-ordinates. MM methods then consider the the interactions within the system as being described by a number of functional forms relating to contributions such as bond stretching, the opening and closing of angles etc. A typical force field has the form:

$$E_{sys} = E_{elec} + \underbrace{E_{str} + E_{bend} + E_{tor}}_{E_{bonding}} + E_{vdW} \tag{2.39}$$

where: E_{elec} is the energy due to electrostatic interactions between the elements of the system; $E_{bonding}$ is the bond energy of the system and typically comprises of

[3] this is almost true, although there are some approximations which may be employed(see 2.2.2.3)

terms due to stretching (E_{str}), bending (E_{bend}), and torsion (E_{tor}) of the interatomic bonds involved in the system. E_{vdW} is the van der Waals energy of the system. All of these various energies are described by a potential in which there are certain parameters which are usually fitted to reproduce empirical or *ab initio* values. A key factor in determining the success of a given force field is its transferability, that is its ability to model systems beyond those for which it has been empircaly fitted. We shall now consider in more detail the various terms in equation 2.39.

2.2.1 Bonding Terms

As stated above the bonding terms usually feature contributions due to bond stretching bending and torsion. The idea is that these properties can be assigned equilibrium values which they would maintain in the absence of any other forces, a given potential is then applied to penalise the system for any perturbation away from this reference value. As torsional contibutions are not considered in the models used during the course of this thesis the discussion shall be limited to bond stretching and bending.

The potential energy of a typical bond as a function of the interatomic separation is classified as the bond stretching contribution to the total system energy and is described particullarly well by the Morse potential:

$$V(r) = D_e[1 - exp[-a(r - r_0)]]^2 \tag{2.40}$$

in which D_e is the depth of the potential energy well minimum and $a = \omega\sqrt{\mu/2D_e}$, where μ is the reduced mass and ω is the frequency of bond vibration, which is related to the force constant of the bond k, by $\omega = \sqrt{k/\mu}$. r_0 is the equilibrium value of the bond. This is the form of the potential which is used in this thesis, however it is quite common for bond stretching to be described by a more simplistic model in cases where the bond length is not expected to deviate from the equilibrium value significantly, in such cases Hooke's law is commonly employed

$$V(r) = \frac{k}{2}(r - r_0)^2 \tag{2.41}$$

Hooke's law is also used to describe the deviation of a bond angle from a given reference value, in this case interatomic setaration (r) is replaced by bond angle (Θ):

$$V(\Theta) = \frac{k}{2}(\Theta - \Theta_0)^2 \tag{2.42}$$

The distortion of a bond angle is rather less energetically unfavourable than bond stretching or compressing a fact reflected by the generally lower values for force constants in bond angle, as opposed to bond stretching potentials.

2.2.2 Non-Bonding Interactions

Non-bonding interactions do not depend on any bonding interation between atoms and are "through space" interactions, they are usually divided into two categories; electrostatic interactions and van der Waals interactions and generally depend on interatomic separation in some inverse manner.

2.2.2.1 Electrostatic Interactions

Electrostatic interactions arise due to the fact that different components of the system have different affinities for electrons (electronegativity), resulting in an uneven charge distribution. One common way to model this is to assign fractional point charges to the different nucleii according to their electronegativity. Thus for a water molecule which is neutral overall, the oxygen atom is considered to posess a net negative charge equal to the sum of a net positive charge on the hydrogen atoms. Within this paradigm it is then possible to consider the electrostatic interaction between two atoms using Coulomb's law:

$$V = \sum_{i=1}^{N_A} \sum_{j=1}^{N_B} \frac{q_i q_j}{4\pi\epsilon_0 r_{ij}} \tag{2.43}$$

Where N_A and N_B are the number of point charges in each atom, q_i and q_j are the values of the point charges, r_{ij} is the separation between the charges and ϵ_0 is the permativity of free space. One problem with this method of calculation is that the sum is not necessarily convergent over all values when one considers a system using periodic conditions. A common method for overcoming this is the Ewald summation method [117] which considers the charges in reciprical space as well as in real space, resulting in the summation becoming definitely convergant and hence calculable.

2.2.2.2 Van der Waals Interactions

Van der Waals interactions arise as a consequence of the Pauli exclusion principle, which results in interatomic electron density being reduced as nucleii approach, which in turn results in a repulsive interaction between two partially sheilded nucleii. This effect can be modeled using high level quantum mechanical calculations, however, as the essence of potential models is be be readily calculable, we require a simple potential form for calculating this component of the overall system energy. Perhaps the most widely used potential for representing the van der Waals interaction is the Lennard Jones potential:

$$v(r) = 4\epsilon[(\frac{\sigma}{r})^{12} - (\frac{\sigma}{r})^{6}] \tag{2.44}$$

in which r is the interatomic separation, and also two adjustable parameters, σ; the collision diameter, and ϵ; the well depth which is the minimum of the potential

energy. The expression obviously contains an attractive and a repulsive component. The attractive part which varies to the power of 6 can be theoretically justified from arguments arising from treatment of dispersion with models such as the Drude model. The repulsive 12 power term is less readily justified on a theoretical basis, as quantum treatments suggest a repulsive component which decays exponentially. However the use of a power of 12 can be justified on pragmatic grounds when considering large systems as this term is readily computed by squaring the power 6 term. Since the systems treated during the course of this thesis are not "large" enough to justify this simplification the more realistic Buckingham Potential is used to calculate van der Waals interactions, where repulsion is indeed calculated using an exponential function:

$$v(r) = \epsilon[\frac{6}{\alpha - 6} exp[-\alpha(r/r_m - 1)] - \frac{\alpha}{\alpha - 6}(\frac{r_m}{r})^6] \tag{2.45}$$

This expression contains three adjustable parameters, ϵ is as in the Lennard-Jones potential, r_m is the separation at which the potential energy is a minimum, and α. The major drawback of the Buckingham Potential is that after a certain cutoff distance the attractive term becomes strongly dominant resulting in a large attractive energy which leads to the fusing of nuclei, thus it is common to have a cutoff separation below which the Buckingham potential term is not employed.

2.2.2.3 The Shell Model

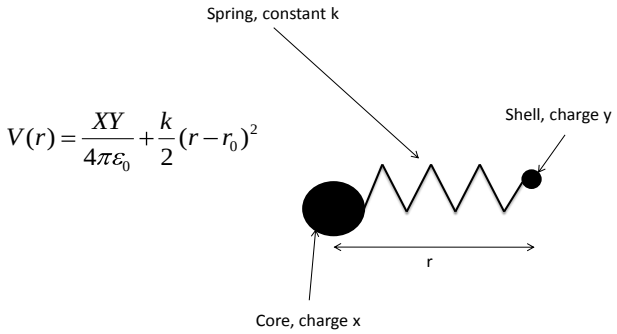

Figure 2.4: The shell model, the nucleus and the shell interact through an electrostatic interaction and a harmonic spring.

As stated earlier electron contributions are generally ignored in molecular mechanics models. However in some systems the polarization of particular atoms can have a significant effect on the system and in such cases it would be advantageous to include the effects of polarization of the electon cloud in some way. One method for

achieveing this with relatively little additional computational expense is to employ the Shell Model of Dick and Overhauser [120]. This model considers the electon cloud as a point charge attached to the nucleus via a harmonic spring(figure 2.4).

2.3 Energy Minimization[90]

The energy minimization problem is this: given a system with energy E which depends on independent variables $x_1, x_2, \ldots, x_i$, find the values of x_i for which E is a minimum. At a minimum point the first derivatives with respect to x_i of E are zero and the second derivatives are positive:

$$\frac{\partial E}{\partial x_i} = 0; \frac{\partial^2 E}{\partial x_i^2} > 0 \tag{2.46}$$

For standard analytical functions these values may be found by calculus methods, however given that the energy in chemical systems is dependent on the cartesian coordinates of the atoms involved, the energy functions of interest are much more complex and must be found by numerical methods. Numerical methods in principle involve varying the coordinates until these conditions are met. This still seems like a simple enough proposition, however there exists another, more challenging, problem as represented in figure 2.5; it is this, in a potential energy landscape there generally exists more than one point where the criteria for a minimum are met. In this case we have both local and global minima, the global minimum being the minimum of the minima. The question now is how can we be sure that the minimum which we have found is a global minimum. The answer, in short, is we can't, not without exploring the full energy landscape. However if we can be sure that we have sampled enough of the potential energy landscape then we can be confident in our global minimum. So now we must sample the energy landscape to a suitable extent, this is not a trivial problem given the expense incurred in electronic structure calculations. In many cases it is more practical to sample the energy landscape using cheaper molecular mechanics methods followed by an electronic structure refinement of the lowest energy configurations from these calculations. However, as computer resources improve and more sophisticated and cost effective electronic structure methods are developed, the goal of full energy landscape exploration by *ab initio* methods is becoming more feesible. As molecular dynamics are dealt with elsewhere we will not look at them here but rather explore yet another restricting factor in energy landscape sampling.

This sampling problem is confounded by the energy barriers which exist in the energy landscape, it is entirely possible that during the course of a dynamics simulation a system may become stuck in an energy well which is not the global minimum, but which has an energy barrier too high to allow escape. We will consider first methods which are used to search for a local minimum then later consider methods which can be used to sample larger areas of the potential energy surface.

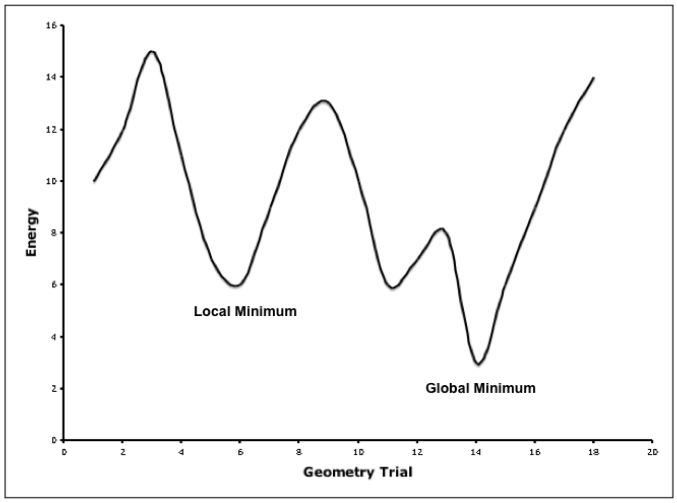

Figure 2.5: A 2D schematic representation of the global versus local minimum problem.

2.3.1 Local Minima Searching

The methods we shall consider for local minimum searching are both what are called first order minimization methods, the steepest descent method and the conjugate gradient method. They are called first order methods as they locate the minimum by following the first derivate of the potential energy. The methods start from a configuration k which can be represented by a multi-dimensional vector x_k.

2.3.1.1 The Steepest Descent Method

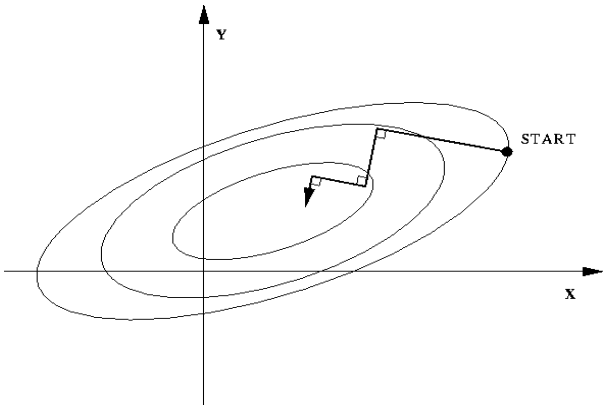

Figure 2.6: The steepest descent method of energy minimization, the algorithm follows the gradient of the function to the minimum value in the centre[a].

[a]Figure adapted from http://trond.hjorteland.com/thesis

The steepest descent method (figure 2.6) proceeds by following the direction paralell to the net force on the system calculated for each iteration, which is equivalent to walking down a hill in the steepest direction, this can be represented by a unit

vector s_k defined by the gradient vector g_k

$$s_k = \frac{-g_k}{|g_k|} \tag{2.47}$$

2.3.1.2 The Conjugate Gradient Method

The method of steepest descent has a major disadvantage when the minimum is located in a long narrow valley, in this case the steepest descent method can yield configurations which oscillate about the minimum without satifying the convergence criteria. In a conjugate gradients minimization the gradients at each step are orthogonal and conjugate to the gradient at the previous step.The method moves in a direction v_k from a point x_k, where v_k is calculated from the gradient at the point k and the gradient from the previous direction v_{k-1}:

$$v_k = -g_k + \gamma_k v_{k-1} \tag{2.48}$$

where γ_k is a scalar given by:

$$\gamma_k = \frac{g_k \cdot g_k}{g_{k-1} \cdot g_{k-1}} \tag{2.49}$$

Within these expressions all gradients and directions must conform to the following constraints:

$$g_i \cdot g_j = 0 \tag{2.50}$$

$$v_i \cdot \mathscr{V}''_{ij} \cdot v_j = 0 \tag{2.51}$$

$$g_i \cdot v_j = 0 \tag{2.52}$$

In which $\mathscr{V}''_{ij}$ is a matrix of vectors representing the second derivative of the potential in the direction of i and j. As the conjugate gradient method relies on information from the previous step it is obviously necessary to begin with the initial step using another method, in our case the steepest descent method.

2.4 Molecular Dynamics[90]

Newton's laws of motion can be stated as follows:
1. A body continues to move in a straight line at constant velocity unless a force acts upon it.
2. Force equals the rate of change of momentum.
3. To every action there is an equal and opposite reaction.

The trajectory of a body can be obtained by solution of the differential equations contained within the expression $F = ma$ where F is force, m is mass and a is acceleration;

$$\frac{d^2x_i}{dt^2} = \frac{F_{x_i}}{m_i} \tag{2.53}$$

which describes the motion of a body of mass m_i along one coordinate x_i with the force in that direction being F_{x_i}

The idea behind moelcular dynamics is that we can solve Newton's Laws of Motion for a system of interacting bodies, in our case the chemical system of interest, and calculate a trajectory for the components of the system in time. The first practical difficulty which we encounter in trying to realise this idea is that our systems consist of many bodies, which are under the influence of a continous potential with all particle motions coupled together, the method which we use to tackle this problem is called the finite difference method.

2.4.1 Finite Difference Methods

The core idea of the finite difference method is that we can break the course of a trajectory into individual stages separated by a small, constant, time step δt. By then claculating the forces on the particles at a time t we can calculate a trajectory, which we use to propagate the positions of the particles and obtain a new configuration $r(t+\delta t)$. The forces are assumed constant during the timestep and at the new configuration forces are once again calculated and the next configuration $r(t+2\delta t)$ is calculated.

There exist many algorithms for solving the equations of motion using finite differences, although all share the assumption that the postitions and dynamic properties of the system can be approximated using a Taylor expansion:

$$r(t+\delta t) = r(t) + \delta t v(t) + \frac{1}{2}\delta t^2 a(t) + \frac{1}{6}\delta t^3 b(t) + \ldots \quad (2.54)$$

$$v(t+\delta t) = v(t) + \delta t a(t) + \frac{1}{2}\delta t^2 b(t) + \frac{1}{6}\delta t^3 c(t) + \ldots \quad (2.55)$$

$$a(t+\delta t) = a(t) + \delta t b(t) + \frac{1}{2}\delta t^2 c(t) + \frac{1}{6}\delta t^3 d(t) + \ldots, \quad (2.56)$$

in which v is the velocity (first derivative of position with respect to time), a is the acceleration (second derivative), b is the third derivative of position with respect to time etc. The most popular method for solving the equations of motion is probably the Verlet Algorithm[121], which uses the positions and accelerations from the previous step, $r(t-\delta t)$ and $a(t-\delta t)$ to calculate the postitions at $t+\delta t$. We can state the following relationships:

$$r(t+\delta t) = r(t) + \delta t v(t) + \frac{1}{2}\delta t^2 a(t) + \ldots \quad (2.57)$$

$$r(t-\delta t) = r(t) - \delta t v(t) + \frac{1}{2}\delta t^2 a(t) + \ldots \quad (2.58)$$

which combined lead to

$$r(t+\delta t) = 2r(t) - r(t-\delta t) + \delta t^2 a(t) \quad (2.59)$$

Clearly the Verlet algorithm will not calculate explicitly the velocities, and these

must be calculated retrospectively using the difference between configurations $r(t+\delta t)$ and $r(t-\delta t)$ divided by the time.

$$v(t) = [r(t+\delta t) - r(t-\delta t)]/2\delta t \tag{2.60}$$

The Verlet algorithm has the advatages that its implimentation is straightforward and its memory requirements quite modest. However, it does have a number of inherant probelems, particularly that new configurations are calculated from the difference between two relatively large terms, $2r(t)$ and $r(t-\delta t)$ and one relatively small term, $\delta t^2 a(t)$, which can lead to a loss in precision. Other difficulties arise from the fact that velocity must be calculated retrospectively and that the method relies on the previous step and thus is not a self-starting algorithm.

One variation on the Verlet algorithm which attempts to address the question of precision is the so called "leap-frog" algorithm wich uses the following relationships:

$$r(t+\delta t) = r(t) + \delta t v(t+1/2\delta t) \tag{2.61}$$

$$v(t+\delta t) = v(t+1/2\delta t) + \delta t a(t) \tag{2.62}$$

To impliment the algorithm, the velocities at $t+\delta t$ are calculated from the positions at $t-1/2\delta t$ and the acceleration at t. The positions are then calculated from these velocities and the positions at t and the velocities are calculated from:

$$v(t) = \frac{1}{2}[v(t+1/2\delta t) + v(t-1/2\delta t)] \tag{2.63}$$

That is the velocities must leap over the positions at t to caculate their values at $t+1/2\delta t$. The advantages over the standard Verlet algorithm are that the velocity is included explicitly and that the differences needed to calculate the trajectory are smaller, thus precision is improved.

2.4.2 Molecular Dynamics Ensembles

Molecular dynamics is traditionally performed using an ensemble (a collection of states) with constant number of particles (N), volume (V) and total energy (E), known as an NVE ensemble. Conversion between results from ensembles with different quantities held constant is possible, but only strictly in the thermodynamic limit, i.e. infinite system size. As the thermodynamic limit is clearly not practical for simulation purposes, different ensembles may be employed depending on the system and properties desired from that simulation. In the case of the simulations performed in the course of this thesis the properies we are interested in are calculated in the NVT ensemble. In the case of simulations using classical potentials the equilibrium volume is determined by an equilibration run in the NPT ensemble where the volume is allowed to fluctuate, so as to equilibrate system pressure, the production run is then performed in the NVT ensemble. In the case of *ab initio* dynamics the volume is chosen to give experimental densities.

2.4.3 Constatnt Temperature Dynamics

It is often desireable to maintain a constant temperature during a molecular dynamics simulation. This may be the case because temperature effects are being simulated, or during simulated annealing in which the minimum is located by succesivly running the simulation at lower temperature. In our case, the experiments to which the simulations relate are generally constant temperature experiments, thus to simulate them as faithfully as possible a constant temperature dynamics is required. We will now consider a number of methods which can be employed to regulate the temperature.

The temperature of a system is related to the average kinetic energy of the particles in that system:

$$\langle K \rangle_{NVT} = \frac{3}{2} N k_B T \tag{2.64}$$

where $\langle K \rangle_{NVT}$ is the average kinetic energy, N is the number of particles, k_b is the Boltzmann constant and T is temperature. Thus one immediately apparent and obvious way to change the temperature of a system is to change the velocities of the particles which constitute it, as this will change the kinetic energy. If we have a system at time t with temperature $T(t)$ and the velocities are multiplied by a factor λ, the resultant temperature change can be calculated from the expression

$$\Delta T = \frac{1}{2} \sum_{i=1}^{N} \frac{3}{2} \frac{m_i (\lambda v_i)^2}{N k_B} - \frac{1}{2} \sum_{i=1}^{N} \frac{3}{2} \frac{m_i v_i^2}{N k_B} \tag{2.65}$$

which leads to

$$\lambda = \sqrt{T_{new}/T(t)} \tag{2.66}$$

so the simplest way to reach a desired temperature T_{req} is to multiply the velocities by a factor $\lambda = \sqrt{T_{req}/T(t)}$.

This method can be considered somewhat brutal as it rescales temperatures at all times to the required temperature with no allowance for a fluctuation about the desired value, a refined version of this idea was introduced by Berendensen *et al.*[122] in which the system is coupled to an external heat bath which is fixed at the desired temperature and regulates the system by a flow of thermal energy between the system and the bath. The velocities at each step are scaled so that the change in velocities is proportional to the difference in the temperatures of system and bath, the proportionality constant τ defines how tightly the system and the bath are coupled. In this scheme the scaling factor is calculated from

$$\lambda^2 = 1 + \frac{\delta t}{\tau} \left(\frac{T_{bath}}{T(t)} - 1 \right) \tag{2.67}$$

where δt is the timestep. Strictly speaking however, neither of these methods produce canonical ensembles, and as such are employed only in the initial equilibration

stage of an MD simulation. The rescaling of velocities can artificially preserve temperature differences between components of the system, resulting in the phenomenon of hot solvent and cold solute. One method which can be employed in order to generate a rigourous cannonical ensemble is the extended system method.

The extended system method was introduced for constant temperature dynamics by Nosè and Hoover [123, 124]. In this method the temperature bath is considered as an intrinsic part of the system and treated as an extra degree of freedom, s. The kinetic (k_{res}) and potential (V_{res}) energies of the reservoir are given by

$$V_{res} = (f+1)k_BT\ln s \tag{2.68}$$

$$k_{res} = (Q/2)(ds/dt)^2 \tag{2.69}$$

where f is the number of degrees of freedom in the physical system and Q is a parameter which can be considered as the fictitious mass of the reservoir. The magnitude of Q determines the degree of coupling between the physical system and the reservoir. In the limit of infinite Q the situation is that of conventional dynamics and the system and reservoir do not inteact.

Each state generated in the extended system corresponds to a state in the real, physical system. However, velocities and times in the real and extended systems are not directly related. The timestep of the real and extended systems, δt and $\delta t'$ respectively are related by

$$\delta t = s\delta t', \tag{2.70}$$

and as the value of s can fluctuate, so too does the physical timestep.

2.4.4 Constant Pressure Dynamics

As mentioned earlier, constant pressure dynamics are used in the simulation herein in order to establish an equilibrium volume. They are also useful for simulating pressure induced phase transitions, where a number of simulations at constant pressure are required.

Many of the methods for regulating system pressure are similar to those for temperature regulation. In this case pressure is maintained by adjusting volume, just as temperature was maintained by adjusting velocity. Berendsen [122] also introduced an expression for a rate of change of pressure in a system coupled to a pressure bath. In this scheme the volume is scaled by λ:

$$\lambda = 1 = \kappa\frac{\delta t}{\tau_P}(P - P_{bath}), \tag{2.71}$$

where κ is the isothermal compressability, and can be comined with the relaxation constant, τ_P. Scaling the volume by λ is equivalent to scaling the atomic coordinates by $\lambda^{1/3}$

$$r_i' = \lambda^{1/3}r_i \tag{2.72}$$

As with constant temperature dynamics there is also an extended system approach to constant pressure dynamics, introduced by Andersen [125]. Again the system is coupled to an extra degree of freedom, in this instance the kinetic and potential energies of the pressure reservoir, k_{res} and V_{res} respectively are given by

$$V_{res} = \frac{1}{2}Q(dV/dt)^2 \tag{2.73}$$

$$k_{res} = PV \tag{2.74}$$

where P and V are pressure and volume and Q is, once again, the fictitious mass of the coupled reservoir and, as before, determines the degree of coupling between reservoir and physical system. In the extended system method, the coordinates of the extended and physical system, r'_i and r_i respectively are related by

$$r'_i = V^{1/3} r_i \tag{2.75}$$

2.4.5 *Ab Initio* Molecular Dynamics (AIMD)[126]

Classical molecular dynamics approaches, which use predefined potentials derived from empirical data or independent electronic structure calculations to elucidate the the evolution of a many-body system with time, is a well established and powerful tool in molecular modeling. The traditional route followed by such approaches involves breaking up the full system interactions into two,three and many-body, and Coulombic and short-range etc (as described in section 2.2) contributions to be represented by suitable functions. Despite the tremendous success of such methods a number of serious drawbacks exist, among the principal problems are systems in which many atomic types, and thus many potentials, are required and systems in which the electronic structure changes qualitatively with time: systems which may be considered "chemically complex".

Due to the fact that *ab initio* theories are ideally not dependent on the system or its state, they can be used to explore system states where not much is known, which makes them an interesting option for studying molecular dynamics (MD) simulations. The drawback, as ever, lies in the computational cost of such simulations which restricts the size of system and the length over which an MD simulation may be run. Furthermore, if problems are encountered due to some of the assumptions of the theory, one cannot, as with empirical methods, simply re-parameterize it. Rather we must move to a higher level of theory which further compounds the problem of computational cost.

Ab initio dynamics simulations can be viewed from a number of perspectives. They can be considered from the viewpoint of classical trajectory calculations [126]; an approach with its origins in gas phase MD in which a global potential energy surface is constructed in the first step, either empirically or using electronic structure methods. In the second step the dynamical evolution of the nuclei on this surface is

generated using classical or quantum mechanics. Such an approach however suffers from a so called "dimensionality bottleneck", arising from the fact that a system with N bodies has 3N-6 degrees of freedom, the work load for such systems increases roughly as 10^N.

The basic idea underlying practical *ab initio* MD methods which avoids the dimensionality bottleneck is to carry out electronic structure calculations "on-the-fly" as the MD trajectory is created; thus electronic degrees of freedom are treated as active and not solved beforehand. One method which can be used is to solve the static electronic structure problem at each time step, referred to as Born-Oppenheimer Molecular Dynamics (BOMD).

2.4.5.1 Born-Oppenheimer Molecular Dynamics

In BOMD the standard BO approximation as stated in section 2.1 is applied to decouple electron and nuclear motion. The electronic degrees of freedom of the system are considered to be always in equilibrium, meaning that the forces on the nuclei arise only as a result of the atomic coordinates. Thus the the forces are calculated by solving a time-independent Schrödinger equation. Leading to the following equations of motion:

$$\begin{aligned} M_I\ddot{\mathbf{R}}_I &= -\nabla_I min_{\Psi_o}\langle\Psi_o|\mathcal{H}|\Psi_o\rangle - \nabla_I E^{II} \\ E_o\Psi_o &= \mathcal{H}\Psi_o \end{aligned} \tag{2.76}$$

where M_I are the masses of the nuclei, $\mathbf{R}_I$ are the positions of the nuclei, ∇_I is the derivative with respect to $\mathbf{R}_I$, Ψ_o is the wave function, $\mathcal{H}$ is the hamiltonian, E_o is the ground state energy and E^{II} is the nucleus-nucleus interaction energy,

$$E^{II} = \Sigma_{I<J}\frac{Z_I Z_J}{|\mathbf{R}_I - \mathbf{R}_J|} \tag{2.77}$$

where Z_I is the charge of the nucleus I.

Treating the nuclei classically, they move in a potential

$$V(\mathbf{R}_I) = min_{\Psi_o}\langle\Psi_o|\mathcal{H}|\Psi_o\rangle + E^{II} \tag{2.78}$$

One can now perform a dynamic simulation, just as in classical MD, as if the atoms were moving in this potential, the only difficulty being the calculation of $V(\mathbf{R}_I)$ and $-\nabla V(\mathbf{R}_I)$. Unfortunately this is rather a large difficulty and in order to use this method for many atoms on a reasonable timescale the calculation of the ground state energy must be simplified.

The Born-Oppenheimer MD (BOMD) simulations which are presented in this thesis were run using the Quickstep module of the cp2k suite of software (CP2K)[127], which employs the GPW method as described in section 2.1.7.

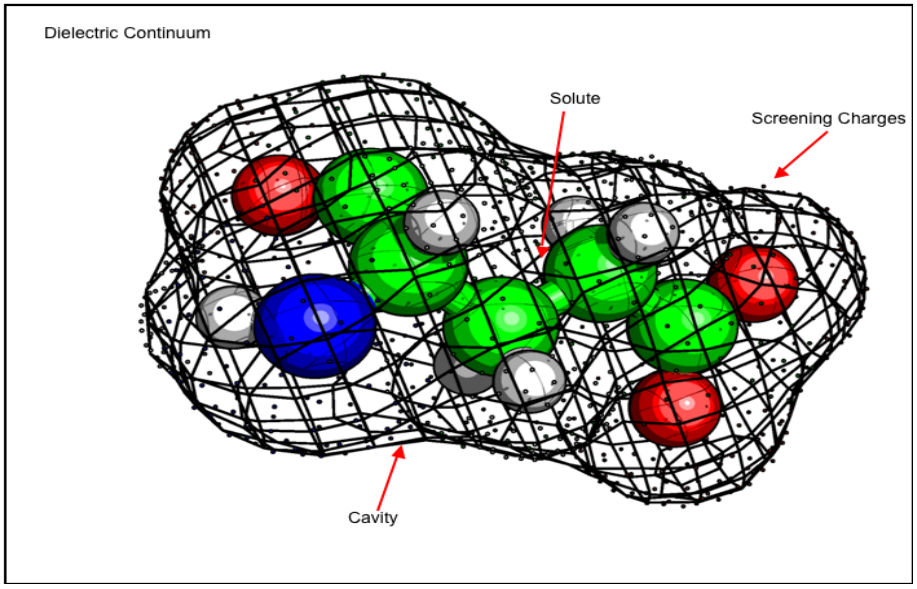

Figure 2.7: The PCM model for implicit treatment of solvent effects.

2.5 Solvation

Many chemical processes of interest, and indeed all those considered in this thesis, take place in the solution phase. It is, therefore, clearly desirable that the effects of the solvent be incorporated into calculations of any properties which we wish to consider. In this section different methods for achieving this are presented.

When representing solvation, two approaches are commonly applied. The first is to model the solvent implicitly, i.e. to include the solvent's effects directly when solving the Schrödinger equation of the system. The second is to include the solvent explicitly, i.e. to include actual molecules of solvent surrounding the system of interest. Of these methods the second clearly provides a physically more realistic scenario. However, it introduces extra particles into the system and, given the scaling constraints, can quickly become infeasible as the number of solvent molecules rises. It is also possible to consider a hybrid of the two methods in which the molecule is surrounded by a limited number of solvent molecules which in turn includes an implicit model.

2.5.1 Implicit Solvation Methods

The origins of an implicit model for solvation effects can be traced back to Born (1920) and Onsager (1936). Born[128] derived the free energy of solvation for placing a charge within a spherical cavity in a solvent and Onsager [129] extended this to a dipole within a spherical cavity. The Born model calculates solvation energy as the work done in moving a point charge from vacuum to a spherical cavity within a continuum. Whilst an extremely simple model it is, however, very effective in the case of the solvations of ions.

The Onsager model is appropriate for many more species, in this model the solute dipole inside a cavity is considered. The implementation of the Onsager model employed for the results herein is based on the Polarizable Continuum Method (PCM), specifically the integral equation formalism of the PCM (IEFPCM) [130, 131]. In the PCM model the solvent is represented by a homogenous continuum medium which is polarised by the solute placed in a cavity in the bulk of the dielectric. A complete description of solvation energy involves four terms:

$$W_T = \Delta G_{el} + G_{cav} + G_{dis} + G_{rep} \tag{2.79}$$

where W_T is the work necessary to transfer a molecule from vacuum to a fixed position in a solvent at constant temperature, pressure and chemical composition.

2.5.1.1 Electrostatic Solvation Energy

The electrostatic interactions of the solute with the solvent are taken into account through an interaction potential $\hat{V}^R$ which acts as a pertubation on the solute Hamiltonian:

$$\hat{H}^0\Psi^0 = E^0\Psi^0 \qquad in\,vacuo; \tag{2.80}$$

$$[\hat{H}^0 + \hat{V}_R]\Psi = E\Psi \qquad in\,solution \tag{2.81}$$

where $\hat{H}^0$ is the Hamiltonian of the solute in vacuo, Ψ^0 and Ψ are the solute wavefunctions in vacuo and solution respectively.

For the purpose of calculating solvent effects, the wave function is replaced with a molecular charge distribution $\rho^e_M(r)$, which is the sum of nuclear and electronic charges.

The quantum formulation of the basic electrostatic and continuum model requires the simultaneous definition of two problems, namely: (1) the quantum mechanical problem of computing the electron distribution ρ^e_M, with fixed nuclei, in the presence of the solvent reaction potential Φ_σ; (2) the electrostatic problem of determining Φ_σ and its interaction energy with ρ^e_M. We therefore have a typical nonlinear problem, as Φ_σ and $\hat{V}_\sigma$ depend in turn on ρ^e_M and the solution requires an elaboration of an appropriate strategy. The most intuitive approach consists of performing a self-consistent iterative procedure, by solving alternately the quantum problem to determine $\rho^e_M$and the classical electrostatic problem to determine Φ_σ, and is achieved by using a Self Consistent Reaction Field (SCRF).

The dipole of the solute induces a dipole in the surrounding continuum, which results in an electric field inside the cavity, which is called a reaction field. The reaction field then interacts with the solute dipole providing additional stabilization for the whole system. The SCRF model has been refined by Menucci and co-workers [130, 131] to use a cavity of the shape of the molecule which is built from a series

of spheres centred on each atom, the solute charge is then represented as a series of charge points spread out on the resulting cavity surface.

SCRF models have been applied successfully to investigate the effects of solvation in many chemical systems and for various properties. However, there are certain cases for which the continuum representation of the solvent is not sufficient: for example, if hydrophobic effects are present, the continuum model will not represent them. Another example is where specific solvent-solute interactions are important such as hydrogen bonding in water. In such cases it may be necessary to use explicit solvation.

2.5.1.2 Cavity Definition

The definition of the solute surface is also a question of the definition of the cavity which the molecule, M, occupies in the continuum and is an important consideration when implementing implicit solvation methods. The shape and size of the cavity are crucial factors with an ideal cavity able to reproduce the shape of M with the inclusion of the whole of $\rho_M^e(y)$, and the exclusion of spaces which can be occupied by the solvent. If a cavity is too large, solvent effect would be reduced, whereas a cavity which is too small introduces serious errors in the evaluation of interaction energies for portions of $\rho_M^e(y)$ near the . Similarly a cavity of the wrong shape induces distortions in the description of the reaction field. In the original PCM [131] the cavity is defined by spheres with radii R_α centered on the nuclei. The radius of the sphere R_α is proportional to the van der Waals radius :

$$R_\alpha = f R_\alpha^{(vdW)} \tag{2.82}$$

The most popular reference set of radii is the United Atom Topological Model[132]. The original value proposed for f was 1.2, this was a only rough estimate. However there is clear evidence that $R_\alpha^{(vdW)}$ should be the lower limit of the radius and that f should be slightly greater than 1 [133]. The original estimate of $f = 1.2$ was obtained by considering results for the energy decomposition [134] of a few $M \cdot S_n$ clusters (M = H_2 O, CH_3 OH, H_2 CO, NH_3, CH_3 NH_2, S = H_2 O, CH_3 OH,NH_3, CH_3 NH_2, CH_4, Ar). Subsequent work based upon studies of radial distribution functions from molecular dynamics and hydration energies of free molecules[135, 136] suggest that a value of $f = 1.2 - 1.25$ is reasonable.

For charged species the factor of f should be reconsidered because of the non-linear effects in the polarisation with high fields which may result in negative deviations from linearity, due to saturation, or positive deviations due to charge migration in the field gradient (electrostriction)[135]. These two physical effects suggest changes of the f factor in opposite directions. Studies based on super-molecule[137] and Monte Carlo[138]simulations have suggested a value of $f = 1.10 - 1.15$ and, more recently, a study[139] using HF/6-31+G(d) and the MST model has shown

that in the IEF-PCM formalism, as well as the MST model, a reduction of 8% in the cavity size relative to standard scalings for neutral species can lead to improved accuracy.

2.5.1.3 Cavitation Energy, ΔG_{cav}

ΔG_{cav}, is the hypothetical work needed to construct the cavity, defined as above, within the dielectric continuum. Several methods are available for the calculation of ΔG_{cav} based on the size and shape of the cavity and different parameters associated with the solvent in question.

The cavitation model employed in the PCM is based on the formulation of Pierotti [140] which uses an expansion in terms of the solute volume radius R_{MS}:

$$G_{cav} = K_0 + K_1 R_{MS} + K_2 R_{MS}^2 + K_3 R_{MS}^3 \tag{2.83}$$

in which the coefficients K_i are expressed in terms of solvent properties; molecular radius and numerical density, and also in terms of solution properties; pressure and temperature. This definition assumes a spherical solute, but was expanded by Claverie *et al.*[141] to account for cavities constructed from overlapping spheres:

$$G_{cav} = \sum_{1}^{n} \frac{A_i}{4\pi R_i^2} G_{cav}(R_i) \tag{2.84}$$

in which the contribution of each sphere to the overall expression scales with its exposed surface area A_i

2.5.1.4 Free Energy Changes From Continuum Methods

As the PCM and other implicit solvation models account for changes in vibrational energy by using some of the parameters for calculating the non electrostatic terms it is not meaningful to calculate free energy changes for a reaction simply by applying standard gas phase frequency techniques to an SCRF calculation. Rather frequency calculations are performed in the gas phase and solvation energies of reactants are then applied in order to obtain the free energy changes in solution. This is illustrated in figure 2.8 in which we would calculate

$$\Delta G_{sol} = \Delta G_{vac} + \Delta G_{solvB} - \Delta G_{solvA} \tag{2.85}$$

2.5.2 Explicit Solvation and Perdioc Boundary Conditions (PBCs)

If one is to model solvation explicitly by including "real" solvent molecules then an obvious question arises: how many explicit solvent molecules are necessary for a realistic representation, as the solvent molecules are obviously themselves "solvated"

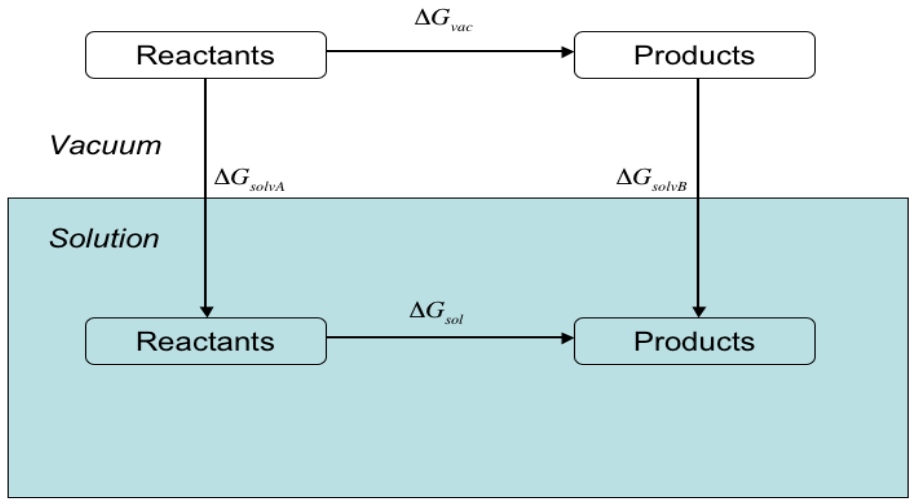

Figure 2.8: The thermodynamic cycle used to calculate free energy changes incorporating solvation energy.

by other solvent molecules and these effects too may be of importance. In some respect by including only a finite number of solvent molecules one is, in effect, only modeling a bubble of molecules within a vacuum. An elegant and relativly simple solution to this problem is to use Periodic Conditions (PBCs). This allows a relatively small number of particles to behave as if they are part of a bulk system. The molecules are placed inside a box of given dimensions, which is then surrounded by identical boxes and so on (figure 2.9). The coordinates of the particles in an image box can simply be calculated by adding or subtracting an integer to the coordinates of the original box. Should a particle leave the box it will be replaced by its image entering from the other side; thus the contents of the box remain constant. The particles in the original box now interact with particles all around them. It should be noted that the use of PBCs is not restricted to liquid phases, indeed the technique was developed in the solid state modeling community and is particularly useful when modeling crystal structures as a periodic repetition of a basic unit cell.

2.6 Calculation of Nuclear Shielding

The theory for the calculation of nuclear shielding tensors proceeds from the fact that in the presence of an external magnetic field (B) the momenta of the electrons are affected. Meaning that the usual momentum operator ($p = (\hbar/i)\nabla$) is replaced by a perturbed momentum operator

$$p' = p + \mathrm{e}A \tag{2.86}$$

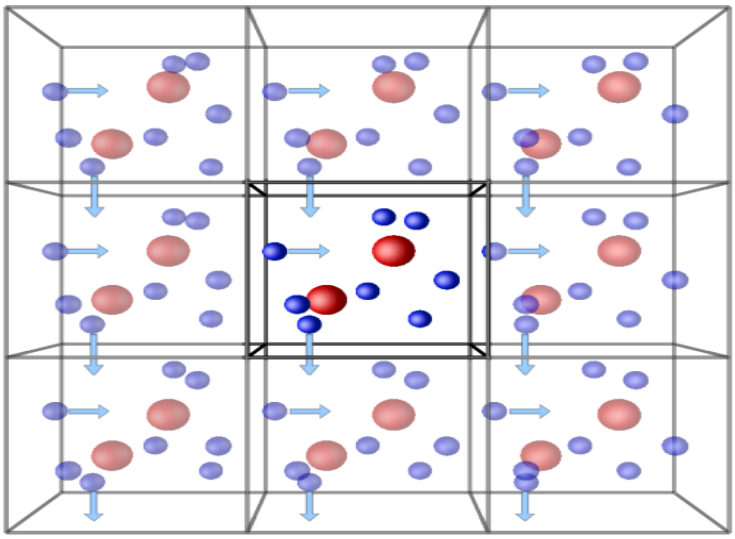

Figure 2.9: A representation of a 2D system surrounded by periodic images[a].

[a]Figure adapted from http://isaacs.sourceforge.net/phys/pbc.html

A is the vector potential due to the applied field B, and can be defined as

$$A = \frac{1}{2}B \times r, \text{div}A = 0, \text{curl}A = B. \tag{2.87}$$

The new momentum operator is substituted into the Hamiltonian for the system, and the applied magnetic field is selected to lie in the $+z$ direction. Resulting in the Hamiltonian:

$$\begin{aligned} H &= \frac{1}{2m}\sum_j (\hbar^2\nabla_j^2 + V) - \sum_j \left(B + \left(\frac{\mu_0}{4\pi}\right)\frac{2\mu}{|r_j|^3}\right)m_{zj}^0 \\ &+ \sum_j \frac{e^2}{8m}\left(B + \left(\frac{\mu_0}{4\pi}\right)\frac{2\mu}{|r_j|^3}\right)^2 (x_j^2 + y_j^2) \end{aligned} \tag{2.88}$$

where μ is the magnetic moment of the nucleus concerned. Now, H may be written as

$$H = H_0 + H_1 + H_2 \tag{2.89}$$

Where the terms on the right hand side correspond to the terms on the right hand side of 2.88. This makes explicit the fact that this problem may be treated using perturbation methods and sets the stage for solving the problem of nuclear shielding tensors using the finite perturbation theory (FPT) approach [142]. Within this approach the shielding tensor ($\sigma_{A\alpha\beta}$) is evaluated from the second order derivative of the electronic energy with respect to the nucleus magnetic moment (μ_a) and the applied magnetic field (B)

$$\sigma_{A\alpha\beta} = \left[\frac{\partial^2 E(\mu_A, B)}{\partial\mu_{A\beta}\partial B_\alpha}\right] \tag{2.90}$$

The FPT method considers a perturbed Hamiltonian $H(\lambda)$ expressed in terms of a number of external perturbations $\lambda_1, \lambda_2, \ldots$ and the corresponding operators

$H_1, H_2, \ldots$. Using the Hellmann-Feynmann theorem it is then possible to calculate the derivatives, finally leading to the expression

$$\left[\frac{\partial^2 E(\lambda_1,\lambda_2)}{\partial\lambda_1\partial\lambda_2}\right]_{\lambda_1=\lambda_2=0} = \left[\frac{\partial}{\partial\lambda_2}\langle\Psi(\lambda_2)|H_1|\Psi(\lambda_2)\rangle\right]_{\lambda_2=0} \tag{2.91}$$

Hence within the FPT framework λ_2 is replaced by B and the shielding tensor is obtained from the first derivative of the expectation value of H_1, which in turn is the derivative of the unperturbed Hamiltonian with respect to λ_1 or μ_A, over $\Psi(B)$ evaluated numerically at $B = 0$. This may be written in terms of first- and second-order contributions as

$$\begin{aligned}\sigma_{A\alpha\beta} &= \langle\Psi_0|H^{(0,1)}_{A\alpha\beta}|\Psi_0\rangle \\ &+ \left[\frac{\partial}{\partial B_\alpha}\langle\Psi(B_\alpha)|H^{(1,1)}_{A\alpha}|\Psi(B_\alpha)\rangle\right]_{B_\alpha=0}\end{aligned} \tag{2.92}$$

where explicit expressions for $H^{(1,1)}_{A\alpha}$ and $H^{(0,1)}_{A\alpha\beta}$ are available [142]. Thus the magnetic shielding tensor for a molecule may be found by means of three perturbed eigenfunction calculations, corresponding to $\alpha = x, y$, and z. A standard SCF procedure as outlined in section 2.1.1, and employing the LCAO approximation may be developed by means of a variational procedure.

There remains, however, one problem with this procedure; the shielding components obtained from such a procedure are only independent of the choice of origin, in principle, if an infinite basis set is employed. Whilst this may not be such a problem for small molecules and nuclei where the use of an extended basis set is a viable option, it would seem to render the foregoing method somewhat unsuitable for larger systems. A number of solutions have been proposed for this problem, and many are frequently employed to good effect. The solution considered herein is the most commoly used one; the so called gauge-invariant atomic orbitals (GIAOs)[4]. These orbitals (θ_μ) are defined from the standard atomic orbitals (χ_μ) by multiplying by the gauge of the vector potential A whose value at the nuclear position r_μ of an atom defined by χ_μ is given by:

$$\theta_\mu(B) = \chi_\mu exp\left[-(\frac{ie}{\hbar})A_\mu \cdot r\right] \tag{2.93}$$

Aside from the removal of the gauge probelm the equation 2.93 ensures that the shielding calculated is due to local contributions as a result of the exponential form of the relationship. This is justifable on the basis that both paramagnetic and diamagnetic contributions to nuclear shielding of electrons decay as the cube of the separation of the nucleaus and the electron.

[4]The name is something of a misnomer, as clear from equation 2.93 these orbitals are defined by the very fact that they are *dependent* upon the gauge. This is frequently covered up by referring to GIAO as meaning gauge-including atomic orbitals

2.6.1 NMR Calculations Within the PCM Formalism

The effect of solvent on nuclear magnetic shielding parameters derived from NMR spectroscopy has been a field of intense interest for some time. A classification of solvent effects into a four categories was proposed by Buckingham *et al.* [143]. These are i) the bulk magnetic susceptibility of the solvent, ii) the magnetic anisotropy of the solvent molecules, iii) van der Waals interactions and iv) long-range electrostatic effects. Whilst in the original classification strong specific interactions (e.g. H-bonding) were not included, these have since been recognised.

In general, it is possible to correct experimental data for the bulk magnetic susceptibility, but in principle there is no way to extract the other four effects from a measurement. It is widely believed that short-range interactions can be handled by a super-molecule approach, by surrounding the solute with a number of explicit solvent molecules [144], while reaction fields provide an effective alternative for long-range electrostatic contributions[145, 146]. In general studies on solvent effects on NMR shielding have been performed on the Nitrogen nucleus [147, 148, 149].

One problem which has been found to occur in continuum treatment of NMR calculations[150] is that, in most cases, the Poisson equation is solved under the assumption that all charge resides within the cavity[151], which leads to a surface polarization density spread out over the cavity. However in practice most quantum mechanical calculations lead to a small tail of charge density penetrating into the continuum region, the long-range electrostatic effects of which, make additional rarely recognised effects to the solution of the Poisson equation[130, 151]. Studies of the effects of charge penetration on free energies of solvation [148] were found to be modest; however large effects were found for NMR shielding constants. A more recent study[150] has shown that both conductor like models[152] and the updated integral equation formalism[130] of the PCM (IEF-PCM) take into account volume polarization effects for solvents with high dielectrics, but not for low-dielectric solutes.

For nuclear shielding calculations, extensive use has been made of the INDO/S-SOS method [142] together with a reaction field solvation model [153, 154]. *Ab initio* calculations have also been performed, by using a spherical cavity with a fixed dipole representation of the solute [144], or a polarizable multipole representation of the solute [146]. Also molecular shaped cavities with complete treatment of the electrostatic potential [145], using the PCM model, have been employed.The PCM model has been chosen for modeling of solvent effects on NMR spectra and in particular nuclear shielding σ_N for the calculations presented in this thesis as it has been shown to be a particularly effective model for long range electrostatic effects. It is chosen also due to the fact that it is extremely diffuse and well tested throughout computational chemistry and also because of the aforementioned study which showed it to treat penetration effects quite well.

2.7 Natural Bond Order Analysis[155, 156, 157]

The method of Natural Bond Order (NBO) analysis provides a means of decomposing a wave-function into components such as natural orbitals (NOs), natural atomic orbitals (NAOs) and natural bond orbitals (NBOs) which are compatible with more "intuitive" pictures of the electronic configuration of molecules.

The NOs (Θ_j) of a wave-function (Ψ) are intrinsic to the wave-function itself and are the eigenorbitals of the reduced order density operator ($\hat{\gamma}$) which is defined as :

$$\hat{\gamma} = N \int \Psi(r_1, r_2, \ldots)\Psi^*(r_1', r_2, \ldots)d^3r_2, d^3r_3 \ldots \tag{2.94}$$

The NOs can now be defined as

$$\hat{\gamma}\Theta_j = n_j\Theta_j \tag{2.95}$$

where n_j is the population of the NO j.

The NAOs of a centre A ($\Theta_j^{(A)}$) can now be described as the effective NOs of the centre A in the molecular environment. In practice the NBO program generates the NAOs from the standard set of atom-centred orbitals (or indeed a set of atom centered orbitals may be generated if, for example, a plane-wave basis set is used). The NAOs are generated by transforming the atom-centered orbitals such that the NAOs are orthogonal between centres. The resultant NAOs differ from standard orbitals in two important respects:

- The NAOs are optimized for the effective atomic charge in the environment
- The NAOs have fringes which have nodal features due the effect of Pauli confinement within the molecular environment.

The NBOs are localized N-centre orbitals (N is typically 1 or 2) which describe the Lewis-like molecular bonding pattern of electron pairs. The calculation of NBOs requires only the wave-function as input, and as such the resultant orbitals are intrinsic to Ψ, just like the NAOs. The NBOs are combinations of Natural Hybrid Orbitals (NHOs) (h_A)which are themselves linear combinations of the NAOs

$$h_A = \sum_j a_j\Theta_j^{(A)} \tag{2.96}$$

There are several types of NBOs defined within the NBO paradigm. These include core orbitals which are effectively the same as the NAO described above, lone pair orbitals which are comprised of a single NHO, and two-centre NBOs (Ω_{AB}) which are linear combinations of hybrid orbitals from each centre.

$$\Omega_{AB} = a_A h_A + a_B h_B \tag{2.97}$$

The NBOs are found by the NBO algorithm by search through the eigenorbitals of the density operator of the wave function, that is, eigenorbitals with a value of n_j in equation 2.95 above a certain threshold. Once established these orbitals may then be partitioned into their constituent hybrid orbitals as in equation 2.97.

2.7.1 Natural Chemical Shielding[158]

The Natural Chemical Shielding (NCS) method allows the partitioning of theoretical NMR shielding tensors, calculated using the GIAO method as described in section 2.6 into magnetic contributions from bonds and lone pairs of the electronic configuration of the molecule. The GIAO method has important numerical advantages over alternative methods for calculating the shielding tensor such as the LORG[159] and IGLO [160] methods, however these alternative methods have the advantage of calculating shielding as a sum of contributions from localized molecular orbitals. The NCS method allows the kind of detailed analysis of the origins of nuclear shielding provided by these methods whilst maintaining the enhanced performance afforded by the GIAO method.

The NCS algorithm works by calculating the shielding contributions of the set of Naturally Localized Molecular Orbitals (NLMOs), which are a sum of Lewis type NBOs and non-Lewis type NBOs, using a series of transformations to relate the regular molecular orbitals to the NLMOs. The shielding tensor is calculated as a combination of contributions from "unperturbed" and "induced" which are analogous to the first and second terms on the right hand side of equation 2.92. The shielding is then further partitioned within these categories to shielding arising from the Lewis and non-Lewis portions of the NLMO. The NCS procedure calculates the shielding contributions of the various elements in the same way as the regular GIAO method, using NBOs rather than the LCAO wave-functions used in section 2.6.

2.8 Computational Methods in This Thesis

The various methods introduced above shall be used during the course of this study to investigate various aspects of pre-nucleation zeolite synthesis. In chapter 5 the potential models introduced in section 2.2 are used along with the molecular dynamics methods introduced (section 2.4) to investigate the effects of silicate clusters on the structure of environmental water.

In chapter 4 we use AIMD methods (section 2.4.5) to investigate the effects of structure directing agents, commonly present in zeolite sytheses, on the structure of environmental water.

First, however, a variety of methods are now used to investigate the NMR chemical shifts of silicate oligomer species present in the pre-nucleation solution. The next chapter shall use many of the methods presented above. Energy minimization

methods (section 2.3) are used to obtain minimum energy geometries of the species involved. The solution environment shall be represented using implicit solvation methods (section 2.5). NMR shifts are investigated using the GIAO method (section 2.6), and further probed using NBO and NCS analyses (sections 2.7 and 2.7.1). In addition the effect of explicit solvation on the chemical shift of some of the species are investigated using AIMD methods (section 2.4.5).

CHAPTER 3

Modelling and Interpretation of ^{29}Si NMR Spectra

3.1 Introduction

As was stated in the introduction to this thesis, ^{29}Si NMR has been on of the most important spectroscopic tools for studying pre-nucleation zeolite synthesis solutions. ^{29}Si NMR offers some of the best data for determining the structures of oligomeric silicate species which exist in the pre-nucleation solution, and has been used to demonstrate the existence of so-called pre-nucleation building units (PNBUs)[5] which have been demonstrated to be related to secondary building units (SBUs) by a structural isomerization. As such ^{29}Si NMR has been one of the key factors in promoting the theory of zeolite crystal growth based on the nucleation of SBUs [49].

Although ^{29}Si NMR has been used for more than 30 years to study pre-nucleation solutions, the past five years has seen a significant increase in the number of silicate species identified in experimental studies. Indeed in a recent study using 2D COSY NMR 52 different oligomers were identified arising from increasingly complex analysis of experimental spectra [44]. The advent of methods such as EXSY [161] also offers the possibility for following the evolution of the solution, and the interaction of oligomers with one-another.

The increased number of species identified means increasingly complex experimental NMR spectra to be deconvoluted. Indeed in a recent study [44] a number of species were found to exist, but could not be distinguished uniquely by the experimental technique. To this end computer modelling provides a valuable aide to experimental data.

There have been many previous studies of the NMR spectra of silicate oligomers performed computationally [52, 162, 163, 164]. In the first part of this chapter

we first address some of the problems which arise in deciding how the oligomeric species should be represented for calculating shifts. We demonstrate the usefulness of the inclusion of an implicit solvent model for improving the accuracy of calculated NMR shielding tensors. We then establish that modelling species in a neutral (fully protonated) state should provide accurate calculated shielding values, such a finding is important as previous studies have used both fully protonated [51] and fully deprotonated [165] models on a seemingly *ad hoc* basis. We then further investigate the parameters of the implicit model of solvation as well as the use of different functionals for calculating chemical shift, in order to fully establish a model which gives accurate chemical shifts, whilst maintaining computational efficiency.

Having established a methodology we then compare our results to an extensive set of experimentally observed and assigned spectra. We investigate the importance of species geometry in determining shielding (chemical shift) and suggest assignments for experimentally difficult to assign peaks.

In addition we present in appendix A a list of calculated chemical shifts for both experimentally identified and hypothetical silicate oligomers (figure 3.1). Such a list, we hope, can prove useful in aiding experimental assignment of spectra.

3.1.1 Nomenclature

Throughout this chapter constant reference is made to the Q^n classification of Si centres. It is important, therefore that this notation be explained before proceeding. The n in this notation denotes the number of oxygens attached to the Si centre which are attached to another Si centre. Thus the silicic acid monomer, species I in figure 3.1 is classified Q^0, whilst the centres in the double 4 ring, species VIIIc in figure 3.1 are all Q^3. In acknowledgement of the important effect which presence of a centre in a 3 ring can have on its chemical shift an additional Δ is used to denote such centres, thus the 3 ring, species III in figure 3.1 has Si centres denoted $Q^{2\Delta}$.

As many species are considered in this section and naming of these species can become cumbersome/confusing each species is also assigned a code number based on the number of silicons. These codes are presented in figure 3.1.

3.1.2 The History of ^{29}Si NMR in Studying Silicate Synthesis Solutions

The earliest attempts at a theoretical rationalization of the relationship between observed ^{29}Si NMR shifts (with respect to TMS) and the structure of the silicon centre were made in the pioneering work of Radeglia and Englehardt *et al.* in the 1970s [166, 167, 168]. They demonstrated that general trends in ^{29}Si NMR shifts could be reproduced satisfactorily by taking into account only the paramagnetic contribution to the chemical shift, approximated from the charge distribution of a

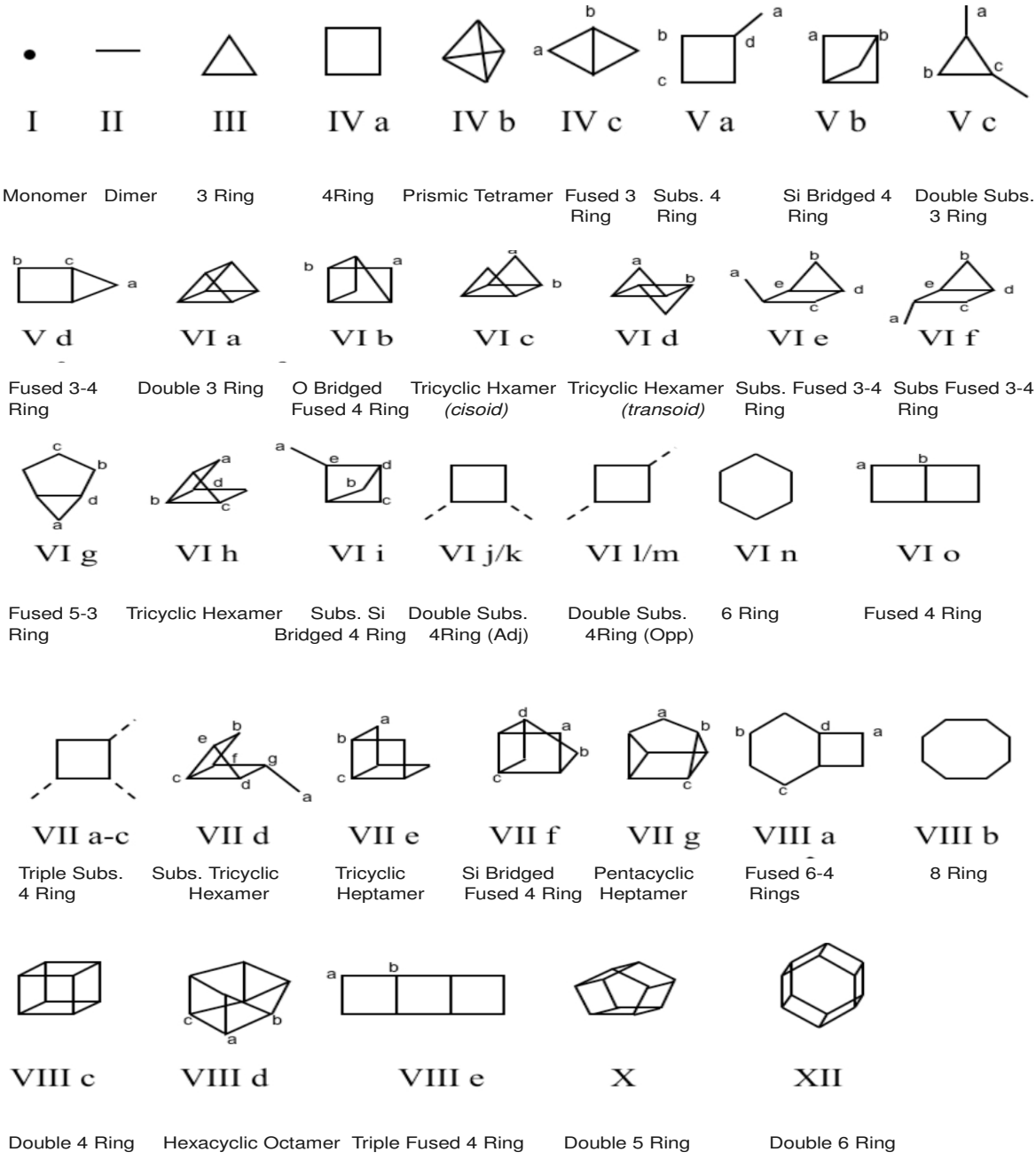

Figure 3.1: Silicate oligomers selected for study, with commonly used names; roman numerals refer to references in the table of chemical shifts. A line represents a Si-O-Si bond. A dashed line represents a dangling monomer which may adopt multiple conformations.

tetrahedral SiX_4 silicon with localized Molecular Orbitals (MOs), the polarities of which may be determined by the electronegitivities (EN) of the substituent atoms X. They showed in this work how the shift (σ) would be expected to decrease in an approximately linear fashion with increasing EN, with the general form:

$$\sigma = -aEN + b \tag{3.1}$$

Subsequent systematic investigations by Lippmaa *et al.* [168] in 1978, using solid state high resolution NMR, showed that the predominant feature determining the Si chemical shift is the degree of condensation of the Si centre. They demonstrated that the shift moves continually down-field as n, in the Q^n notation, increases. Thus, the spectrum of silicate NMR shifts may be divided into different regions determined by the degree of concentration of the species observed, aiding interpretation of complicated ^{29}Si NMR spectra.

In the mid 1980s Grimmer, Radeglia and Engelhardt refined the structure/shift relationship in ^{29}Si NMR [169, 170, 171]. Furthering the work on the degree of Si condensation they derived the relationship that:

$$\sigma = -69.8 - 8.9n, \tag{3.2}$$

with $r^2 = 0.90$. Here n is the same as in Q^n notation, which means that increasing Si condensation by 1, leads to an increase of shielding of $\approx 10ppm$, which is similar to the results of Lipmaa *et al.* [172]. They also calculated a relationship between shift and the mean silicon-oxygen distance, $d\overline{(Si-O)}$ arriving at the relationship:

$$\sigma = -2014 + 1.187 \times 10^4 d\overline{(Si-O)}(nm) \tag{3.3}$$

which they interpret as a general form of an earlier relationship derived for Q^4 units only [167]. The relationship of equation 3.1 was further rationalized in terms of silicate structure [170] by establishing a correlation between σ and the SiOSi angle, established by development of a functional form for the relationship between the bond angle and the electronegativity of the bridging oxygen. The relationship was derived from the degree of s hybridization, ρ, of the oxygen bond orbitals.

$$\rho = \frac{cos\alpha}{cos\alpha - 1} \tag{3.4}$$

thus allowing inferance of a relationship:

$$\sigma = A\rho + B \tag{3.5}$$

which they proceed to calculate as being :

$$\sigma = -247.05\rho + 2.19 \tag{3.6}$$

with a correlation coefficient $r^2 = 0.968$

Concurrently in the early 1980s, Harris and Knight [43], used computer simulations, in conjunction with ^{29}Si-^{29}Si homonuclear decoupling, to identify 18 silicate

species present in the solution phase, with varying degree of certainty. Harris *et al.* [173] later reconfirmed the existence of some of these species using homonuclear correlation spectroscopy (COSY). In the early experiments using COSY the signal to noise ratio (S/N) was too high to provide clear evidence for some of the more esoteric structures which were proposed. However with increased field strength more signals were able to be observed, and hence more and more possible structures have been postulated. In 1988, Knight [45], using increased field strength with COSY experiments, was able to identify sixteen silicate species with more than one type of Si site, as well as six species with a single equivalent site under symmetry, on the basis of chemical shift and connectivity data from the COSY experiment.

Thus far peak assignments had been made under a variety of different conditions, with little study of the effects of different variables such as temperature, different counter cations, varying pH and Si concentration etc. It had been noted in a series of papers in 1984 [173, 174] that increasing the temperature of the sample lead to a broadening of spectrum peaks; an observation attributed to the dynamic exchange of SiO_4^{4-} groups between different solution species[174]. However in their study of the same year [173], Harris *et al.* using selective inversion recovery ^{29}Si NMR, were able to show that below 80°C, while peaks still broaden, no magnetization transfer was observed. They concluded that, while above 80°C broadening may indeed be due to silicate exchange, below there must be other mechanisms involved, which although not involving exchange, are still temperature dependent.

A more systematic study of the effects of environment and structure factors on ^{29}Si shift was presented by Kinrade and Swaddle in 1988[175, 176], in a pair of papers which measured NMR spectra using a variety of different counter cations (M^+), at different [Si]:[M^+] ratios and at different temperatures. From these studies they devised a hierarchy of factors which affect the chemical shift this is presented in table 3.1. The effect of pH they attributed to the fact that increasing pH leads to further deprotonation of Si-OH groups. However, they concede that it is impossible to decouple this from other effects such as M^+-silicate ion pairing, as the pH was changed by increasing the concentration of MOH. Indeed, they comment that, due to the fact that shift depends not only on the [M^+]:[Si] ratio but also on the concentration of M^+, M^+-silicate pairings play a significant role in determining the chemical shift. In these studies peak-shape analysis was also used in order to infer rates and activation energies for site exchange in the silicate species.

The first major systematic *ab initio* modelling study of environmental and structure effects was published by Moravetski *et al.* in 1996[51]. Using Hartree-Fock and coupled perturbed Hartree-Fock they studied the effects of deprotonation and ion pairing on a silicate monomomer, including also hydration by two and four water molecules, finding that while deprotonation caused an upfield shift of $\sim$ 5ppm when hydration and K^+ were included in the model the shift remained within -71$\pm$

0.5ppm. In addition, this paper demonstrated the effect of symmetry on shielding, concluding that lower symmetry leads to lower chemical shift. They were also able to extend the semi-empicial relationship calculated by Englehardt *et al.* for Q^4 species to Q^n species with $n = 1 - 4$, by also taking into account the SiOH bond angle :

$$\sigma = -61.23n\langle\rho(SiOSi)\rangle - 60.45(n-1)\langle\rho(SiOH)\rangle + 6.58 \tag{3.7}$$

Equation 3.6 is shown to be a specific case for $n = 4$. In addition this now lead to the previous assignment of the tetrahedral tetramer at -97.3 ppm being called into question.

Thus far we have considered generally silica solutions containing only alkali metal counter cations. However, in zeolite synthesis the presence of organic cations, particularly tetraalkylammonium (TAA) species in many model systems plays a key role in directing the final crystal structure of the zeolite formed. Solutions containing organic salts were studied using NMR techniques as far back as the early 1980s when Harris and Knight [177] studied solutions containing tetramethylammonium (TMA), tetraethylammonium (TEA), tetrapropylammonium (TPA) and tetrabutylammonium (TBA). The results from this and other studies [6, 7] indicate that the presence of the organic species significantly reduces the occurrence of smaller anions, whilst favouring the existence of the double 3 ring (VIa in figure 3.1) and particularly the double 4 ring (VIIIc in figure 3.1) species. It is also noted that the degree to which these species are favoured decreases as the size of the alkyl chain of the organic species increases, and that the structure directing potency of all TAA species is greatly increased in the presence of organic solvents.

However, here is where consensus on the interactions between TMA and silicate species ends and the precise nature of these interactions has been the subject of intense debate in the literature. In 1998 Kinrade *et al.* published a pair of papers containing a NMR studies of equilibria and kinetics in TAA solutions[6, 7]. In the first of these papers[6] they conclude that, due to the minimal effect of silica on the ^1H and ^{13}C NMR of TAA^+ cations, the interaction between silicates and these cations must be long-range and indirect. They propose that due to the *hydrophobic hydration* of TAA^+ ions the water structure in the vicinity of these species is reordered, stating that if the silicate species caused a similar effect on the surrounding water then an overlap of hydration layers could provide mutual stabilization. Furthermore they state that such interactions may be primarily entropically driven owing to the release of water molecules from the over-structured hydration layer into free solution. They also propose a reaction scheme for the formation of the Q_6^3 and Q_8^3 species:

$$8H_3SiO_4^- + xTMA \rightleftharpoons [Si_8O_{20} \cdot xTMA]^{(8-x)-} + 12H_2O \tag{3.8}$$

$$6H_3SiO_4^- + xTMA \rightleftharpoons [Si_6O_{15} \cdot xTMA]^{(6-x)-} + 9H_2O, \tag{3.9}$$

thus suggesting that rather than the organic cations providing a scaffolding around which silicate structures will grow, they provide stabilization in the opposite manner by surrounding the silicate species.

A contrary conclusion was reached by Kirschhock, Ravishanker *et al.* in a series of three papers[16, 17, 39] published just one year later, using a range of experimental techniques. In terms of pre-nucleation oligomers ^{29}Si NMR and infrared spectroscropy were used to investigate condensation in an aqueous solution containing tetrapropylammonium hydroxide (TPAOH). The spectra obtained were attributed to a number of polysilicate anions containing three and five membered rings, and among the species assigned here, but not previously postulated, were a double 5 ring, a pentacyclic octamer, a capped double 5 ring and a tricyclic undecamer; shown in figure 3.2 . They also concluded that the structure directing role of TPAOH was evidenced by the propesity for the formation of species with a curved hydrophobic surface, which occluded a TPA cation. Using magic angle spinning (MAS) NMR, X-Ray scattering, transmission electron microscopy (TEM) and atomic force microscopy (AFM) they also found evidence for the assembly of the smaller silicate species to form "nanoslabs" with dimensions of 4 x 4 x 1.3 nm which have MFI structure. This view of zeolite assembly was furthered in two subsequent publications [40, 178] again using ^{29}Si NMR where they also assigned a pentacyclic dodecamer which they presented as further evidence for the structure directing role of TPA.

The results presented in this series of papers were subsequently questioned by Kinrade and Knight [41] in which they critique the NMR methods used to identify small silicate species. They suggest that the lack of scalar coupling in assigning signals, relying rather on relative intensities of peaks can ,at best, be considered to provide tentative assignments. They also reassign the peaks from the studies of Kirschhock *et al.* by replicating the experimental conditions but with ^{29}Si NMR enriched TEOS as the source material, thus allowing for 2D COSY spectra to be obtained.

Undeterred by these criticisms Houssin, Kirschhock *et al.* published another paper in 2003 [179], once again studying TPAOH/silicic acid/H_2O solutions using ^{29}Si NMR and small-angle X-ray scattering, in which they again assign signals to a double 5 ring structure and this time finding evidence for the presence of a pentacyclic dodecamer. The course of the reaction is followed from the early stages using ^{29}Si NMR to identify solution species and later using the X-ray scattering techniques to follow the formation of colloidal structures. Once again no decoupling experiments were utilized to gain information about site connectivity. This again incurred criticism from Kinrade and Knight who published a paper in the same journal some years later entitled "Do zeolite precursor species really exist in aqueous synthesis media?"[18] in which they state that "a detailed inspection shows that Barrer *et al.*'s original SBUs are notable by their *almost complete absence*.", they also contend that

Factor Increased	Result	Nucleii Most Affected
STRUCTURE FACTORS		
Local Connectivity	Shielding up to 40ppm	High Local Connectivity
Occourance In A Ring Structure	Deshielding up to 8.5ppm	3 Ring Nucleii
Adjacent Connectivity	Deshielding up to 1ppm	High Adjacent Connectivity
ENVIRONMENT FACTORS		
[MOH]:[Si]	Deshielding up to 2.3 ppm	Least Strained Species
[Si]	Deshielding up to 0.3 ppm	Least Strained Species
Atomic Mass of M+	Shielding up to 1.8 ppm	Least Strained Species
Temperature	Deshielding up to 0.02 ppm	Least Rigid Species

Table 3.1: Hierarchy of structural and environmental factors affecting chemical shift [175].

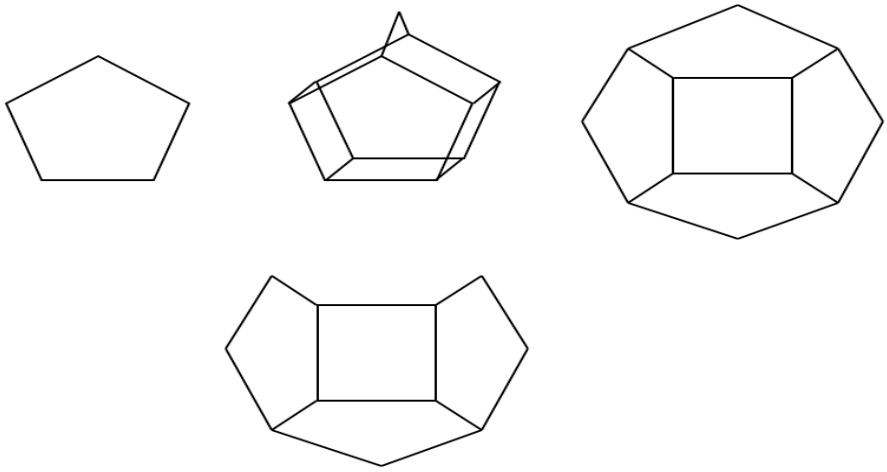

Figure 3.2: Novel species assigned by Kirschhock *et al.* [40, 178, 179]. From left to right; the 5 ring, the capped double 5 ring, the pentacyclic dodecamer and the tetracyclic undecamer.

no species are specific to a given cation or synthesis conditions. Using enriched ^{29}Si solutions they obtained 2D peak correlations and on this basis reassign the double 5 ring peak of Kirschhock *et al.* to the hexacyclic octamer species: due to the fact that the signal, originally assigned to the double 5 ring shows, correlation with other peaks in the spectrum, indicates that it cannot arise from a species with a single unique Si centre. They also reassign the petacyclic dodecamer peak , which would be expected to show two cross peaks, to the species which is named the Si bridged fused 4 rings in this thesis (species VIIf in figure 3.1) as it shows four cross peaks, and lacks cross peaks in the region of the spectrum which would be expected for a petacyclic dodecamer.

Recently advances in NMR technology have allowed for ever more detailed spectra to be observed of pre-nucleation solutions. Cho *et al.* [52], using isotopically enriched samples, were able to propose nine new silicate species and also suggest that several of these species exist in more than one conformer and/or diastereoisomer, which they investigated further using DFT calculations. Using the INADEQUATE method Haouas and Taulelle [5] were able to observe a series of connectivities not before seen, for which they provided possible structures. Knight *et al.* [44] using powerful COSY experiments assigned resonances to 48 structures. One of the most striking successes of this method was to identify many more structures which consist of a ring or cage of silica with a dangling silica monomer attached, which are present in many isomeric forms, but which are impossible to distinguish through experiment alone.

More recent simulation work has also employed powerful modern techniques to give insights into the origins of chemical shift. Krishnamurty *et al.* [164] performed *ab initio* molecular dynamics simulations to investigate the influence of dynamics and solvation on the silicic acid monomer. They found that the solvent has an impact on the electronic structure of the monomer by affecting the polarization, and also that it affected the structure of the species via hydrogen bonding. These simulations suggest that the observed signal of the monomer is the result of a conformational ensemble which can vary by up to 50 ppm. Another technique which has proved useful for providing a theoretical basis for understanding the origins of chemical shifts is the Natural Chemical Shielding (NCS) technique [180], which is based on the Natural Bond Orbital (NBO) approach [156], both of which were explained in chapter 2. This method has been employed to some effect by Tossell *et al.* [181] who used it to explain the electronic structure reasons for the Si-O-Si bond angle relationship to chemical shielding, on the basis of a change in the shape of inter-atomic Si-O orbitals and contributions from lone pairs on the bridging oxygen. Tossell [165] also used this method to investigate fluorine effects on chemical shift.

3.2 This Study

We first establish a methodology for modelling ^{29}Si NMR chemical shifts. In order to do this we investigate the usefulness or necessity of an implicit representation of the solution for improving calculated chemical shifts. Use is made of NBO and NCS analyses to establish the particular reasons for the usefulness of such a representation when modelling the deprotonation of the silicic acid monomer ($Si(OH)_4$ / $SiO(OH)_3^-$).

Having demonstrated the usefulness of the implicit representation of the solvent for modelling changes in chemical shift upon deprotonation we investigate how deprotonation affects Si centres in different structural environments. We investigate further deprotonation of the silicic acid monomer as well as deprotonation of the double 3 ring species (species VIa in figure 3.1). The important results of this section are : a) we establish that a neutral model of oligomeric species should provide accurate chemical shifts when compared to experiment b) the explanation, through use of NBO and NCS analyses, of the reason for the greater effect of varying pH on the chemical shift of more flexiable species, as stated in table 3.1.

The effect of different counter cations on the chemical shift is then investigated. We explain, again using NBO and NCS analyses, the reason for changes in chemical shift as the size of the counter cation is increased, as stated in table 3.1. In addition we explain why Li^+ does not follow this general trend, as observed experimentally[182].

Next we further investigate how the parameters of the implicit solvent model may be adapted to improve chemical shift calculations, and also the effect of different functionals, in order to establish the optimal methodology. We start by comparing the calculated shifts of a set of 9 oligomers to experimental values, varying the cavity scaling of the solvent model and the functional used. The scaling of the cavity may have an effect of calculated chemical shifts, as charge penetration beyond the cavity has been shown to adversly effect calculated shifts in previous studies[150, 151].

Having established our methodology we compare the calculated shifts of an extensive set of oligomers figure 3.1 to experimental data, where available. We demonstrate how our methodology gives improved chemical shifts compared to, to our knowledge, the most extensive set of such calculations performed previously [52]. We also demonstrate a possible problem with our methodology, in cases where internal hydrogen bonding is present. By considering the dimer species ($Si_2O(OH)_6$) in explicit solvent, using *ab initio* molecular dynamics, we show that neglect of surrounding water molecules when modelling such species leads to an over emphasis on internal hydrogen bonding, the geometrical effect of which leads to calculated chemical shifts in poor agreement with experimental values.

We then examine how certain structural factors affect the chemical shift. Considering the presence of the Si centre in different types of rings, and in particular

3 rings. This study allows us to help to establish certain "rules of thumb", which are necessary when trying to assign peaks in experimental spectra. In addition the study of the effect of 3 rings highlights the fact that, if a centre is in many 3 rings, its shift may be affected to the extent that it is in a region of the spectrum with which it may not traditionally be associated, for example a Q^3 centre may appear in a region of the spectrum previously only thought to contain Q^2 centres.

Finally we use our methodology to propose the re-assignment of some peaks assigned experimentally, as well as to propose assignemnts for peaks which could not be uniquely assigned experimentally.

3.3 Methodology

In order to investigate the chemical shift of silicate species found in pre-nucleation solutions it is clearly of great importance that the effect of the environment, i.e. the solution itself, is accounted for correctly in the models employed. It is also important that the model capture the silicate species in the correct state. In this instance the charge state of the species is of primary interest. However, as shall be seen later on, proper representation of the conformational state of the species is also important. For this section the investigation shall be restricted to investigation of solvent effects, charge state, choice of functional and the effect of different counter cations on chemical shift.

3.3.1 Environment

In this section the results of calculations of a silicate monomer upon deprotonation are presented in which various levels of treatment of the immediate environment are included. As a first approximation the species is considered in vacuum; then modelled using an implicit polarizable continuum model; cation effects are considered by including a sodium counter cation; and finally a super-molecule model with three explicit water molecules and the cation is considered. The systems used in this study are shown in figure 3.3, all of these systems are considered both with and without implicit solvation.

All calculations were performed using the Gaussian 03 package[183]. All systems were geometry optimized using the B3LYP [105] functional and 6-31G* basis sets[184]. The geometry optimizations were performed both *in vacuo* and using the integral equation formalism of the polarizable continuum model (IEFPCM) [130] to represent solvation. NMR shielding calculations, NBO and NCS analyses were also performed both *in vacuo* and in the presence of the IEFPCM. For these calculations the PBE functional[104] with aug-cc-pVTZ basis sets[185] for O and Na and aug-cc-pVDZ basis sets[185] for Si and H were used.

An NCS analysis giving a breakdown of various natural orbital contributions to

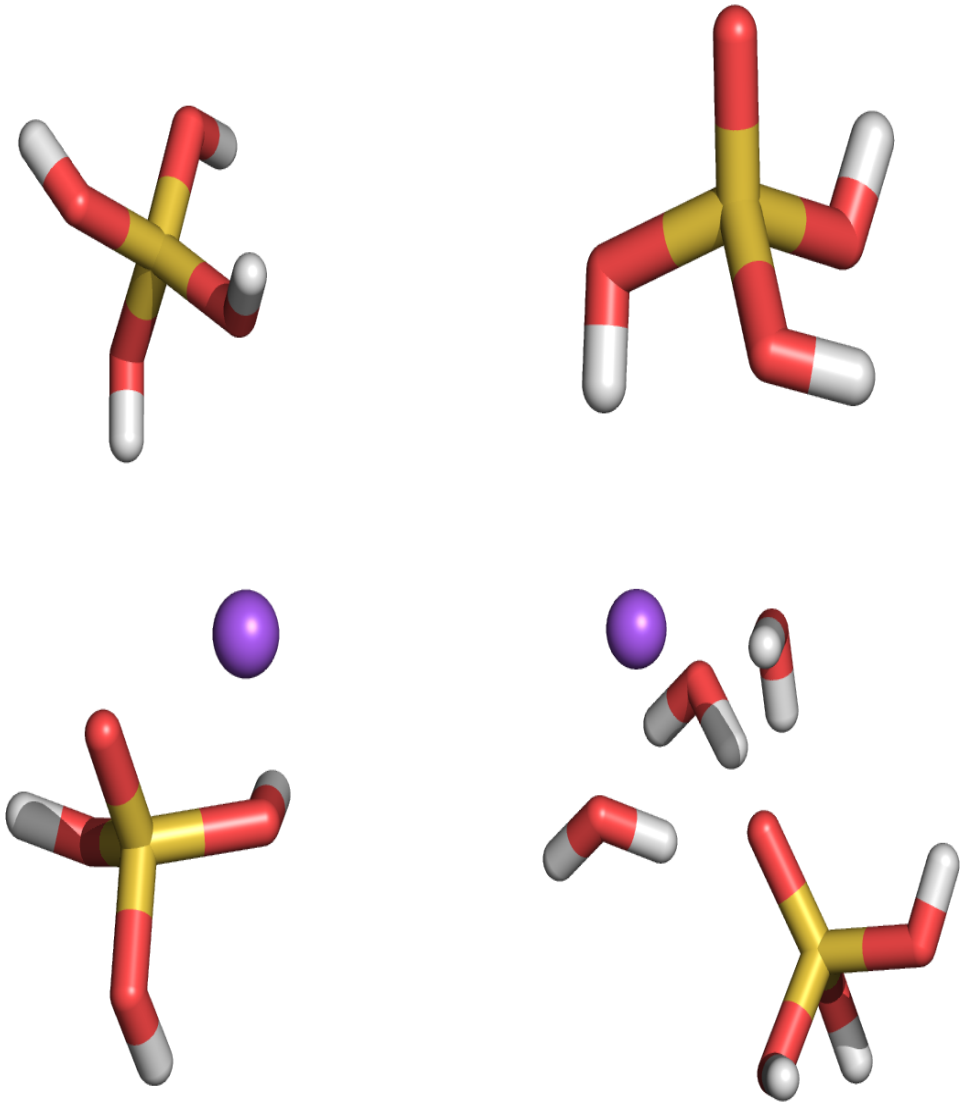

Figure 3.3: The various systems considered for studying the effects of environment. Upper left: The neutral monomer species ($Si(OH)_4$), referred to herein as M. Upper right: The deprotonated monomer with no other species ($SiO(OH)_3^{-1}$), referred to herein as M-1. Lower left: The deprotonated monomer with a sodium counter cation ($SiO(OH)_3.Na$) referred to herein as Na. Lower right: The deprotonated monomer with three explicit water molecules as well as a sodium counter cation ($SiO(OH)_3.Na.3H_2O$) referred to herein as H_2O.

	Vacuum				IEFPCM			
System	M	M-1	Na	H_2O	M	M-1	Na	H_2O
Si-O(1)	-228.46	-204.17	-216.56	-220.64	-227.89	-204.55	-214.81	-219.72
Si-O(2)	-	6.55	7.77	6.30	-	10.66	6.79	6.71
Si-O(3)	-	-1.09	6.02	6.30	-	-4.69	5.43	6.26
OH	-5.95	-3.38	-3.33	-3.37	-5.82	-3.26	-3.26	-3.32
Core s	492.17	491.53	492.41	492.95	492.08	491.49	492.20	492.89
Core p	52.76	46.50	48.16	44.73	51.56	44.76	47.85	43.74
O lp sp	-13.59	-29.99	-29.97	-22.93	-13.86	-30.66	-30.71	-23.71
O lp p	11.57	3.30	3.64	6.03	11.95	3.80	3.92	6.03
σ	389.94	391.17	389.31	389.66	389.55	389.56	388.78	389.61

Table 3.2: Contributions of various classes of NBO to the nuclear shielding and total shielding (σ), all in ppm, of the monomer, both neutral and charged, and in various environments. The system labels refer to figure 3.3, the systems are also considered *in vacuo* and using the IEFPCM representation of the solvent.

overall shielding is presented in table 3.2. The NBOs are split broadly into four categories; inter-atomic Si-O orbitals (Si-O), silicon core orbitals, oxygen lone pair orbitals (O Lp) and inter-atomic O-H orbitals (OH) . Where there are more than one Si-O orbitals they are referred to as Si-O(N), N=1-3, in order of their population, the core orbitals are either s-orbitals or p-orbitals and the O Lp orbitals are either p-orbitals or sp-hybridized orbitals.

Considering the net chemical shielding value (table 3.2), it is clear that the variation upon deprotonation in all cases is rather small, in fact the only case in which the change in calculated shift is greater than 1ppm is that of the *in vacuo* model with no environmental species. This result is in line with experimental results [175, 182], which have shown little to no change in silicic acid chemical shift upon deprotonation. The fact that the model which least agrees with experiment is that *in vacuo* is of little surprise as this is the most primitive of the models used. From these results it is clear that the inclusion of an implicit solvent alone provides a good approximation to more complicated models which include explicitly the environmental species.The NCS breakdown shall now be used in conjunction with a NBO analysis to investigate some of the reasons for these results.

Inter-atomic Si-O Orbitals:

We consider first the NBOs between the Si centre and the deprotonated silanol, compared to the NBO between the Si centre and a protonated silanol in the neutral monomer. In the neutral monomeric species there is only one inter-atomic Si-O NBO per silanol , whilst upon deprotonation (e.g. in $SiO(OH)_3^-$) there are three such orbitals. These orbitals are referred to herein as Si-O(1-3), in order of their population. In the vacuum model, both with and without the presence of the counter cation, the de-shielding contribution from this orbital is increased significantly by more than 10 ppm compared to the de-shielding effect in the neutral species(table 3.3). A number

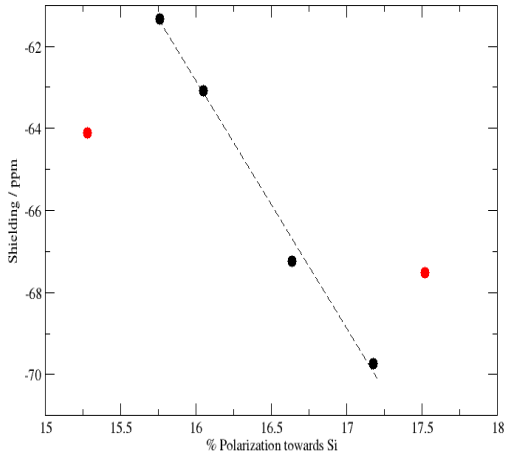

Figure 3.4: Nuclear shielding contribution of the Si-O(1) orbitals versus the % polarization of the NBO towards the Si centre. Black: species with environmental molecules (Na and H_2O in figure 3.3) with and without IEFPCM. Red: species with no environmental molecules (M-1 in figure 3.3) with and without IEFPCM.

Vacuum		%	s	p	d	σ/ppm
M	O	83.92	34.05	65.87	0.08	
	Si	16.08	24.99	72.93	2.05	-57.11
M-1	O	82.26	28.61	71.27	0.12	
	Si	17.52	44.80	53.47	1.68	-67.51
Na	O	82.82	36.30	63.47	0.22	
	Si	17.18	28.53	66.35	4.95	-69.73
H_2O	O	84.24	37.03	62.89	0.08	
	Si	15.76	27.43	70.27	2.25	-61.34
IEFPCM						
M	O	83.91	34.23	65.69	0.07	
	Si	16.09	24.99	72.95	2.02	-56.97
M-1	O	84.72	31.36	68.44	0.20	
	Si	15.28	24.84	64.55	10.47	-64.11
Na	O	83.36	36.41	63.37	0.21	
	Si	16.64	27.72	66.16	5.95	-67.24
H_2O	O	83.95	36.51	63.40	0.08	
	Si	16.05	27.88	69.87	2.21	-63.09

Table 3.3: NBO analysis and shielding contributions (σ) of the Si-O(1) inter-atomic orbitals, with polarization towards each centre (%) and the s, p and d hybridization of the orbitals. The system names refer to figure 3.3.

of factors are responsible for the spread of values for the contribution of this orbital to the nuclear shielding. One important factor in determining the nuclear shielding contribution of this orbital is the extent to which it is polarized towards the silicon centre. As this orbital has a de-shielding effect, the greater the extent to which it is polarized towards the silicon, the greater is its de-shielding effect: a fact borne out in figure 3.4 where the nuclear shielding contribution is plotted against the % polarization towards the silicon, and shows a linear correlation for the majority of the points considered. The two points which do not follow this general trend lead us to consider the final factor which influences the shielding effect of this orbital: the hybrid character of this orbital. The point which falls below the line is that calculated for the deprotonated silicic acid (system M-1 in figure 3.3) in the IEF-PCM solvent. Based on our polarization argument we would expect this orbital to be less de-shielding as it is less polarized towards the silicon than the other cases. However, when we consider the hybrid make-up of this orbital (table 3.3) it is clear that the silicon polarized portion has much greater d-orbital character than any of the other species, which means the orbital is less localized in the bond, therefore the de-shielding effect on the nucleus is greater. Exactly the opposite is true for the same system in vacuum, which is the point falling above the line. This species has a silicon polarized component of the inter-atomic orbital which has less d-orbital character than the other deprotonated species, with greater s-orbital character, meaning it is more localized in the bond and therefore the converse of the case including the IEFPCM may be inferred.

When we take into account all of these factors, the Si-O(1) orbital between the charged oxygen and the silanol is more de-shielding than the equivalent orbital in the neutral silicic acid monomer. However table 3.2 shows that the contribution from this set of orbitals is overall less de-shielding in the charged species than in the neutral. The reason for this is that the deprotonation also has an effect on the other Si-O(1) orbitals between the silicon and the oxygens which are not deprotonated. The effect in this case is to reduce the de-shielding effects of these orbitals by polarizing them away from the silicon relative to the neutral case: these orbitals are only polarized between 11.5-12.5 % towards the silicon in the charged species (table 3.4), compared to around 16% in the neutral species (table 3.3). The inclusion of the IEFPCM has an effect on these orbitals, in general it increases the degree to which they are polarized towards the silicon (table 3.4) resulting in shifts closer to those of the system where explicit waters are also included. The correction is rather small when the monomer is considered in isolation. However the change in the polarization when there is a sodium present is greater, as is the change in the contribution of these orbitals to shielding: in the solvated species this orbital is is almost 12 ppm more de-shielding than the vacuum one. Thus, it is clear that, even when considering the smallest and most symmetric silicate species, a consider-

Vacum		%	s	p	d	σ/ppm
M-1	O	88.48	33.93	66.00	0.07	
	Si	11.52	22.42	54.44	22.71	-44.21
Na	O	89.03	34.08	65.86	0.06	
	Si	10.97	22.01	46.31	31.11	-41.63
H_2O	O	87.57	33.78	66.14	0.07	
	Si	12.43	23.90	47.76	27.92	-54.14
IEFPCM						
M-1	O	88.10	33.10	66.83	0.07	
	Si	11.90	23.08	51.51	25.18	-45.95
Na	O	87.52	33.76	66.16	0.07	
	Si	12.48	22.64	51.70	25.48	-53.82
H_2O	O	87.79	33.80	66.13	0.07	
	Si	12.21	24.41	47.96	27.12	-52.62

Table 3.4: Average NBO analysis and shielding contribution (σ) of the remaining Si-O(1) NBOs between the silicon and protonated silanol groups in the deprotonated monomer, showing % polarization towards each centre, percentage s,p and d character of each orbital and contribution to net shielding (σ). Systems systems named as in figure 3.3.

ation of the solvent is important when modelling the interaction of the silicate and a cation.

Between the silicon and the charged oxygen there are two extra inter-atomic orbitals that contribute to the shielding of the silicon nucleus which are not present in the neutral species. These orbitals contain the electrons which, in the neutral species, are localized in the OH bond of the silanol and the lone pair p-orbital electrons from the deprotonated silanol oxygen. The contributions from these orbitals are generally shielding, with the exception of the Si-O(3) orbitals on both species which have no environmental molecules considered (i.e. the isolated monomer *in vacuo* and in the IEFPCM). Thus, overall they contribute to a shielding of the nucleus relative to the neutral species, due to the fact that, although a shielding influence from the oxygen lone pair is lost, this is replaced by a shielding inter-atomic orbital in the deprotonated case, and the OH orbitals - which have a de-shielding influence on the silicon nucleus - are no longer present in the charged species.

The Si-O(2) orbitals have a shielding effect on the Si nucleus in all systems considered. However it is difficult, using NBO analysis, to ascertain the reasons for the different values for the different species. The reasons for the Si-O(3) orbitals being deshielding in the systems with only the deprotonated monomer considered (system M-1 in figure 3.3) seems to be related to the orientation of this orbital. The orientation of the NBO is expressed by its deviation from the vector between the atomic centres, the so called angle of deviation. The reason that the angle of deviation is important is elucidated in figure 3.5. Neighbouring contributions to nuclear shielding depend on the distance and angle of the contributing electron

density and the nucleus:

$$\sigma \propto \frac{1 - 3cos^2\theta}{r^3}, \tag{3.10}$$

where θ is the angle of deviation, r is the separation and σ is the contribution to shielding. As illustrated in figure 3.5, this value would be expected to reach a maximum at $\theta = 90°$ (in the absence of any other changes). Figure 3.6 shows that in the absence of environmental species the angle of deviation is lower than 90°, whilst with environmental species present it is around 90°. Therefore the reason for the de-shielding effect of these orbitals in the two systems with no environmental species may be due to its orientation.

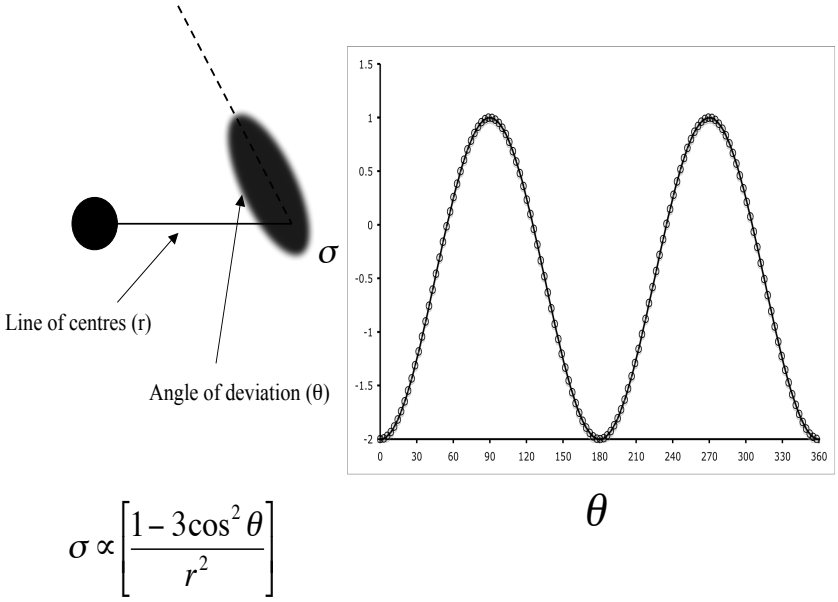

Figure 3.5: Schematic represntation of the angle of deviation, and the dependence of the shift on this angle.

Lone Pairs:

There are two kinds of lone pair orbitals on the silanol oxygens which contribute to the shielding of the silicon nucleus; a p-orbital lone pair, and an sp-hybridized lone pair. The major difference between the charged and neutral species with regards to the p-orbital lone pairs is that the deprotonated oxygen does not have a p-orbital lone pair. This pair of electrons rather, accounts for one of the additional inter-atomic Si-O orbitals. In all of the models this contribution is, therefore, decreased upon deprotonation.

Vacuum	s	p	d	σ/ppm
M	42.54	57.37	0.08	-3.40
M-1	63.56	36.43	0.01	-17.50
Na	61.84	38.12	0.05	-17.75
H_2O	62.69	37.31	0.00	-9.43
IEFPCM				
M	41.88	58.04	0.08	-3.47
M-1	61.09	38.88	0.03	-17.96
Na	60.97	38.99	0.04	-18.15
H_2O	63.24	36.76	0.00	-9.84

Table 3.5: NBO analysis and shielding contribution (σ) of the sp-hybridized lone pair on the silanol and deprotonated silanol groups. With percentage s,p and d character of the orbital, and its contribution to the net shielding.System names refer to figure 3.3

In the case of the sp-hybridized orbitals the contribution to shielding becomes markedly more negative upon deprotonation. The reason for this increased negative shielding is due to the fact that upon deprotonation, this orbital decreases in p character (table 3.5). Reducing from around 58 % in the neutral species to 37-38 % in the various models of the charged species. This change in hybrid character results in the lone pair of electrons being more localized on the oxygen in the charged species, thus being less available for shielding the silicon nucleus.

Summary: The net results of different approximations of the environment on ^{29}Si nuclear shiedling are:

Without the IEFPCM:

- Silicic acid only: shielding of 1 ppm
- Silicic acid plus sodium: de-shielding of 0.6 ppm
- Silicic acid plus sodium plus water: de-shielding of 0.3 ppm

With the IEFPCM:

- Silicic acid only: de-shielding of 0.01 ppm
- Silicic acid plus sodium: de-shielding of 0.9 ppm
- Silicic acid plus sodium plus water: shielding of 0.06 ppm

When both environmental water and the sodium cation are considered in the IEFPCM solvent the shielding is remarkably similar to the situation when only the implicit solvent is included, lending weight to the methodology of representing environmental factors solely by means of the IEFPCM when calculating chemical shift. It is also clear that, whilst the origins of the changes in chemical shift vary quantitatively between the models, the model with only an implicit representation

Charge	0	-1	-2
Si-O(1)	-227.89	-204.56	-189.01
Si-O(2)	0.00	10.66	17.39
Si-O(3)	0.00	-4.69	-9.48
O-H	-5.82	-3.26	-0.70
Core s	491.54	491.49	491.50
Core p	51.56	44.76	38.03
O Lp p	11.95	3.80	0.58
O Lp sp	-13.86	-30.66	-42.18
σ	390.40	390.45	388.25

Table 3.6: NCS breakdown of NBO contributions to shielding of the monomer in various charge states, with total shielding (σ), all values in ppm.

of the solvent does give the same qualitative picture of how the sources of shielding vary upon deprotonation.

Having established the usefulness of the implicit solvent model for representing the changes in chemical shift upon deprotonation this model is now applied to investigate the effects of multiple deprotonations on the monomer ($Si(OH)_4$) and double 3 ring species (species VIa in figure 3.1) to investigate how the charge state may be expected to influence the shift, thus determining the type of model system to be used in later investigations.

3.3.2 Charge State

All calculations in this section are performed using the same parameters as the previous section with the IEFPCM model. However in this section aug-cc-pVTZ basis sets [185] are employed for all atoms, due to the fact that the elctron density on the Si atom would be expected to increase when a neighbouring silanol group is deprotonated and therefore, to provide more realistic picture from a natural bond orbital analysis of the origin of the nuclear shielding when the monomer is attached to two deprotonated silanols ($SiO_2(OH)_2^{2-}$), it is necessary to have additional basis sets on the Si to accept electron density.

Monomer:

The results of nuclear shielding calculations and a natural chemical shielding analysis of the silicate monomer species are presented in table 3.6.

Table 3.6 shows results for the neutral monomer as well as the singly and doubly charged species. With further deprotonation the issue of lack of basis sets on the Si changes, qualitativly, the NBO distribution of electron density, thus the NBO analysis of these charge states is not considered here. The first notable point from the data is how little the first deprotonation affects the net chemical shift: the change is less than 0.1 ppm, which is just as in the previous section. Upon further deprotonation however, the difference is more pronounced with a 2.25 ppm upfield

Charge		%	s	p	d
0	Si	16.09	24.99	72.95	2.02
	O	83.91	34.23	65.69	0.07
-1	Si	12.80	23.15	56.02	20.64
	O	87.20	32.66	67.23	0.10
-2	Si	10.60	22.50	50.41	26.65
	O	89.40	32.24	67.64	0.12

Table 3.7: NBO analysis of the Si-O inter-atomic orbitals in the monomer at various charge states. Showing precentage polarization towards each centre (%) and precentage s,p and d character.

shift in frequency from the singly to the doubly deprotonated monomer. It is striking, however, that the origin of the shielding changes regularly with varying charge states.

As the majority of the effects of deprotonation of the monomer were considered in the previous section the analysis here shall be restricted to those points not already covered. The major de-shielding contribution to silicon nucleus shielding arises due to the inter-atomic NBO between the silicon and the silanol groups. This contribution becomes progressively less negative as the monomer is deprotonated and a breakdown of these NBOs (table 3.7) makes apparent the reason for this decrease. As the silanol groups are deprotonated the percentage of the electron density polarized towards the silicon decreases. This change in polarization is increased further with the second deprotonation and accounts for the less negative contribution from these orbitals.

The contribution from the core s-orbitals shows very little variation between charge states. However the core p-orbitals do show a marked trend towards becoming less shielding as the charge increases, the reason being that as the monomer is deprotonated the paramagnetic contribution becomes more negative (figure 3.7 a), while the diamagnetic contribution remains essentially the same. This can be explained by the energy of the p-orbitals, which increases upon deprotonation meaning that the excitation energy from that orbital is reduced (figure 3.7 b). The excitation energy affects the paramagnetic contribution to shielding according to equation[186]

$$\sigma_A^p(loc.) = -\frac{\mu_0 \hbar^2 e^2}{8\pi m^2} \frac{1}{\Delta E} \langle r^{-3} \rangle_{np} \sum_B Q_{AB} \tag{3.11}$$

where the term $\langle r^{-3} \rangle_{np}$ refers to the average p-orbital radius cubed on the centre of interest, ΔE is the average excitation energy, and Q_{AB} is a bond-order matrix. The result is that an increased average excitation energy leads to a reduced (negative) paramagnetic contribution. Thus as the energy of the occupied orbitals is increased the average excitation energy is decreased and the paramagnetic contribution increases, reducing the overall the shielding contribution.

Considering the contribution from the lone pair p-orbitals on the oxygen. The

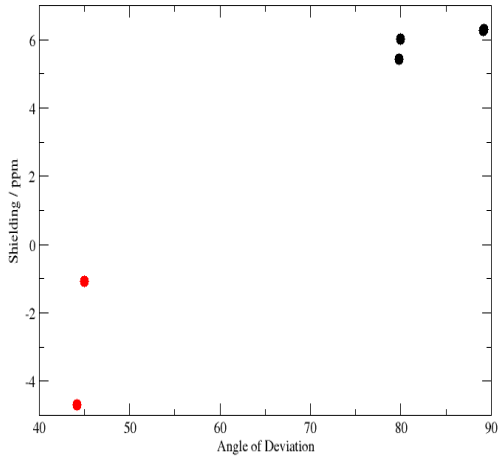

Figure 3.6: Nuclear shielding contribution of Si-O(3) orbitals versus the angle of deviation of this orbital from the Si-O line of centres.Black: systems Na and H_2O with and without IEFPCM. Red: systems M-1 from figure 3.3 with and without IEFPCM.

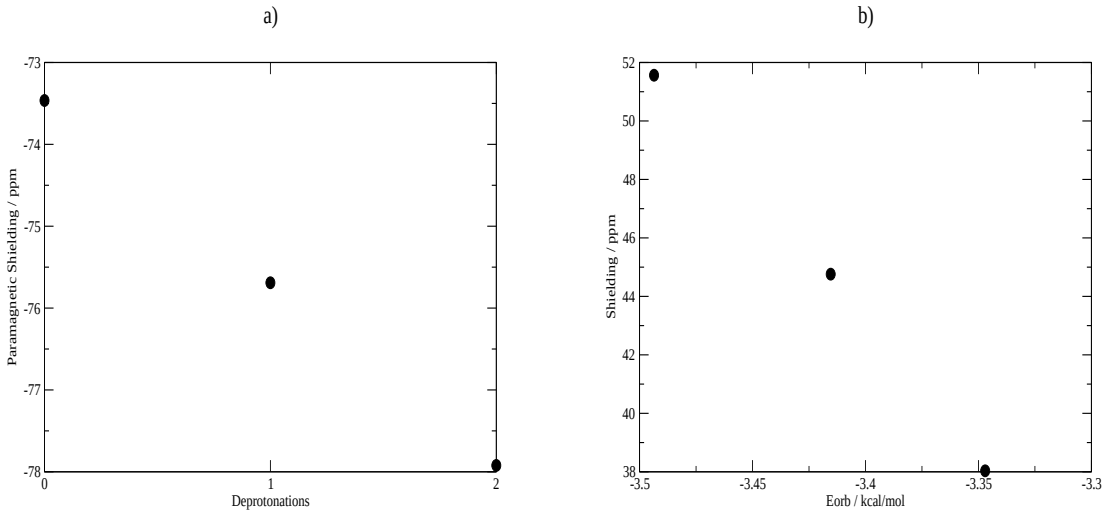

Figure 3.7: a) Change in the paramagnetic shielding of core p-orbitals with deprotonation of the monomer. b) Shielding of core p-oritals versus average core p-orbital energy.

decrease in shielding upon deprotonation(table 3.6) can largely be attributed to the fact that on the deprotonated silanols these orbitals are not present. The decrease, however, does not simply scale with the number of lone pairs present, and some effect such as re-orientation of the remaining orbitals must also affect this contribution.

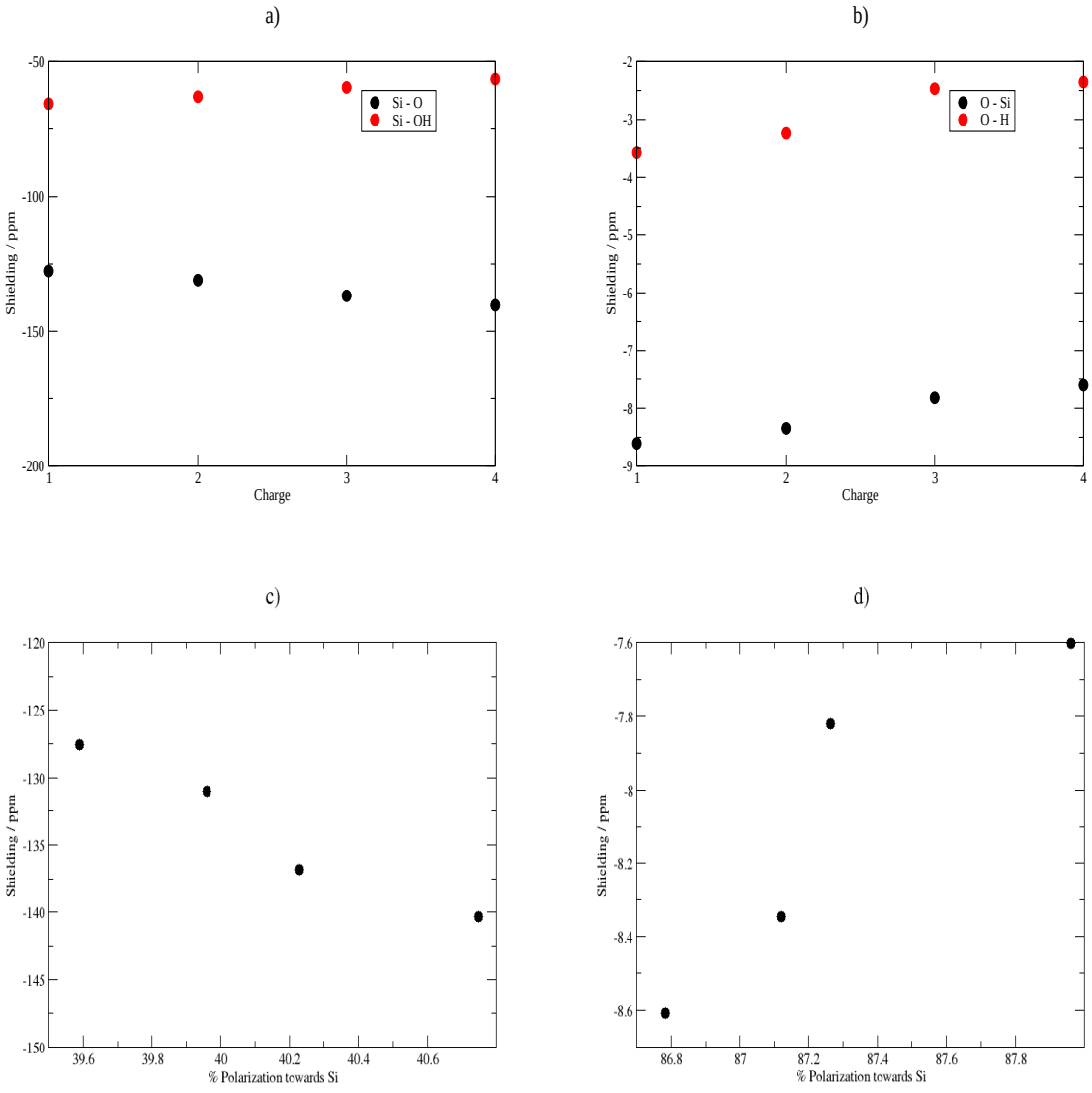

Figure 3.8: Upper; shielding contributions of various NBOs versus the number of deprotonated adjacent OH groups for the $_0Si_{(0-3)}$ centre. Lower; contribution to overall shielding versus % polarization towards bridging Silicon for c) Si-O orbitals, d) O-Si orbitals. The naming of the NBOs is as follows; Si-O is the inter-atomic silicon-bridging oxygen bond, Si-OH is the inter-atomic silicon-silanol oxygen bond, O-Si is the inter-atomic bond between the bridging oxygen and the neighbouring silicon, O-H are inter-atomic orbitals on the silanol group.

Double Three Ring (species VIa in figure 3.1):

In order to investigate the effects of deprotonation on a Q^3 silicon centre, two effects must be taken into account. Firstly deprotonation of a silanol group attached to the centre will obviously be expected to have an effect. Secondly, the nature of

the next neighbour silicon is also known to affect the nuclear shielding of a silicon: so that the effects of the deprotonation of a silanol attached to a neighbouring silicon must also be considered in this instance. This also raises the question of whether the deprotonation of a silanol on an adjacent silicon affects a silicon attached to a deprotonated or a protonated silanol in the same manner. In order to investigate this systematically, a new nomenclature (illustrated in figure 3.9) is defined for silicon types ${}_n\mathrm{Si}_x$, where n is the absoute charge of the silanol of that silicon and x is the number of silicons attached to deprotonated silanols which are nearest neighbours to the centre, thus ${}_0\mathrm{Si}_{(0-3)}$ and ${}_1\mathrm{Si}_{(1-3)}$ are investigated herein.

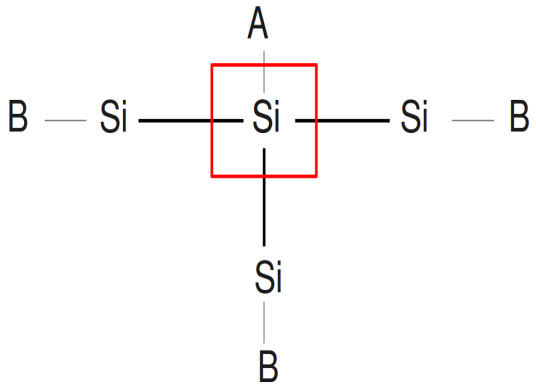

Figure 3.9: Explanation of the ${}_n\mathrm{Si}_x$ notation. Referring to the highlighted Si centre, n relates to the absolute charge of silanol A (0 = protonated, 1= deprotonated), x is the number of silanols (B) which are deprotonated. For example the Si centre attached to the deprotonated silanol in a singly deprotonated double 3 ring (species VIa in figure 3.1) would be referred to as ${}_1\mathrm{Si}_0$, whilst all adjacent centres would be ${}_0\mathrm{Si}_1$

In addition to the four classes of orbitals introudced in section 3.3.1 we also consider the orbital between the bridging oxygen and the nearest neighbour silicon, referred to as O-Si.

Concentrating first on ${}_0\mathrm{Si}_{(0-3)}$, the different contributions to shielding from Si-O, O-Si and OH orbitals as x is increased are plotted in figure 3.8.

The upper panels of figure 3.8 show the contributions from the inter-atomic orbitals. Of these contributions, three of them become less de-shielding as the adjacent silanols are deprotonated, the exception being the Si-O inter-atomic orbitals. Indeed, when the changes in the different contributions are summed together they almost cancel one another out, with the net difference between the first and the last species considered less than 1.5 ppm. Essentially all of the changes in these contributions are due to a shifting around of electron density. Particularly in the case of the Si-O and O-Si orbitals this can be directly correlated to the change in

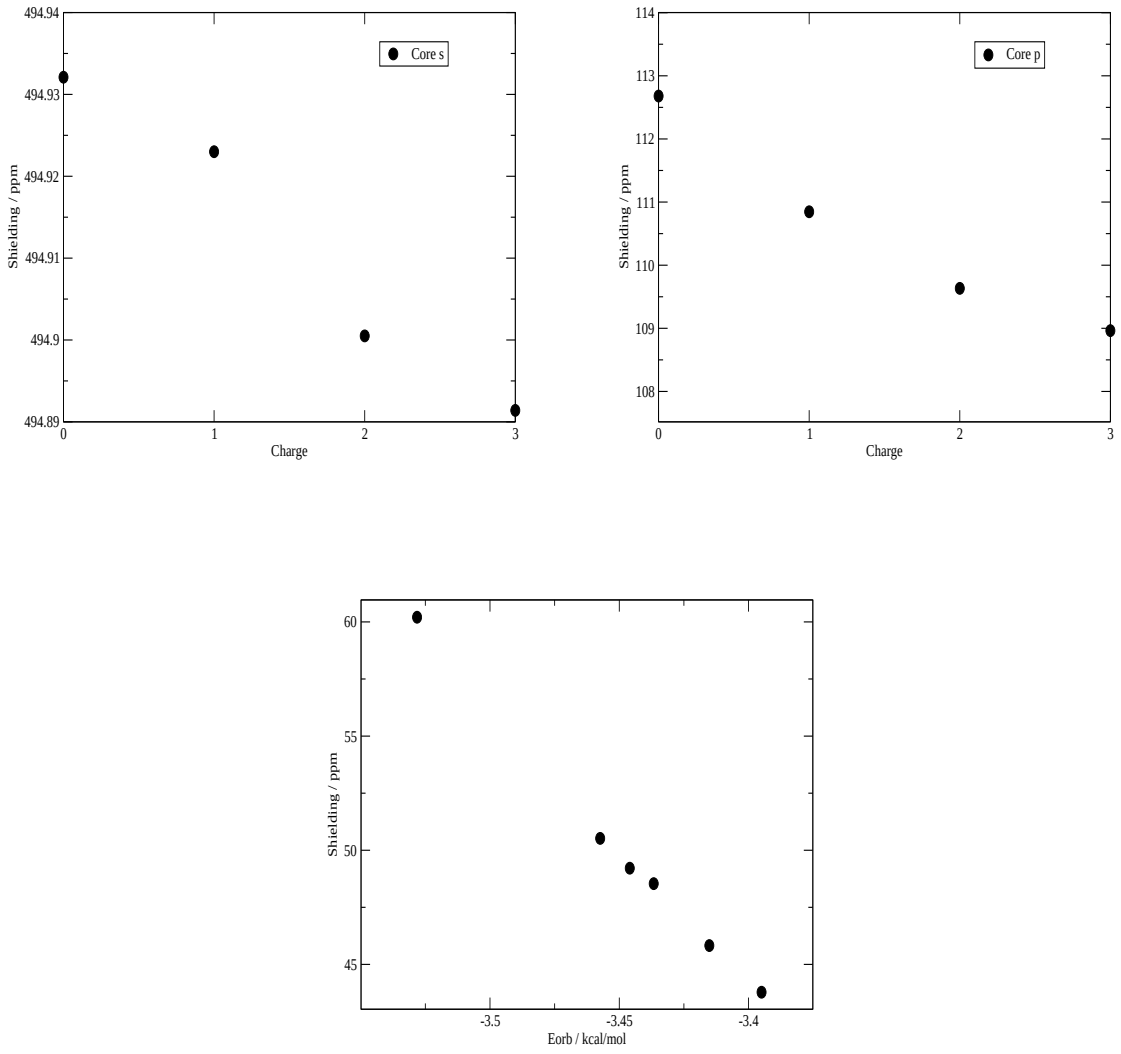

Figure 3.10: Upper; contributions to shielding from the core Si orbitals for the ${}_0\mathrm{Si}_{(0-3)}$ centre. Lower; shielding versus average energy of the core p-orbitals.

shielding, the Si-O orbitals become more polarized towards the silicon, thus their de-shielding effect on the silicon centre increases (figure 3.8 c). The O-Si orbitals on the other hand also become more polarized towards the neighbouring silicons and away from the bridging oxygen, resulting a less pronounced de-shielding effect. The contribution, and consequently the change in contribution from the O-Si orbitals is less than from the Si-O orbitals, as would be expected.

Turning to the core orbitals of the silicon (figure 3.10) the change in the contribution from the p-orbitals is clearly far more significant than the change in the core s-orbitals. That the core s-orbitals are more or less impervious to changes in local environment, be it condensation of the centre or other less pronounced effects, is a general feature found throughout the silicates and is not surprising as they are the least exposed part of the electronic structure. The change in the p-orbitals is primarily a consequence of a change in the paramagnetic nuclear shielding effect of these orbitals. Whilst the diamagnetic shielding remains more or less the same when the surrounding centres are deprotonated the paramagnetic portion becomes more de-shielding. An explanation for this can be found by considering Pople's formulation [186] for nuclear shielding contributions, and in particular the local paramagnetic shielding contribution (equation 3.11). We see that as the energy of the orbital increases so the contribution to overall nuclear shielding decreases (figure 3.10 lower panel). As noted previously, in the analysis of deprotonation of the monomer, this decrease is due to an increase in the negative paramagnetic shielding. Thus as the orbital energy increases, the excitation energy of this orbital decreases and so the net contribution to shielding decreases as well, as predicted by equation 3.11.

The lone pair orbital contributions from both bridging and silanol oxygens are considered in figure 3.11. There are two sets of lone pairs which show consistent trends with deprotonation of the neighbouring silanols: the p-orbital lone pair on the bridging oxygens, and the sp-hybridized lone pair on the silanol atached to the centre in question. The reasons for the observed trends are considered in figure 3.11. We see how (figure 3.11 d) the bridging oxygen p-orbital contribution varies with deprotonation of the neighbouring silanols and how this affects its contribution to shielding. As the neighbouring silanols are deprotonated, the angle at which this orbital sits on the oxygen becomes progressively favourable for overlap with the silicon orbitals (figure 3.11 a), thus providing more electron density towards the silicon centre, which, in turn, results in a greater contribution to the nuclear shielding. Conversely, the lone pair sp-hybridized orbitals on the silicon's own silanol become less shielding. This is as a result of the fact that as the neighbouring silanols are deprotonated this orbital becomes more s-hybridized (figure 3.11 b), meaning that the electron density is more localized on the oxygen itself, and thus less availabe for shielding the silicon nucleus.

It is clear from the above analysis that the shifting of the electron density upon

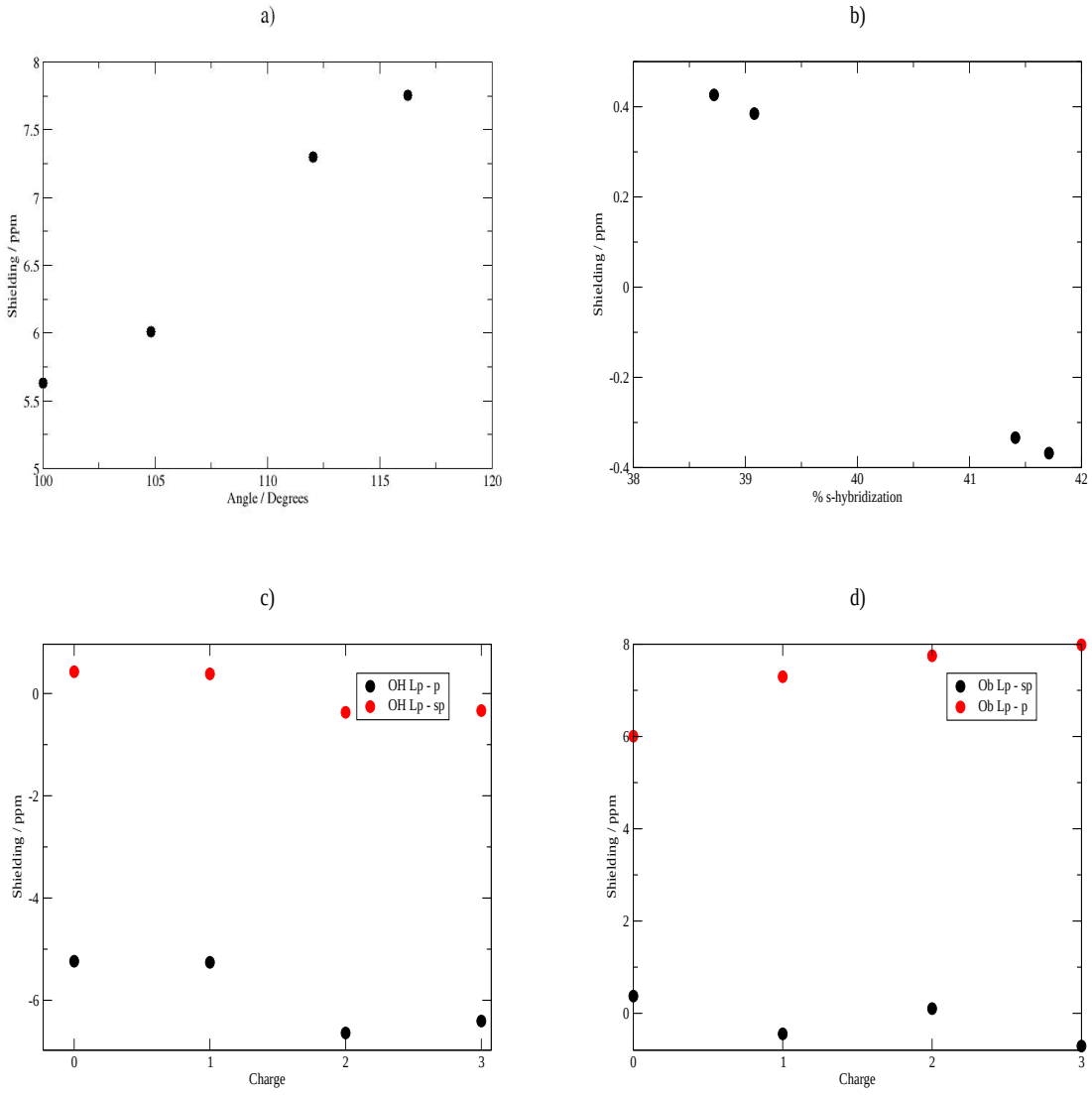

Figure 3.11: Upper; contribution to overall shielding versus a) the angle of the bridging oxygen p-orbital lone pair, b) % s-hybridization of the silanol sp lone pair. Lower; shielding contributions of various NBOs versus the number of deprotonated adjacent OH groups for the ${}_0\mathrm{Si}_{(0-3)}$ centre. The labelling of the orbitals is as follows OH refers to a lone pair on a silanol, Ob refers to a lone pair on a bridging oxygen, sp are sp-hybridized, p are p-orbital lone pairs.

deprotonation leads to increases and decreases in many of the contributions to the shielding of the silicon nucleus attached to a protonated silanol, but that many of these changes serve to negate each other. The net effect is that successive deprotonation of neighbouring silanols leads to a net de-shielding of the silicon nucleus in question (figure 3.12).

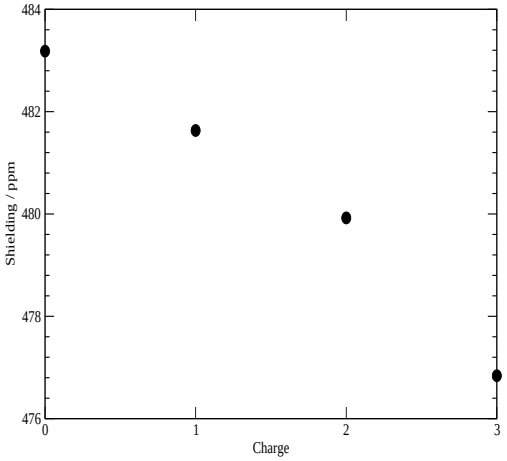

Figure 3.12: Total shielding of the ${}_0\mathrm{Si}_{(0-3)}$ centre with deprotonation of adjacent OH groups.

The effects of neighbouring deprotonations on a silicon attached to an already deprotonated silanol shall now be considered.

The silicon to bridging oxygen and silicon to deprotonated silanol oxygen (figure 3.13) NBOs show very clear and opposite trends as the neighbouring centres become deprotonated. The NBOs to the bridging oxygens become more de-shielding with deprotonation as they do in the case where the silicon is attached to a neutral silanol. However, the silicon to deprotonated oxygen becomes less de-shielding as deprotonation proceeds, similar again to the silicon to protonated oxygen case considered earlier. The reasons for these trends are simple enough to explain and are presented in the lower panels of figure 3.13 . We see that as the NBO becomes more polarized towards the silicon centre it becomes more de-shielding, which would be expected as they are net de-shielding orbitals. Greater polarization towards the silicon centre would be expected to increase their influence on that centre. The difference arises from the fact that as the adjoinoing silanols are deprotonated the silicon to silanol NBO becomes less polarized towards the silicon, thus less de-shielding; conversely the silicon to bridging oxygen NBO becomes more polarized towards the silicon and thus more de-shielding.

Considering now the core orbital contributions to the shielding (figure 3.14), as mentioned previously it is not surprising that there is little effect on the core s-

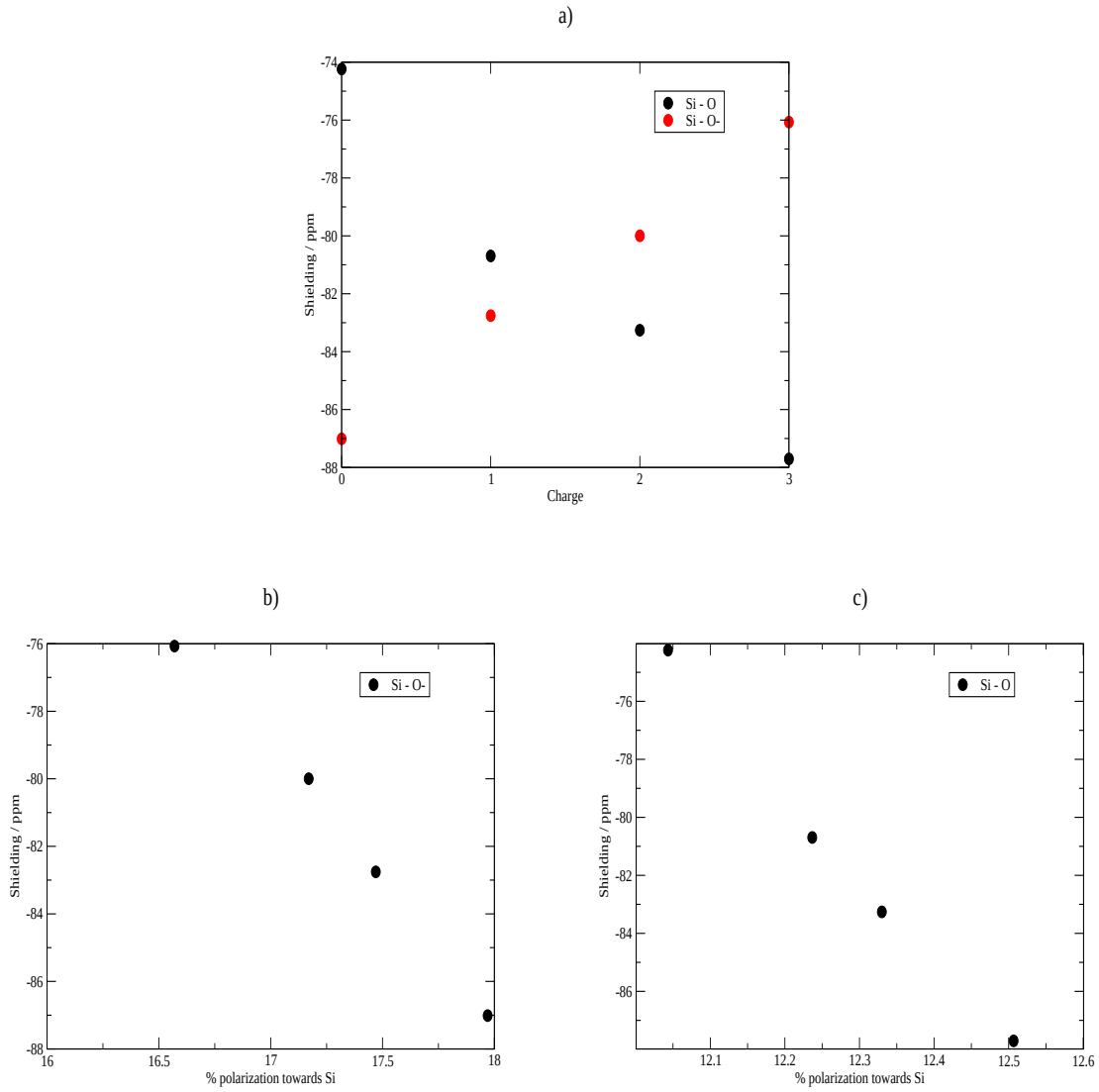

Figure 3.13: Upper; shielding contributions of various NBOs versus the number of deprotonated adjacent OH groups for the $_1Si_{(0-3)}$ centre. Lower; contribution to overall shielding versus polarization towards silicon of: b) the silicon to deprotonated oxygen NBO, c) the silicon to bridging oxygen NBO.Orbitals are labeled as follows; Si-O : silicon to bridging oxygen, Si-O- : silicon to deprotonated silanol.

orbitals. The core p-orbitals do not follow a regular pattern as the neighbours are deprotonated: initially the shielding effect decreases, but upon transition from one to two deprotonated neighbouring silanols the shielding increases, then decreases again when three neighbouring silanols are deprotonated. As figure 3.10 showed the shielding of all of the core p-orbitals considered are strongly correlated to the energy of the orbitals themselves. Thus a configuration with two deprotonated adjacent silanols has a more stable set of core p-orbitals than that with either one or three deprotonated neighbouring silanols.

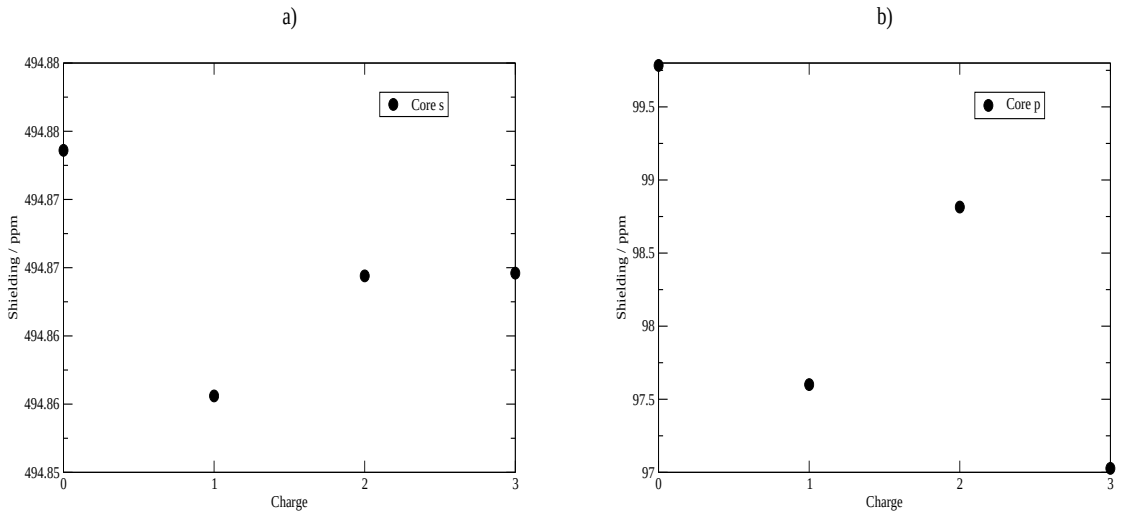

Figure 3.14: Shielding contributions of core NBOs versus the number of deprotonated adjacent OH groups for the ${}_1\mathrm{Si}_{(0-3)}$ centre.

The lone pairs on the bridging and deprotonated silanol oxygens show less well defined trends than in the case with the protonated silanol attached (figure 3.15). An exception to this is the lone pair p-orbitals on the silanol, of which there are now two. The fact that there are two of these orbitals is interesting in itself, as this is due to the fact that the excess electrons resulting from the deprotonation occupy the extra orbital compared to the protonated oxygen. This differs from the deprotonation of the monomer in which the excess electrons are moved to an extra Si-O NBO. The contribution from the extra lone pair is similar to that of the extra inter-atomic NBO, and as such there is little difference in the net change in shielding depending on the location of the excess electrons. The reason for the change in the contribution from this p-orbital upon deprotonation is probably the change in its orientation, resulting in less favourable overlap with the silicon centre as the neighbours are deprotonated. Unfortunately the reference orientation of these centres (set within the program) changes during the optimization process and as such little meaningful comparison can be made of the differing angles against the contribution to nuclear shielding, as was possible in the previous case.

Summary

As was the case with the protonated centre, the silicon attached to a deprotonated silanol in a Q^3 environment undergoes net de-shielding (figure 3.16) as the neighbouring silanols are progressively deprotonated. Meaning that all centres attached to a deprotonated centre will undergo de-shielding upon further deprotonation of that centre. But this is counteracted by that fact that the silicon attached to the silanol which is deprotonated itself becomes more shielded upon deprotonation. Furthermore the experimental NMR spectrum is gathered on a timescale meaning that the signal gathered is that due to an ensemble of the various positions of deprotonation (i.e. a timescale which allows for movement of protons between oxygens) this means that the observed signal will show very little difference regardless of the net charge state of the species. This situation is obviously somewhat different for the Q^0 centre investigated previously where changes are more pronounced, and not offset by neighbouring silicons, however this difference was also relatively small.

The above conclusion has two important consequences. First it helps to explain the experimental observation, mentioned earlier (section 3.1), that less rigid species are more succeptible to changes in shift depending on pH. The less rigid species obviously contain fewer highly condensed (Q^3) silicon centres, thus have fewer neighbouring silicons to counteract the shielding/de-shielding effects of deprotonation, meaning that any net changes in charge state will be more readily observed in their spectra as pH varies. The second consequence is that, due to the small to negligible changes upon deprotonation it would seem rasonable, in the absence of reliable evidence, to use fully protonated clusters to model NMR shifts from here on in. It would be no less reasonble to assume fully deprotonated clusters, however fully protonated species will tend to be better behaved in simulations, and as such represent the obvious choice.

Having thus far considered the effects of two environmental elements on the NMR spectra of small silicates, (the charge state and the solvation) another consideration shall be investigated. The nature of the cation present in the solution is known to modify the chemical shift of silicon in these oligomers [175]. An investigation of alkali metals, the effects of which on Si NMR experiments have been studied, shall now be presented.

3.3.3 Cations

In order to consider counter cation effects the deprotonated monomer ($SiO(OH)_3^-$) is considered in the presence of a charge balancing metal ion, we consider Li^+, Na^+, K^+ and Rb^+. Both Na^+ and K^+ are commonly used in zeolite synthesis and are also present in many NMR experiments on pre-nucleation solutions. Whilst Li^+ and Rb^+, less often used in synthesis, are chosen in order to investigate systematically the effect of increased metal radius on the chemical shift and due to the fact that

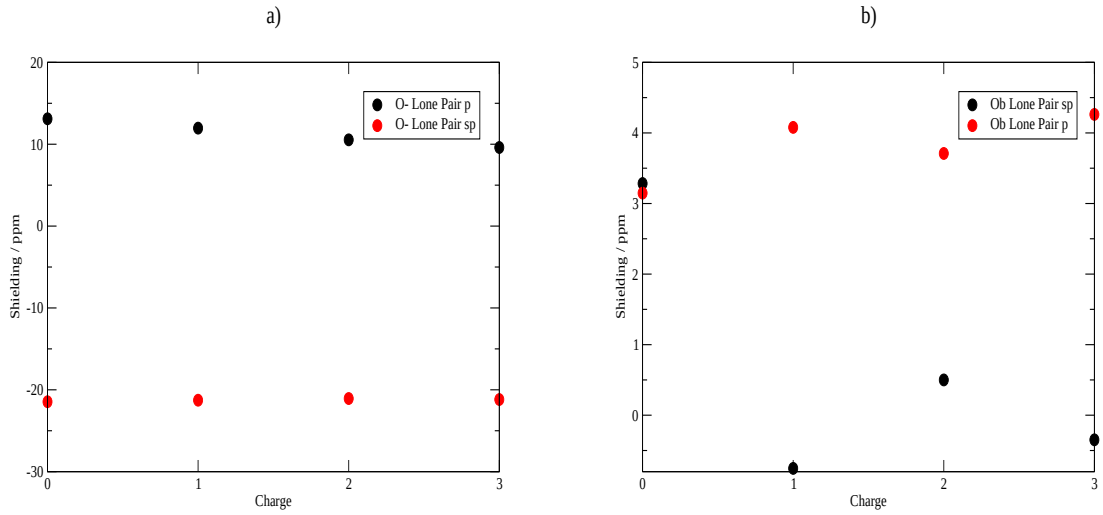

Figure 3.15: a) Shielding contribution of lone pair NBOs on the deprotonated silanol, b) shielding contribution of lone pair NBOs on bridging oxygens, both versus the number of deprotonated adjacent OH groups for the $_1\mathrm{Si}_{(0-3)}$ centre.

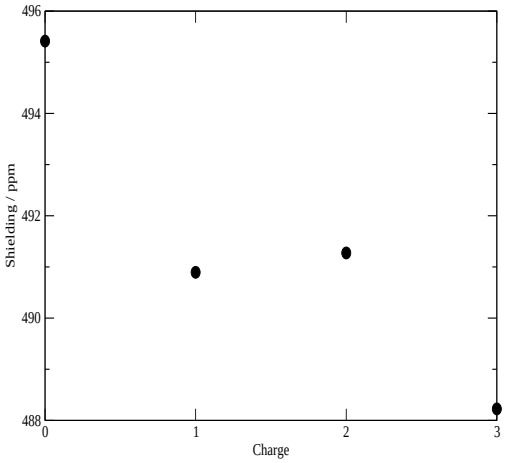

Figure 3.16: Total shielding of the $_1\mathrm{Si}_{(0-3)}$ centre with deprotonation of adjacent OH groups.

NMR experiments of silicate systems with these species have been performed. We compare our results to the experimental results of Kinrade and Knight who consider Na^+, K^+ and Rb^+ [175] and also Wijnen *et al.* who consider Li^+, Na^+, K^+ and Rb^+ [182] . It should be noted here that the aug-cc-pVNZ basis sets used in the other sections of this chapter are not available for K or Rb and thus the TZV basis sets of Schäfer *et al.* [187, 188] are employed for all counter cations in the following calculations. Other than this the parameters of the calculations are the same as the previous sections in which the IEFPCM was included.

The results of the simulations and analyses are presented in table 3.8. As noted in table 3.1 an increase in the atomic mass of M^+ is expected to result in an increase in the shielding of silicon, which is observed in the experimental investigation of Na^+, K^+ and Rb^+ [175]. The calculated values here also follow the trend, with the exception of Li^+ : a fact also noted experimentally [182]. The reasons for the general trend, and anomaly of Li^+ shall now be considered in more detail from the NCS analysis of contributions to shielding.

	Li	Na	K	Rb
Si-O(1)	-213.70	-213.81	-212.75	-211.25
Si-O(2)	7.69	8.33	8.45	6.86
Si-O(3)	2.78	0.42	0.92	2.54
O-H	-3.63	-3.07	-2.68	-2.18
Core s	492.74	492.37	492.11	492.07
Core p	16.22	15.47	15.46	15.31
O Lp sp	-16.63	-16.88	-16.81	-16.59
OH Lp sp	-11.45	-12.08	-12.67	-13.45
OH Lp p	4.93	4.33	3.53	3.05
σ	391.19	385.89	386.66	388.52

Table 3.8: Deprotonated monomer nuclear shielding (σ) and NCS analysis of NBO contributions to overall shielding in the presence of a series of alkali metal cations. All shielding values are in ppm.

Inter-atomic Si-O Orbitals:

The most populated inter-atomic orbital has a net de-shielding effect. This effect generally decreases as the radius of the metal ion increases. However for Li^+ the value is very similar to the value for Na^+, this contribution is significantly less in the presence of Rb^+ than for the other cations. The value of this contribution is dependent to a large extent on the degree to which the orbital is polarized towards the silicon and the larger cations tend to result in the orbital being polarized more towards the oxygen and less towards the silicon. The correlation between ionic radius and the degree to which the orbital is polarized towards the silicon is clear in figure 3.17 a). Whilst this explains most of the observed trend, it does not address the de-shielding in the presence of Li^+. To explain the fact that this orbital is less de-shielding in the presence of Li^+ than Na^+ the NBO results need to be further

examined(table 3.9). We see now that, whilst the NBO is more polarized towards the silicon in the presence of Li^+, the orbital itself also has less d-orbital character than in the presence of Na^+. Thus the electron density is more localized in the bond itself in the presence of Li^+, meaning that its (de-shielding) effect on the Si centre is less, explaining the outlying behaviour of Li^+.

For the remaining two Si-O orbitals, which make a smaller contribution to the net shielding, the degree of polarization towards the silicon *increases* with increasing cation radius (figure 3.17 b). This can explain the trends observed in the series Na^+,K^+,Rb^+, where the shielding influence of these orbitals is seen to increase with ionic radius. Again the Li^+ case is more difficult to explain, and in this case the nature of the orbital itself gives no extra insight. We might speculate that the orientation of the orbital changes in the presence of Li^+, thus changing its contribution.

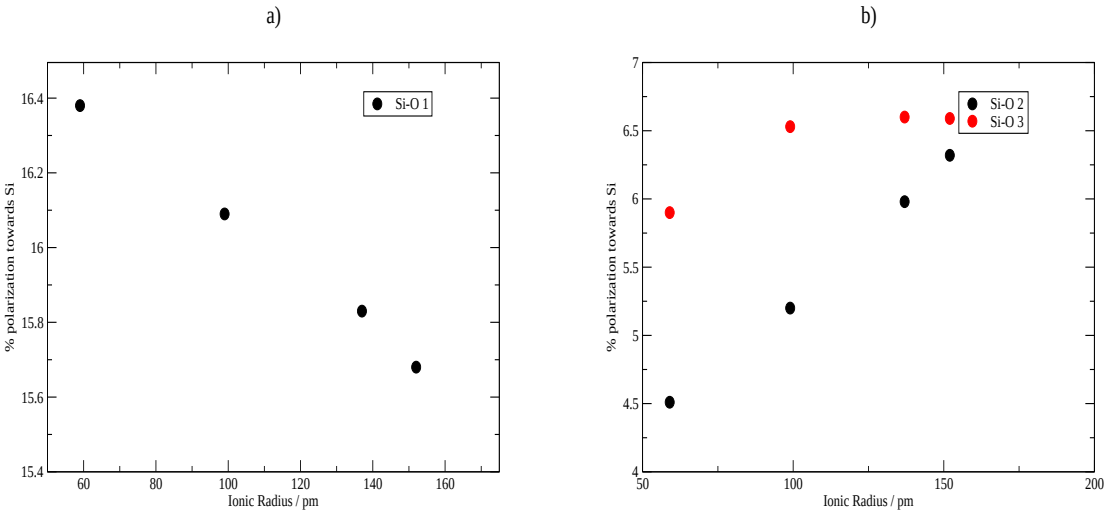

Figure 3.17: Degree to which the Si-O inter-atomic NBOs are polarized towards the silicon centre versus the ionic radius of the counter cation. Si-O N refers to the order of population of the orbitals N=1: most populated.

Cation		%	s	p	d	σ/ppm
Li	O	83.62	33.76	66.02	0.01	
	Si	16.38	26.99	66.17	6.66	-66.57
Na	O	83.91	34.02	65.78	0.20	
	Si	16.09	26.43	65.24	8.15	-66.70
K	O	84.17	33.35	66.45	0.20	
	Si	15.83	26.03	64.77	9.04	-65.80
Rb	O	84.32	32.67	67.13	0.20	
	Si	15.68	25.75	64.59	9.49	-64.81

Table 3.9: NBO analysis and shielding contribution (σ) of the Si-O(1) NBO in the presence of alkali metal cations. Showing percentage polarization towards each centre, percentage s,p and d character.

Core Orbitals:

The core s-orbitals show very little variation in contribution to shielding with the change of cation. The core p-orbitals, however, in conjunction with the inter-atomic orbitals, are to a large extent responsible for the higher shielding observed in the presence of Li^+. The contribution from these orbitals generally decreases with increasing cation radius. However, it is clear from figure 3.18 a) that this decrease is far more pronounced between Na^+ and Li^+ than the other cations. As in previous sections, much of the trend observed in the contribution from the core p-orbitals can be related to the average energy of the orbitals. The energy of this orbital increases as the ionic radius of the counter cation increases (figure 3.18 b). This increase leads to a decrease in the shielding contribution of these orbitals, explained by the same argument as used in sections 3.3.1 and 3.3.2.

Lone Pairs:

The final major contribution to nuclear shielding which shall be considered is that from the lone pairs on the oxygens. Perhaps surprisingly, the contribution from the lone pair on the deprotonated oxygen (an sp-hybridized lone pair), which is closest to the cation, shows very little variation with the change of cation.

The sp-hybridized lone pairs on the other oxygens show a linear tendency to become more de-shielding as the ionic radius of the cation increases (figure 3.19 a). The p-orbital lone pair on the other oxygens shows the same trend, becoming less shielding as the cation radius increases. The reasons for both sets of lone pairs becoming less shielding as the cation radius increases is that, as the cation becomes larger the average Si-O bond length increases also (figure 3.19 c). As the bond length increases so there is less electron density from the oxygens available for shielding the nucleus.

Summary:

For the series Na^+,K^+,Rb^+ the effects of the inter-atomic orbitals become more de-shielding with increased cation radius. The contributions from the oxygen lone pairs of electrons become less de-shielding with increasing cation radius, and the core orbitals do not vary to a great extent. The net result of this is that the decreased de-shielding due to the lone pairs is greater than the increased de-shielding of the inter-atomic orbitals and hence the silicon becomes more shielded with increasing cation radius.

Li^+ shows different trends for both the inter-atomic orbitals and the lone pair orbitals, these differences along with the fact that the core p-orbitals have a greater shielding effect in the presence of Li^+ account for the experimentally observed fact that a silicic acid monomer in the presence of Li^+ has a more shielded Si nucleus than in the presence of Na^+ [182].

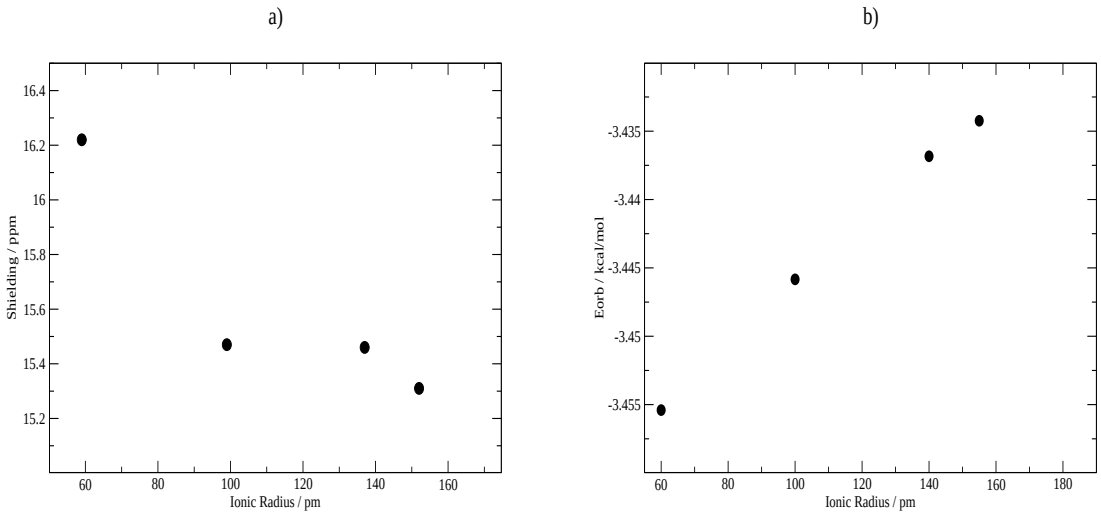

Figure 3.18: a) Core p-orbital contribution to nuclear shielding versus cation radius. b) Average p-orbital energy versus cation radius.

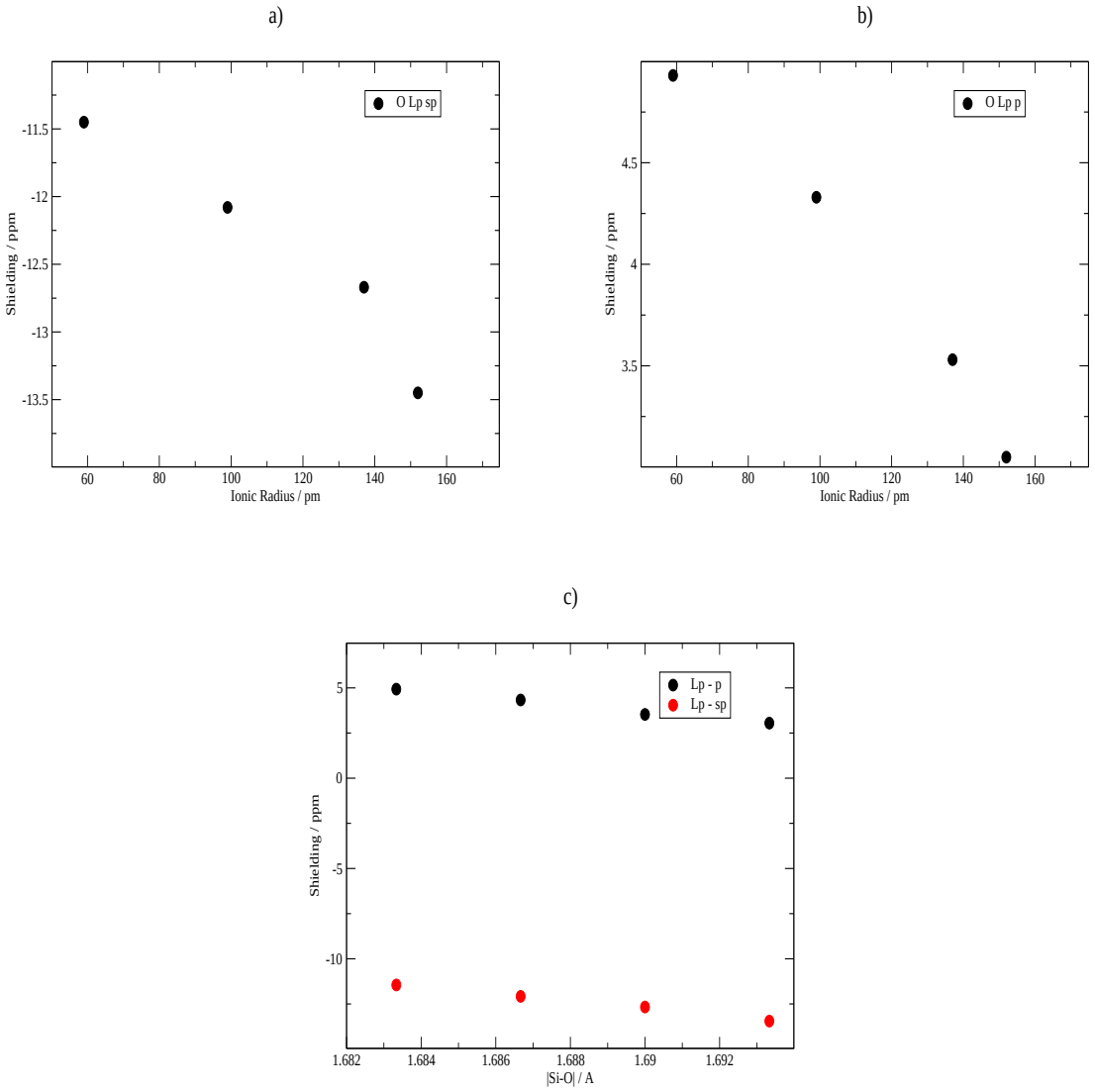

Figure 3.19: a) Silanol sp-hybridized lone pair contribution to shielding versus cation radius, b) Silanol p-orbital lone pair contribution to shielding versus cation radius, c) Lone pair contributions versus average Si-O bond length in Å.

3.3.4 Functionals and Cavity Scaling

It has now been established that the IEFPCM provides a good estimation of the effects of solvation on the silicic acid monomer whilst maintaining computational efficiency. It has also been shown that in the absence of any specific evidence for the actual charge state of the species in solution, a fully protonated species should show little difference in shift from a fully deprotonated one. Using this information we now consider the effect of different functional forms of DFT and parameters for solvation on an extended set of silicates, to further optimize our methodology.

DFT methods were chosen due to their successful previous use in the calculation of Si chemical shifts, in particular B3LYP[103, 105] was shown to provide accurate Si shifts [189, 190] when used in conjunction with the 6-311+G** basis set. The PBE functional[104] has also been shown to produce accurate Si chemical shifts [163, 162], although it is important to note that most of these cases the calculations are for solid state zeolite species and as such do not include solvation.

As mentioned earlier, solvation effects on nuclear shielding has been a subject of interest for some years[147, 148, 149], although these studies have been primarily nitrogen chemical shieldings. However a recent study using explicit solvation [191] proved successful in predicting chemical shifts for a $Si(OH)_4 \cdot (H_2O)_8$ cluster. In many of the NMR studies using continuum methods [150, 151] charge penetration outside the cavity has been cited as a possible source of errors. One method which may possibly lead to a reduction in these errors is the increase of the size of the cavity, to this end calculations have been performed using cavity scaling factors of 1.2,1.4 and 1.6 of the van der Waals radius.

All calculations in this section were performed using the Gaussian 03 program [183]. The set of neutral monomers used was species I, II, III, IVa, Vb, Vd, VIa, VIIIc and VIIIe in figure 3.1. All of these species were geometry optimized using the B3LYP [105] functional and 6-31G* basis sets[184]. The geometry optimizations were performed using the integral equation formalism of the polarizable continuum model (IEFPCM) [130] to represent solvation. The IEFPCM was used with cavity scalings of 1.2, 1.4 and 1.6 time the van der Waals radii. The calculation of NMR shielding was also performed in the presence of the IEFPCM with these cavity scalings. For the calculation of NMR shielding tensors two functionals were used, B3LYP [105] and the PBE functional[104] with aug-cc-pVTZ basis sets[185] for O and aug-cc-pVDZ basis sets[185] for Si and H. All calculations were performed in serial on a local cluster, gemoetry optimizations taking between 12 minutes for the smallest species up to 6 days for the largest, NMR calculations took between 8 minutes and 2 days.

Chemical shifts are obtained by subtracting the shielding from the reference value for TMS, calculated using the same level of theory and basis sets;

$$\delta_{species} = \sigma_{species} - \sigma_{TMS} \tag{3.12}$$

Functional	f_{opt}	f_{NMR}	Error	r^2	Functional	f_{opt}	f_{NMR}	Error	r^2
B3LYP	1.2	1.2	3.341	0.8958	PBE	1.2	1.2	2.857	0.9170
B3LYP	1.2	1.4	3.395	0.8965	PBE	1.2	1.4	3.242	0.8443
B3LYP	1.2	1.6	3.572	0.8975	PBE	1.2	1.6	3.352	0.9138
B3LYP	1.4	1.2	3.912	0.8621	PBE	1.4	1.2	3.251	0.8817
B3LYP	1.4	1.4	3.862	0.8349	PBE	1.4	1.4	3.270	0.8804
B3LYP	1.4	1.6	3.506	0.8626	PBE	1.4	1.6	3.280	0.8814
B3LYP	1.6	1.2	3.347	0.8676	PBE	1.6	1.2	2.868	0.9065
B3LYP	1.6	1.4	3.383	0.8628	PBE	1.6	1.4	2.877	0.9046
B3LYP	1.6	1.6	3.398	0.8687	PBE	1.6	1.6	2.875	0.9069

Table 3.10: Average absolute errors in ppm and regression coefficients for combinations of functional and cavity scaling factor for optimisation, f_{opt}, and NMR, f_{NMR}, calculations, on neutral species.

The results of the invesigation of different methodoligies for calculating chemical shifts are summarized in table 3.10. The most important point to note is that the performance of the PBE functional is superior to that of the B3LYP functional, both in terms of the average absolute error in calculated chemical shift; values between 2.85 and 3.35 as opposed to 3.34 - 3.91, and more importantly in terms of reproducing the trends observed in experimental results; reflected by superior r^2 values.

It is also worth noting that in almost all cases cavity scaling factor of $f_{opt} = 1.2$ in the optimization step provides the structures with the lowest average absolute error and the best r^2 values: in agreement with the convention that $f_{opt} = 1.2$ is the optimum value [135, 136]. An increase in error is observed as f_{NMR} is increased from 1.2 to 1.6, which can be considered to be due to the fact that in the species studied the Si nucleus is surrounded by other atoms in the species means that charge penetration from Si would not be a major factor in these calculations. Hence increasing cavity size produces little improvement in terms of removing charge penetration issues.

It is worthy of mention that the r^2 values in this evaluation include chemical shifts of two species whose shifts are shown to have unusually large deviations from experimental values (the dimer and 4 ring species), due to errors in the calculation of their geometries (a point further discussed in section 3.3.6), and that the removal of these species from the analysis results in an r^2 value for PBE 1.2/1.2 calculated shifts of 0.98, clearly adding to confidence in the method. All calculation presented from here on are carried out using this methodology.

3.3.5 Testing the Methodology

Having now established an optimal methodology the results obtained using this methodology are now tested against the most extensive previous computational study of ^{29}Si NMR shifts [52]. In this study the effects of solvation were *not* accounted for. The full list of calculated shifts and deviations from experimental values for our study and this previous study are given in the appendix A.

For the purposes of comparison to experimental chemical shifts and to a previous systematic study [52] only species which have calculated chemical shifts with no major explicable deviation from the experimental values are considered when calculating average error. Thus for species such as the dimer, or 4 ring, which have multiple minima, some of which show large discrepancies, which shall be rationalized later, only the conformation which most closely matches the experimental value is considered. This also means that many species with "dangling monomers" (-Si(OH)$_3$) were not considered for the purposes of comparison: once again the reasons will be discussed in more detail presently. The same criterion is applied when calculating the same values from the work of Cho *et al.* [52].

For Q^1 species it is noted that in these results all shifts are found to be up frequency of the experimentally observed shift. In comparison to the first experimental study [5] there is only one value, that of the dimer species, thus no standard deviation could be calculated, however comparing to the second experimental study [44] there are 4 points, the standard deviation of the errors from the new methodology is only 1.29 ppm, which is the same as that in the data of Cho *et al.* [52].

For Q^2 species there are 7 points of comparison with reference [5] and 20 points of comparison with reference [44], both of which show a general trend for calculated chemical shift to be down-frequency of the experimentally assigned value, by an average of 1.27 and 1.52 ppm respectively, whilst these represent a larger average error than calculated for reference [52] (0.58 ppm to high frequency) the value of standard deviation is lower 1.24 and 1.74ppm compared to 2.53 ppm in reference [52].

Q^3 species are compared to 6 and 15 data points from reference [5] and refernce [44] respectively. As with Q^2 species the trend is for calculated shift to be down frequency of experimental, by 1.81 ppm compared to reference [5] and -2.02 compared to reference [44] an increase on the discrepancies observed for the Q^2 species, however while the error increases the standard deviation remains similar, 1.24 and 1.64 ppm respectively, unlike reference [52] which shows an average error of +2.28 ppm, with a standard deviation of 3.23 ppm. These results demonstrate the usefulness of the IEFPCM when calculating chemical shift, by being even better able to recreate experimentally observed values than *in vacuo* studies, which have already proved extremely useful in interpreting experimental data [52]. The discussion which follows will look in more detail at different subsections of the species studied.

3.3.6 Species With One Unique Centre

The species studied with only one unique Si NMR centre, which have been identified experimentally, are the monomer, dimer, 3 ring, 4 ring, double 3 ring, double 4 ring and prismic tetramer species (structures I, II, III, IVa, VIa, VIIIc and IVb respectively in figure 3.1). These represent all of the single unique Si centre species

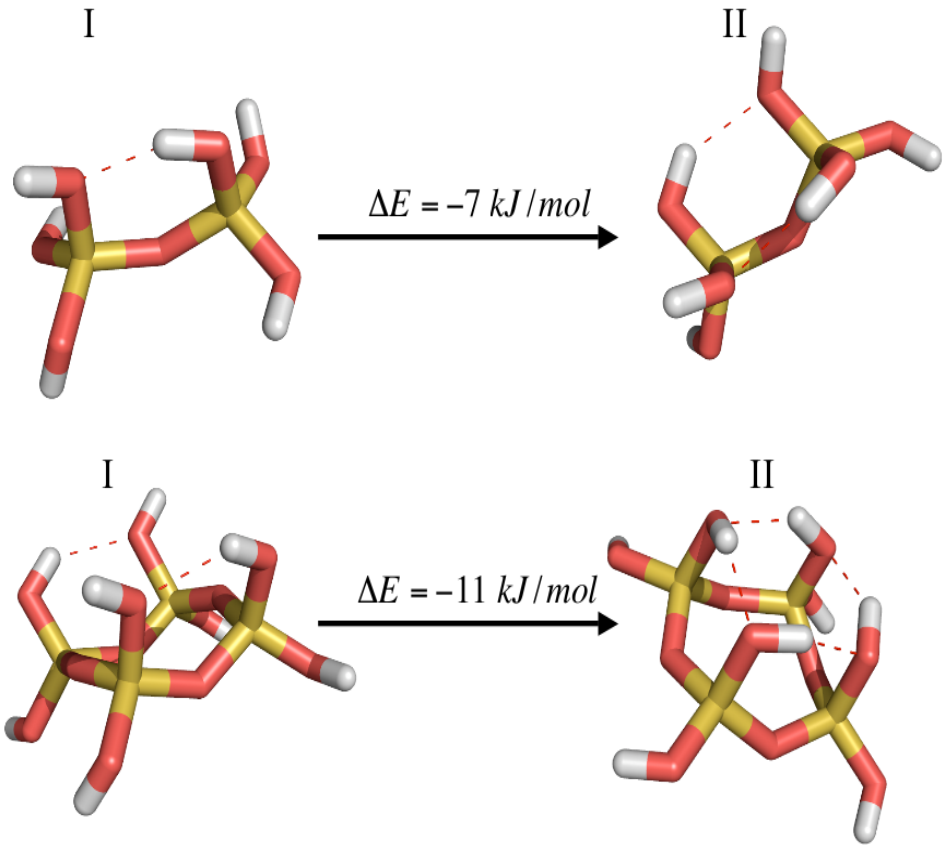

Figure 3.20: The two conformations of the dimer and 4 ring. The difference in energy between the species is shown. Atom colours: Si - yellow, O - red, H - white; hydrogen bonds are highlighted with dashed lines.

identified experimentally by 2D NMR studies [5, 44]. As can be seen from table 3.11, agreement with experiment is, on the whole, very good. However, three species - namely the dimer, 4 ring and the prismic tetramer - have conformations with a calculated shift which is considerably up frequency of that assigned experimentally. The differennt conformations of the dimer and 4 ring are shown in figure 3.20. Whilst this may suggest an inaccuracy in our methodology let us consider each case in turn to determine the root of the discrepancy.

			Error/ppm Ref. [5]			Error/ppm Ref. [44]	
SPECIES	δ calc. /ppm	Q^1	Q^2	Q^3	Q^1	Q^2	Q^3
I*	-71.05	0.50			na		
II Conformation I	-78.04	2.90			1.63		
II Conformation II	-73.70	7.16			5.92		
III	-84.06		-1.69			-2.90	
IVa Conformation I	-88.83		-0.23			-1.74	
IVa Conformation II	-82.82		5.78			4.27	
VIa	-91.47			-2.15			-3.36
VIIIc	-100.03			-1.04			-1.86
IVb	-82.05			16.06			13.98

Table 3.11: ^{29}Si Calculated chemical shifts compared to experimental assignments from [5] and [44] , showing errors for Si centres with different degrees of condensation. Conformations I and II refer to figure 3.20.*: Q^0 centre.

Considering first the dimer and 4 ring species (shifted by 7.16 and 5.92 and 5.78 and 4.27ppm up frequency of the experimental value respectively with respect to reference [5] and reference [44] respectively). Both of these have alternative low energy conformations presented in figure 3.20. These local minima, close to the global minimum, were identified during a high temperature molecular dynamics run used as a conformational search tool. The substantial difference, in both cases, between the local and global minima is that the global minimum has more internal hydrogen bonds than the nearby local minimum. The relative energies of the conformations are presented in figure 3.20. In both cases conformation II with a higher degree of internal hydrogen bonding is calculated to be energetically favourable. However the highly hydrogen bonded conformation also results in a calculated chemical shift which is farther from the experimental value than the less hydrogen bonded conformation (table 3.11).

Is, therefore, the discrepancy as a result of a poor representation of the effect of hydrogen bonding on the electronic structure, or because the conformation itself is not representative of the actual minimum? To investigate further, the hydrogens involved in H-bonding in the dimer conformation II were rotated through 180 degrees whilst holding all other coordinates of the species stationary. The resulting structure has a chemical shift of -72.50 ppm, which is 1.2 ppm further up frequency than that of conformation II, thus demonstrating that the discrepancy of the calculated shift

here does not arise as a result of an erroneous electron distribution due to hydrogen bonding effects.

As will be shown presently the reason for these erroneous conformations and shifts here and more generally for species with internal H-bond interactions, can be attributed to the changes in Si-O-Si bond angles; caused directly by the neglect of explicit solvation. Implicit solvation models can perform well on energetics since they are parameterised to reproduce solvation free energies. However as they cannot describe the directional nature of hydrogen bonding, the geometries may be significantly in error in comparison to the true aqueous environment. The effect of the inclusion of an explicit representation of the surrounding water shall be considered in section 3.3.9. We shall now briefly consider why internal hydrogen bonding may lead to erroneous calculated chemical shifts.

As was mentioned in the introduction to modeling of ^{29}Si shifts the Si-O-Si bond angle is of major importance in determining ^{29}Si shift, to the extent that quantitative relationships between this angle and the chemical shift have been derived [162]. The origin of this relationship has been elucidated by Tossell *et al.* [181] who showed how the change of Si-O-Si bond results in a change in shape and hybridization of the inter-atomic orbitals, a movement in the lone pair electrons on the oxygen and a change in the contribution from the core p-orbitals. Thus even small deviations in this angle may lead to changes in the chemical shift. Since internal hydrogen bonds result in a reduction of this angle they thus also affect the chemical shift.

The third species, for which the calculated shifts and those assigned experimentally are in significant disagreement, is the prismic tetramer. Here there is no additional internal hydrogen bonding which may cause the discrepancy. We therefore suggest that this signal has been mis-assigned. This and other re-assignments are dealt with in section 3.5.

3.3.7 Species With More Than One Unique Centre

The species with more than one unique Si NMR centre which were studied and the calculated chemical shifts are considered in table 3.12. Compared to experiment we see an improvement relative the previous section; a result of the reduced structural flexibility of the species studied in this section compared to those species with a single unique silicon centre. Again these results show a tendency for the calculated shift to be down frequency of the experimental values by $\sim$ 2 ppm, with the discrepancy increasing with the degree of condensation of the Si centre. The average discrepancies are 1.40 ppm and 2.18 ppm for Q^2 and Q^3 compared to [5] and 1.97 ppm and 2.28 ppm compared to [44]. The standard deviations of the average errors are in all cases less than 2 ppm.

Only one species shows a deviation from experimental values of greater than 4 ppm, namely the *cisoid* conformer of the tricyclic hexamer species (structure VIc in

figure 3.1). The rationale for differentiating between the *cisoid* and *transoid* (structure VId in figure 3.1) conformations is not explicit in the source of the assignment [44]. However the original assignment was made on the basis of the intensity of the signals [42]. The rationale being that the *transoid* conformation would be expected to be more stable than the *cisoid* conformation. Our simulations show the opposite to be true, the *cisoid* species being 16 kJ mol^{-1} more stable. Thus suggesting that a mis-assignment may be responsible for this discrepancy, this is dealt with further in section 3.5.

		Error/ppm Ref. [5]			Error/ppm Ref. [44]		
SPECIES	δ calc. / ppm	Q^1	Q^2	Q^3	Q^1	Q^2	Q^3
VIIIe	-91.41		-3.51				
	-99.10			-2.20			
Vd	-90.21		-1.51		-2.87		
	-91.77			-2.17			-3.70
	-83.67		-1.37			-2.83	
Vb	-88.84		-2.24			-3.66	
	-97.79			-3.49			-4.92
VIIId	-92.23			-2.03			-2.72
	-93.79			-0.99			-2.51
	-99.43			-0.33			-1.93
VIb	-85.26		1.64			0.23	
	-93.63			0.17			-1.32
VIIg	-90.18					-2.31	
	-92.26						-3.47
	-93.19						-3.37
VId	-89.54						-0.75
	-84.20					-2.52	
VIc	-92.06						-4.52
	-84.01					-2.58	
VIg	-82.10					-1.06	
	-89.34					-1.96	
	-89.42					-1.83	
	-92.20						-2.65
VIIf	-89.53					-3.00	
	-87.80					-0.20	
	-98.83					-3.96	
	-95.61						0.23
VIIe	-87.10					0.13	
	-95.52						-1.30
	-95.83						-0.05

Table 3.12: Calculated NMR shifts (δ) of species with more than one unique Si centre, compared to values assigned in references [5] and [44]. Species labels refer to figure 3.1.

3.3.8 Substituted Species

The final set of species which were considered were those which are made up of previously described species with one or more monomer groups attached (substituted species). In light of the results presented above, which highlight that fact that internal hydrogen bonding caused by the lack of consideration of explicit water molecules when determining structures, and due to the flexible nature of these "dangling" substituants, it would be reasonable to assume in advance that these would represent possibly the most troublesome class of species to model. This indeed is borne out in the results presented in table 3.13.

These results suggest that the calculated shift for the dangling Q^1 substituant is the most susceptible to these effects and great care must be exercised when modeling. Indeed in many cases the inclusion of explicit water molecules is necessary to allow elucidation of the species structure in solution. However the effects of the substituant on the parent structure are rather better modeled and allow for the use of modeling to aide assignments which prove impossible without.

It is possible to calculate the shift with a degree of confidence in many cases. However, in order to be able to predict whether or not a calculated shift is likely to be reasonable we must establish a criterion. Table 3.13 includes a root mean squared deviation (RMSD) value. This is the RMSD of the ring or cage structure between the structure with and without the dangling group atached. For this calculation only the Si and O atoms in the ring or cage were included (i.e. silanols were ignored). The species which have centres with a large discrepancy between the calculated and experimental shifts are VIf and VIId in figure 3.1. Skeletal representations of the substituted and unsubstituted ring structures are shown in figure 3.21. The high RMSDs for both of these species are mirrored by the differences between experimental and calculated shift. This allows us to propose a "rule of thumb", that if the RMSD of a species with a dangling monomer and its unsubstituted equivalent is greater than 0.3 Å, then an error in the calculated chemical shift is likely due to a discrepancy between the calculated and "true" solution geometry.

3.3.9 The Effects Of Internal Hydrogen Bonding

As mentioned in the section on species with one unique centre (section 3.3.6), internal hydrogen bonds can result in a chemical shift showing a large deviation from the experimental value. It was also noted that these discrepancies are not due to any direct effect of the hydrogen bond on the electronic state of the species, but rather arise indirectly through distortion of the conformation. The different local minima were shown in figure 3.20 along with the difference in energy between the conformations, the dimer species with internal hydrogen bonding is 7 kJ mol^{-1} more stable, which would suggest that it should be the dominant species in the NMR spectrum.

SPECIES	δ calc. /ppm	Error/ppm Ref. [5] Q^1	Q^2	Q^3	Error/ppm Ref. [44] Q^1	Q^2	Q^3	RMSD / Å
Va	-77.44				1.46			0.077
	-84.40					2.39		
	-87.68					-0.45		
	-93.98						1.02	
Vc	-78.34				0.63			0.238
	-91.35						-2.07	
	-81.92					-1.47		
VIi	-80.11				-0.78			0.211
	-84.58					0.68		
	-84.06					1.36		
	-94.46						-1.68	
	-95.69						-2.37	
VIe	-79.56				0.60			0.225
	-84.00					2.99		
	-85.00					-1.79		
	-90.44						2.76	
	-91.08						3.11	
	-94.85						-0.15	
VIf	-75.10				-3.77			0.331
	-84.73					3.69		
	-86.94					-0.10		
	-90.66						2.51	
	-91.20						3.03	
	-89.69						-5.83	
VIId	-74.35				-4.71			0.310
	-86.38					-0.77		
	-89.77						2.38	
	-89.58						1.42	
	-92.73						4.17	
	-93.17						-1.46	
	-92.98						-2.11	

Table 3.13: Calculated NMR shifts (δ) for species with dangling monomers compared to values assigned in ref. [5] and ref. [44]. RMSDs between substituted and unsubstituted species are also presented.Species labels refer to figure 3.1.

However it is clear that experimentally this is not the case , similarly for the 4 ring the structure with a crown of hydrogen bonds (conformation II in figure 3.20) is 11 kJ mol^{-1} more stable than conformation I in figure 3.20, yet has a calculated shift which has a large discrepancy from the experimental value. Why is it that conformations which have lower energy are not observed in experimental spectra?

One reason for the favouring of these structures in the calculations may be because, while the IEFPCM was utilized in order to include solvent effects, such an implicit model fails to take into account correctly the specific hydrogen bonding which can exist between water molecules and the silicates in solution. Thus if water-silicate hydrogen bonding is important it will not be accounted for in our model. In order to demonstrate the importance of explicit water when internal hydrogen bonding is present, the results of a molecular dynamics (MD) simulations of the dimer molecule in explicit water using and *ab initio* MD method are now presented.

The dimer species was subjected to a molecular dynamics simulation using the Quickstep code within the cp2K package [127]. The molecule was placed in a unit cell with 32 water molecules, with dimensions set to reproduce a water density of 0.997 g l^{-1} plus the volume of the dimer, estimated from its van der Waal's radii. The BLYP functional was used, with GTH pseudopotentials, DZVP basis sets and a cutoff of 280 Ry. The system was equilibrated with temperature re-scaling for 5 ps. Re-scaling was then removed and the run was continued for a further 15 ps in an NVT ensemble with a time step of 0.5 fs, resulting in an average temperature of 351.47 K, the fluctuations of energy and temperature during the simulation are shown in figure 3.22. The Si-O-Si bond angle distribution from the molecular dynamics run (figure 3.23) shows a normal distribution shape and has a maximum value at 149 °.

One of the most striking features of the dynamics simulation is the fact that a bond angle of 122 ° is *never* sampled: this is the bond angle of conformation II in figure 3.20, which has a chemical shift of anomalously high frequency. It was also found that during the course of the MD simulation no internal hydrogen bonds were formed in the dimer.

A sample of 7 minima from the MD simulation were then relaxed without explicit water molecules, but using the IEFPCM. In each case, an internal hydrogen bond formed. However none of the structures have the double internal hydrogen bond of conformation II. Analysis of the structures (table 3.14) of these minima reveals that six of the seven have a RMSD value of less than 0.03 Å from each other and have energy differences of less than 0.3 kJ mol^{-1}, indicating that they represent essentially the same minimum. The other minimum, structure five, meanwhile, has an average RMSD from the other structures of 0.262 Å and represents the lowest energy conformation of the group, by 0.1 kJ mol^{-1}. Structure number 2 has the

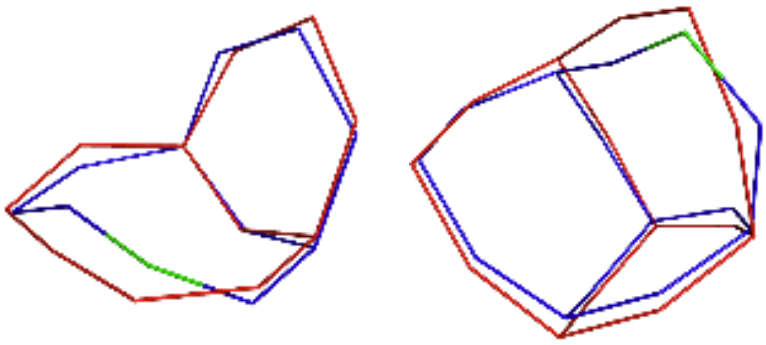

Figure 3.21: The VIf (left) and VIId (right) species, both with dangling monomers (blue) and without (red). The site of substitution is highlighted in green.

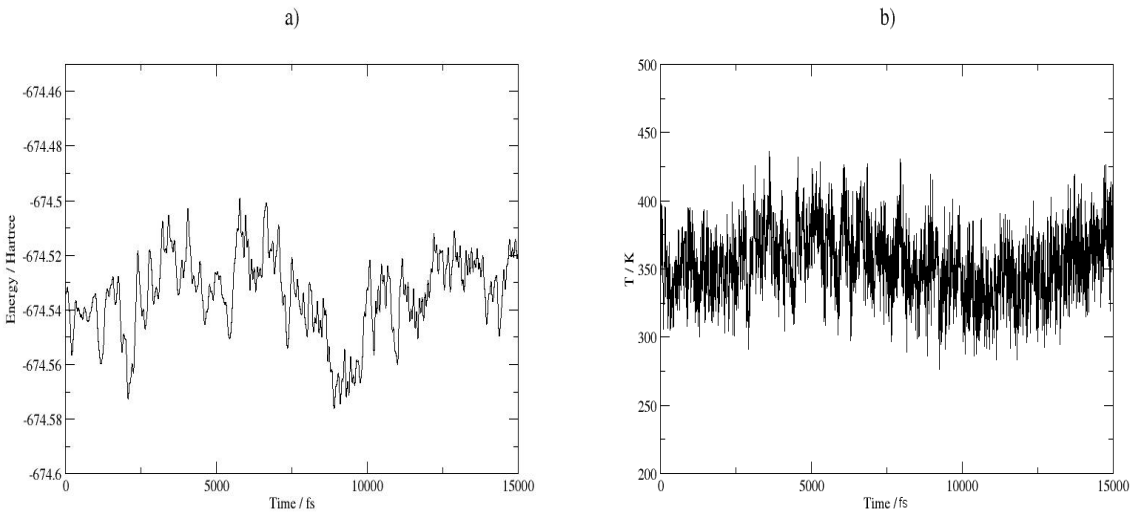

Figure 3.22: a) Energy and b) temperature fluctuations during the course of the production MD simulation of the dimer in explicit water.

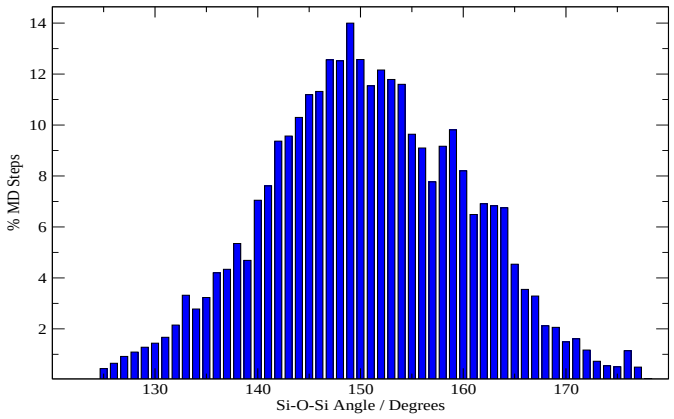

Figure 3.23: The percentage of structures against SiOSi bond angle from the MD run.

exact same structure as conformation I in figure 3.20, used to calculate chemical shift. The chemical shifts of the six similar conformations also show very little variation, $\sim$ 0.2 ppm and only by $\sim$0.5 ppm for structure five, which also displays a smaller Si-O-Si angle, once again reinforcing the point that the Si-O-Si bond angle plays a crucial role in determining the chemical shift.

Structure	E /kJ mol^{-1}	$\langle$ RMSD$\rangle$/Å	$\langle$ SiOSi $\rangle$/Degrees	δ/ppm
1	-2913064.4	0.064	137.30	-78.05
2	-2913064.5	0.061	137.28	-78.04
3	-2913064.4	0.064	137.26	-78.20
4	-2913064.3	0.061	137.75	-78.22
5	-2913064.6	0.262	135.31	-77.63
6	-2913064.4	0.054	137.20	-78.02
7	-2913064.4	0.067	137.21	-78.01

Table 3.14: The energies, RMSD compared to the other conformations in the table , SiOSi bond angle and chemical shift with respect to TMS (δ) of seven minima from the MD simulation of the dimer molecule in water.

A summary of species with internal H-bonding, listing the average Si-O-Si bond angle adjacent to the H-bonded hydroxyl group ($\langle$ Si-O-Si $\rangle$) and the difference between calculated and experimental shift ($\Delta\delta$) is presented in table 3.15. Such a summary highlights the fact that the species with internal hydrogen bonding do indeed tend to show shifts up frequency of the experimental value in direct contrast to the general trend as found in section 3.3.6.

There is one exception in this analysis: species VIIIe from figure 3.1. The reason that this species is not affected by the internal hydrogen bonding is that the number of Si-O-Si linkages between the hydrogen bonding silanols is sufficient that the bond angle is not affected by the presence of the internal hydrogen bond.

These results also correlate with the conclusion of van Santen *et al.* [12] that errors in calculated activation energy barriers are also due to an overestimation of intramolecular H-bonding iteractions due to the neglect of solvation.

Species [Centre]	$\langle$ Si-O-Si $\rangle$/Degrees	$\Delta\delta$/ppm
II	123.0	7.16
IVa	131.0	5.78
VIo [a]	131.5	3.32
VIIIe [a]	150.4	-3.49

Table 3.15: Errors compared to reference [5] in chemical shift ($\Delta\delta$) of species (code as in figure 3.1) with internal H-Bonding and Si-O-Si bond angle of bonds adjacent to the H-Bonded hydroxyl groups.

3.4 Chemical Shift And Species Geometry

In order to facilitate the assignment of NMR peaks to solution species it is necessary to develop certain "rules of thumb" which enable an educated guess as to the source of a peak to be made. As mentioned in the introductory section a number of rules exist relating to Si site condensation, presence in a ring, adjacent connectivity etc. (table 3.1). Having demonstrated the viability of a method of geometry optimization and chemical shift calculation using an implicit solvent, as well as its limitations and possible pit-falls this method is now used to elucidate certain structural features which can be expected to affect the chemical shift in pre-nucleation silicate species.

3.4.1 Quantitative Structure Shift Relationships

Computer modeling provides an extremely useful tool for the development of such relationships, as it allows the direct investigation of the effects of conformation and composition on the chemical shift, indeed Moravetski *et al.* [51] developed the semi-empirical relationship between Si-O-Si and Si-O-H bond angles and chemical shift; equation 3.7. This relationship however was derived for a set of highly symmetrical molecules. As will be shown in this section, for molecules with differing degrees of symmetry this relationship ceases to provide a reasonable description, either quantitatively or indeed qualitatively, to the chemical shift of a species.

The inherent deficiencies of this relation are highlighted in table 3.16.For example the double 4 ring (species VIIIc in figure 3.1) the Si-O-Si bond angle between each pair of silicons is smaller than that for the hexacyclic octamer (species VIIId in figure 3.1). Consequently the angle/shift relationship (equation 3.7) would predict a more de-shielded nucleus in VIIIc, however the fact that each Si centre is attached (via oxygen) to another Q^3 Si centre, as opposed to alternating $Q^{3\Delta}/Q^3$ centres in the VIIId, compensates for the effect of the reduced angle and, as our calculations and experimental assignment show, it has the lowest frequency shift of this series of centres. Thus whilst this relationship is useful for assigning the peaks of the species which make up the final zeolite structure it proves less so in determining intermediates in the process.

Species [Centre]	⟨SiOSi⟩/Degrees	δ_{rel}/ppm	δ_{calc}/ppm	δ_{expt}/ppm
VIIIc	146.82	-94.2	-100.03	-98.17
VIIId [c]	151.03	-97.7	-99.43	-97.61
VIIf [c]	148.15	-96.3	-95.61	-94.87
VIb [b]	140.07	-91.7	-93.63	-92.31
VIIe [c]	147.14	-95.8	-96.82	-95.82
VIh [d]	146.80	-94.1	-99.16	-95.65

Table 3.16: The average Si-O-Si angle , chemical shift calculated from the relationship of Moravetski *et al.*[51] (δ_{rel}), chemical shift calculated by our method (δ_{calc}) and experimentally assigned chemical shift (δ_{expt})[44], for centres at the apex of two 4 rings, labels refer to figure 3.1.

3.4.2 Presence in a Ring

When a Si centre occurs in a ring it is de-shielded relative to a centre not in a ring, by up to 8.5 ppm (table 3.1). This is indeed the case in our calculations. However, certain other subtleties exist which can be used to aide a more refined assignment of NMR peaks. In particular, by considering chemical shifts arising from species with one unique Si centre and their relation to the geometric properties of the species under consideration, it becomes clear that a dependence on ring size of the species exists.

For Q^2 species the chemical shift moves down frequency as ring size increases from three to four (fig 3.24) then moves gradually back up frequency as ring size increases. Figure 3.24 shows that for Q^3 species the shift moves down frequency until the five membered ring. After this there is a much more gradual move up frequency than observed in the Q^2 series. This means that shifts observed in the region of the double 4 ring, such as that assigned to the prismic tetramer (which shall be discussed in a later section), might, in fact, be due to larger cage species, such as the double 8 ring.

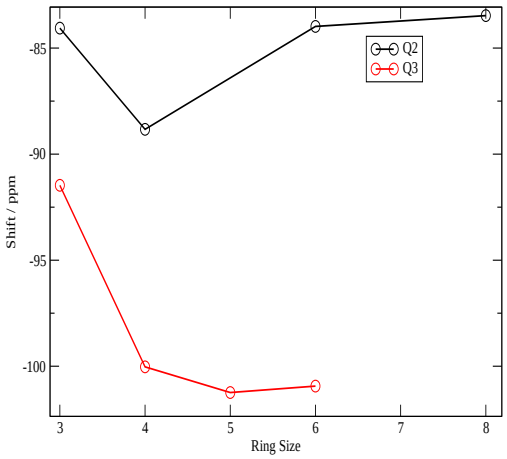

Figure 3.24: Chemical shift of Q^2 and Q^3 species versus the size of ring in the species.

Another important fact to note is that nuclei from different species, but in seemingly similar environments can have very different chemical shifts. An example of this is the difference between the Q^3 Si in the tricyclic hexamer and the hexacyclic octomer (centre b in VIc and centre a in VIIId from figure 3.1). While the picture presented in figure 3.1 would suggest that these environments are very similar, it becomes clear on closer inspection that much information can be gained about species structure from comparing different shifts for nuclei which are ostensibly the same; meaning that rational guesses can be made as to the structure responsible for

a certain shift not only on the basis of the range into which that shift falls but also its position within that range.

In order to illustrate this point, a number of cases are considered. First the case of Si centres which occur at the vertices of two 4 rings. A skeletal representation of the environments of these atoms in these species: the double 4 ring, the Si bridged fused 4 rings, the O bridged fused 4 rings, the hexacyclic octamer, the tricyclic heptamer and the tricyclic hexamer (structures VIIIc, VIIf, VIb, VIIId, VIIe and VIh in figure 3.1) is shown in figure 3.25, with the chemical shifts reported in table 3.16. In general these results show that as the structure becomes more open the shifts move down frequency. Hence the highly strained oxygen bridged fused 4 rings species has the highest frequency shift. As the number of atoms bridging the gap between the corners of the fused 4 rings increase, so the structure becomes less strained: thus we see structure VIIf which has 3 bridging atoms has a shift calculated to be ~ 5 ppm down frequency of the oxygen bridged analogue (structure VIb) (with only one bridging atom). The tricyclic heptamer (structure VIIe), which also has 3 bridging atoms, but this time on the same face, has a larger still average Si-O-Si bond angle, and is another $\sim$ 4ppm down frequency according to our calculations.

Figure 3.25: Skeletal representations of the environment of Si centres at the vertices of fused 4 rings in a Q^3 environment, double 4 ring; orange, silicon bridged fused 4 rings; red, oxygen bridged double 4 rings; cyan, hexacyclic octamer; blue , trticyclic heptamer; magenta and tricyclic hexamer; green

Considering now Q^3 Si centres which occur at the vertices of 3 and 4 rings. In this case 6 species are considered: the double 3 ring, *cisoid* tricyclic hexamer, *transoid* tricyclic hexamer, the pentacyclic heptamer, the hexacyclic octamer and the fused 3-4 ring (structures VIa, VIc, VId, VIIg, VIIId and Vd in figure 3.1). Once again these oligomers have varying degrees of symmetry from the highly symmetric double 3 ring (VIa) to the fused 3-4 rings (Vd) species which has only one plane of symmetry. It should be noted also that the shifts arising from the conformers of the tricyclic hexamer species the experimental assignments have been reversed in this table with respect to experimental assignments. This reassignment shall be justified in section 3.5.

This series of centres provides further evidence of the deficiencies of a system of assignment based solely on Si-O-Si and Si-O-H angles. The range of shifts calculated

from equation 3.7 (table 3.17) is significantly wider (6.9 ppm) than those to which they are experimentally assigned (1.6 ppm). Whilst our calculated chemical shifts also display a wider range (2.7 ppm), this is far closer to the experimental picture than that derived from equation 3.7. Furthermore the calculated values recover the trends observed in the experimental data, merely amplifying differences observed experimentally. This over-emphasis being quite possibly due to the over-emphasis of a single conformation in the calculated values, rather than the ensemble which would be expected to contribute to the observed shift.

Certain sub-groupings are also possible within these species. VIc (tricyclic hexamer *cisoid*),Vd (fused 3-4 rings) and VIa (double 3 ring) species all have calculated shifts within 0.5 ppm of one another: the Si centre in question is a member of a 3 ring and a 4 ring only. Slightly lower in frequency are VIIg (pentacyclic heptamer) and VIIId (hexacyclic octamer), both of which have a similar chemical shift: in these species the Si centre belongs to a 3, 4 and five membered ring.

Species [Centre]	⟨SiOSi⟩/Degrees	δ_{rel}/ppm	δ_{calc}/ppm	δ_{expt}/ppm
VIa	135.05	-88.5	-91.47	-89.11
VIc [b]	134.52	-87.6	-92.06	-88.79
VId [b]	138.40	-93.1	-89.54	-87.55
VIIg [c]	146.26	-94.5	-92.26	-88.79
VIIId [a]	135.00	-87.8	-92.23	-88.60
Vd [c]	135.20	-87.8	-91.77	-88.07

Table 3.17: The average Si-O-Si angle, chemical shift calculated from the relationship of Moravetski *et al.*[51] (δ_{rel}), chemical shift calculated by our method (δ_{calc}) and experimentally assigned chemical shift (δ_{expt})[44] of centres at the apex of a 4 and 4 ring, labels refer to figure 3.1.

In many of the species studied in this thesis the silicon centre is present at the connection of more than one type of ring, examples of such centres are presented in table 3.18, in which the combination of rings, as well as the average value for a Si centre occurring in that environment are given. Interestingly, the trends observed for these shifts are very similar to those for shifts arising from centres present in only one ring. Hence presence at the connection of a 4 ring and 3 ring results in a shift some 5 ppm down frequency of the shift of a centre at the connection of two 3 rings. Similarly, if the centre is at the connection of a 3 ring and a five ring the shift is moved a further 1.24 ppm down frequency.

Considering the cage type species, in which the Si centre may be present at the meeting point of 3 rings, much the same trends are observed. A centre at the junction of a three, four and 4 ring is some 2.5 ppm up frequency of a centre at a three, four and five ring, and 5.8 ppm up frequency of a centre at three 4 rings. The shift of this centre is in turn 3.5 ppm up frequency of a centre at the junction between two 4 rings and one five ring. Thus we can state a general trend: 3 ring centres are $\sim$ 5ppm de-shielded compared to 4 ring centres, which are in turn $\sim$

2.5 ppm de-shielded with respect to five ring centres, which holds in the case where multiple rings are present.

Rings	Species [Centre]	δ/ppm	Average δ
3R3R	IVc [b]	-85.91	
3R4R	Vd [c]	-91.77	
	VId [b]	-89.54	
	VIc [b]	-92.06	
	VIe [d]	-90.44	
	VIe [e]	-91.08	
	VIf [d]	-90.66	
	VIf [e]	-91.20	-90.96
3R5R	VIg [d]	-92.20	
3R4R4R	VIh [b]	-89.51	
	VIId [c]	-89.77	-89.64
3R4R5R	VIh [c]	-91.53	
	VIIg [c]	-93.19	
	VIIId [b]	-93.79	
	VIId [d]	-89.58	
	VIId [e]	-92.73	-92.16
4R4R4R	Vb [b]	-97.79	
	VIi [d]	-94.46	
	VIIe [c]	-96.82	
	VIb [b]	-93.63	-95.68
4R4R5R	VIh [d]	-99.16	
	VIIf [d]	-98.83	
	VIIId [c]	-99.43	-99.14

Table 3.18: Average chemical shift (δ) values for Si centres at the apex of various rings (NR), the species labels refer to figure 3.1 .

3.4.3 Presence in a Three Ring

As mentioned in the introduction the presence of the silicon centre in a ring can have an effect on its chemical shift, and this effect is particularly pronounced if the silicon is present in a 3 ring. The effect, however, of the presence of the silicon in more than one 3 ring has not previously been quantified, although we note that assignments of such species have been made [52]. As the power of NMR spectrometers increases and spectra can be analyzed in more complex ways, studies of pre-nucleation solutions identify increasing numbers of silicate oligomer species. Thus it is possible that many more three-silicon rings are possibly present. It has, therefore, become important

to be able to theoretically quantify the effects of the occurrence of a silicon centre in different numbers of 3 rings. In order to systematically study this effect, species with Q^2, Q^3, and Q^4 centres in a 3 ring must be considered. These species have silicons occurring in between zero to four rings and are shown in figure 3.26.

In order to categorize these species according to the number of 3 rings present a new notation is introduced. Based on the standard Q^n notation, we introduce an additional subscript nC, where n denotes the number of 3 rings in which the silicon of interest occurs. So for example for a Q^4 silicon in two 3 rings we write Q^4_{2C}.

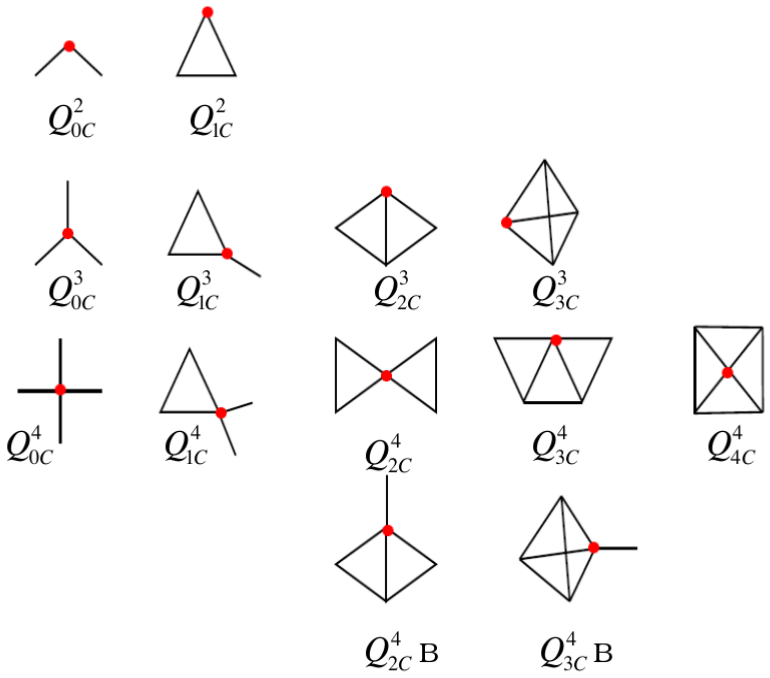

Figure 3.26: The 3 ring species used in the study. A line represents a Si-O-Si linkage, the centre of interest is highlighted in red.

The calculated nuclear shielding values for these species are presented in table 3.19 and we now examine the various trends evident in this data. In the case of Q^3 and Q^4 species, present in one 3 ring (i.e. Q^4_{1C} and Q^3_{1C}), the shielding is reduced by 4.2 ppm and 3.2 ppm relative to Q^4_{0C} and Q^3_{0C}shifts respectively. In the case of Q^2 this de-shielding is 2.2 ppm. This difference between Q^2 and the other centres can be explained by the fact that shifts calculated for Q^2 centres we are generally lower than experimental values, while for Q^3 and Q^4 species this is reversed. Thus the difference between the de-shielding of Q^2 and Q^3/Q^4 species caused by presence in a 3 ring would be expected to be an artefact of the method rather than an effect which we would expect to be observed experimentally.

Concentrating on the effect of moving from one to two centres, there are two

Q^4_{2C} species possible: the second of these (Q^4_{2C}B) is more comparable to the Q^3_{2C} species, as it is essentially the same species with a monomer attached to the silicon centre. The amount of de-shielding in the case of the Q^3 species is $\sim$ 5.8 ppm, for the Q^4_{2C}B species this is again larger, $\sim$ 7.3 ppm. If we consider the first of the Q^4_{2C} species the de-shielding effect of the extra 3 ring is somewhat less, $\sim$ 2.7 ppm. It is noteworthy that the second Q_{2C} species features a Si-O-Si bond which is involved in an additional 3 ring, whereas the first species does not: this point will be considered in more detail presently.

C	Q^2	Q^3	Q^4	Q^4B
0	477.00	486.81	496.21	
1	475.73	483.61	492.09	
2		477.79	489.34	484.72
3		472.84	469.26	480.12
4			396.85	

Table 3.19: Nuclear shielding (in ppm) of the species from figure 3.26

Examining the effect of moving from two to three three member rings again there are two Q^4 species possible, and one Q^3 species. The difference between the Q^4_{2C}B and Q^4_{3C}B species is comparable to that between Q^3_{2C} and Q^3_{3C}, again the de-shielding effect of an extra ring is similar, $\sim$ 4.9 ppm for the Q^3 case and $\sim$ 4.6 ppm for the Q^4 case. Again in the same range as the change from one to two centres. Thus we can say that presence of each successive 3 ring, with an extra Si-O-Si bond shared between two 3 rings results in de-shielding of between 4.5 and 6.5 ppm. The Q^4_{3C}A species has fewer Si-O-Si bonds shared between 3 rings, however its structure is significantly more strained than the second Q^4_{3C}B species, and it is significantly more de-shielded, by $\sim$ 10.9 ppm.

The final species to consider is the Q^4_{4C} species, which has all four of its Si-O-Si bonds involved in two 3 rings and is highly strained. Thus it comes as little surprise to find that is significantly de-shielded with respect to the other species: almost 100 ppm de-shielded compared to the species with no 3 rings involved. In fact it is de-shielded with respect to the mono-silicic acid species, having a chemical shift relative to TMS of just 5 ppm.

It should be noted that during the course of this study a number of other Q^4 species were proposed to investigate the effects of presence of a 3 ring on silicon nuclear shielding, these are presented in figure 3.27. However, during the course of geometry optimization, all of these species underwent rearrangement to another species, and thus are considered too unstable to exist in the pre-nucleation solution. It is concluded from this observation that it is impossible for a Si-O-Si bond to be present in any more than two 3 rings due to geometric constraints, such structures can therefore be eliminated from further consideration.

3.5 (Re)Assignments

3.5.1 Tricyclic Hexamer

It was mentioned in section 3.4.2 that the assignments of shifts to the *transoid* and *cisoid* isomers of the tricyclic hexamer (species VIc and VId in figure 3.1 respectively) had been reversed from those made experimentally [44]. The reassigned shifts obviously give a better fit to the theoretical spectrum, however this alone is not sufficient to make a reassignment. The reasons for the reassignment will now be presented.

The assignment in the recent experimental study [44] and other studies [45] [52] appear to be based on an earlier experimental assignment made by Harris and Knight [43, 42]; but in fact both species were proposed as early as 1976 [192]. In their paper Harris and Knight note that one of the multiplets is more intense than the other. They state that as the *cisoid* isomer may convert more readily into another species (the double 3 ring) this means that the *transoid* isomer is probably more stable. Thus they assign the more intense peak to the *transoid* isomer.

The energies of both of the conformations have been calculated at B3LYP/6-31G* level and it is found that the *cisoid* isomer that is the more stable 16 kJ mol^{-1}. Moreover, this enhanced stability of the *cisoid* isomer was also found in other theoretical studies [52]. Therefore, it is proposed that the more intense of the signals is actually due to the *cisoid* isomer based on these energetic arguments. Moreover the calculated shifts fit better to the experimental values when such a re-assignment is made. The original theoretical and experimental spectra are shown in figure 3.28.

3.5.2 Prismic Tetramer (species IVb in figure 3.1)

It was noted in section 3.3.5 that one of the cases for which there is very poor agreement between calculated and experimental values was the prismic tetramer species pictured in figure 3.29. The discrepancy between calculated and experimentally assigned shifts in this case was particularly large, the calculated value being 16.06 and 13.98 ppm up-frequency of the experimentally assigned value relative to references [5] and [44] respectively.

The prismic tetramer species is comprised of a series of interlinked 3 rings, which we denoted Q^3_{3C} in section 3.4.3 where the chemical shift was found to be at high frequency relative to other Q^3 species. The other species in section 3.3.5 which showed discrepancies beyond normal from the experimental shift involved internal hydrogen bonding resulting in overly acute Si-O-Si angles. The prismic tetramer on the other hand has no internal hydrogen bonding and is, in fact, a very rigid structure. As such, the geometry would be expected to be correct and is ruled out as a possible source of error in the calculation.

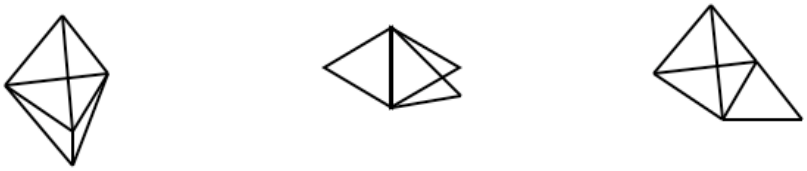

Figure 3.27: The theoretical 3 rings which could not be geometry optimized. A line represents a Si-O-Si linkage.

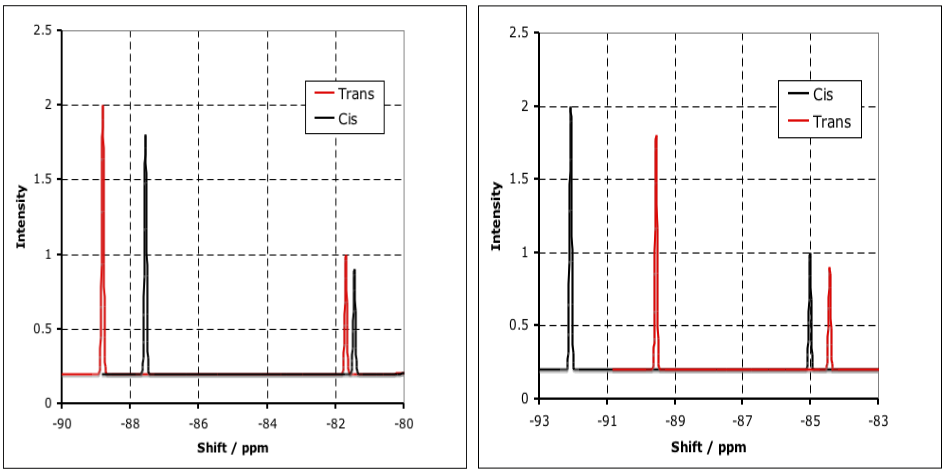

Figure 3.28: (a) Experimental [44] and (b) calculated spectra for the *trans* and *cis* isomers of the tricyclic hexamer.

The previously quoted assignments of the prismic tetramer experimentally [5, 44] were based on former assignments: the original assignment of this species was made by Kinrade and Swaddle [193]. This assignment was based on the increase in longitudinal nuclear magnetic relaxation time as a function of increased temperature, and was described as having being made "tentatively". Given that the original assignment is tentative, that little possible source of error in the calculation is evident and the shift matches other calculated trends for 3 rings it is suggested that the experimental assignment of this peak is erroneous. Moreover, the prismic tetramer structural motif is not found in any final zeolite crystals. This peak is more likely to be due to another cage species, such as the double 6 ring (XII in figure 3.1), which was calculated in section 3.4.2 to have a shift slightly up-frequency of the double 4 ring, or possible a consequence of two stable charge states of the double 4 ring, which have slightly different shifts.

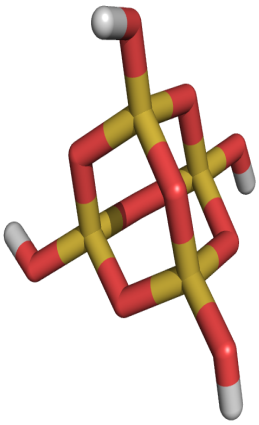

Figure 3.29: The structure of the prismic tetramer species.

3.5.3 4 Rings

The 4 ring species (structure IVa in figure 3.1) has been observed with between 1 and 4 dangling Q^1 silicas [44]. However although the number of peaks observed suggest that most possible combinations are extant, deciphering between the different ones proved difficult. The experimentally observed chemical shifts relative to the monomer species are presented in table 3.20. These shifts, although un-assigned, are expected to arise from substituted 4 ring species. From these data it is obvious that changes in the substituant shift are minor and, as such, do not represent a very useful tool for distinguishing between conformers. However, the variation in the shift of the parent structures are more pronounced. The species possibly responsible for these peaks are presented in figure 3.30.

Knight *et al.* [44] have tentatively made two assignments which are that the

third signal is due to species IId and the first peak is due to species IIc. These assignments were made on the basis of Q^2 - Q^3 coupling and assuming the *trans* substituted species to be the more stable conformer. The more intense observed peak being the one at 24.446 ppm (these assignments are relative to the monomer resonance which was not provided in the original paper but calculated here to be 71.05 ppm: thus the peaks are 95.451 ppm and 95.050 ppm) , was assigned to IId. The results of the calculations are presented in table 3.21 which shows the chemical shift, the energy relative to other possible isomers and the RMSD from the parent strucuture. The calculations show that the *trans* conformer is indeed more stable, by 10 kJ mol^{-1}. The calculations also show Q^3 peaks at 89.25 ppm for the *cis* and 95.00 ppm for the *trans* conformers. Thus the calculated shifts concur with the experimentally observed spectrum. The RMSD of these species from an unsubstituted 4 ring are also within the limit of reliability established in section 3.3.8, adding confidence to the prediction. The experimental and calculated shifts are presented in figure 3.31. The difference in calculated shifts are clearly more pronounced in the calculated spectrum, but the trends are the same.

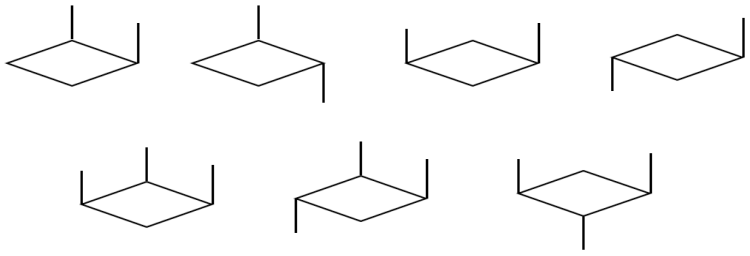

Figure 3.30: The conformers of the substituted 4 Ring which give rise to the unasigned peaks in table 3.20. Thes species will be refered to from here on as, from the top, left to right; IIa;IIb;IIc;IId; IIIa; IIIb; IIIc.

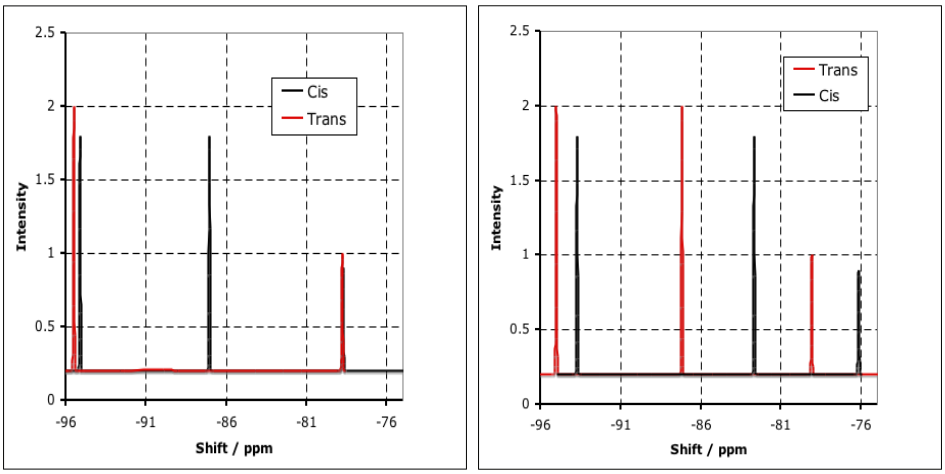

Figure 3.31: Experimental (a) and calculated (b) spectra for the species IIc and IId.

Considering now species IIa and IIb. Once again the *trans* isomer is more stable,

this time by 6 kJ mol $^{-1}$. The smaller difference in energies (compared to the case above) can explain the lack of any discrimination from the experimental spectrum regarding the intensity of the resonances. This time the Q^3 shift in the *trans* isomer is significantly up-frequency of the *cis* isomer: -93.70 ppm and -98.58 ppm respectively. The RMSDs of both species are also within the reliability limit of section 3.3.8. Thus signal 4 can be assigned to IIb and signal 8 to IIa.

No 4 ring species with three monomers attached were assigned experimentally, nor any information provided regarding relative intensities. In this case the differences between the shifts observed experimentally are also smaller, all three Q^3 shifts are within 0.25 ppm of one another. The RMSDs of the calculated structures from an unsubstituted 4 ring are also larger for the calculated structures than for those with two monomers attached. On this basis any assignment made from the calculations should be treated with caution, however we postulate that species IIIa matches to experimental shift number 5, species IIIb to shift 9 and IIIc to shift 2.

3.6 Conclusions

A number of issues regarding calculation and assignment of silicate species using ^{29}Si NMR have been covered in this chapter. In the first instance it was shown that a IEFPCM model provides a good approximation to more complicated cluster models which include explicit water molecules. The effects of charge state on chemical shift were then investigated in order to determine what type of model systems to employ. It was shown here that whilst deprotonation at Q^0 and Q^3 sites changes the electron distribution in qualitatively different ways, the net result is still that experimentally observed nuclear shielding (and hence chemical shift) would be expected to change very little with charge state. On the basis of this is was proposed that model systems of fully protonated silicate species would provide a good approximation of the experimental spectra of chemical shifts.

The influence of various alkali metal cations was then investigated, and it was found that, in general, the silicon centre becomes more shielded as the cation radius increases, as has been observed experimentally [175]. However the Li^+ cation proved to be an exception, as observed experimentally [182]. The anomalous behaviour of Li^+ was explaind by use of NCS and NBO analysis. These revealed that the contribution from core p-orbitals in the presence of Li^+ was considerably more shielding than in the presence of other cations. Which was explained by the greater energetic stability of these orbitals in the presence of Li^+ and, in conjunction with different trends for both the inter-atomic orbitals and the lone pair orbitals, explains why Li^+ is anomalous in this series.

The methodology of using the IEFPCM and different functional forms of DFT was also tested. The cavity size in the IEFPCM was varied to check for the influence

Q^1 / ppm	Q^3 / ppm	J(Q^2Q^3)	No. Q^1
-78.71	-95.10	Y	2
-78.76	-94.18	N	3
-78.76	-95.50	Y	2
-78.81	-94.46	M	2
-78.81	-94.12	N	3
* -78.9	-95.1	M	2
-78.90	-95.70	Y	2
-79.91	-95.41	M	2
-79.18	-94.03	N	3

Table 3.20: NMR peaks of doubly and triply substituted 4 rings observed by Knight *et al.* [44] showing substituant shift (Q^1), parent structure shift (Q^2) and presence of a Q^2 - Q^3 coupling (Y: present, N: not present, M: possibly present).* : Experimental data less accurate for these peaks. Note values in the original paper were reported relative to the silicic acid monomer Si chemical shift, we have modified them by -71.05 ppm, the calculated value for the monomer Si chemical shift.

Species	δ_a	δ_b	δ_c	$\Delta E/kJmol^{-1}$	RMSD/ Å
IIa	-79.28	-84.48	-98.58	6	0.19
IIb	-76.15	-82.66	-93.70	0	0.22
IIc	-76.62	-84.73	-89.25	10	0.22
IId	-79.07	-87.16	-95.00	0	0.24
IIIa	-79.17	-83.65	-96.15	15	0.33
IIIb	-80.35	-85.94	-93.25	4	0.22
IIIc	-80.66	-86.66	-98.02	0	0.25

Table 3.21: Calculated chemical shifts (δ) in ppm, relative energies and RMSDs from an unsubstituted 4 ring of the species in figure refConformers

of charge penetration of the cavity effects on the calculated shieldings. In addition GGA and hybrid methods for calculating the shift were compared by using the PBE and B3LYP functionals. It was found that a combination of the PBE functional with the standard model of the IEFPCM (cavity scaling 1.2) produced the best replication of experimental shifts. This model was then tested on an extended set of experimentally assigned shifts. It was shown the the model with a PCM representation of the solvent and the PBE functional compared favourably to previous theoretical studies using B3LYP and no solvent.

The major drawback of the method was found to occur when silicate species had the possibility of forming internal hydrogen bonds between silanol groups, it was found that in such cases formation of internal hydrogen bonds could lead to a poor estimation of the chemical shift. This was tested by performing molecular dynamics simulations of one such species (the dimer, species II in figure 3.1) in explicit water. This simulation revealed that hydrogen bonding to environmental water was preferred to internal hydrogen bonding, resulting in different geometries from the case with just the IEFPCM representation of the solvent. The chemical shifts of minima extracted from the MD run with explicit solvation were found to concur better with experimental data.

The methodology was then used to investigate the effects of the presence of silicon centres in various types and combinations of ring structures. It was found that the effect of presence in a 3 ring (de-shielding of ~ 8 ppm) was roughly additive as the number rings increased, and that a centre attached to a Si-O-Si bond which shares 3 rings was more de-shielding than being attached to Si-O-Si bonds in only one 3 ring. It was also shown that certain sub-regions could be ascribed within spectrum regions - traditionally only split between Q^1, Q^2, $Q^{3\Delta}$ and Q^3 regions - on the basis of the different ring types in which the silicon is present.

Finally the methodology was used as a tool with which to help assignment of experimentally observed peaks which are difficult to assign merely from experiment. The assigned peaks of the tricyclic hexamer were shown to possibly be in the wrong order. The shifts previously assigned to the prismic tetramer was shown to be incorrect and more likely due to another cage type species, possibly the double 8 ring or a different stable charge state of the double 4 ring. Finally, experimentally unassignable shifts of various isomers of the 4 ring with dangling monomers were then assigned on the basis of calculated shifts.

CHAPTER 4

Structure Directing Agents and Water Structure

4.1 Introduction

In the introduction to this thesis (section 1.3.4) a mechanism for the nucleation of zeolites involving the formation of a clathrate hydration layer of a cation has been posited [62, 63]. This theory was developed, to a large extent, based on the existence of hydrates of "template" molecules (see section 1.3) which have structures isomorphic to the zeolite frameworks which they are used to synthesize [60, 59]. These hydrate structures have been identified in the solid phase, at low temperatures. However, it is difficult to identify such structures under the conditions of zeolite synthesis, typically involving a liquid phase at higher temperatures, using experimental techniques.

In this chapter the hydration layers of some common template molecules are simulated, in order to analyze the results of the simulations to search for the presence of such structures, or fragments of such structures in their hydration layers. We first analyze the hydration layers of tetraalkyl ammoniums and neopentane in order to search for evidence of structuring using radial distribution functions, which can be compared to experimental results obtained under similar conditions. In this section we show how both charge and the length of the alkyl chain in the solute affect the structure of the hydration water.

A specifically developed analysis program is then employed to search for the presence of rings of water and fragments of hydrate structures in the hydration layers of a number of common templates. These simulations again reveal the importance of the charge and length of the alkyl chain in determining the types of water structure found in the hydration layer, in addition the effects of amine groups in stabilizing rings is demonstrated.

We shall first begin however by introducing previous studies, both experimental and computational, which have investigated the effects of tetraalkyl ammoniums on the water in their hydration layers.

4.1.1 Water Structure and Tetraalkyl Ammoniums

It is generally well accepted that liquid water has a large amount of inherent structure [194], more controversial however is defining a measure by which this structure can be quantified. X-Ray and neutron diffraction, which are the most commonly employed techniques for measuring water structure, give us structure factors which can yield, after Fourier transformation, pair correlation functions (PCFs) which are related to the probability of finding the centre of a particle within a given distance of the centre of another particle. However, these types of studies give results for liquid water which are similar to those of liquid Argon, a non-structured liquid [195]. It is thus clear that more refined measurements are necessary,and to this end partial-pair correlation functions, those between oxygens and hydrogens in water molecules, have been determined and yield more information [196].

Measures of water such as stiffness, the work necessary to create a cavity in the water; openness, the difference between bulk molar volume and intrinsic molar volume; and order, the deficit in molar entropy with respect to the gas phase, have been proposed and investigated [197, 198]. Generally the order in liquid water is attributed to the network of hydrogen bonds, thus the number of hydrogen bonds per water molecule appears to be an attractive measure of structure in water, particularly when considering the effects of solute molecules on the water structure. Experimentally the number of hydrogen bonds has been studied by X-ray absorption (XAS) and X-ray Raman (XRS) spectroscopies. However interpretation of the results of these studies lead to differing views of the overall structure of the liquid. European groups [199, 200] favoured an interpretation in which the minority of molecules are arranged tetragonally, as in ice, whilst American investigators [201, 202] favoured a model in which water is predominantly arranged in a tetragonal environment. Clearly in this respect computer simulations have an inherent advantage, as the exact position of all particles in the system is known a priori. However even given the positions of the particles debate still exists as to how exactly one should define a hydrogen bond, the most generally accepted criteria being geometric and energetic ones [203, 204]. Geometrically the distance between oxygens, the length of the bond and the O-H-O angle defines hydrogen bonds. These criteria have been applied during *ab initio* simulations of liquid water to yield an average number of hydrogen bonds per water of 2.8 [203] .

It has been shown, using Neutron diffraction measurements of partial PCFs, that strongly hydrating ions result in the re-orientation of water molecules in their hydration sphere [205]. This ordering effect is revealed through an increase of the

sharpness of the peaks in the PCF. The tetraalkyl ammonium cations (TAAs) however are classed as apolar solutes, due to the presence of hydrophobic chains, and as such are far less hydrating, and the effects of this class of apolar solutes on water structure in the hydration layer is far less well defined than those of strongly hydrating ions. It has been shown that a hydration layer certainly does exist [206]; this does not necessarily imply any significant ordering of the water in the hydration layer though. PCFs of tetraethyl ammonium (TEA) fluoride revealed little evidence of ordering of water beyond 2.5 A. Tetramethyl ammonium (TMA) clathrates have been identified with a small number of water molecules, yet with hydrogen bonding networks intact [207, 208]. PCFs for oxygen and nitrogen in TMA have been used to reveal that in solution the water molecules tend to be oriented in such a way as to straddle the TMA cation.

A study by Turner *et al.* [206] using neutron diffraction revealed that there was very little change in the PCFs between the water hydrogens (HH), the water hydrogens and other atom types (HX) and between other atom types only (XX), from these studies they concluded that there is little appreciable change in the structure of water in the vicinity of TMA. The important results of this study, and a subsequent study on TPA and TBA [209] are presented in figure 4.1.

The behaviour of other TAAs (other than TMA) has shown that water molecules encage the alkyl chains and that this in turn leads to a stabilization of the water network [209]. This has also been supported by evidence from calculated hydration free energies, Raman spectroscopy and transport measurements [210, 211] all of which point towards the effect of the alkyl chains as stabilizing the water network. In addition simulations have also suggested ordering effects due to the correlation between the number of water molecules in a hydration layer and the entropy of solution of an alkane [212]. This view however has not gone unchallenged [213], and it has been suggested the thermodynamic data can be explained by water solute interactions alone, without recourse to any change in water interactions with itself [214]. Turner and Soper carried out a comprehensive series of neutron diffraction measurements on solutions of TAAs [209].Unlike their earlier studies of TMA greater evidence of structuring was found in longer chain TAAs. They found a change in the peak position of the second peak in the HH correlation compared to pure water, corresponding to an increased number of "ideal" hydrogen bonds. It was also observed, in this study, that the first intermolecular OH peak was higher and sharper in the presence of the solutes, which hints at a reduced number of possibilities in the conformational ensemble of the water molecules. The study also showed that the average number of hydrogen bonds per water molecule was more or less consistent with that for pure water: supporting a model whereby the solute is present in a cage which maintains the water network about it. There have also been NMR studies of water molecules in the vicinity of TAAs, [215] which show a reduced

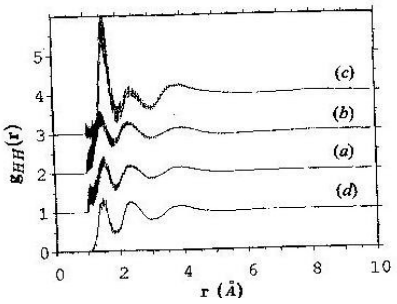

(i) HH Correlations

Concentration/m	c_H	Peak Å	Coordination number	Peak Å	Coordination number (a)	Coordination number (b)
2·0	0·54	1·55	1·1 ± 0·2	2·35	4·8 ± 0·2	2·6 ± 0·1
5·0	0·42	1·49	1·0 ± 0·2	2·33	3·9 ± 0·2	2·3 ± 0·1
8·0	0·34	1·59	1·0 ± 0·4	2·41	2·4 ± 0·3	1·5 ± 0·2
Water[c]	0·67	1·48	1·0 ± 0·1	2·35	5·5 ± 0·2	3·3 ± 0·1

[a] Result of integration over whole peak.
[b] Result of integration up to maximum of peak (doubled).

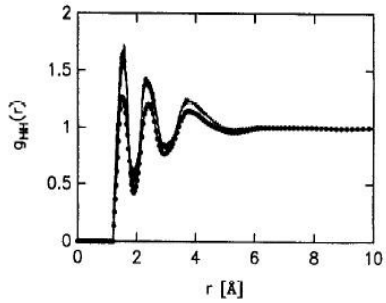

Solute	c_H[b]	Coordination number Peak position 1.5 Å	2.4 Å	R[c] 2.4 Å peak
Ethanol	0.591	1.0±0.1	4.7±0.2	1.96
t-butanol	0.586	0.9±0.1	4.5±0.2	1.95
Pr_4NBr	0.494	1.1±0.1	4.5±0.2	2.00
Bu_4NBr	0.505	1.1±0.2	4.4±0.2	2.05
Water	0.667	1.2±0.1	4.8±0.1	1.99

Figure 4.1: Results of experimental investigations of the effects of TAAs on water structure. Top left: the HH partial pair correlation from reference [206], for water with a) 2.0 m, b) 6.0 m and c) 8.0 m TMA, d) pure water. Note that lines a - c have been displaced on the graph for clarity, also the increase in the heigth of the first peak with concentration of TMA is due to the reduced number density of H atoms, not increased structure. Top right: peak positions and coordination numbers for the first two peaks of the HH partial pair correlation in the presence of various concentrations of TMA, note the coordination number of the second peak is calculated in two ways; a) integration over the whole peak, b) integration up to the peak maximum. Bottom left: The HH partial pair correlation from reference [209], for water in the presence of TBA (full line)and TPA (dashed line) and for pure water (dots). Bottom right: coordination numbers and peak to trough ratios (the peak heigth divided by the average of the minima either side of the peak) of the peaks in the HH partial pair correlation of water in the presence of TPA and TBA, important results are highlighted.

mobility of water molecules close to the alkyl chains. The general conclusion of most experimental studies of solvation of TAAs is that they tend to enhance the structure of environmental water, with the exception of TMA which tends to disrupt the water network structure.

The hydration layer of TMA has been studied using molecular dynamics simulations, [216], using empirical potentials to model interactions, employing the TIP4P model [217] for water. The advantage of simulations over the experimental methods is that the water molecules in the hydration layer can be studied whilst ignoring those beyond. Furthermore in all studies of hydration layers which examine PCFs or radial distribution functions (RDFs) it is necessary to employ a correction to the function which takes into account the excluded volume of the solute; in a simulation this is easier to apply to the data, and the methodology for doing so is discussed in section 4.2.1. The study of Madan and Sharp [216] revealed a change in the HH correlation function in the presence of the solute similar to that which was found for a cooling of pure water by 20 degrees. They also found increased peak to trough ratios of the RDFs (that is the height of the a peak maximum divided by the average value for that peaks minima) for HH and OO, indicating an increase in the order. They postulate that the reason why the features observed in the simulation are more pronounced for TMA (more like experimental results for longer chain TAAs) is due to the fact that in the experiments there were many water molecules not involved in the hydration layer that any effects in a net measurement of the PCFs. It was also found that though the changes in the RDFs were relatively small much larger changes were simultaneously found in the hydrogen bonding between waters: leading to the conclusion that RDFs alone give insufficient information about changes in water structure. Krienke and Opalka [218] also performed molecular dynamics of water in the hydration layer of TMA, this time employing a modified SPC/E model [219] for water. These studies revealed, like the experimental studies of Turner *et al.*, that the solvent is arranged tangentially around the TMA molecule.

4.2 Methods

4.2.1 Radial Distribution Functions

Radial distribution functions between a pair of species which are presented in this section were calculated from histograms calculated retrospectively for the MD simulation. The bins for the collection of histogram data were set to a width of 0.03 $\mathring{A}$. In general the radial distribution function,for atoms type X and Y, is then calculated from a frequency histogram using the formula

$$g_{xy}(r) = n_{xy}(r)/(V(r)\rho_y) = \rho_{xy}/\rho_y \tag{4.1}$$

where $n_{xy}r$ is the frequency of finding an atom Y at a distance of between r and $r+\delta r$ of an atom of type X; ρ_y is the bulk density of the atom type Y; $\rho_{xy}(r)$ is the local density of Y at a distance r from X; and $V(r)$ is the volume of the spherical shell around X between r and $r+\delta r$. In the case of pure water simulations, or indeed any homogenous solvent, $V(r) = 4\pi r^2 \delta r$. However in the situation where we have a solute in the solvent, and particularly in cases such as those simulated herein where the solvent/solute ratio is low, it is important to realize that a significant proportion of any spherical annulus which we are calculating may pass through the solute, and as such represents an area where solvent molecules cannot be found. Failure to take this into account when calculating an RDF from a frequency histogram would result in a pair correlation density which would be lowered for no intrinsic reason; this is known as the excluded volume effect[209]. Experimentally this correction is made by assuming a spherical excluded zone due to the solute , a convenient approximation as it give an analytic radial dependance of local atom density. The RDF for X and Y is then multiplied by the Fourier transform of the calculated scattering function for the spherical cavity. This "excluded zone effect" is somewhat easier to take into account in simulations(figure 4.2). Again we assume a spherical cavity for the solute molecule, which would be expected to be very close to the real situation in the case of most of the solutes considered here and we can calculate the portion of any given annulus which is excluded by the solvent (V_s) using simple geometric formulae:

$$\begin{aligned} V_s &= 2\pi r \delta r (r - (r^2 - r_s^2 + r_x^2)/2r_x) \\ &\qquad for, |r_s - r| < r_x < (r_s + r) \\ &= 0 \qquad for, r_x > (r_s + r), or, r_x < |r_s - r|; r > r_s \end{aligned} \tag{4.2}$$

In this formula r is the radius of the annulus, r_s is the solute radius, and r_x is the distance from atom X to the centre of the solute. When the excluded volume of a given annulus is calculated the number density of the atoms Y found within that annulus is then weighted by the ratio of volume outside solute to the total annulus volume $(V - V_s)/V$.

4.2.2 Searching For Rings

As part of the analysis of the molecular dynamics simulations the number of different types of rings in the hydration layer water has been calculated. But in order to calculate the number of rings, we must first have a definition of what we mean by a ring. In this case we have defined a ring as a path back to a given origin water molecule, M_0. In practice we start by defining all of the water molecules which are "attached" to M_0, this set is now the group of molecules M_1. We say that a molecule belongs to the set M_1 if the distance between its oxygen atom and the oxygen atom of M_0 is within the first peak of the oxygen - oxygen RDF. When the

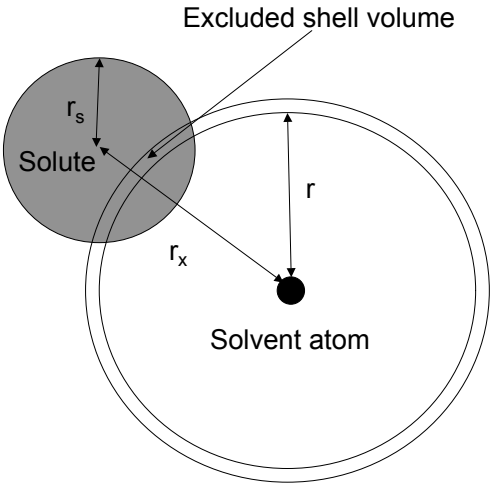

Figure 4.2: Correction of RDF for the solvent excluded effect.

set M_1 is defined we then define the next set M_2, which are all waters "attached" to molecules in M_1, excluding M_0. At this stage if an element of M_2 is the same as an element of M_1 we have found a water ring of order three, or a three-ring. We then move on to the molecules attached to M_2, these are M_3, if an element of M_3 is an element of M_1, for a different path, we have found a four-ring. If an element of M_3 is an element of M_2 for a different path then we have found a five-ring, and finally if an element of M_3 is the same on two different paths we have found a six-ring. We also check whether $M_3 = M_0$, in which case we have a three-ring. We then move on to M_4, which we check for the distance from M_0, if this is more than three times the connectivity distance we disregard the element, as we cannot return to M_0 within six steps, and we are searching for rings up to size six. If $M_4 = M_0$ we have a four-ring, this procedure is continued up to M_6.The structure of the search is shown in figure 4.3. The search is carried out for all atoms in the hydration layer of the solute, defining each one in turn as M_0, when a ring is identified we store its indices in a matrix of rings of that type. After all rings have been identified we then refine our set of rings, using the indices we search for shorter rings within the four, five and six-rings, if a shorter ring is identified within a larger one the larger one is rejected. We also remove all double counting of rings at this stage of the procedure, after this we are left with a set of uniquely defined rings, which are stored in a new matrix, with an extra element, initially zero, added, the reason for this extra element will be explained now.

After analysis each step of the MD the sets of unique rings identified are compared to those from the previous step of the MD, if the same ring existed in the

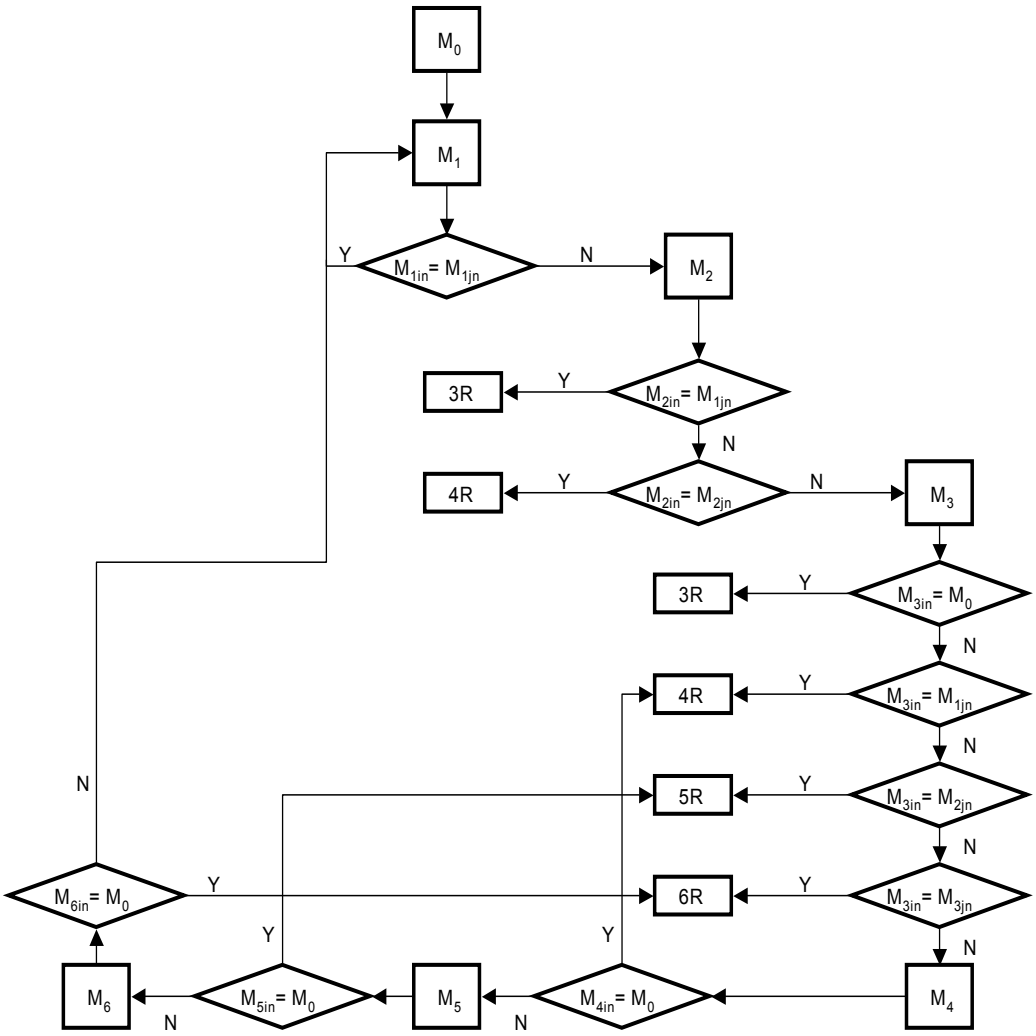

Figure 4.3: Flow diagram showing the steps used to determine ring structures from coordinates.

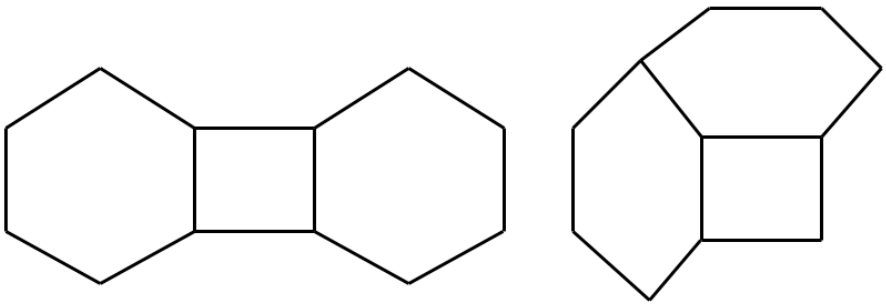

Figure 4.4: Fragment topologies which have been searched for by comparison of unique ring indices.

previous step of the MD then the extra element of the matrix is incremented by one, if a ring from the previous step has no equivalent in the present step then its extra element is dumped into a matrix which stores the lifetimes of each ring during the simulation, this allows us to investigate the stabilizing effect of different solutes on different ring types.

The program has also been adapted to search for different fragments of structure in the water structure. For example the two topologies shown in figure 4.4 are of particular interest and can be simply identified by searching through the indices of the unique rings, topology A is identified when a given four-ring shares its four elements with two six-rings, structure B is identified when a given four-ring shares three of its elements with two six-rings (two elements with each six ring), and the six rings in question share two of their elements, one of which is in the four ring also.

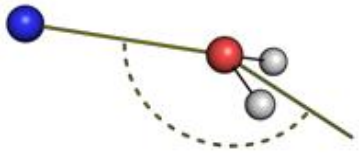

Figure 4.5: The tilt angle between an ion and hydrating water.

4.3 This Study

In the current study we first test the viability of using *ab initio* molecular dynamics (AIMD) methods to simulate the hydration layers of some structure directing agents (SDAs) commonly employed in zeolite synthesis. Specifically we compare the RDFs obtained for the hydration water of TMA with those obtained experimentally [206] and with the results of previous simulations which employed empirical potentials [216]. In addition we compare the effects of incrasing the length of the alkyl chain in a TAA by comparing the RDFs of TMA and TEA, the results which we obtain are similar to those found experimentally when the effects TPA and TBA on the RDFs of hydration their layer water were compared [209]. We also investigate the manner in which the water is oriented in the hydration layer by calculating a "tilt angle" between the vector from the centre of the solute and the negative of the dipole vector of the water (figure 4.5), revelaing the importance of charge and alkyl chain length in determining the ordering of the hydration layer water.

We then employ AIMD methods to study the hydartion layers of some other commonly used SDAs, namely amino adamantane, n-propylamine, piperidine and methyl piperidine. In this section we investigate the propensity of the various SDAs to form rings of water in their hydration layers, comparing the frequency and stability of rings of orders 4-6 occuring during the simulations. These results again demonstrate how factors such as charge, hydrophobicity and the presence of an amino group affect the water structuring in hydration layers.

Finally by searching for clusters of water rings which resemble zeolite framework topologies we are able to show that TMA forms the most clusters with a topology similar to the SOD cage which was found experimentally to be a clathrate hydrate of TMA [59] (figure 1.8).

Solute	Volume / Å^3	Number of Waters
TMA	1141.82	32
TMA Dilute	1965.00	58
TEA	1233.30	32
Neopentane	1144.45	32
N-propylamine	1525.00	37
Amino adamantane	1700.00	40
Charged amino adamantane	1706.49	40
Piperidine	1570.82	46
Methyl piperidine	1579.61	46

Table 4.1: Cell compositions for the NVT production runs of SDAs in water.

4.4 Results

4.4.1 Model Systems

All simulations in this section were performed using the Quickstep module, in the cp2k package [127]. In all cases a DZVP basis set with GTH psseudopotentials was used. A cutoff of 280 Ry was employed. The systems were generated by immersing the solutes in a box of pre-equilibrated water molecules. These systems were then run in the NPT ensemble for 3 ps in order to find an equilibrium volume. The results of the volume equilibration simulations are presented in figure 4.6. The compositions of the cells used in the subsequent NVT simulations are presented in table 4.1.

The data for calculated RDFs and ring searching were obtained from 10 ps runs in the NVT ensemble, with the exception of the dilute TMA cell, which was run for 6 ps, in all cases a timestep of 0.5 fs was employed. The systems were first equilibrated in the NVT ensemble with temperature re-scaling, with a limit of 350±50 K. The production runs were performed at 350 K with temperature re-scaling removed. The energies of the production runs are presented in figure 4.7.

These simulations were performed on the HPCx supercomputer as well as UCL's Legion supercomputer. 10 ps runs typically took 60 hours to complete running on 16 parallel processors.

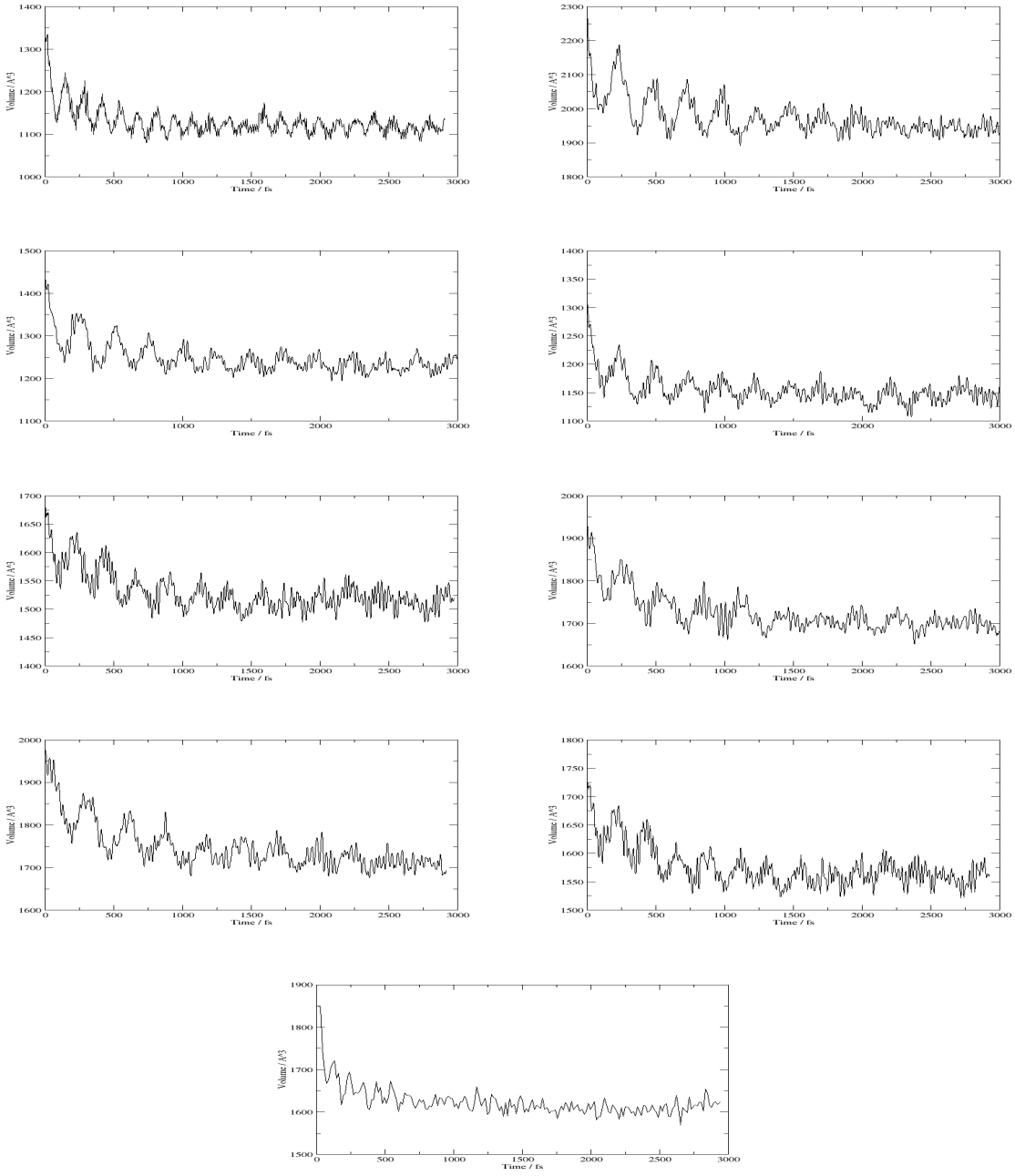

Figure 4.6: Volume Vs time results from NPT simulations of the SDA solutes, used to calculate volume for the NVT simulations. The solutes are, from the top, left to right: TMA, dilute TMA, TEA, neopentane, n-propylamine, amino adamantane, charged amino adamantane, piperidine and methyl piperidine.

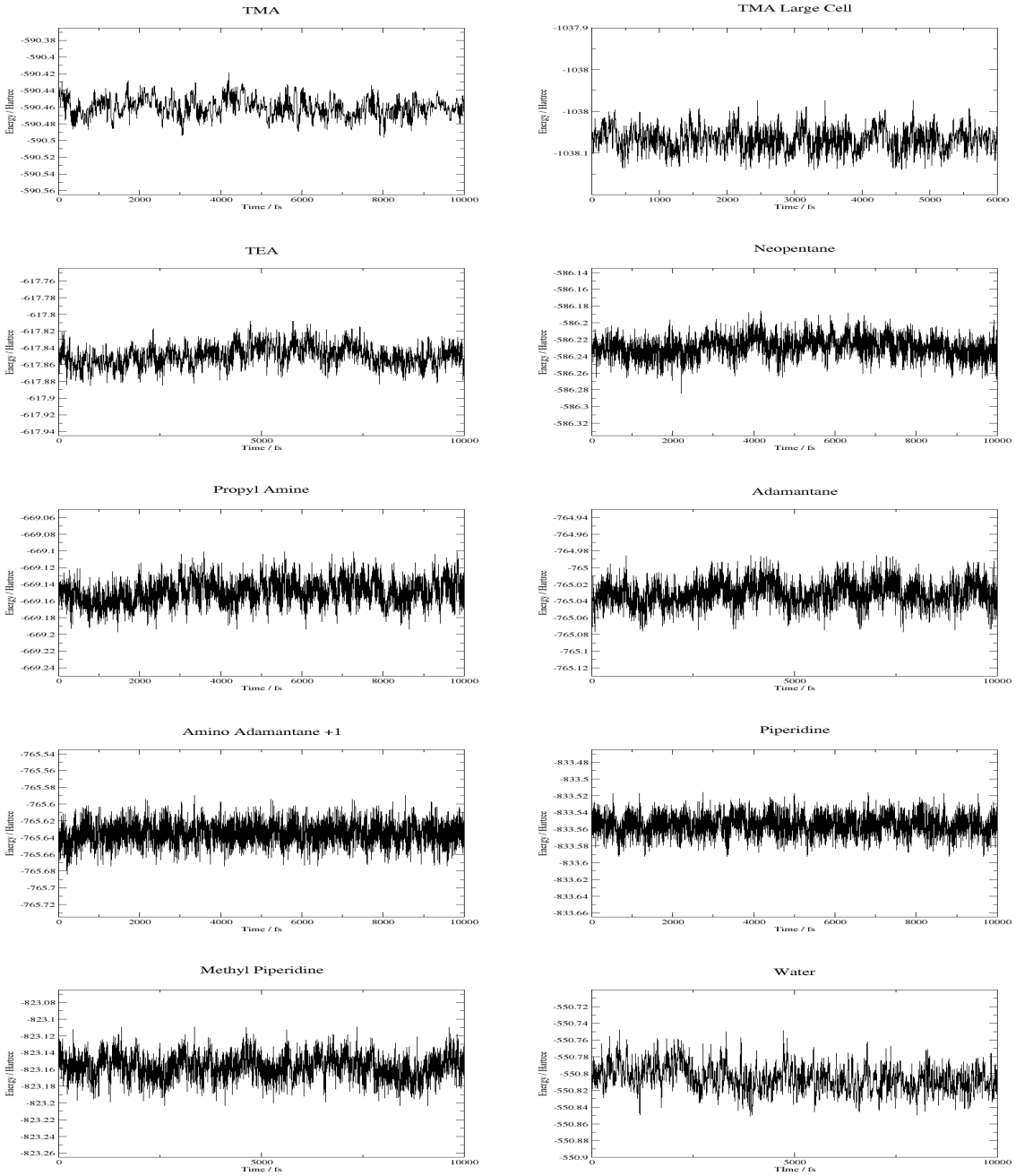

Figure 4.7: Energy fluctions from NVT simulations of the SDA solutes.

Species	RDF	Peak	M_s	M_f	N_x	R_c
Water	HH	2.35	1.81	2.90	5.46	1.75
TMA	HH	2.32	1.81	3.00	5.23	2.10
TEA	HH	2.33	1.81	3.00	5.17	2.19
Neopentane	HH	2.35	1.81	2.93	4.87	2.59
Water	OO	2.77	0.00	3.15	4.05	2.88
TMA	OO	2.75	0.00	3.15	3.57	6.16
TEA	OO	2.77	0.00	3.15	3.56	6.53
Neopentane	OO	2.75	0.00	3.15	3.75	6.20
Water	OH	1.90	1.40	2.45	1.04	8.82
TMA	OH	1.90	1.40	2.45	0.83	6.50
TEA	OH	1.91	1.41	2.46	1.02	7.62
Neopentane	OH	1.76	1.41	2.47	0.99	14.67

Table 4.2: Important results from RDFs, showing the peak position, minima before and after the peak M_s and M_f, coordination number (N_x), and peak/trough ratio (R_c)

4.4.2 TAA RDFs

One of the most commonly used measurements for determining the structure of a liquid phase is the RDF, in this section results of *ab initio* molecular dynamics simulations of Tetra Methyl Ammonium (TMA) ,Tetra Ethyl Ammonium (TEA), and Neopentane are presented. The oxygen-oxygen (OO), oxygen-hydrogen (OH), and hydrogen-hydrogen (HH) RDFs are presented. Certain other structural features are measurable from RDFs, including a measure of the degree of structuring of a peak, the ratio of the peak maximum to minimum - in the present analysis the lowest non-zero minimum is used - and the coordination corresponding to a given peak; the coordination number is calculated by integrating over a peak and weighting the result by the average atomic number density of the solution:

$$n_{xy}(r) = 4\pi\rho \int_{r_1}^{r_2} r^2 g_{xy}(r) dr \tag{4.3}$$

then multiplying by the concentration of the atom to get the number of neighbouring atoms:

$$N_y^{(x)}(r) = c_y n_{xy}(r) \tag{4.4}$$

For solutions in which the density of atoms in the simulation is lower than in the simulation of pure water, i.e. all solute systems the peak of the RDF must increase in height in order to maintain the same coordination number, thus the correction discussed in section 4.2.1 has been applied to all results, using values for the the radii of the solutes determined from the nitrogen (or central carbon in the case of neopentane)-oxygen RDF, the values (the first non-zero point on the RDF) which were obtained were 3.46 Åfor TMA, 3.77 Åfor TEA, and 3.48 Åfor neopentane.

The choice of solutes used in this section allows for a systematic comparison of a number of factors which may be expected to affect the influence of a solute on

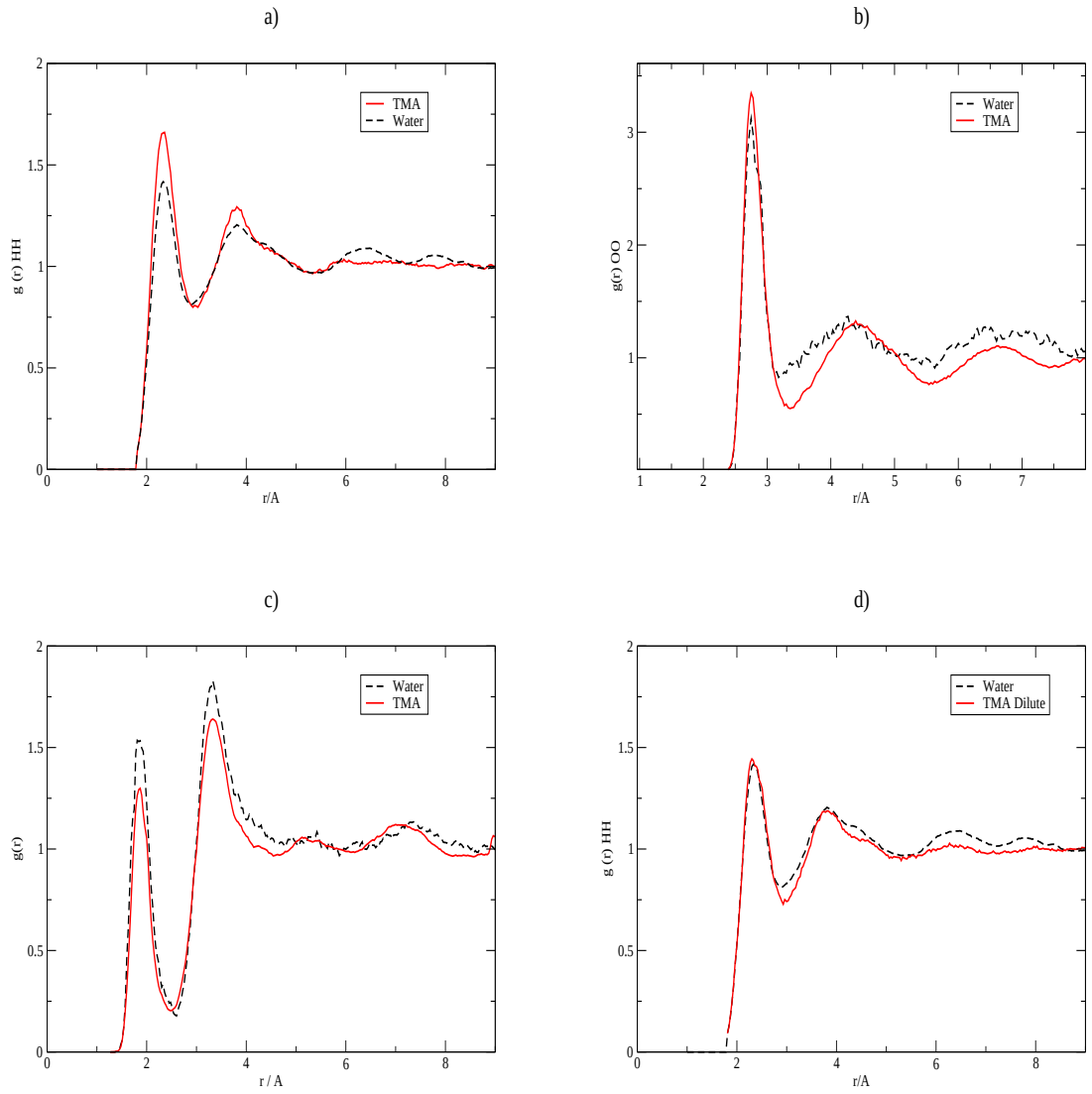

Figure 4.8: Radial distribution functions for pure water and water in the presence of TMA. a) Hydrogen Hydrogen RDF; b) Oxygen Oxygen RDF; c) Oxygen Hydrogen RDF; d) Hydrogen Hydrogen RDF for a more dilute sample of TMA.

a solvent; the comparison of TEA with TMA allowing examination of the effect of the length of the alkyl chain (and thus hydrophobicity); while comparison of TMA with Neopentane allows examination of the importance of charge on the changing of solvent structure. In all cases, the simulation cell contains the solute and 32 water molecules, with a cell size chosen to maintain a water density the same as that for the pure water simulation which was 0.96 gl−1, which was achieved by calculating the solvent excluded volume of the solute, and increasing the volume of the simulation cell accordingly. For purposes of clarity, all RDFs are included along with the RDF to which comparison is most relevant. All important measurements from the RDFs are also presented in table 4.2.

Focusing first on figure 4.8, a comparison of the results of the simulation of pure water, and TMA in water. Visual inspection of the RDFs reveals that in general

the inclusion of TMA results in a more well defined RDF, with the exception of the OH RDF. In the HH RDF the position of the first inter-molecular peak (the intra-molecular peak has been suppressed in the analysis) is shifted very slightly (-0.03Å) in the presence of TMA compared to pure water. The coordination number of this peak is reduced in the presence of TMA, which represents a shift away from a tetrahedral structure in the water molecules, this was also observed experimentally [206], as presented in figure 4.1. The reduction of the coordination number in the presence of a TAA solute is in line with experimentally observed trends, albeit for slightly larger TAAs [209], in which a decrease of 0.3 was observed in the presence of tetrapropyl ammonium (figure 4.1). A similar change (0.23) is observed in our simulations, although our absolute values a slightly higher. The ratio R_c is observed to increase in the presence of TMA, this increase (a measure of peak sharpness) is an indication that the number of conformations which the hydrogens of water may adapt relative to one another is reduced by the presence of TMA. Again this increased ratio compares well to experimental results for larger TAAs [209] (figure 4.1). The result of a more defined RDF however does not tally with experimental results on TMACl in water solutions [206] (figure 4.1), though it matches with the observations of previous simulation studies which used empirical potentials [216]. In the previous simulation paper [216] it was suggested that the lack of any evidence of peak sharpening from experimental results could be attributed to the concentration of TMA used in the experiments. They speculate that contributions to the RDF from both bulk water and water which is hydrating Cl may mask the effects of TMA on its hydration water. In order to determine how the presence of excess water may be expected to affect the RDF a further simulation of TMA in the presence of 58 water molecules was performed for 5ps. The HH RDF obtained from this simulation , presented in figure 4.8 and compared to pure water, quite clearly it shows that in this RDF the water and solution results are almost indistinguishable, thus lending weight to the argument that the lack of experimental evidence of structuring is due to excess bulk water. It is also worth noting here that when later experiments on larger TAAs were performed [209], which did reveal some degree of change in the HH RDF the solution concentrations were specifically chosen such that each TAA would have only enough water molecules for just one hydration layer.

The OO RDF also provides useful information regarding the structure of the water. This measure is less commonly presented due to the fact that experimentally all that can be determined by neutron scattering experiments is the correlations of D and X, where D is deuterium and X is all other atoms, thus an XX RDF will include artifacts from correlations other than those from OO alone. In our simulations we see a similar change in peak position as in the HH RDF (-0.02Å) compared to pure water, indicating that nearest neighbours move slightly closer in the presence of TMA. Integration of this peak to get the coordination number shows

us that the number of nearest neighbours is decreased in the presence of TMA, in pure water this number is just over 4, which is coherent with the tetrahedral model of water structure, the decrease in the presence of TMA gives a further indication that water in TMA's hydration layer is distorted out of the preferred tetrahedral arrangement. The ratio of this peak is also significantly increased by the presence of TMA, indicating a more limited conformational space for OO pairs. Although as stated, there is little in the way of reliable experimental evidence for OO RDFs in the presence of TMA the results of our simulations are similar to previously obtained simulation results [216].

The OH RDF provides information regarding the hydrogen bonding structure of the water molecules. In this case we have again suppressed the intra-molecular peak so that the first peak in the RDF corresponds to direct hydrogen bonding between water molecules. There is little evidence of any shift in the position of this first peak compared to pure water; the value of 1.90 Å; essentially that of an ideal hydrogen bond length, so this is perhaps unsurprising. However the coordination number of the peak reveals interesting evidence of the changes which TMA induces in the water network. We see a reduction from 2.08 in pure water (a value which combined with the 4.05 of the OO RDF again fits a tetrahedral model) to 1.65 indicates that the structure of the water network has been affected in the hydration layer. This reduction in value fits in with the definition of TMA as a water network "structure breaker" [194].

The results for the hydration water of TEA are now compared to those just discussed for TMA. The RDFs for both species are presented in figure 4.9, together with a histogram of the tilt angle. The tilt angle is defined as the angle between the vector from the centre of the TAA to the water oxygen and the dipole vector of the water molecule, and reveals the manner in which water is oriented about the solute.

The first inter-molecular peak position of the HH RDF shows very little change compared to that for TMA , but again it is slightly lower than in the pure water simulation. Although the peak height of the TEA peak is slightly higher than that of the TMA, the coordination number revealed by integrating over the peak is lower in the TEA case. The reduction is 0.06, which we suggest is due to the relatively lower concentration of water in the TEA cell rather than any intrinsic reason. Although no experimental evidence is available to compare coordination numbers in the presence of TEA and TMA there is data for comparing the numbers for two TAAs; namely Tetra Propyl Ammonium (TPA) and Tetra Butyl Ammonium (TBA) [209], Here it was found that increasing the length of the alkyl chain by one methane group, going from TPA to TBA, resulted in the coordination number of the first inter-molecular HH RDF peak is reduced by approximately 0.1. Thus we suggest that our results here give rise to a similar trend both qualitatively and quantitatively, upon increasing the hydrophobic nature of the TAA solute. The peak ratio (R_c) from

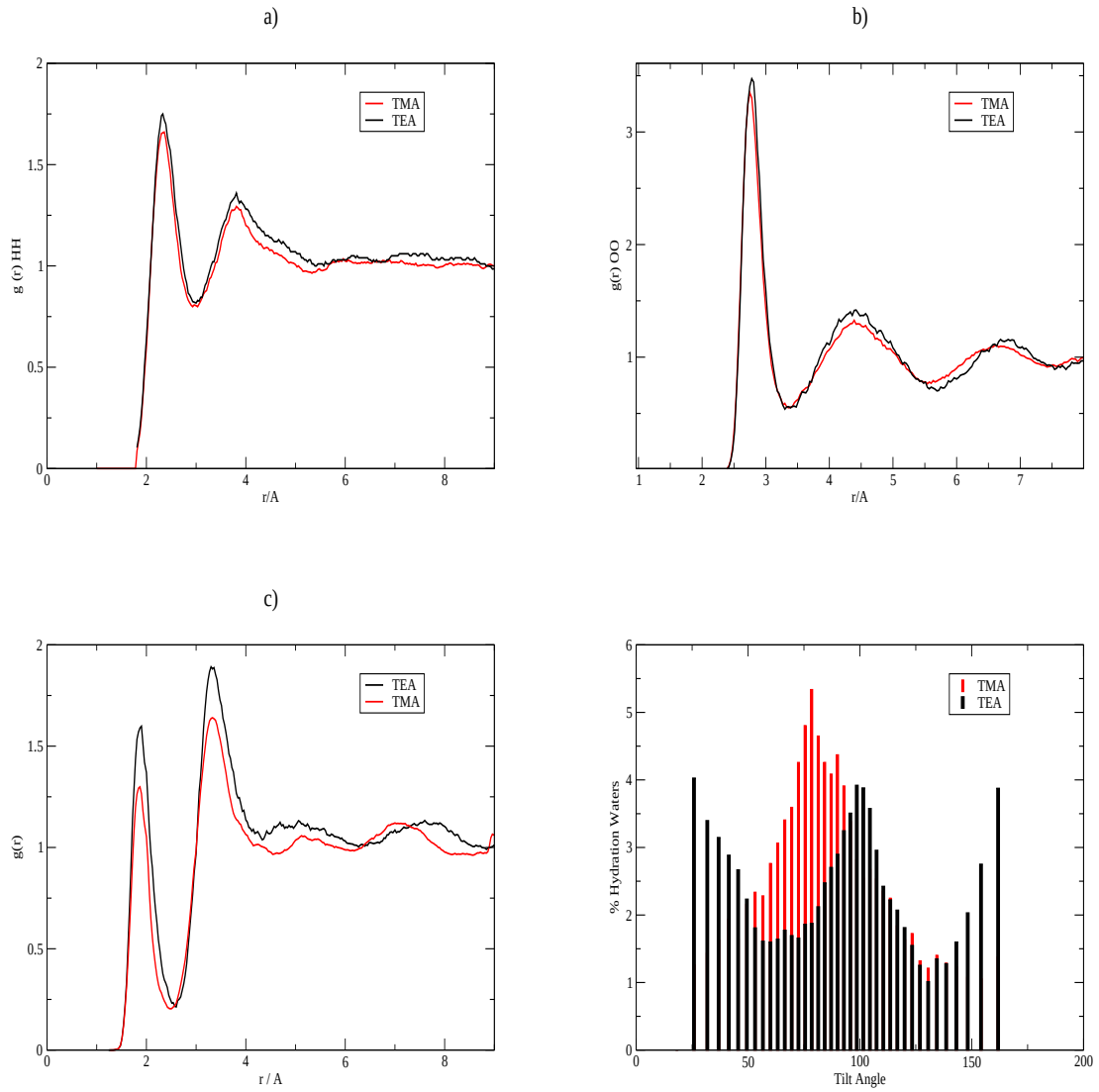

Figure 4.9: Radial distribution functions for water in the presence of TMA and TEA. a) Hydrogen Hydrogen RDF; b) Oxygen Oxygen RDF; c) Oxygen Hydrogen RDF; d) TIlt angle of water molecules in the hydration layer.

the TEA sample shows an increase compared to TMA by 0.09, indicating a reduced conformational space which the hydrogens may adopt relative to one another, again agreeing qualitatively and quantitatively with experimental results for TPA and TBA, which show an increase in the ratio of 0.05 for TBA [209].

The OO RDF again appears very similar to that for water around TMA, the first peak being shifted slightly and is now at the same position as in pure water, while the coordination number is very similar to that for TMA. The peak ratio does show an increase consistent with NMR data [220] which shows that in the concentrated solutions of hydrophobic TAAs the mobility of water molecules is reduced, which would necessarily lead to a smaller conformational space being sampled, and thus a sharper RDF peak.

While the OO and HH RDFs show little change between TMA and TEA save for a more pronounced effect in TEA, the OH RDF shows a qualitative difference between the two solutions. Whilst the first peak remains in the same position, the coordination number and the peak ratio change noticeably. The change in coordination number suggests a water structure closer to that of pure water, with just over two hydrogens bonding on average to the oxygen via inter-molecular bonds. Again this is consistent with the definitions of ions as "structure making" or "structure breaking" in which TEA is considered as a borderline case [194].

The tilt angle between the cation centre and the water dipole moment (figure 4.9 (d)) are also revealing as to the different hydration layer conformations in the presence of the two ions. The TMA angle distribution follows very much a normal distribution with the maximum being at 82° which corresponds to a situation whereby water molecules straddle the ion, with the water lying perpendicular to the ion, as found in previous simulation studies [218]. In TEA a more complicated distribution is found, while there still remains a peak corresponding to a straddling situation at 100°, there are also peaks at lower angles which corresponding to a situation whereby the O-H bonds point towards the centre of the ion, and at even higher angles where the oxygens point towards the centre of the ion. One explanation for this more disperse alignment behaviour is that as the alkyl chains in TEA are longer, the water molecules can arrange themselves about the alkyl chain itself, rather than the situation in the vicinity of TMA where the solute resembles much more of a cationic hard sphere.

Finally concentrating on the effect of Neopentane on the surrounding water, Neopentane is not used as a structure directing agent, rather this simulation, as stated earlier, is intended to decipher to what extent the structuring effects of TMA may be attributed to its space filling properties, and to what extent the directs the ordering of water.

The effects on the HH RDF of Neopentane are certainly more pronounced than those in TMA, while the peak position is the same as pure water the coordination number and peak/trough ratio are affected. The coordination number is reduced considerably more than in TMA to 4.87, compared to 5.23 for TMA and 5.46 for pure water. The peak ratio is increased from 2.10 to 2.59. The OO RDF is also sharpened with respect to TMA with a peak ratio of 6.20 compared to 6.16. However the average coordination number of nearest neighbour oxygens is increased relative to TMA; 3.75 compared to 3.57. Again the OH RDF gives the largest and most revealing changes of all of the RDFs. In this case the peak position is considerably altered, to 1.76 Å, which represents a significant distortion away from the ideal geometry for a hydrogen bond. The number of hydrogen bonds per oxygen is higher than TMA and more similar to that found in pure water. The peak ratio/trough ratio however is drastically increased, being more than twice that of the TMA hydration water.

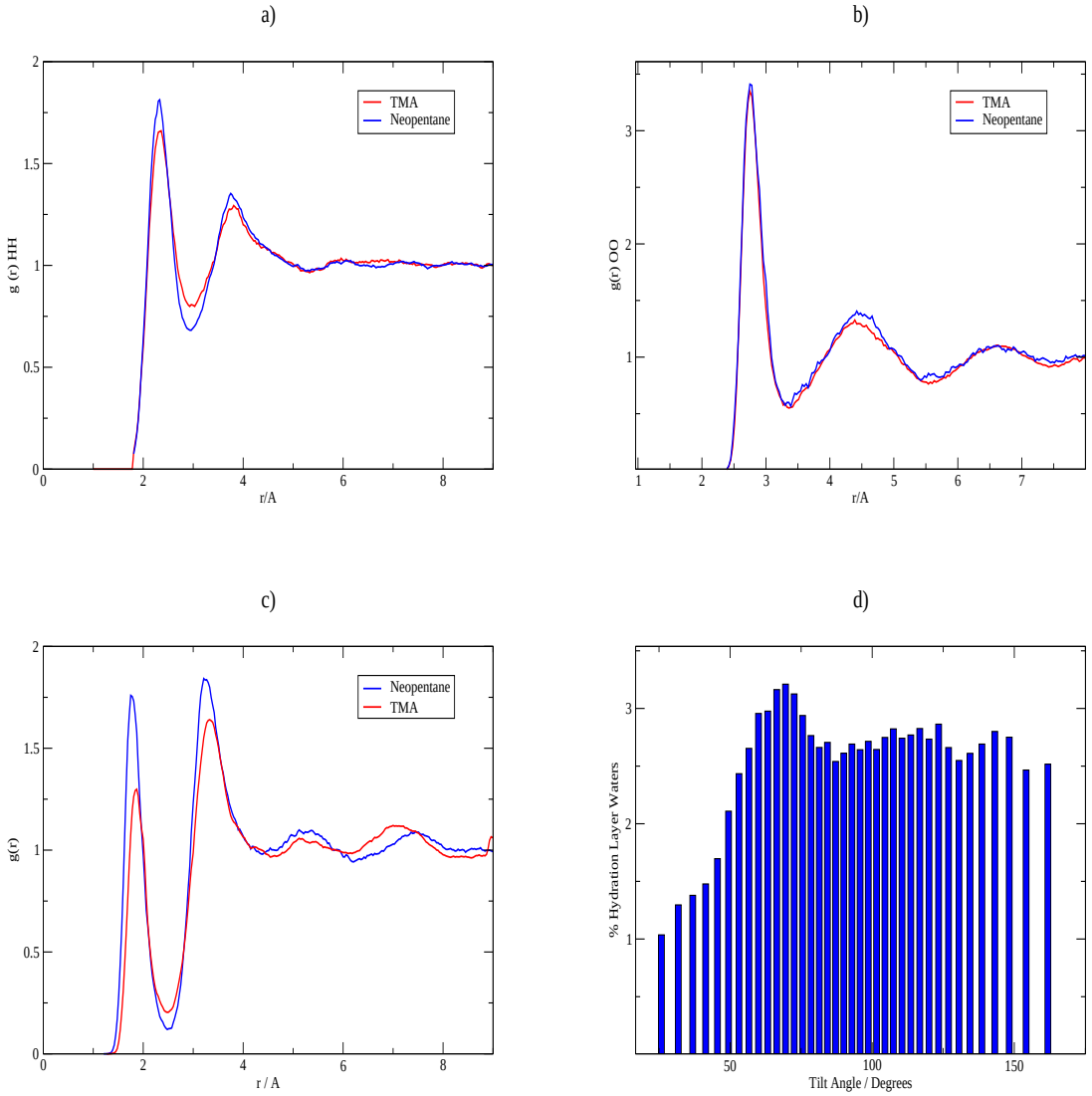

Figure 4.10: Radial distribution functions for water in the presence of TMA and Neopentane. a) Hydrogen Hydrogen RDF; b) Oxygen Oxygen RDF; c) Oxygen Hydrogen RDF; d) TIlt angle of water molecules in the hydration layer of Neopentane.

The tilt angle analysis (figure 4.10) reveals that in the hydration layer of Neopentane there is little preference for any particular orientation of the surrounding water, with no discernible peak. A slight peak around 80° suggests some preference for the straddling position as found in TMA hydration water, however this is far less pronounced in this case.

In general the more hydrophobic Neopentane results in a more well defined RDFs, suggesting a reduction in the mobility of individual water molecules, whilst there is also clearly a change in the nature of hydrogen bonds found in the water surrounding Neopentane, compared to pure water and the TAA solutions studied here. The analysis of the tilt angle also suggests the importance of the charge in forming a hydration layer which lies perpendicular to the solute surface, such an arrangement of water molecules would be considered to be an important factor in the formation

of clathrate type structures in the hydration water which would be necessary if the water templating of zeolite crystallization is to be considered, we can thus conclude that the charge of TAA cations is a crucial feature if we expect them to direct crystal structure by this means.

It is also clear from the comparison of TEA and TMA that qualitatively the hydrophobicity, or alkyl chain length, affects the patterns of structuring found in the environmental water. Obviously TMA and TEA are present in the syntheses of many types of zeolite framework, and there are structures which either of them can form. This is perhaps to be expected as the cation present is only one of the factors which would be expected to have an influence on the growth of a crystal. However our evidence that both have different effects on the surrounding water may be of importance, if we are to accept the idea of clathration as a step in certain crystal nucleation processes.

The data from the RDFs provides useful information as to the different ways in which solutes affect the water structure in their hydration layer, however it is difficult from a two dimensional measure such as an RDF to infer much detail about the three dimensional structure of the water network in these systems. In order to be able to evaluate the extent to which TAAs and indeed other structure directing agents form hydration layers which may influence the final crystal structure it is necessary to look at other measures of the the types of structure formed. In the next section the formation of rings of water in hydration layer will be considered in order to asses the possibility that the structure directing agent activity may (at least partially) be due to their influence on the water structure.

4.4.3 Ring Formation

In addition to the TAAs studied in the previous section results are presented here for a number of other SDAs. Amino adamantane represents a class of bulky SDA, some of whose effects are expected to be due to space filling properties. Simulations of amino adamantane with the amine group protonated were also performed to consider the importance of the amine group for water structuring properties, as well as to investigate the influence of charge. Piperidine and methyl piperidine are also considered, whilst these species are less space filling than the others, the comparison of piperidine and methyl piperidine, where the nitrogen is somewhat occluded from surrounding water by the presence of the methyl group, allows for further investigation of the importance of a lone pair donating nitrogen. Finally n-propylamine is also considered as this is the one species for which previous modeling work in the context of water structure and zeolite templating has been performed, using a Monte-Carlo approach [64]. All species studied are presented in figure 4.11.

The ring forming statistics of the TAAs (including neopentane) are presented and compared to those in pure water in figure 4.12, in this graph the number on

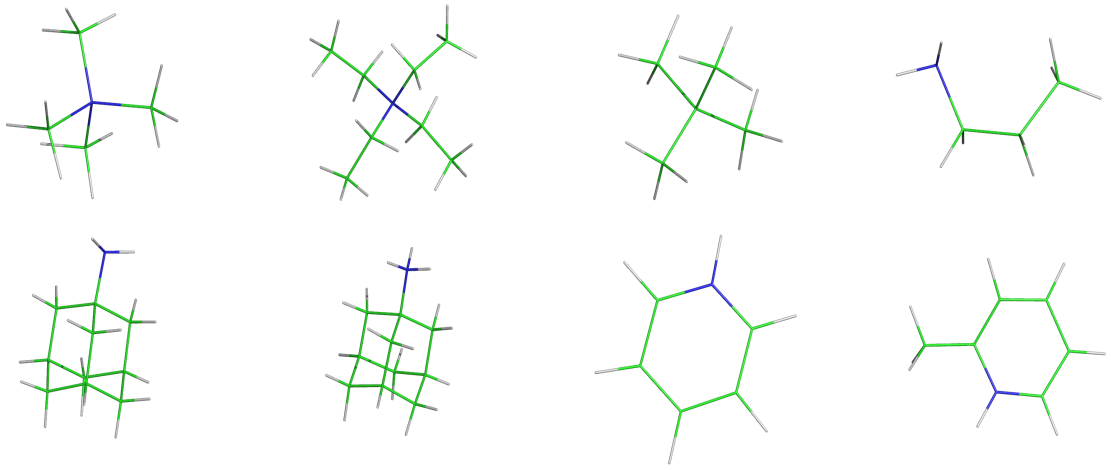

Figure 4.11: The SDAs studied in this section, from the top left to right; TMA, TEA, neopentane, n-propyl amine, amino adamantane, amino adamantane (positively charged), piperidine, and methyl piperidine. Green: carbon, blue: nitrogen, white: hydrogen.

the y-axis is the normalized number of rings found in the SDA's hydration layer, the number is calculated from:

$$N_r = \frac{N}{sN_w} \tag{4.5}$$

where N_r is the normalized number, N is the number of that type of ring found during the whole course of the simulation, s is the number of steps and N_w is the average number of waters in the SDA hydration layer. Using this normalization ensures that there is no bias due simply to the fact that an SDA has a larger hydration layer than another.

The statistics show that all of these species result in an increase in the number of five and six rings of water formed compared to that observed in pure water, in the case of five rings this is a 139-fold increase in the presence of neopentane, a 136-fold increase in the presence of TEA, and a 75-fold increase in the presence of TMA. For six rings the increase is somewhat less pronounced, 23 fold for both TMA and neopentane, and 45 fold for TEA. In the bulk water there are rather more four rings than five or six rings found , so as we would expect from this the change in number of rings is again less pronounced; here we find a $\sim$ 1.3 fold increase in neopentane; a $\sim$ 1.9 fold increase for TMA and very slight decrease in the simulation with TEA. The similarity in the number of six rings in the hydration layers of TMA and neopentane suggests that this behaviour is due to space filling in the water network, while the larger TEA forms almost twice as many six rings as these species. The situation in the formation of five rings is rather different, TEA and neopentane show similar numbers in this respect, if n-propylamine is considered as well the formation of five rings is similar to neopentane and TEA, this suggests that a hydrophobic chain is important in the formation of five rings, and while TMA has some hydrophobic character, this is counteracted by its charge, resulting in less

five rings being formed. TMA shows the greatest propensity for formation of four rings in its hydration layer, which may perhaps be due to the fact that the charge results in a more contracted hydration layer compared to neopentane, whilst the size has the same effect compared to TEA. The more contracted hydration layer would result in less volume for open rings to form and may explain the greater number of four rings. It is interesting to note here that TMA is the only SDA known to form zeolite structures with no five rings, and whilst these numbers in no way suggest that TMA is averse to five rings of water in its hydration layer, it is of the species studied, that which shows the most capability of such behaviour.

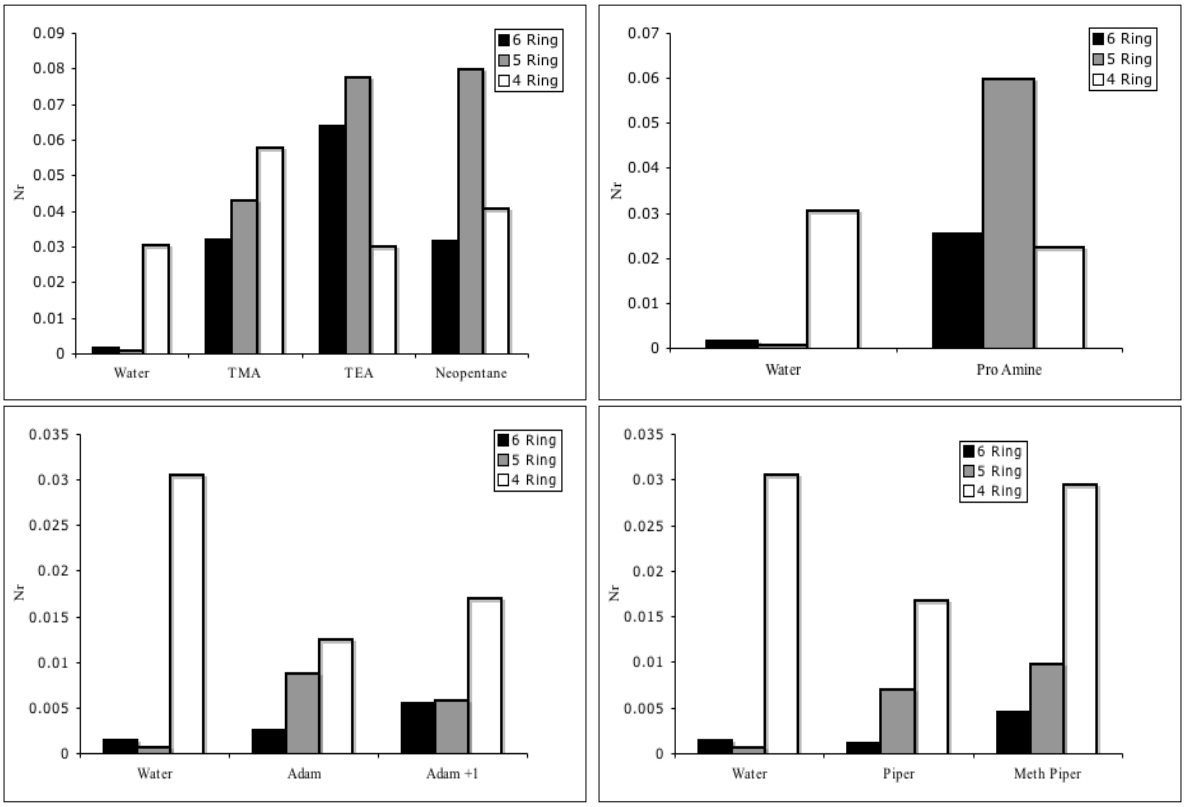

Figure 4.12: Normalized numbers of different ring types found in the hydration layers of the SDAs studied in this section.

The lifetimes of the types of ring found in the hydration layer can also be revealing as to how the various SDAs stabilize the different water structures. In figure 4.13 it can be seen how important the charge of the TAAs is in increasing the lifetimes of rings in the solution. Both TMA and TEA promote stability of rings compared to pure water, while neopentane actually decreases the stability. The lifetimes of the rings is also enhanced with the increasingly hydrophobic surface of TEA compared to TMA. This is consistent with experimental results which show that, at a concentration of TAA in which there is just enough water for a hydration layer of each apolar ion, the mobility of solvation waters is decreased due to contact with the hydrophobic surface of the solute [220]. Whilst n-propylamine has the apolar properties of the TAAs, it does not have a charge under neutral pH or the high pH of

hydrothermal synthesis conditions, rather its primary electronic interaction with the solvent water is via the lone pair of the amine group. The results for n-propylamine again highlights the importance of the charge in the TAAs in stabilizing all types of rings, as all rings are shorter lived in the n-propylamine hydration layer compared to bulk water. The presence of the alkyl chain however does increase the lifetimes of the structures relative to neopentane, in which the hydrophobic surface is much more spherical.

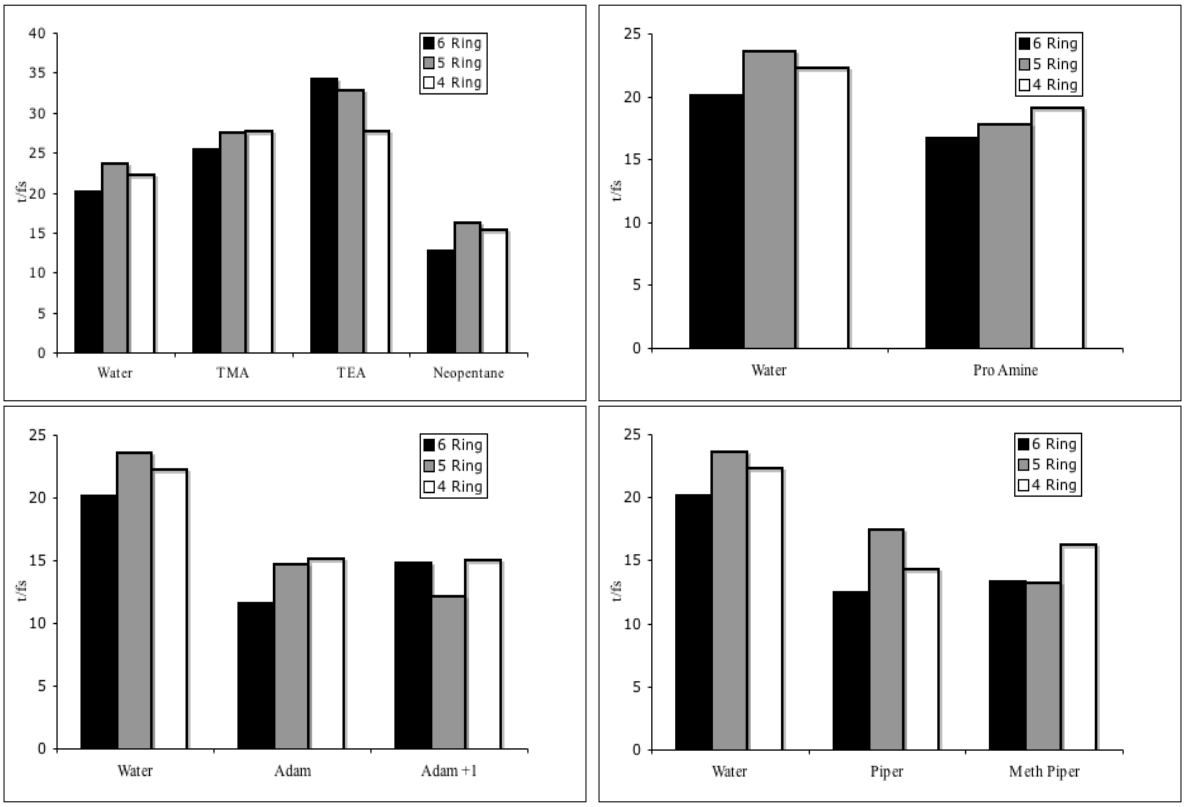

Figure 4.13: Lifetimes of different ring types found in the hydration layers of the SDAs studied in this section.

Focusing on the larger aminoadamantane species it is clear from figure 4.12 that the ring forming tendencies of these species is significantly less pronounced than either the TAAs or n-propylamine. The simulations of these species in water contains a larger number of solvating molecules to reflect the fact that when aminoadamantane is used in the synthesis of for example DD3R the concentration used is considerably lower CITE than the concentration of TAAs generally used in synthesis. The concentration used in our simulations is still considerably higher than synthesis conditions; a ratio of 50 H_2O : 1 aminoadamantane, compared to a synthetic ratio of 673-822 . However it is clear that even at our relatively high concentrations the effects on the solvating water are much reduced compared to the TAAs and n-propylamine. What we do observe however is that five and six rings form more in the presence of the SDA, while four rings form less. There is also a difference between the charge states, the neutral species favouring five rings and the

charged species favouring four and six rings. The lifetimes of the ring species are all diminished with respect to pure water, which in combination with the results for TAA suggest that a simply charge and a hydrophobic surface alone are not enough to enhance ring lifetime, as the charged amino adamantane species possesses both properties. Rather a charge de-localized across a hydrophobic surface is the optimal situation for the stabilization of water rings.

Piperidine and methyl-piperidine are both simulated in concentrations similar to amino adamantane, as they are generally employed in zeolite synthesis in these concentrations. As was the case in amino adamantane the number of four rings found in the hydration layer is diminished for both solutes, while the number of five and six rings is increased, although not as noticeably as for the TAAs or n-propylamine. The methylated species has a greater tendency to form all types of ring, which is perhaps related to the larger hydrophobic surface. The lifetimes of all rings are again diminished with respect to pure water, and it is interesting that in this instance, as for aminoadamantane that the presence of an amino group seems to stabilize five rings more (or destabilize them less relative to others), the methylated species with the partially occluded nitrogen having less long lived five rings.

It is also possible from the simulations to look at the number of rings formed in the vicinity of a particular moiety of the SDA, and we shall now consider this for the non-TAA species. The results for the normalized number of rings with a centre of gravity within 5 Åof the nitrogen atom of the aminoadamantane, piperidine, methyl piperidine and n-propylamine species are presented in figure 4.14. One of the most striking features of this data is the effect of protonation of the amine group in aminoadamantane. The positively charged species has far fewer of each type of ring in its vicinity. This may be due in some part to the fact that the hydrogens of the charged amine may participate directly in hydrogen bonding with the local water, thus disrupting the networks of water in this region. It is also clear that the occlusion of the nitrogen in piperidine by the methyl group in methyl piperidine leads to a reduction in the number of rings around this moiety; even accounting for the excluded volume as a result of the methyl group there appears to be a definite reduction in the number of five rings in this region, though the lower number of six and four rings could easily be accounted for as an artifact of the excluded volume. There is also strong evidence from the data to suggest that amine groups favour the formation of five rings of water in some way, as evidenced in n-propylamine, the effects of occlusion of nitrogen in methyl piperidine and the protonation of amino adamantane.

4.4.4 Clathrate Fragments

Clearly from the above analysis of the formation of rings of water the three species with the greatest tendency to form rings are TMA, TEA and n-propylamine. In

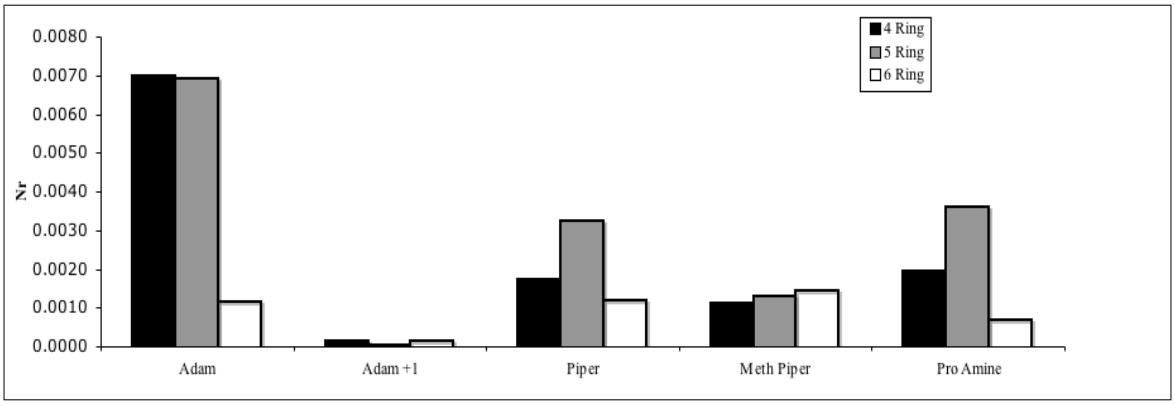

Figure 4.14: Normalized number of rings of water occurring within 5Åof the SDAs.

this section the connectivity of these rings is now investigated, in particular the connectivity between six and four rings and the connectivity of five rings to six rings. Structures with the topologies shown in figure 4.15 are searched for in the data, using the technique described in section 4.2.2. The topologies, consisting of six and four member rings , represent a fragment of the structure of a TMA hydrated structure which has been experimentally characterized [59], and which is isomorphic with sodalite, for which of course TMA is used as a SDA. The fragment with five rings connected to six rings is a fragment of the MTN framework topology for which n-propyl amine is used as a SDA, and which has been shown using Monte-Carlo simulations to be a favourable hydration structure for n-proply amine [64].

The results of this search regarding the lifetime and number of these fragments found during the course of the simulation are presented in figure 4.16. These results show that TMA does show an increased tendency to form fragments of the sodalite type structure The fragment is found in $\sim$ 10 % of the steps during the MD simulation, compared to $\sim$ 3 % in the TEA simulation and $\sim$ 6 % in the n-propylamine simulation. It is also found more often than the five ring structure which is found in $\sim$ 3 % of the TMA simulations. The average lifetime of this fragment is also enhanced in the presence of TMA, it is 82.6 fs, compared to 63.8 and 66.4 in the presence of TEA and n-propylamine respectively. Figure 4.17 shows snapshots from the TMA MD simulation showing this fragment around the solute.

Fragments consisting of five and six rings shows a clear preference for the presence of n-propylamine, being present in $\sim$ 21 % of the steps during the MD, however TMA has the most stable examples of this structure with an average lifetime of 63.9 fs, the average lifetime in the presence of n-propylamine is perhaps surprisingly short at 41.0 fs.

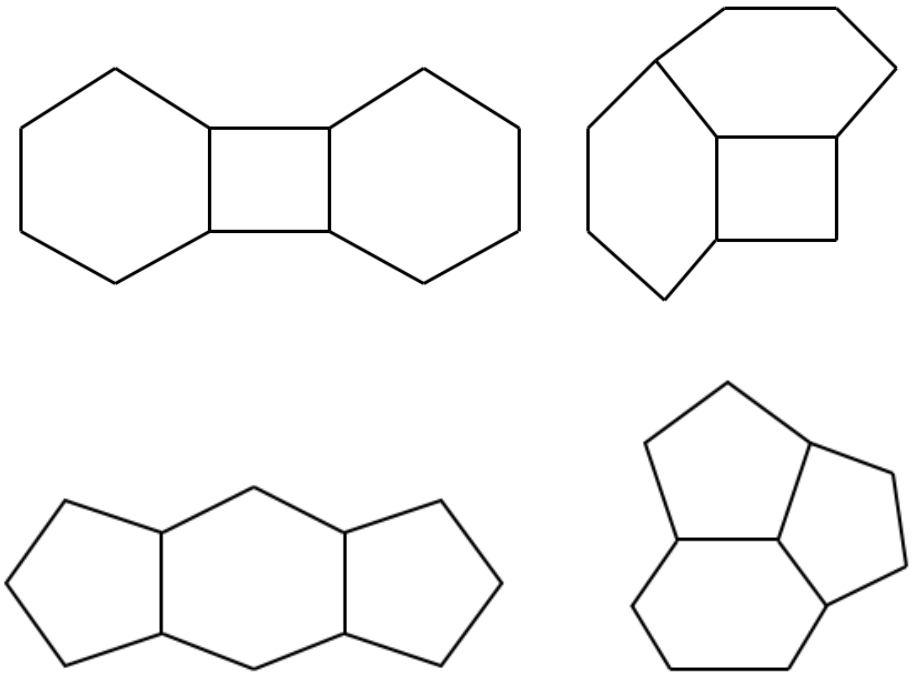

Figure 4.15: Fragment topologies which have been searched for by comparison of unique ring indices.

4.5 Conclusions

In this chapter it has been shown how various SDAs can influence the structure of the water in their hydration layer, and how this effect may have an influence on the nucleation and final crystal structure of a zeolite. The results give fresh impetus to a hypothesis of crystal growth which has largely been neglected since the mid 1990s.

It has been demonstrated through analysis of RDFs that TMA and TEA have structuring effects on water at the kind of concentrations which are used in zeolite syntheses. The RDFs revel that TEA has a larger effect on the surrounding water than does TMA, which matches with experimental observations on the effect of increasing alkyl chain length in larger TAAs [209], it has also been demonstrated that the lack of evidence in experimental RDFs of structure around TMA may be due to the masking effect of bulk water in the experimental data. In addition to this the tilt angle of hydration water has been used to demonstrate the fact that water molecules straddle the hydrophobic surface of TMA, whilst a more disorganized layer exists around the larger chains of TEA. Simulation of neopentane in water allowed investigation of the importance of charge in the structuring effect of TMA, and demonstrated that the charge is important in causing the straddling of TMA. OH RDFs reveal how TMA results in a reduction in the hydrogen bond network in water compared to bulk, while in TEA the network is more or less intact, these

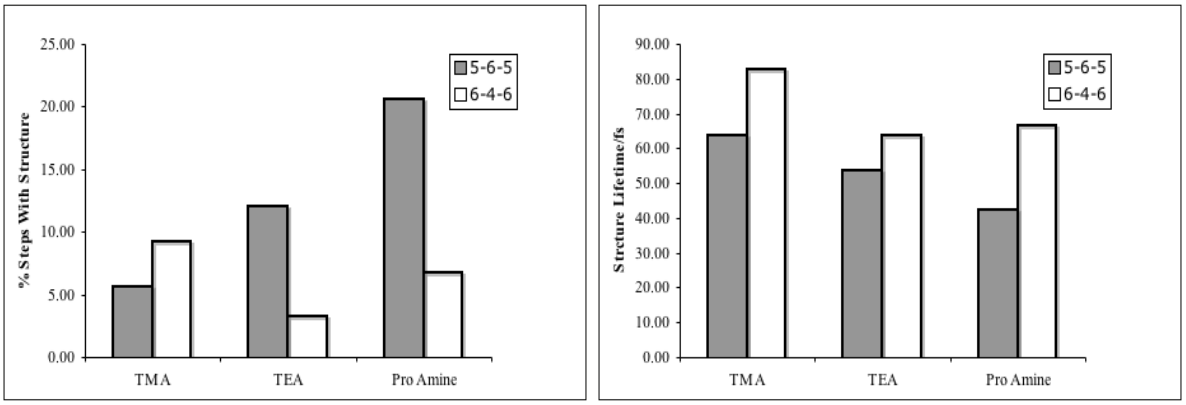

Figure 4.16: Numbers and lifetimes of the clathrate fragments found in the hydration layers of TMA, TEA and n-propylamine.

results add a quantitative element to the assignment of TMA as a water structure breaker and TEA as a borderline case in the structure maker/breaker designation [194].

Using a specially developed code the populations and stabilities of various types of rings of water, from three rings up to six rings has been investigated in the hydration layers of the TAAs as well as various other types of SDAs. These results demonstrated how TEA has a generally greater ring forming effect than TMA, but that TEA results in less four rings, it was also shown that the charge on TMA was important for the formation of four rings, as neopentane shows less four ring formation and more five ring formation than TMA. This is interesting in light of the fact that TMA is used in the synthesis of some of the only Zeolites which do not have five rings in the final crystal structure. n-propylamine was also demonstrated to have a large impact on the number of larger rings found in the water of its hydration layer. The other SDAs which were investigated were amino adamantane, both neutral and charged, and piperidine and methyl piperidine. These SDAs which are used in synthesis mixtures in generally lower quantities than the TAAs showed a significantly smaller effect on the number of rings formed.

In addition the ring searching code was modified to look for rings in the locality of the nitrogen atoms of the tertiary amine species as well as the quaternary amine in charged amino adamantane. The striking result from this analysis was how tertiary amines seem to encourage the formation of five rings of water, demonstrated by comparison of the charged and uncharged amino adamantane, and the piperidine species. This is an intriguing finding a warrants further investigation, possibly using higher level cluster methods.

Finally certain fragments of clathrate structures in the hydration layer of TMA, TEA and n-propylamine were searched for, these searches show how TMA has a grater number of fragments resembling the structure of sodalite, for which it directs, than the other species, while n-propylamine has a greater number of fragments

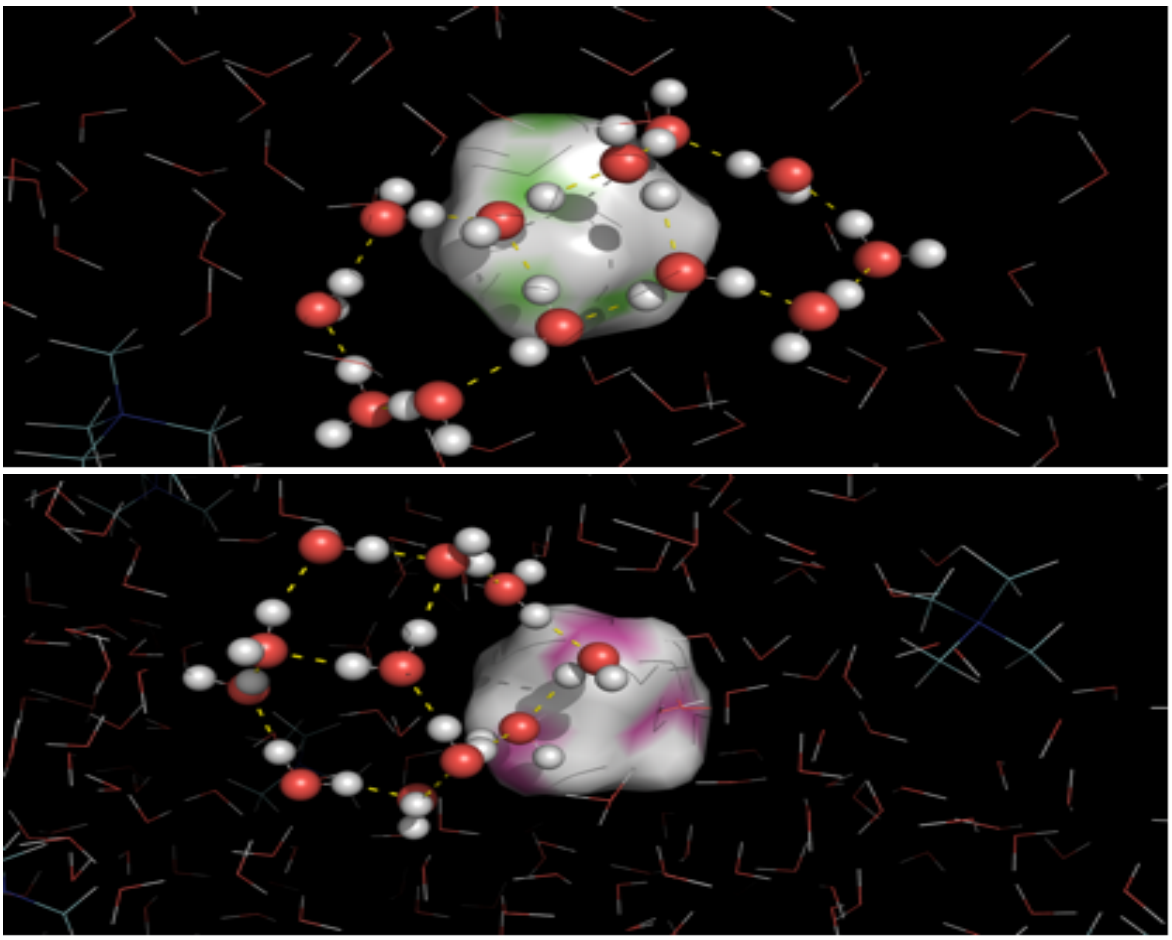

Figure 4.17: MD snapshots showing the existence of clathrate fragments in the solvation layer of TMA during the simulation.

resembling part of the MTN framework for which it directs than the other two.

Overall the results of this chapter have demonstrated that for a number of SDAs the water structuring effects closely resemble the effects of the species on Zeolite structure in a synthesis, these are generally structures which posses either charge and/or alkyl chains. The effects of the other SDAs studied were less marked, although the importance of the tertiary amine group in forming five rings of water is clear. Of course even for those SDAs which do structure water in a way similar to Zeolite for which they direct many other Zeolite phases are possible with them, however as many factors effect the final structure, such as pH, temperature, concentration etc. this is hardly surprising, and while water structuring followed by dynamic replacement by silicate and crystal nucleation has been demonstrated by some of these results to be a plausible mechanism it is most likely merely one element in the incredibly complex process of nucleation and crystal growth.

CHAPTER 5

Silicate Species and Solution Properties

5.1 Introduction

As was shown in the previous chapter the components of a zeolite synthesis can result in a significant re-ordering of the water in their vicinity. It has also been shown that zeolite crystals form individual hydration layers at their surface, which are different to bulk water [221]. The presence of such water layers was shown to affect the diffusivity and surface geometries of these crystals. The presence of water around silicate clusters has been shown to play an important role, specifically in determining the free energy of adsorption of tetramethyl ammonium (TMA) to the face of two silicate species, namely the prismic hexamer (double 3 ring, species VIa in figure 3.1) and the cubic octamer (double 4 ring, species VIIIc in figure 3.1)[222, 223, 224]. This is believed to be due to the entropy change associated with the overlap of the hydration layers of TMA and the silicate species. Furthermore, it has been suggested, on the basis of NMR experiments, that entropic contribution due to ordered hydration layers may be responsible for the assembly of template/silicate species in pre-nucleation solutions [6, 63]. In this chapter we simulate these two species in solution and demonstrate the existence of distinct, ordered layers of water surrounding them.

In the majority of the studies mentioned above, the silicate species in which ordered hydration layers are postulated to exist are cage-type oligomers, including the cubic octamer and the prismic hexamer. Due the size of these species and their hydration layers, the molecular dynamics simulations necessary for investigation of hydration layers are too expensive to be performed using first principles molecular dynamics, such as were used in the previous chapter. Therefore, in this chapter, the less computationally demanding technique of inter-atomic potentials is employed.

Such an approach allows longer time-scales to be accesed, meaning that properties such as the residence time of water in the hydration layers can be calculated. There exist many potentials for silica, as will be discussed below, however few of these potentials are developed specifically for oligomeric cluster species. The first task in this chapter is, therefore, to modify an existing potential, used for crystalline silica, in order to better suit the clusters to be modelled. The modified potential is then applied to the cubic octamer and the prismic hexamer species to investigate their influence on hydration water structure.

The work presented herein is the result of a collaboration with Prof. Steve Parker and Wojtek Gren in Bath University. This collaboration was made possible by a junior research fellowship from the Thomas Young Centre, and was also carried out as part of the nanogrowth project [225].

Before considering the results of our calculations a review of the development of silica potentials shall be presented. This overview is by no means complete, but is intended to cover all of the major developments in the use of potentials for modelling zeolite systems. Afterwards a review of how these potentials have been utilized for the study of the pre-nucleation phase of zeolite synthesis solutions shall also be presented.

5.1.1 Silica Potentials

The history of inter-atomic potentials for modelling silicates can be traced back almost thirty years. The earliest simulations were performed using purely ionic models [226] and demonstrated that the use of simple two body short-range models with the Buckingham potential (equation 2.45) could successfully predict structural properties of several members of the pyroxenoid class of minerals. Such models were subsequently shown to be useful in modelling other common classes of minerals [227, 228]. However issues were known to exist with this extremely simple treatment of mineral systems, manifested in the inability of the models to describe elastic, dielectric and dynamical data for α-quartz. These problems were first addressed by supplementing the simple Born model of the crystal systems with specific bond bending, or three-body terms[229] (equation 2.42). A three-body term was introduced essentially to penalise distortion of O-Si-O bond angles away from the ideal tetrahedral geometry. Another important addition to this model was the inclusion of the polarizability of the oxygen atoms by the introduction of a shell model as described in section 2.2.2.3. This revised model corrected many of the deficiencies of the original as shown by its enhanced performance in tests on structural and elastic properties.

To this point the parameters used in inter-atomic potentials for silicate systems were primarily fitted to empirical macroscopic data, although it should be mentioned that parameters such as the oxygen to oxygen Buckingham potential parameters

were taken from quantum calculations of simple systems, in this case the interactions of two O^{2-} ions[226]. However, the next development in deriving silicate potentials was to base parameters on *ab initio* simulations of the potential energy surface (PES) of silicate clusters. The first such potential was reported by Lasaga and Gibbs [79]. Who initially derived an ionic type potential from the PES of orthosilicic acid ($Si(OH)_4$). This ionic model was shown to be very similar to others derived empirically. As with fully ionic models mentioned previously the potential had problems in recreating the elastic properties of silica polymorphs. These deficiencies led the authors to derive a covalent potential model based on bond lengths, angles and torsions by fitting to the Hartree-Fock (HF) calculated PES of disilicic acid ($Si_2O(OH)_6$). The potential models derived were able to better reproduce these structural and elastic properties. Subsequently these covalent potentials were used to mimic the topography of the PES of various silicate clusters and to investigate the structural, dynamical and elastic properties of minerals and glasses [80].

An *ab initio* derived two body potential was developed in 1988 by Tsuneyuki *et al.* [230] for the crystalline states of silica. The derivation of this particular potential differed from previous *ab initio* derived potentials in that the silica cluster used to derive the parameters was SiO_4^{4-} rather than fully protonated orthosilicic acid, the cluster being neutralized by e^+ particles. The interaction between the atoms of the system were then modelled by a Coulomb interaction, Born-Mayer-type (BMH) repulsion and a dispersive interaction. The method was shown to successfully reproduce the dynamic stability of most common silica phases. Other force-fields developed around this time were based on *ab initio* force constants for orthosilicic acid and disilicic acid [231]. Whilst these force fields neglected the Coulomb interaction, they were shown to calculate the vibrational frequencies of silicas, giving values consistently approximately 15 % higher than experiment: entirely consistent with the fact that they were derived using HF theory and a 6-31G* basis set, which generally gives a similar systematic discrepancy.

Thus far we have considered potentials based either on empirically or theoretically calculated parameters: each method has its strengths and weaknesses. The former, whilst providing a good match to previously measured experimental values, suffers from a lack of the degree of theoretical rigour which would provide confidence that the potential forms are representing, in a realistic way, the underlying physics of the system. Such confidence in the degree to which the potentials represent fundamental realities is desirable if the potentials are to be trusted to perform outside of the training set for which they are derived. The latter, whilst possessing this physical basis, suffers from the fact that the systems upon which they were based tended to be very small. Although they represent these systems well, the actual physics of larger systems contains features incommensurate with smaller systems. The essential problem is that good fits to small cluster data can be found

with a whole range of parameters. Thus *ab initio* potentials suffer from much the same training set problems as empirical potentials, albeit for different reasons. A pragmatic solution to this problem was proffered by van Beest *et al.* [232]. Their potential was derived initially using *ab initio* clusters to parameterize nearest neighbour interactions, but takes into account the fact that large (essentially infinite) crystal systems rely on more than just nearest neighbour interactions by fitting to empirical parameters too. Such a scheme was shown to result in a potential with good accuracy and portability.

One important factor which had not yet been accounted for was the lack of any description of electron correlation in the HF models which were used to derive force field potential models. The first method which was used to include correlation effects was to calculate the PES using local density approximation density functional theory (LDA-DFT)[233]. In the LDA-DFT formalism, as discussed in section 2.1.3.1, the exchange and correlation effects are accounted for by an approximate functional. Thus, although correlation will not be described exactly, some measure can be introduced to the potential derivation, at the expense of exact exchange provided by the HF method. This potential was derived on a purely *ab initio* basis using the same potential form as earlier work [229] and indeed was very similar to that potential, but showed an appreciable improvement. The inclusion of correlation was also expected to improve calculations of vibrational frequencies and an improvement on the model of van Beest *et al.* [232] was shown. The inclusion of some degree of exact exchange in the derivation of potentials was achieved by parameterizing to a set small molecular clusters calculated using the hybrid exchange-correlation functional B3LYP [102, 103, 234]. The use of this potential resulted in structures with Si-O bonds longer than usually calculated and favouring of lower symmetry structures than usually calculated, both of which are ascribed to the inclusion of electron correlation in the derivation [234].

Due to the fact that the majority of (early) simulations of silicates were interested in bulk structures and properties the issue of the effective modelling of the hydroxyl group has not yet been mentioned. The problem with the hydroxyl group compared to the other elements of the silica systems is that the connectivity of the group is very much covalent, thus pair potential models, which found so much success with modelling the bulk, are not able to represent this interaction properly. Accurate modelling of the hydroxyl (or silanol) group is important if issues such as zeolite acidity and surface simulations are to be considered. This problem was first tackled by van Beest *et al.* [235] who modelled the hydroxyl group as an effective single atom, using parameters which were fitted to PES calculations of an alumino-silicate dimer. Of course, the problem of how to represent a covalent interaction does not arise if one employs a force field type potential such as those mentioned previously [79]. Hill and Sauer developed a force field potential from HF calculations of a training

set of four silicate clusters ranging in size from two to twelve silicon atoms[81], and encompassing chain, ring and cage structures. This potential was shown to reproduce *ab initio* geometries of clusters other than training set ones, and bulk phases with some success. This force field methodology was subsequently extended to include alumino-silicates [236] and was shown to predict the structures of alumino-silicates with bridging hydroxyl groups with roughly the same accuracy as an earlier derived empirical model which included shells on the oxygens [237]. An *ab initio* ion pair model including shells was developed by Schröder and Sauer [238], this potential has essentially the same form as earlier empirically derived potentials [229] but with one significant difference; the lack of an r^{-6} parameter in the Buckingham potential. This model was shown to be an improvement on the force field model described earlier [236] in describing strongly varying parameters such as the T-O-T bond angle, with the reason being, essentially, that the force field penalises heavily for far from equilibrium values. It was also shown to have advantages over the empirical shell ion pair model in predicating lattice vibrations.

Recently the issue of surface hydroxyls in silica has been approached using DFT derived potentials [239]. Parameterized using of state-of-the-art techniques for modelling periodic systems using hybrid functionals, and employing the B3LYP functional to parameterize the simple shell model mentioned previously, this potential was shown to be able to deal with a wide variety of hydrogen bond configurations between surface hydroxyls and compared well with DFT results. In addition it was shown to predict structures, energies and vibrational modes of bulk structures as well as existing potentials.

Another issue which arises, when employing potential models, is that the charge of each atom type is fixed in the simulation *a priori*, thus changes in the local environment of an atom (for example a change in co-ordination number) are not accounted for in terms of the charge on the atom; as would happen in a real system. This problem can become particularly acute when trying to simulate phase changes in a material. A solution was proposed based on readjusting the charges of the atoms in the system *a posteriori* based on information regarding the local structure [240]. The charges of the atomic centres in this scheme are updated at regular intervals during the simulation based on the charge equilibration procedure of Rappe and Goddard [241]. In addition to the electrostatics, short range forces are also included in this model via a Morse-Stretch potential term,

$$U_{ij}(R_{ij}) = D_0[e^{\gamma(1-R_{ij}/R_0)} - 2e^{\gamma/2(1-R_{ij}-R_0)}], \tag{5.1}$$

which was parameterized to match experimental data for α-quartz and sishovite as representative four and six coordinated systems. This potential form was shown to describe well the pressure-induced transition from α-quartz to sishovite. Subsequently this potential has also been used to simulate properties of vitreous silica structures [242, 243].

A different approach to using either an ionic or three-body potential to model SiO_2 systems was proposed by Wilson *et al.* in 1996 [244]. This model used an essentially ionic model but included a more realistic description of polarization of the atoms in the system. The resultant potential was shown to eliminate the problems faced by ionic BMH type potentials and three-body potentials in calculating the network vibrations of amorphous SiO_2: namely the the overestimation by the former of the bending frequency of the Si-O bond [245, 246] and underestimation by the latter of the asymmetric stretching frequency of the SiO_4 tetrahedra [244]. More recently this approach has been incorporated into a potential which has been derived to fit DFT-GGA data [247], where again a Morse-Stretch potential is used (equation 5.1), which was fitted to data for silica at 3000K and zero pressure, under which conditions silica is a liquid. The potential was shown to predict structures of both liquid and low pressure crystalline silica.

The final potential scheme described in this section is the recently developed reactive force field model for SiO_2 systems (ReaxFF) [248]. This model uses a general force field model for the system energy, with the QEq method for charge consistency [241]. Unlike traditional force fields however, ReaxFF can also simulate breaking and forming of bonds, in order to facilitate this it was necessary to include Coulomb and van der Waals forces, thus the model incorporates elements of both force fields and pair potential models. The parameters used were fitted to both cluster data calculated using hybrid DFT and periodic system data using GGA DFT. This method has found much use in simulating dynamic properties of silica systems [249, 250] and has been extended to other systems such as ZnO [251].

5.2 Methodology

In this chapter a number of types of simulations have been performed. These include DFT optimizations of silicate clusters, which were performed *in vacuo* using the B3LYP[103, 105] functional and a 6-31G* basis set to obtain electronic energies of the training set of 33 oligomers, which were used to modify the potential. The training set was chosen to represent a large array of silicate oligomers which are present in the pre-nucleation zeolite synthesis solution, ranging from the silicic acid monomer, to small chain species, rings type species and cage type species. The inter-atomic potential geometry optimizations were carried out by performing a zero kelvin molecular dynamics simulation in the DLPOLY [78] code. The energies which are obtained from DLPOLY are lattice energies, whilst those from the DFT simulations are electronic energies and, in order to compare the two sets of energies, it has been necessary to apply a correction to the lattice energies based on the number of different atoms present;

$$E_{el} = E_{lat} + n_{Si}\Delta E_{Si} + n_O\Delta E_O + n_{OH}\Delta E_{OH} + n_{H_2O}\Delta E_{H_2O} \tag{5.2}$$

	$\Delta E_{Si}/eV$	Δ_O/eV	$\Delta E_{OH}/eV$	$\Delta E_{H_2O}/eV$
New	-3016.919196	-4415.64087	-3252.359	-2069.5898
Old	-3019.532605	-4414.498128	-3251.1669	

Table 5.1: Energy terms used to convert lattice energies from the old and new potentials to electronic energies as in equation 5.2

Where E_{el} is the electronic energy, E_{lat} is the lattice energy, n_X is the number of atoms of type X in the system and ΔE_X is the correction term for atom type X. The values for ΔE_X were obtained by performing a least squared fit to the DFT energies for the data set, and the values are given in table 5.1. Note that oxygen atoms are treated differently depending on their position, either hydroxyl (OH), water (H_2O) or bridging (O), also the correction value for water was chosen to match the electronic energy of B3LYP/6-31G* water as this is the value to which the potential was fit. The interactions in the potential models were represented by a number of common potentials: the Buckingham potential (equation 2.45), the Morse potential (equation 2.40), three body bond angle potentials (equation 2.42) and Coulombic interactions (equation 2.43) which are calculated using the Ewald summation method, the methodology also employs the shell model for all oxygens (see section 2.2.2.3).

We also performed simulations of various silicates including full explicit solvation with water. For these simulations a minimized structure of the species to be solvated was first immersed in a box of pre-equilibrated water measuring 20Å x 20 Å x 20 Å, from which all water in close contact with the solute species was then removed. This system was then allowed to find an equilibrium volume by running it for 1,000,000 steps of 0.5 fs in the NPT ensemble. Once an equilibrium volume was established the system was the converted to the NVT ensemble and equilibrated for a further 10,000 steps of 0.5 fs, followed by production runs of 10,000,000 0.5 fs steps, resulting in simulations of 5 ns. Due to the fact that not all simulation cells contain the same number of water molecules, we need to extract the energy of the solvated species from the simulation in order to perform energy comparisons:

$$E_{sol} = E_{sys} - n_{H_2O}E_{H_2O}, \tag{5.3}$$

where E_{sol} is the energy of the solvated molecule, E_{sys} is the average energy of the total system from the MD run, n_{H_2O} is the number of waters in the system and E_{H_2O} is the average energy of bulk water molecule calculated from a similar MD simulation of pure water.

The structure of water surrounding the prismic hexamer and cubic octamer (species VIa and VIIIc in figure 5.1) was visualized by calculating the oxygen and silicon density during MD simulations of these species surrounded by water. The density was calculated using an electron density calculating code which was modified to read atomic species rather than electrons, and which outputs a format readable by

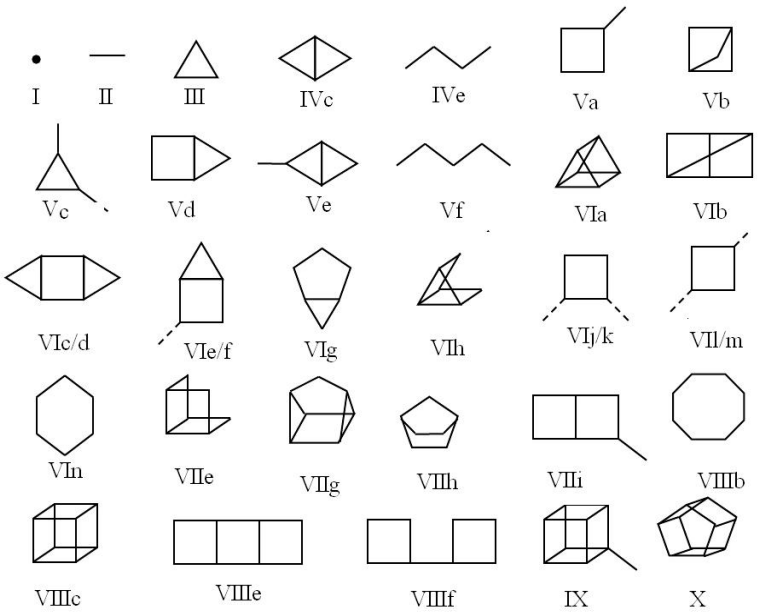

Figure 5.1: The silicate oligomers used for modification of the potential, a line represents an Si-O-Si bond.

materials studio [252]. For this analysis it was necessary to ensure that the soulte species remained in the same position at each step, which was achieved in post-processing by re-orienting the system co-ordinates from the simulation trajectory at each step. The results of this analysis, shown in figures 5.8- 5.14, show a projection of the density calculated during the simulation.

5.3 Results

5.3.1 Modification of the Potential

The oligomers used as the training set for fitting a potential to DFT energies are presented in figure 5.1. A table of old and new parameters for the potentials used is presented in table 5.2, and the difference between DFT and potential total energies is presented in table 5.3.

We now discuss the performance of the new potential which, overall, shows a smaller deviation from the DFT energies than the old potential; the standard deviation of the new potential is also lower than that of the old one, the average energy difference between DFT calculated values and valus calculated using the potentials . Thus we can say that overall the values from the new potential should give us a more reliable estimate (if we consider DFT to be reliable) of the relative and absolute energies of the oligomers. Whilst this is hardly surprising, as the new potential was derived in order to better match these energies, some trends are worth

Species				
	q/e	CSI/eV/Å^2		
Si	4.00000			
O (core)	0.84800			
O (shell)	-2.84800	74.92040		
OH (shell)	0.90000			
OH (core)	-2.30000			
H	0.40000			
OW (core)	1.25000			
OW (shell)	-2.05000	209.44960		
HW	0.40000			
Morse Potential				
	D/eV	a/Å^{-1}	r_0/ Å	Reference
OH (shell) - H	7.05250	3.17490	0.92580	[253]
OW (shell) - HW	6.20371	2.22003	0.92367	[254]
Buckingham Potential				
	A/eV	ρ/Å	C/eVÅ^6	
O(shell)-O(shell)*	22764.00000	0.14900	38.88000	
O(shell)-O(shell)	22764.00000	0.14900	27.88000	[255]
O(shell) OW(shell)	22764.00000	0.14900	15.46000	[253]
O(shell)-OH(shell)*	22764.30000	0.14900	19.44000	
O(shell)-OH(shell)	22764.30000	0.14900	13.94000	[253]
Si-O(shell)	1283.90730	0.32050	10.66160	[229]
Si-OH(shell)*	983.55600	0.32050	5.33080	
Si-OH(shell)	983.55600	0.32050	10.66160	[253]
Si-OW(shell)	983.55600	0.32050	10.66160	[254]
OH(shell)-OH (shell)	22764.30000	0.14900	6.97000	[253]
OH (shell)-OW(shell)	22764.00000	0.14900	15.46000	[254]
Three-body Poential				
	$k/eVrad^{-2}$	$\theta_0/degrees$		
O(shell)-Si-O(shell)*	5.49630	109.46667		
O(shell)-Si-OH(shell)*	5.49630	109.46667		
OH(shell)-Si-OH(shell)*	5.49630	109.46667		
O(shell)-Si-O(shell)	15.49630	109.46667		[229]
O(shell)-Si-OH(shell)	15.49630	109.46667		[253]
OH(shell)-Si-OH(shell)	15.49630	109.46667		[253]
Intra-molecular Coulombic	subtraction (%)			
HW-HW	50			[253]
OW(shell)-HW	50			[253]

Table 5.2: The parameter used in the interatomic potential models, * denotes modified values in the new model. All parameters ar labeled as in relevant equations, CSI refers to core-shell interaction, which is a harmonic spring potential.

Species	New Δ E (kJ mol^{-1})	Old Δ E (kJ mol $^{-1}$)
I	31	19
II	37	25
III	17	8
IVc	36	50
IVe	20	8
Va	24	22
Vb	27	31
Vc	30	40
Vd	3	1
Ve	25	41
Vf	25	41
VIa	41	41
VIb	28	44
VIc	33	37
VId	18	18
VIe	14	9
VIf	6	8
VIg	11	12
VIh	9	5
VIj	16	13
VIl	6	0
VIm	1	1
VIn	17	14
VIIe	26	42
VIIg	6	0
VIIh	29	36
VIIi	14	18
VIIIb	18	26
VIIIc	26	58
VIIIe	4	10
VIIIf	1	8
IX	27	55
X	38	82
Average	20	25
St. Dev.	12	20

Table 5.3: Comparison of the energy differences between old and new potentials for the training set and the DFT calculated energy, the species numbers refer to figure 5.1.

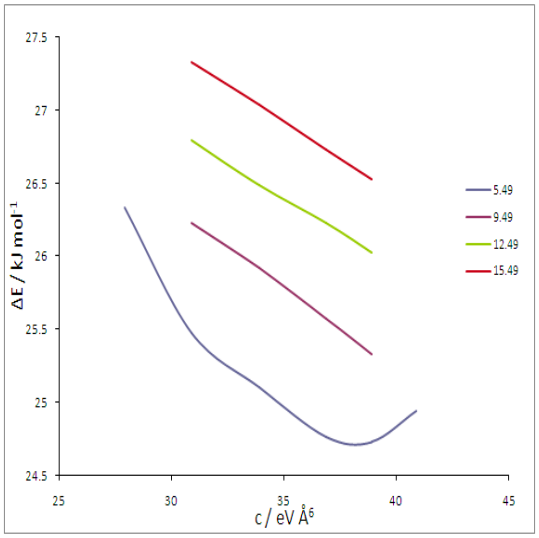

Figure 5.2: The energy difference between DFT and potential calculated values with the variation of the c parameter in the morse potential. The differeces were calculated at various values of k in the three-body term, these are given in the legend in units of eV rad^{-2}

discussing further, in particular there are cases where the new potential does not perform as well as the old one. Indeed, the old potential shows a smaller deviation from the DFT energy in the linear species and small rings (dimer, tetramer, three-ring, substituted four-rings). As the species become larger and more condensed, with a higher proportion of Q^3 sites, the new potential performs significantly better e.g. double four-ring and double five ring species. Where the old potential performs better for larger species the difference in performance is always small. This result is encouraging as the cases in which the application of such a potential is necessary would involve larger silicates where modelling with *ab initio* methods is impractical.

The variation of the average energy difference between the DFT caluclated and values and those calculated using the potential as the parameters were vairied is presented in figure 5.2. This shows that there is a minimum in this difference at the new value of c, in the morse potential. It also shows a reduction in the difference as the value of k, in the three-body term, is reduced.

As mentioned, it is hardly surprising that a potential specifically fitted to a data set performs better on that data set than one which is not fitted to it. Thus it is important to go beyond the data set and also to consider how the potential replicates the trends in various reactions which the silicate oligomers may undergo. To this end a series of different reaction energy changes are now compared to the same energies obtained from DFT. However, we note from the outset that these DFT energies were calculated at a different level of theory to those used to fit the potential, being calculated using the GGA functional BLYP and numerical basis sets[256] . The reactions considered are a series of chain growths, ring closures and addition of a monomer to a ring. These reactions are presented in figure 5.3. They

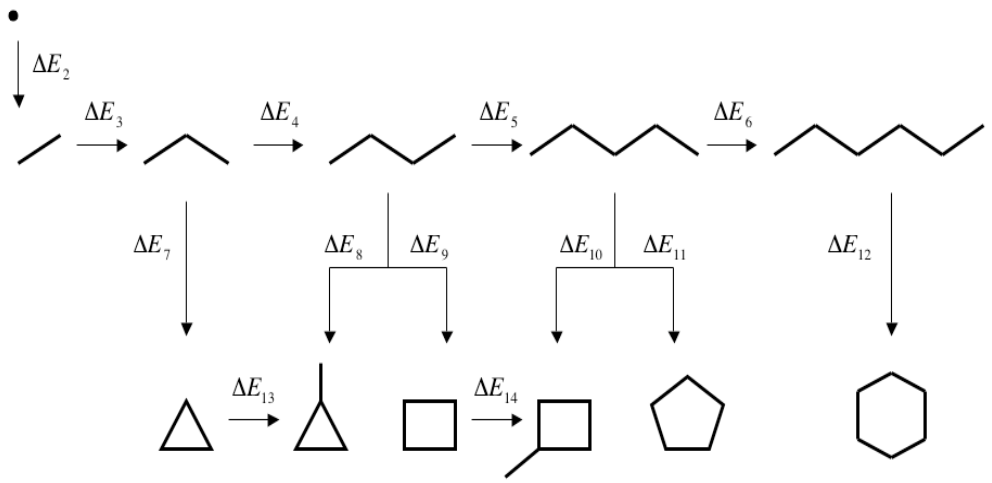

Figure 5.3: The reactions considered to compare to DFT, a line represents an Si-O-Si bond.

take the generic form;

$$Si_nO_{(n-1)}(OH)_{(2n+2)} + Si(OH)_4 \rightleftharpoons Si_{(n+1)}O_n(OH)_{(2n+4)} + H_2O \quad (5.4)$$

$$Si_nO_{(n-1)}(OH)_{(2n+2)} \rightleftharpoons Si_nO_n(OH)_{2n} + H_2O \quad (5.5)$$

Comparisons of the reaction energies obtained by the modified and older potential are plotted in figure 5.4. Firstly, it is clear that the energies of reaction computed using both potentials are universally higher than those calculated using DFT, although it is possible that this is an artifact of the use of exact DFT energy for water in the calculations in equations 5.4 and 5.5. However, the primary concern of this comparison is to see if trends in the DFT energies of reaction are replicated by the potentials. Examining the energies of chain growth in figure 5.4 a), this shows that both potentials replicate, in general, the DFT prediction that growth of larger chains is less energetically demanding than growth of shorter chains via condensation. An exception to this trend is the formation of a trimer from a dimer (reaction 3), compared to the formation of a tetramer from a trimer (reaction 4) where the DFT energy is lower for reaction 4, but both potentials predict reaction 3 to have the lower energy. Another discrepancy which exists is that the old potential shows the formation of a hexamer from a pentamer (reaction 6) to be more energetically demanding than the formation of a pentamer from a tetramer (reaction 5), this is not the case with the new potential, which shows the same trend as DFT.

Considering now the formation of ring structures from condensation of chains (equation 5.4), the results are plotted in figure 5.4 (c). The energies of all of these reactions are less energetically favourable than the formation of chains, both from DFT and the potentials. It should be noted that this is the zero kelvin electronic energy, and DFT calculations show that, when free energy is calculated at synthesis

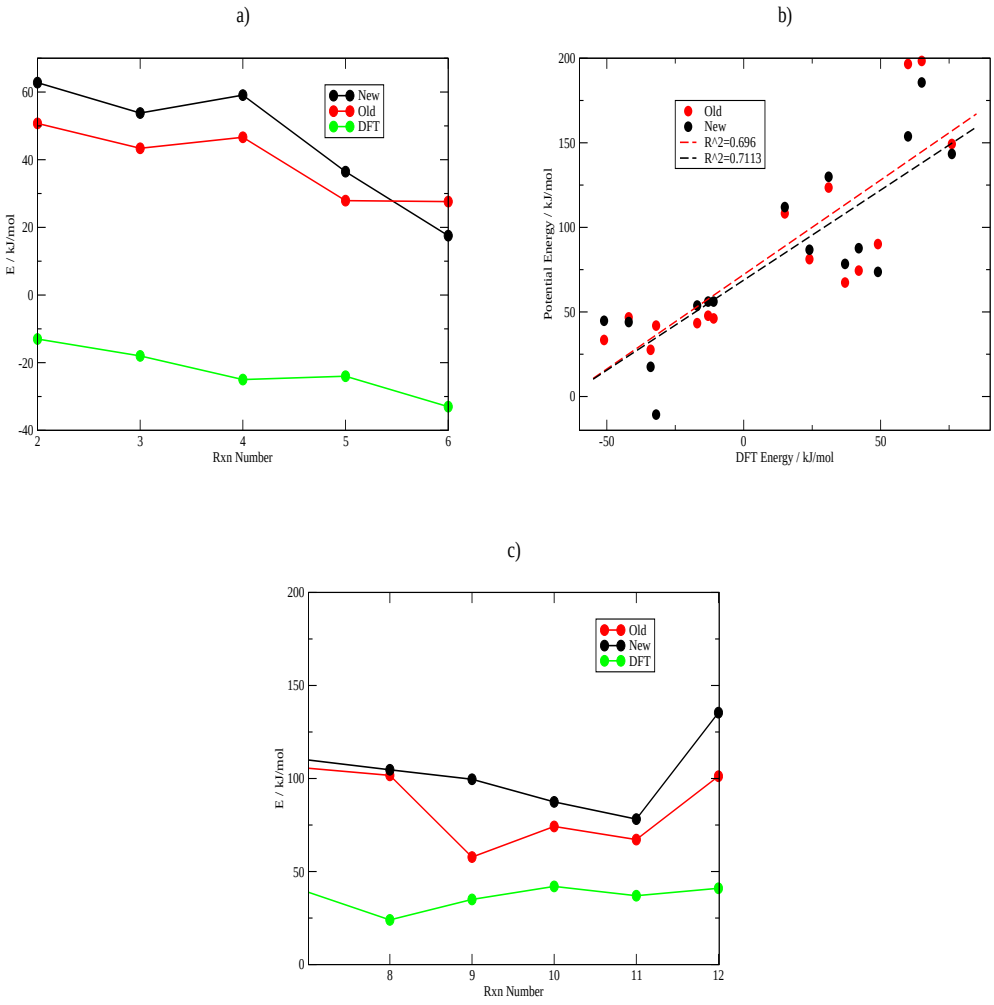

Figure 5.4: Comparison of DFT versus Potential calculated energies for the reactions in figure 5.1. a) Chain forming reactions. b) Overall trends in reactions. c) Ring forming reactions.

temperatures with the inclusion of solvent effects, the formation of rings is generally preferred [9]. Thus this finding does not necessarily contradict experimental data showing silicate solutions to contain many ring type structures, and no chains longer than the pentamer [257]. Both potentials show that the formation of a four ring from a tetramer (reaction 8) is favourable to the formation of a three ring with a dangling monomer from a tetramer (reaction 9), which is the opposite of the DFT result, and is somewhat to be expected given the fact that potentials are know to have issues when dealing with silicate three rings[258] . The new potential however does not have such a pronounced discrepancy between reactions 8 and 9 as the original one. Both potentials predict that the formation of a five ring from a pentamer (reaction 11) is favourable compared to the formation of a four ring with a dangling monomer from a pentamer (reaction 10), as found by DFT. Both potentials also concur with DFT that the formation of a six ring from a hexamer (reaction 12) is more demanding than reaction 11. The older potential, however, predicts that reaction 12 is less demanding than the formation of a three ring from trimer (reaction 7), which is the opposite of what is predicted by both the new potential and DFT calculations.

The overall correlation between the potentials and DFT is plotted in figure 5.4 b), which also has the R^2 value from a linear regression, and shows the new potential to give a marginally better fit to this data than the old one.

We have limited ourselves to this point to considering only reactions at zero Kelvin to demonstrate the improvements of the modified potential over the older one. However, for the potential to be of practical use we would wish to simulate clusters in environments which resemble the real solution. Thus, to test the applicability of the potential to real systems, reaction energies in full solvation are now considered.

The reactions considered are the dimerization of various charge states of the monomer, and also the deprotonation of the monomer and dimer. These results will demonstrate the ability of the potential to give meaningful results beyond the neutral charge data set which it was fitted to. The compositions and lattice vectors of the systems used for these simulations are presented in table 5.4, and the energies are presented in figure 5.5. The energies of the species in solution for this section were calculated as in equation 5.3.

It should be noted that the results presented for the potential are the difference in energy between the reactants and the products, whilst the DFT energies, taken from literature [9] are enthalpy changes involved. The results for dimerizations calculated using the potential are considerably more endothermic than the DFT results, which may be partially due to the neglect of translational, vibrational and rotational energies in the potential calculations. There is also the possibility that solvent reorganization, which is not considered in the DFT calculations which employ an implicit solvent model, may contribute to the change in energy. However, aside from the somewhat different scale in the energies, the potential model manages

Solute	Water	Cell Length/Å
$Si(OH)_4$	338	20.14132
$SiO(OH)_3^-$	339	20.16484
$SiO_2(OH)_2^{2-}$	339	20.14725
$Si_2O(OH)_6$	331	19.97590
$Si_2O_2(OH)_5^-$	331	19.97549
$Si_2O_3(OH)_4^{2-}$	334	19.99166
OH^-	255	18.31911
H_2O	256	18.18796

Table 5.4: Cell compositions and length of the cubic cell vector for the calculation of the energies of dimerization and deprotonation.

Deprotonations	
1	$Si(OH)_4 + OH^- \rightleftharpoons SiO(OH)_3^- + H_2O$
2	$SiO(OH)_3^- + OH^- \rightleftharpoons SiO_2(OH)_2^{2-} + H_2O$
3	$Si_2O(OH)_6 + OH^- \rightleftharpoons SiO_2(OH)_5^- + H_2O$
4	$SiO_2(OH)_5^- + OH^- \rightleftharpoons SiO_3(OH)_5^{2-} + H_2O$
Dimerizations	
1	$Si(OH)_4 + Si(OH)_4 \rightleftharpoons Si_2O(OH)_6 + H_2O$
2	$Si(OH)_4 + SiO(OH)_3^- \rightleftharpoons SiO_2(OH)_5^- + H_2O$
3	$SiO(OH)_3^- + SiO(OH)_3^- \rightleftharpoons SiO_3(OH)_5^{2-} + H_2O$
4	$Si(OH)_4 + SiO_2(OH)_2^{2-} \rightleftharpoons SiO_3(OH)_5^{2-} + H_2O$

Table 5.5: The deprotonation and dimerization reactions as in figure 5.5

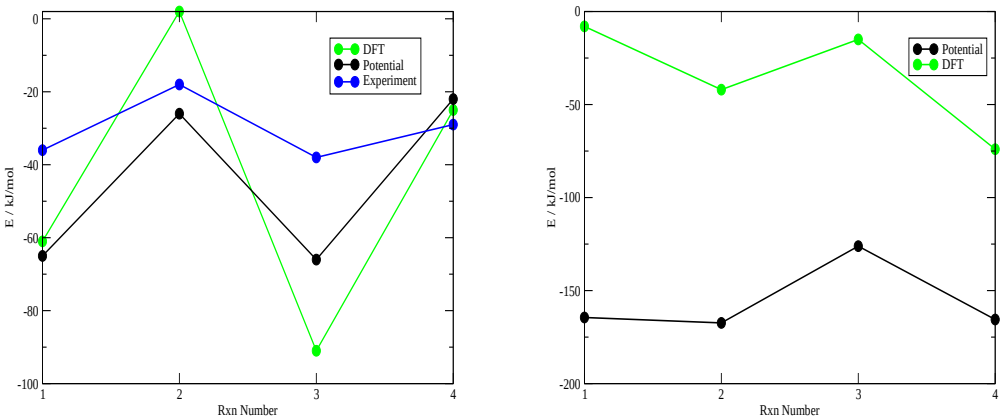

Figure 5.5: The calculated energy changes using the modified potential, and enthalpy changes previously calculated using DFT for deprotonation (left) and dimerization (right) reactions. The reactions are numbered as in table 5.5.

to recreate well the trends determined by DFT for the different dimerizations. We particularly note that the reactions between two charged monomers to form a double charged dimer (rxn. 3) and two neutral monomers to form a neutral dimer (rxn. 1) are less favourable than the reactions between a charged and neutral monomer to form a charged dimer as in the DFT calculations.

The reliability of the potential is further demonstrated by considering the deprotonation energies for which comparisons to experimental results[259] are possible, as well as to DFT values. Both the potential model and DFT manage to recreate the experimentally measured trends, which were calculated from pKa values. The potential model performs particularly well in this regard, with all values being within 30 kJ mol^{-1} of the experimental values. The fact that the potential in this case actually gives a better representation of the energy change in the system than the DFT model may be an indication of the importance of energy released when water restructures around the charged molecule (a factor not considered in the DFT calculations), which is supported by the ability of DFT calculations where mixed implicit/explicit clusters, in which hydration waters of the silicate monomer and counter cations are included in the simulation,to give free energy changes to within "chemical accuracy". Obviously such high-level cluster calculations are possible but computationally demanding and scale in such a way that the time taken to perform such a calculation quickly becomes prohibitive as larger silicate oligomer are considered. Thus it is obviously useful to have a potential model which gives reasonably good quantitative agreement, whilst allowing access to larger systems and simulations of dynamic as well as static properties of the systems.

Having demonstrated this quantitative reliability of the modified version of the potential results of such larger simulations will now be presented. This modified potential can now also be used for simulation of large silicate clusters such as those proposed by Kirschhock *et al.* [178], and for the investigation of systems at the on-set of nucleation. In addition it may prove useful for simulating the interactions of silicate clusters with zeolite crystal surfaces, and other such systems involved in crystal growth.

In the next section we consider the deprotonation of the prismic hexamer and cubic octamer (species VIa and VIIIc in figure 5.1) as well as the effect which thwy have on surrounding water. These two species in particular were chosen as the effect of ordered water in their hydration layer has been proposed as a key factor affecting the adsorption of tetrametyl ammonium (TMA) to their surfaces [222, 223, 224], which in turn was used to explain the experimental observation that these species are predominant in pre-nucleation solutions containing TMA [6, 7].

5.3.2 Deprotonation of Prismic Hexamer and Cubic Octamer

In this section the deprotonation of the prismic hexamer (PHex) and cubic octamer (COct) (species 6a and 8d in figure 5.1) shall be considered. It is important to have some idea of the charge state of these species in the pre-nucleation solutions which we intend to model since, as we shall show in the next section, the charge state of these species is extremely important in determining how they structure surrounding water. Generally these species have been considered in either fully protonated [51] or fully deprotonated [165] states, although experimental studies of the charge state have been made [260] there are few such studies and the data not conclusive. The experimental difficulties associated with such measurements makes modelling a valuable tool for such investigations, but the relatively large size of these oligomers and the previously mentioned importance of environmental water restructuring make high-level simulations difficult or even intractable. Thus the modified potential from the previous section provides a useful method for these calculations.

In order to calculate energies of deprotonation of these species, the various charge states have been modelled immersed in boxes of water, with compositions and lattice vectors provided in table 5.6. Again, energies of the solvated species were calculated as in equation 5.3 and the results are presented in figure 5.6. The first deprotonation of the PHex is energetically favourable, however the second deprotonation, which was chosen to be on the silanol furthest from the original deprotonation, is unfavourable relative to both the minus one and neutral species. The third deprotonation is again unfavourable relative to the second. After this however the deprotonations become more favourable, the $PHex^{4-}$ species is some 250 kJ mol^{-1} more favourable than $PHex^{0}$, whilst $PHex^{5-}$ is less favourable than this, $PHex^{6-}$ is the most favourable of all. Similarly, the COct favours more deprotonated states. Although, as mentioned previously, unambiguous determination of the charge states of silicate species in these solutions is difficult, what work has been done [260] suggests that the PHex would be in a charge state of minus six, and that the COct would be in a charge state of between minus six and minus eight. Our calculations concur with these findings.

5.3.3 Hydration of the Cubic Octamer

The structure of water molecules in the vicinity of the COct both fully protonated and fully deprotonated are now considered. Two dimensional structure from radial distribution functions (RDFs) and three dimensional plots of the density of water oxygens are used to investigate how the water arranges itself in the presence of these species.

Solute	Water	Cell Length/Å	Solute	Water	Cell Length/Å
Octamer	314	19.76822	Octamer -8	321	19.90928
Octamer -1	314	19.73252	Hexamer	328	20.08742
Octamer -2	315	19.84782	Hexamer -1	327	20.08970
Octamer -3	317	19.86105	Hexamer -2	328	20.21669
Octamer -4	320	19.96864	Hexamer -3	329	20.03307
Octamer -5	319	19.88870	Hexamer -4	327	20.11868
Octamer -6	320	19.91577	Hexamer -5	327	20.11868
Octamer -7	321	19.87548	Hexamer -6	327	20.11868

Table 5.6: The molecular composition and cell lengths for the simulation of deprotonation of the prismic hexamer and cubic ocatemer.

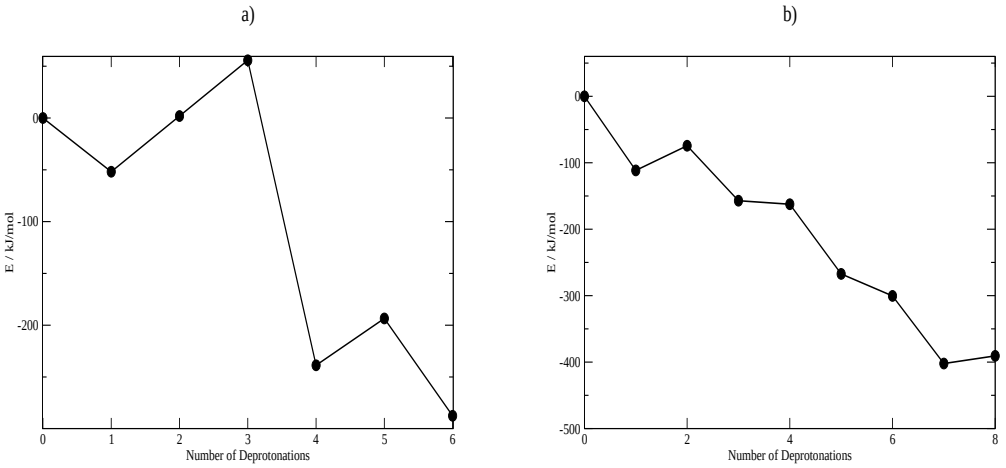

Figure 5.6: The calculated energy changes using the modified potential of progressive deprotonations of the prosmic hexamer (a), and cubic octamer (b).

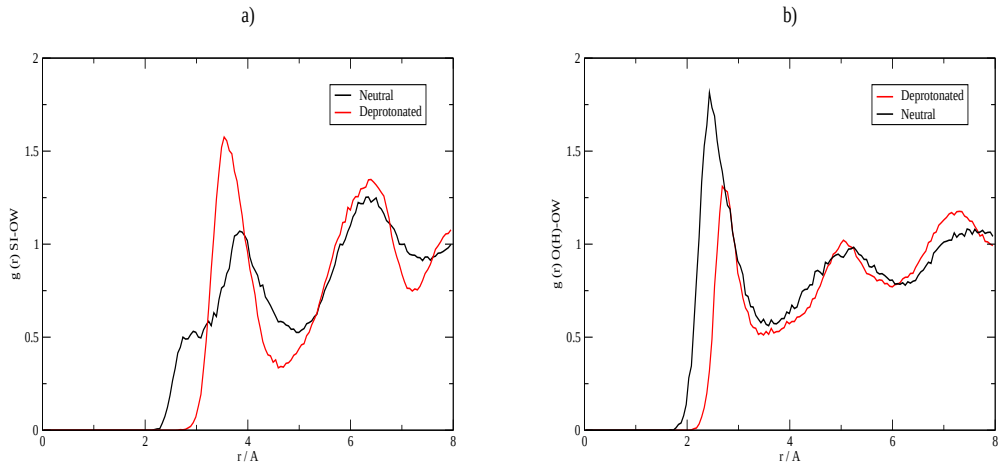

Figure 5.7: The radial distribution functions for the cubic ocatamer and water. a) Silicon to water oxygen RDF. b) Silanol to water oxygen RDF (neutral), and silicate oxygen to water oxygen RDF (deprotonated).

	q	M_1/ Å	M_2/Å	$N(r)$	R	T_R/fs	M_1/Å	M_2/Å	$N(r)$	T_R/fs
Octamer	0	2.25	4.97	12.89	2.02	12.93	4.97	7.47	48.57	11.18
Octamer	-8	2.81	4.66	11.76	2.96	20.98	4.66	7.23	53.43	17.15

Table 5.7: Information about the hydration layers of the cubic octamer. The start and finish of the peaks;M_n, the number of waters within the hydration layer; $N(r)$, the maximum to minimum ratio of the first peak; R and the residence time of a water molecule in the hydration layer T_R.

RDFs from the simulations of neutral and deprotonated octamers are presented in figure 5.7. The silicon to water oxygen RDF reveals different patterns between the two charge states. The RDF of the neutral octamer has a shoulder before the first peak, with a coordination number (obtained as in equation 4.4) of 1.08. Further examination reveals this to be water molecule which is acting as a hydrogen bond acceptor from the silanol group. Such a water will obviously not be present near the deprotonated silanol.

The degree to which the water is ordered in the first peak has been estimated by the ratio between the peak maximum and non-zero minimum (table 5.7) and shows that the peak of the RDF for $COct^{8-}$ is sharper than that of $COct^0$, indicating greater order in the vicinity of the charged species. The silanol to water oxygen RDF (figure 5.7 b)),for $COct^{8-}$ is smaller in amplitude than $COct^0$. However, this is primarily due to the fact that the bridging oxygens of the silicate framework are also included along with the silanol oxygens. The peak of the RDF from $COct^{8-}$ is shifted to a greater distance than that of $COct^0$, closer to the "ideal" hydrogen bond length which corresponds to an oxygen-oxygen separation of 2.7 Å. The coordination number at both peaks is very close to one, indicating that in both cases a hydrogen bond network is present between the silicate and the surrounding water.

Additional information regarding the hydration layers is presented in table 5.7, which includes the number of water molecules found on average in the first and second layers, as well as the average residence time of a water molecule in these hydration layers. This shows that the first hydration layer of $COct^0$ contains, on average, around one more water molecule than that of $COct^{8-}$, but that the deprotonated octamer hydration layer is more stable than that of the neutral octamer, with an average residence time more than 8 fs longer. The second hydration layer of the charged octamer contains around five more waters than the neutral species, and again the charged species hydration is more stable with a residence time also around 8 fs longer.

The study of the RDFs and associated properties gives some indication of the different nature of the hydration layers depending on the charge of the silicate solute. They show that the deprotonated species has a less populated, but more ordered and stable first hydration layer than the neutral species. Moreover the second hydration layer is more populated and stable for the deprotonated species. In order to gain further qualitative insights in to the hydration layer structure the density

of water oxygens during the course of the simulation, relative to a fixed position of the octamer were determined. Figure 5.8 shows the hydration layers surround the octamers. From these plots it is clear, as suggested by the RDFs, that the hydration layer structure is dependent on the charge state of the octamer. The charged octamer has three distinct hydration layers - although the third layer is somewhat less pronounced than the first two - whilst only two hydration layers appear around the neutral species. This is likely due to the longer range of the electrostatic effects of the deprotonated silanols on the water molecules. The shape of the hydration layers also seems to depend on the charge. Whilst the neutral species has an almost completely cubic structuring effect, the charged species has layers which show distinct indentations at the faces of the octamer, and does not have the 90° "corners" of the neutral species. Figure 5.9 shows plots of higher isodensity of the oxygen, revealing how in the first hydration layer the water orients differently according to the charge of the silanols. With neutral silanols there are four density spots per face of the octamer, while for the charged silanols there is one spot of density in the centre of the face, corresponding to the indentations visible in the lower isodensity plot.

The results presented above have interesting consequences when one considers possible entropic driving forces for the aggregation of clusters to form zeolite crystals. If such a driving force exists, with entropy being increased by the clusters coming together and releasing ordered hydrating water into the bulk solvent, then the effect when two COcts join could be expected to have a long range, up to 20 Å for the $COct^{8-}$ species.

In addition the differences depending on charge state have important consequences for the adsorption of organic cations onto the face of the COct. That TMA^+ adsorbs onto the faces of the COct and stabilizes it by forming a scaffolding has been postulated by a number of researchers [6, 7, 222, 223, 224]. Some elegant modelling performed by the group of Vlachos *et al.* [223] demonstrated how a layer of six TMA^+ molecules would bind to the outside of the octamer. In addition they performed potential of mean force (PMF) simulations to calculate the free energy and entropy of such adsorption. We can now consider the PMF profiles, determined by Vlachos *et al.*,in terms of the hydration layer densities which are plotted here. The TMA^+ was shown to displace the water at the centre of the face whilst leaving the silanol water network intact [223], a situation which would, presumably, be somewhat different if the octamer were neutral. The PMFs also show that the entropy of adsorption is unfavourable, with an entropy increase begining at separation of around 11 Å between the TMA^+ and the COct [223]. Considering now the silicon to water oxygen RDF (figure 5.7 a). The first peak starts at 2.8 Å for the deprotonated species. The average length of a side of the octamer is found to be 3.14 Å, from the silicon to silicon RDF, and thus the distance from the centre of the octamer to the inner edge of the first hydration layer is 2.8 + 1/2(3.14) = 4.37 Å. Similarly,

the distance to the outer edge of this hydration layer is calculated to be 6.23 Å. In another paper Vlachos *et al.* calculate a TMA hydration layer between 2.4 and 4.1 Å [222] from the methyl carbon, which, given the carbon to nitrogen distance in TMA^+ of 1.52 Å, corresponds to a nitrogen hydration layer between 3.92 and 5.62 Å from the central nitrogen. With these values we can compare overlapping hydration layers with entropy changes calculated from the PMF, a schematic of the process is presented in figure 5.10. The hydration layers of TMA^+ and the COct would first overlap at 11.8 Å separation; slightly higher, but quite close to the 11.4 Å at which the entropy of adsorption begins to increase. The entropy reaches a maximum at 10 Å which corresponds to the outside of the octamer hydration layer being located 3.9 Å from the TMA^+, and the outside of the TMA^+ hydration layer being 4.4 Å from the octamer. Thus the outer edges of each hydration layer are at the inner edge of the other, corresponding to maximum overlap between the two layers. In this scenario the water at the face of the TMA^+ octamer, which we see in the density plot, would be incorporated into the hydration layer of the TMA^+, thus reducing the orientational freedom of other waters in this layer. Such a loss of orientational freedom has been postulated as the reason for this increase in entropy [223]. A minimum in the entropy of adsorption then occurs at 8.5 Å, which corresponds to the inner edge of each hydration layer being concurrent. At this stage the water at the octamer face has probably been displaced, as has part of the TMA hydration layer, but the TMA hydration layer has not yet fully overlapped with the areas of water density around the silanols, so the degree of ordering of the water is decreased.

5.3.4 Prismic Hexamer Hydration

The patterns observed in the silicon to water oxygen RDF (figure 5.11 a) for the PHexs upon deprotonation are similar to those discussed in the preceding section. Again, there is a shoulder at the leading edge of the first peak due to water hydrogen bonding to the silanol, in a manner not present, nor possible, for the deprotonated species. The first peak of the silicon to water oxygen RDF also shows a more ordered structure around the charged species, the ratio increase in this instance being even more pronounced than for the COct: 1.91 to 3.41. Analysis of the number of water molecules present and stability of the hydration layers is also presented in table 5.8, again showing that there is approximately one less water in the hydration layer of the charged species compared to the neutral molecule, but that the first hydration layer of the charged species is more stable with a residence time of almost 1 fs longer. The second hydration layer of both species contains almost the same number of waters on average, with the charged species layer being longer lived, this time by 0.87 fs.

The silanol to water oxygen RDF (figure 5.11 (b)) again shows largely similar behaviour to the COct RDFs, with the charged hexamer RDF having a first peak

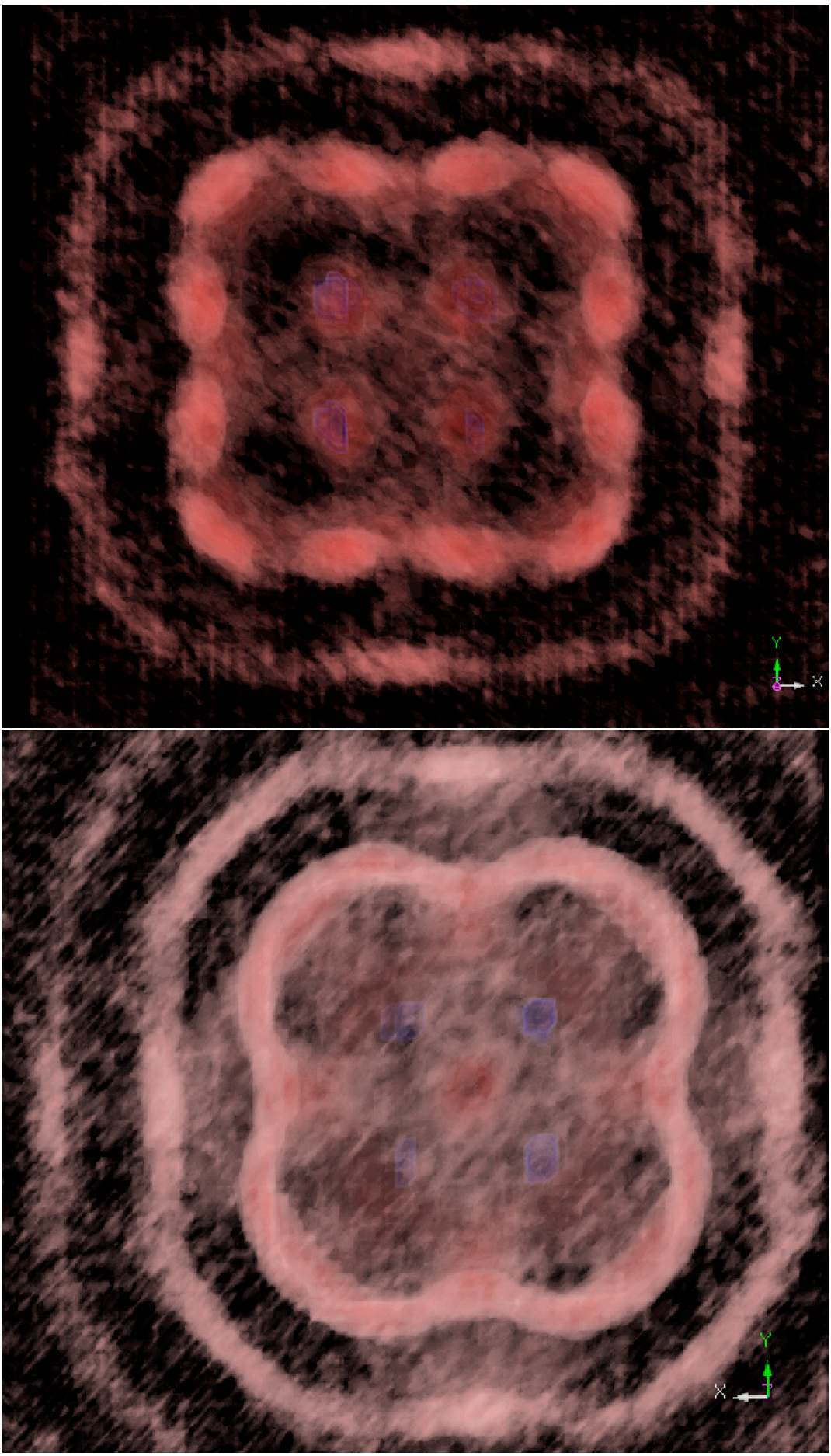

Figure 5.8: Density plots of water oxygens around the cubic octamer, red represents oxygen density, blue represents silicon density. Upper panel neutral species, lower panel deprotonated species.

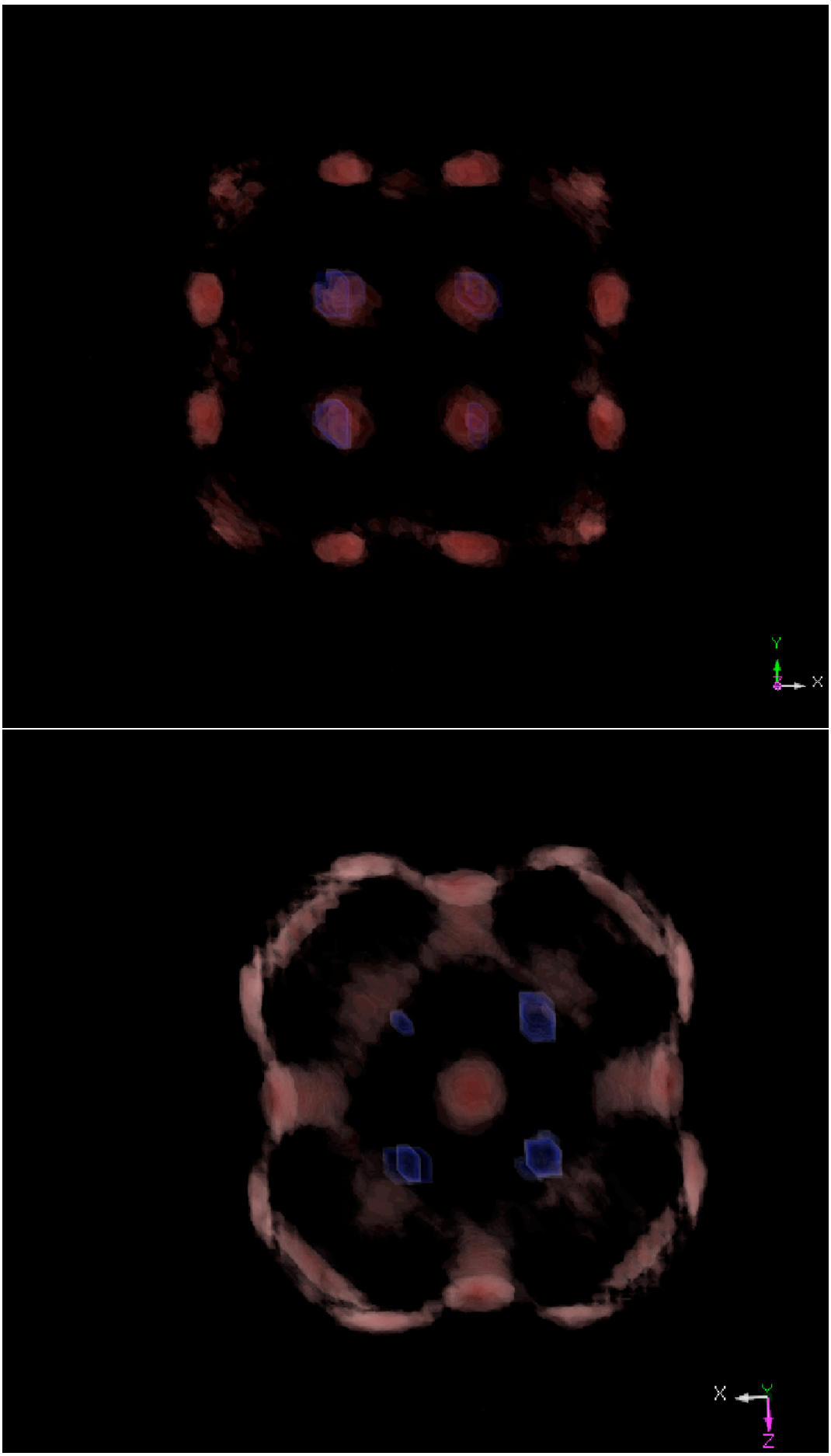

Figure 5.9: Density plots of water oxygens around the cubic octamer, red represents oxygen density, blue represents silicon density. Upper panel neutral species, lower panel deprotonated species.

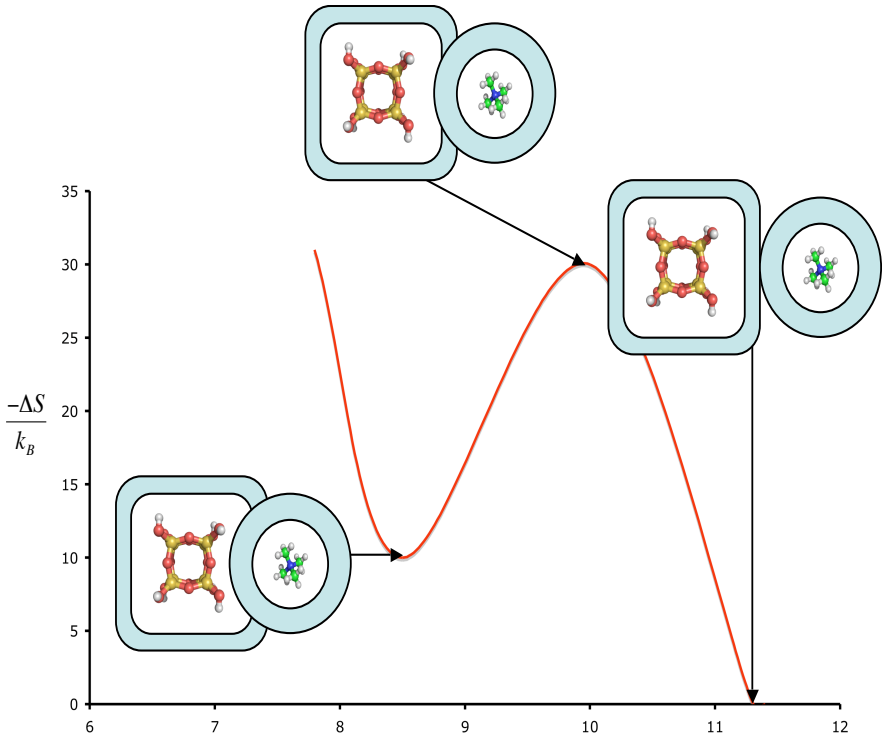

Figure 5.10: Schematic representation of the correspondence between hydration layer positions and entropy of adsorption of TMA^+ to the cubic octamer.

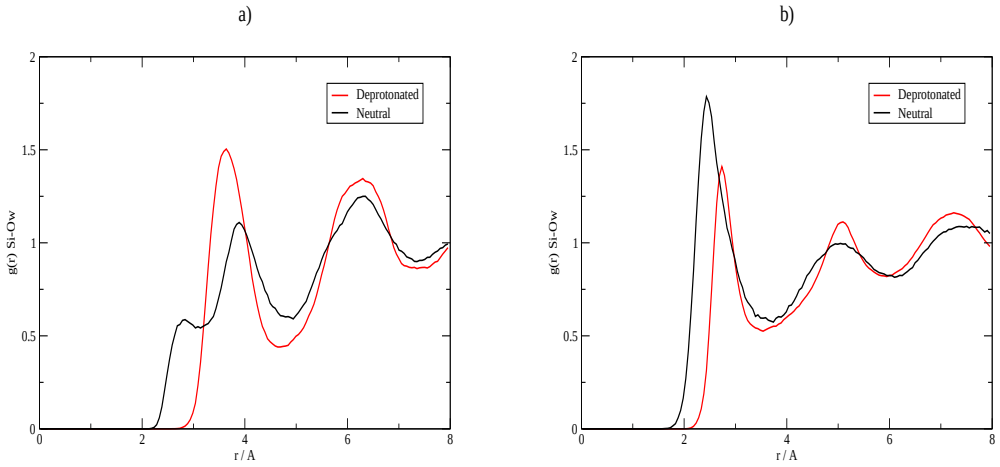

Figure 5.11: The radial distribution functions for the prismic hexamer and water. a) Silicon to water oxygen RDF. b) Silanol to water oxygen RDF (neutral), and silicate oxygen to water oxygen RDF (deprotonated).

	q	M_1/Å	M_2/Å	$N(r)$	R	T_R/fs	M_1/Å	M_2/Å	$N(r)$	T_R/fs
D3R	0	2.39	4.92	13.83	1.91	12.08	4.92	7.45	47.45	10.24
D3R	-6	2.41	4.95	12.78	3.41	12.93	4.95	7.47	47.37	11.17

Table 5.8: Information about the hydration layers of the prismic hexamer. The start and finish of the peaks;M_n, the number of waters within the hydration layer; $N(r)$, the maximum to minimum ratio of the first peak; R and the residence time of a water molecule in the hydration layer T_R.

closer to the "ideal" hydrogen bond oxygen-oxygen distance of 2.7 Å than the neutral hexamer. The coordination numbers at the maximum of this peak are slightly higher in the hexamer than in the octamer, and higher in the neutral species than the charged species: around 1.34 and 1.20. Again indicating that both species maintain a network with the surrounding water via hydrogen bonds.

Figure 5.12 plots the water oxygen density surrounding the neutral PHex. Once again a second hydration layer is clearly visible, however, compared to the COct, the region between the hydration layers has more density within it, suggesting perhaps that the ordering effect of the PHex is not as strong as that of the COct. There is also some suggestion, from these images, that the density is more well-defined parallel to the four-ring face, when viewed along the three-ring axis. There is also evidence of a weak third hydration layer parallel to the four-ring face. The same density plot but only showing regions of higher oxygen isodensity is shown in figure 5.13. When viewed along the four ring face the regions of density are located similarly to those of the first hydration layer of the COct, with four spots of density on the face of the four-ring. However viewing along the three-ring face reveals only a shell of density around the outside of the face, with very little density on the face itself. The effects of deprotonation of the PHex on the first hydration layer are shown in figure 5.14. Viewing along the four-ring axis it can be seen, again as for the deprotonated COct, that there is an area of oxygen density at the centre of the face, and the four areas of density in the neutral species are lost. The view along the three-ring axis shows that, as for the fully protonated species, there is little oxygen density on this face.

The contrast of the density on the three-ring face with the four-ring face may explain simulation results of the entropy of adsorption of TMA^+ to this face [223]. These results showed that the entropy profile for adsorption to the three-ring face of the PHex follows much the same profile as the adsorption to the COct, but with one important difference: the adsorption to the PHex is overall entropically favourable. In their paper Valchos *et al.* showed how the entropy increase upon adsorption of TMA^+ at the COct was due to a loss of orientational freedom of the hydration water, as the water on the COct face was incorporated into the TMA^+ hydration layer. The density plots presented here show that there is little water density sitting on the three-ring face. This means that adsorption at the three-ring face of the PHex of TMA^+ would not result in the loss of orientational freedom upon adsorption to the COct, explaining why there is a net entropy gain from the adsorption of TMA^+

to the PHex.

The PMFs of adsorption of TMA^+ to the PHex [223] also show a maximum in entropy at a greater distance than from the COct by 0.4 Å. The RDFs of the hexamer hydration layer, presented here in figure 5.11, show that the outer edge of this hydration layer is some 0.2 Å further out than the octamer hydration layer. Thus maximum overlap of hydration layers, which was invoked to explain the entropy peak in the octamer adsorption occurs at a larger separation, as revealed in the PMF.

5.4 Conclusions

An established silica potential [254], which was derived for the simulation of bulk silica, has been modified to better simulate silicate cluster species. The re-parameterization was achieved by comparison to the energies and geometries of a training set of 33 oligomer species. These are species which have been identified as existing in pre-nuclearion zeolite solutions [5, 8, 44] and for which we have calculated geometries and energies from chapter 3. A number of terms in the potential were modified: the Buckingham potential parameter which accounts for polarization (α in eqn. 2.45) has been changed for the interactions between silicon and bridging oxygens, hydroxyls and bridging oxygens and bridging oxygen to bridging oxygen; in addition the three body term has been modified by relaxing the spring constant for all three body terms. These modifications were made in order to reduce the energetic penalties incurred by species containing three rings. The modified potential overall reduced the average difference and standard deviation of differences between the energy calculated from DFT and the energy calculated using the potentials.

To further test the modified potential comparisons were made to reaction energies for a number of common silicate reactions, namely chain growth and cyclization. In both of these cases, the modified potential was shown to reproduce the trends of DFT calculations more faithfully than the older potential. In simulations which were carried out with full solvation, the new potential was also shown to match well with both DFT and experimental values for the deprotonation of the silicic acid monomer and dimer species. Finally dimerization reactions were considered as a test case. In this instance the potential also recreates the trends for relative dimerization energies determined by DFT for different charge states. It should be stated that in the test cases which were performed on species not in the original training set the older potential also performs remarkably well, but that the modified potential shows some minor improvements in recreating the trends determined by DFT methods.

This modified potential was then applied to modelling the effects of silicate clusters on the structure of hydration water. It has been shown previously that water is structured at the surface of crystal zeolites [221], however these simulations show

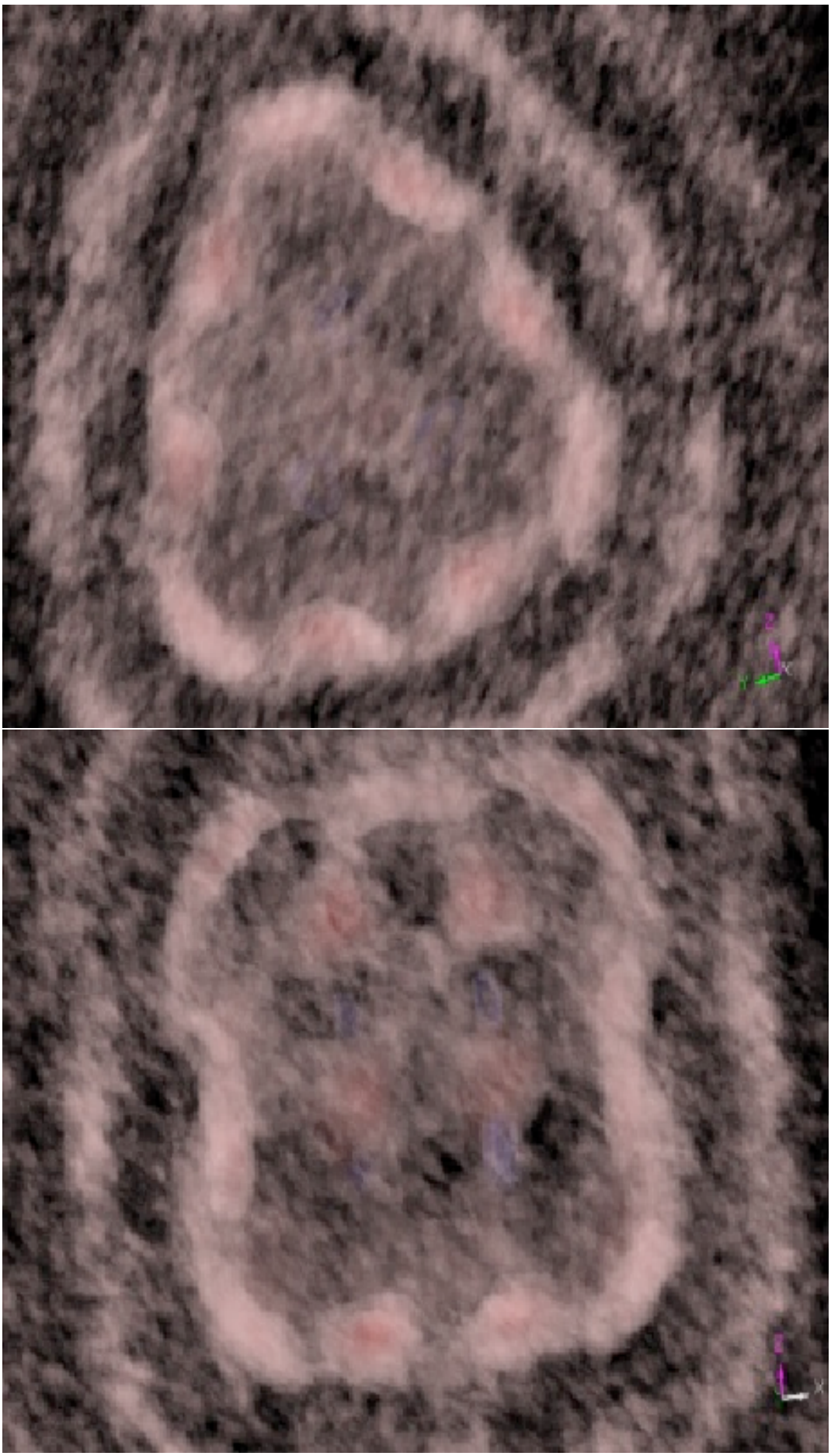

Figure 5.12: The water density surrounding the prismic hexamer in fully protonated state. Upper panel; viewed along the three ring axis, lower panel; viewed along the four ring axis. Red represents oxygen density, blue represents silicon density.

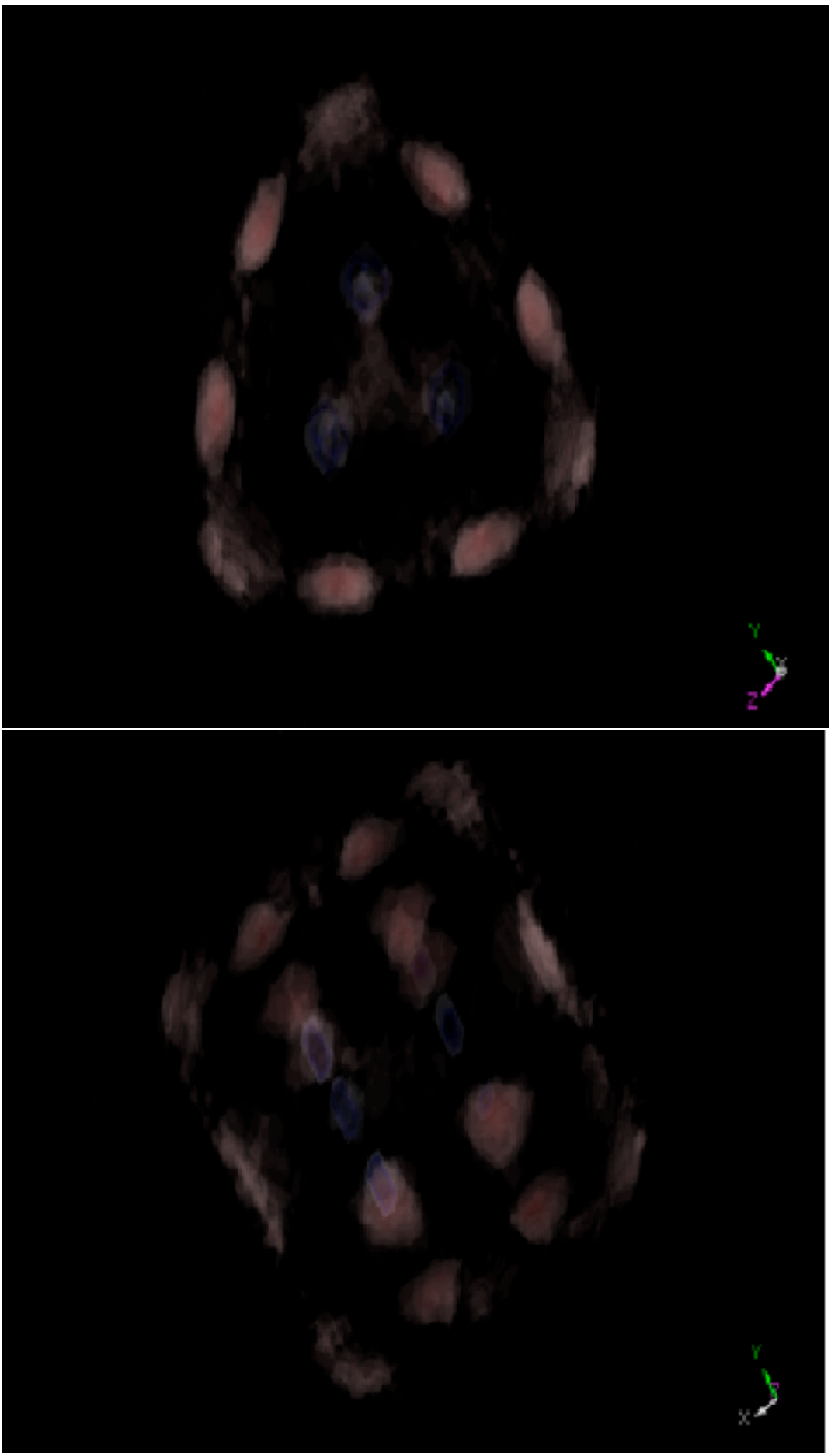

Figure 5.13: The first hydration layer water density surrounding the prismic hexamer in fully protonated state. Upper panel; viewed along the three ring axis, lower panel; viewed along the four ring axis. Red represents oxygen density, blue represents silicon density.

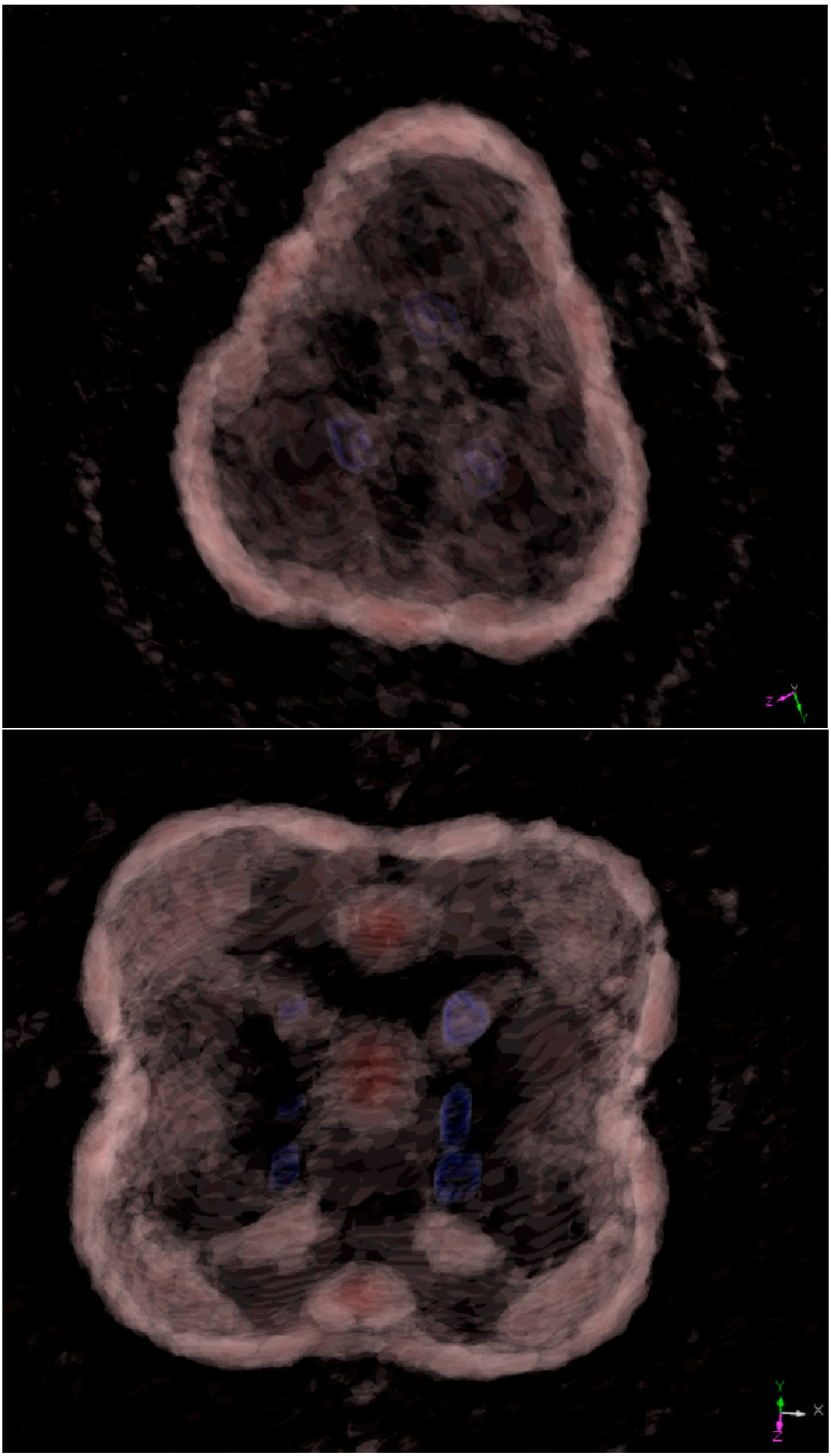

Figure 5.14: The first hydration layer water density surrounding the prismic hexamer in fully deprotonated state. Upper panel; viewed along the three ring axis, lower panel; viewed along the four ring axis. Red represents oxygen density, blue represents silicon density.

for the first time how smaller silicate species also have a significant effect on the surrounding water. The cubic octamer and prismic hexamer species were shown to have between two and three distinct hydration layers. Furthermore it was demonstrated how the structure of these hydration layers is dependent upon the charge state of the solvated species. Finally the presence and position of the hydration layers was matched to previous PMF calculations of the entropy of adsorption of TMA^+ to these species [223], demonstrating how hydration layer overlap affects the entropy of association of these species.

CHAPTER 6

Conclusions

The express purpose of this thesis was to further the understanding of the early stages of zeolite synthesis by both aiding experimental investigations of pre-nucleation solutions and probing factors which are beyond the reach of current experimental techniques. In order to achieve this a number of modelling techniques have been employed throughout; ranging from cluster modelling using hybrid DFT methods to molecular mechanics using inter-atomic potentials. Due to the complex nature of the processes of the early stages of crystal growth a number of different factors have been explored individually, however all are of relevance in understanding some of the fundamental factors which are involved in these important systems. The results cover the nature and distribution of the silicate species present, the role of structure directing agents (SDAs) prior to nucleation and the effects of silicate species on the surrounding medium. Amongst the results from this investigation, the most important are now summarized.

- A methodology employing an implicit solvation models can produce, at relatively little computational expense, calculated ^{29}Si NMR chemical shift results which are comparable to more expensive calculations involving super-molecule clusters.

- In the absence of conclusive evidence regarding the charge state of silicate species, the use of fully protonated models represents a reasonable standard. This result is important for further modelling of NMR chemical shifts, as previous studies have tended to use either fully protonated, or fully deprotonated models on an *ad hoc* basis. The result does not in any way undermine previous results, as both models were found to give similar results, regardless of the nature of silicon centre. It does, however, put such assumptions on a firmer footing for future use.

- Suggestions for reassignments of a number of species previously assigned. The reversal of the assignments of peaks to the *cis* and *trans* isomers of the tricyclic hexamer species was suggested, based on both energetic and calculated shift results. These assignments had been made previously on the basis of peak intensities [43], which has subsequently been used as the standard for assignment of these peaks [5, 44, 52], due to the inability of 2D-NMR alone to discriminate between isomers definitively. We also question the assignment of the prismic tetramer species [5, 44], which had a calculated chemical shift with a large discrepancy from the assigned value, this large difference is in accordance with earlier modelling studies [162], which also questioned this assignment. The methodology was also applied to the assignment of cyclic tetramers with two or more -$OSi(OH)_3$ units attached. Such a configuration leads to the existence of multiple isomers which, as noted previously, are indistinguishable using 2D-NMR alone. These series of assignments/reassignments are important in the context of improved experimental NMR techniques, which result in the observation of ever more species and also in terms of following the evolution the species using techniques such as exchange spectroscopy (EXSY), which offers the potential for following the inter-conversion of species. Clearly if information is to be gained from following the evolution of such systems it is important that signals be correctly assigned.

- The de-shielding effect of presence of a silicon centre in a single three-ring is accentuated by its presence in further three-rings. This finding has implications for the the future assignment of signals based on their position in the spectrum, we now fid that a Q^4 species environment may have a shift in the region of the spectrum previously thought to be populated exclusively by Q^3 species, provided the centre is present in multiple three-rings. Indeed, the same situation is found for Q^3 species in Q^2 regions.

- Certain species with a high degree of internal hydrogen bonding result in a calculated chemical shift which shows a large discrepancy from the experimental value. It was demonstrated through the use of MD simulations with an explicit representation of the water, that the internal hydrogen bonding is replaced by water-silicate hydrogen bonding. This result which has implications for the use of static cluster models for the investigation of the energetics of silicate species, suggesting that in such cases it is advisable to include (at least partially) an explicit representation of the solvent, to avoid spurious conformations.

The effect of SDA molecules on hydrating water were also investigated. The role which SDA molecules play in the crystal growth has been the topic of debate for more than 10 years [178, 40, 222, 223]. In this section we revisited a hypothesis proposed in the early 1990s [61], based on the exemplary iso-morphism of certain zeolite

frameworks and clathrate hydrates [60, 59]. In this hypothesis water is structured around the SDA, followed by dynamic replacement by silicates, leading to the formation of seeds for nucleation of the crystal. This hypothesis received considerable attention around the time of its conception [64, 63], however for various reasons, not least the difficulty of experimental identification of such water structures under synthesis conditions, it has been relatively neglected of late. The key findings of this section are now summarized.

- Radial distribution functions (RDFs) demonstrated how the hydration layer of tetraalkyl ammoniums (TAAs) have an increased degree of order relative to bulk water. These results also demonstrated how previous experimental findings, that tetramethyl ammonium (TMA) has little ordering effect on its hydration layer [206], could be explained by the masking effect of the inclusion of bulk water in the systems which were analyzed. By employing an analysis which considers only hydration layer waters it was shown that the RDFs were sharpened to a significantly greater degree in the pesence of TMA, compared to those analyses which considered all water in the simulation cell. It was also demonstrated, using a tilt angle analysis, that TMA, tetraethyl ammonium (TEA) and neopentane order their hydration water in different ways, a finding which is not apparent from RDF analysis alone. This finding has implications for the importance of charge and hydrophobic surface for the formation of a well defined hydration layer.

- A specifically developed program, which analyzes the hydration layers for the presence of rings in the water structure, was employed to demonstrate how different SDAs result in qualitatively different patterns in the water. In addition, the code is able to search for certain structural motifs which are representative of different crystal phases of zeolites. The occurrence of a structural motif was show to correspond to the crystal structures for which certain SDAs direct, in particular TMA and n-propylamine. Furthermore, we demonstrated how certain aspects of the SDAs are important for the formation of rings in the hydrating water. In particular the presence of a charge was shown to be important in the TAAs and the effect of amine groups ($-NH_2$) in stabilizing five-rings of water was shown. The results of these investigations provide fresh impetus to a hypothesis which has largely neglected recently. sWwhilst they by no-means demonstrate a single definitive role of SDAs in directing for a particular zeolite crystal they do demonstrate a property which is probably one of many factors involved in their undoubted role in synthesizing specific crystals.

Finally we investigated the effect of some of the silicate species identified by NMR techniques on the surrounding water. Due to the relatively large size of these systems

it was necessary to use inter-atomic potentials to model them. The important results were as follows.

- A new inter-atomic potential for modelling silicate oligomers was developed by modifying a potential derived for solid state silicates. This potential was shown to offer improved results for the energetics of some key reactions involving pre-nucleation species. It was also shown to be able to reproduce experimental values from deprotonation of the silicic acid monomer and dimer to within 30 kJ mol^{-1}, but, more importantly, to reproduce the experimental trends. Such a potential may be useful in the future for the modelling of larger pre-nucleation systems (including explicit treatments of their environments) than are accessible using *ab initio* methods.

- The cubic octamer (CO) and prismic hexamer (PH) species were shown to energetically favour highly deprotonated states, in accordance with the (admittedly limited) experimental data [260].

- The structuring effects of the CO and PH on surrounding water were demonstrated by analyzing the water density from MD simulations. These analyses show how both species have at least two distinct hydration layers, which are affected by the charge state of the species. This result is important as it demonstrates the possibility of an entropic driving force for the aggregation of silicate species, via the release of hydration layer water into the bulk solution.

6.1 Future Work

Having established a reliable protocol for the calculation of NMR chemical shifts (as well as its limits) further investigation of possible silicate oligomers would provide reference values for future experimental studies. In addition, this thesis deals only with pure silicate oligomers, as alumino-silicates are of equal importance a similar study of these species would provide useful information.

It would be desirable to investigate the water structuring effects of a larger group of SDAs, thus testing further the correlation between SDA water structuring and crystal structure directing effects.

Concerning the possibility of an entropic driving for for the aggregation of silicate oligomers an investigation using methods such as constrained molecular dynamics would provide further insights into this process. As with the initial section, the extension of this study to include alumino-silicates would be desirable.

Bibliography

[1] H. van Bekkum, E. M. Flanigen, P. A. Jacobs, P. A. Jansen, *Introduction to Zeolite Science and Practice*, Elsevier Publications, **2001**.

[2] R. M. Barrer, *J. Chem. Soc. Ind.* **1945**, *64*, 130–133.

[3] R. M. Barrer, *J. Chem. Soc.* **1948**, *128*, 127–133.

[4] C. S. Cundy, P. A. Cox, *Chem. Rev.* **2003**, *103*, 663.

[5] M. Haouas, F. Taulelle, *J. Phys. Chem. B* **2006**, *110*, 3007 – 3014.

[6] S. D. Kinrade, C. T. G. Knight, D. L. Pole, R. T. Syvitski, *Inorg. Chem.* **1998**, *37*, 4272–4277.

[7] S. D. Kinrade, C. T. G. Knight, D. L. Pole, R. T. Syvitski, *Inorg. Chem.* **1998**, *37*, 4278–4283.

[8] S. A. Pelster, W. Schrader, F. Schuth, *J. Am. Chem. Soc.* **2006**, *128*, 4310–4317.

[9] M. J. Mora-Fonz, C. R. A. Catlow, D. W. Lewis, *Angew. Chem. Int. Ed.* **2005**, *44*, 3082–3086.

[10] M. J. Mora-Fonz, C. R. A. Catlow, D. W. Lewis, *J. Phys. Chem. C* **2007**, *111*, 18155–18158.

[11] T. T. Trinh, A. P. J. Jansen, R. A. van Santen, *Phys. Chem. Chem. Phys.* **2009**, *11*, 5092–5099.

[12] T. T. Trinh, A. P. J.Jansen, R. A. van Santen, *J.Phys. Chem. B* **2006**, *110*, 23099–23106.

[13] A. R. Felmy, H. Cho, J. R. Rustad, M. J. Mason, *J. Sol. Chem.* **2001**, *30*, 509–525.

[14] P. P. E. A. de Moor, T. P. M. Beelen, R. A. van Santen, L. W. Beck, M. E. Davis, *J. Phys. Chem. B* **2000**, *104*, 7600–7611.

[15] C. E. A. Kirschhock, R. Ravishankar, F. Verspeurt, P. J. Grobet, P. A. Jacobs, J. A. Martens, *J.Phys. Chem. B* **1999**, *103*, 4965–4971.

[16] C. E. A. Kirshhock, R. Ravishanker, F. Versperut, P. Grobet, P. A. Jacobs, J. A. Martens, *J.Phys. Chem. B* **1999**, *103*, 4960–4964.

[17] C. E. A. Kirschhock, R. Ravishankar, L. V. Looveren, P. A. Jacobs, J. A. Martens, *J.Phys. Chem. B* **1999**, *103*, 4972–4978.

[18] C. T. G. Knight, J. Wang, S. D. Kinrade, *Phys. Chem. Chem. Phys.* **2006**, *8*, 3099–3103.

[19] R. M. Barrer, *Hydrothermal Chemistry of Zeolites*, Academic Press, **1982**.

[20] R. Ju, W. Pang, J. Yu, Q. Huo, J. Chen, *Chemistry of Zeolites and Related Porous Materials : Synthesis and Structure*, Wiley : Singapore, **2007**.

[21] D. P. Serrano, R. van Grieken, *J. Mater. Chem.* **2001**, *11*, 2391 – 2407.

[22] R. F. Lobo in *Handbook of Zeolite Science and Technology* (Eds.: S. M. Auerbach, K. A. Carrado, P. K. Dutta), Marcel Dekker, Inc., **2003**, pp. 65 – 91.

[23] M. Estermann, L. B. McCusker, C. Baerlocher, A. Merrouche, H. Kessler, *Nature* **1991**, *352*, 320–323.

[24] C. Rohrig, H. Gies, B. Marler, *Zeolites* **1994**, *14*, 498–503.

[25] B. Sulikowski, *Hetrog. Chem. Rev.* **1996**, *3*, 203–268.

[26] D. W. Breck, *Zeolite Molecular Sieves*, Wiley : New York, **1974**.

[27] E. M. Flanigen, D. W. Breck, *Crystalline Zeolites, V - Growth of Zeolite Crystals from Gels*, **1960**, 137th Meet. ACS, Div. Inorg. Chem.

[28] R. M. Barrer, J. Baynham, F. Bultitude, M. Meir, *J. Chem Soc.* **1959**, 195.

[29] S. P. Zhandov, *ACS Adv. Chem. Ser.* **1971**, *101*, 20.

[30] S. P. Zhandov, N. N. Samulevich in *Proc. 5th Intl. Conf. Zeolites* (Ed.: L. V. C. Lees), Heyden: London, **1980**, p. 75.

[31] F. Roozeboom, H. E. Robson, C. S. S., *Zeolites* **1983**, *3*, 321–328.

[32] P. K. Dutta, D. C. Shieh, *J. Phys. Chem.* **1986**, *90*, 2331–2334.

[33] P. K. Dutta, D. C. Shieh, M. Puri, *J. Phys. Chem.* **1987**, *91*, 2332–2336.

[34] P. P. E. A. de Moor, T. P. M. Beelen, B. U. Komanschek, O. Diat, R. A. van Santen, *J. Phys. Chem. B* **1997**, *101*, 11077–11086.

[35] P. P. E. A. de Moor, T. P. M. Beelen, R. A. van Santen, *Microporous Mater.* **1997**, *9*, 117–130.

[36] P. P. E. A. de Moor, T. P. M. Beelen, R. A. van Santen, *J. Phys. Chem. B* **1999**, *103*, 1639–1650.

[37] P. P. E. A. de Moor, T. P. M. Beelen, R. A. van Santen, K. Tsuji, M. E. Davis, *Chem. Mater.* **1999**, *11*, 36–43.

[38] R. I. Walton, D. O'Hare, *J. Phys Chem. Sol.* **2001**, *62*, 1469 – 1479.

[39] C. E. A. Kirshhock, R. Ravishanker, P. Grobet, P. A. Jacobs, J. A. Martens, B. J. Schoeman, P. Vanoppen, S. Storck, W. F. Maier, *J.Phys. Chem. B* **1998**, *102*, 2633–2639.

[40] C. E. A. Kirschhock, S. P. B. Kremer, P. J. Grobet, A. P. Jacobs, J. A. Martens, *J.Phys. Chem. B* **2002**, *106*, 4897 – 4900.

[41] C. T. G. Knight, S. D. Kinrade, *J.Phys. Chem. B* **2002**, *106*, 3329–3332.

[42] R. K. Harris, C. T. G. Knight, *J. Chem. Soc. Faraday Trans. 2* **1983**, *79*, 1539–1561.

[43] R. K. Harris, C. T. Knight, *J. Chem. Soc. Faraday Trans. 2* **1983**, *79*, 1525–1538.

[44] C. T. G. Knight, R. J. Balec, S. D. Kinrade, *Angew. Chem.* **2006**, *46*, 8148–8152.

[45] C. T. G. Knight, *J.Chem.Soc. Dalton Trans.* **1988**, 1457–1460.

[46] F. Taulelle, *Current Opinion in Solid State and Materials Science* **2001**, *5*, 397 – 405.

[47] J. Lu, A. Mondal, B. Moulton, M. J. Zaworotko, *Angew. Chem. Int. Ed.* **2001**, *40*, 2113–2116.

[48] S. A. Bourne, J. Lu, A. Mondal, B. Moulton, M. J. Zaworotko, *Angew. Chem. Int. Ed.* **2001**, *40*, 2111–2113.

[49] F. Taulelle, M. Pruski, J. P. Amoureux, D. Lang, A. Bailly, C. Huguenard, M. Haouas, C. Gerardin, T. Loiseau, G. Ferey, *J.Am. Chem. Soc.* **1999**, *121*, 12148–12153.

[50] P. C. M. M. Magusin, V. E. Zorin, A. Aerts, C. J. Y. Houssin, A. L. Yakovlev, C. E. A. Kirschhock, J. A. Martens, R. A. vanSanten, *J.Phys. Chem. B* **2005**, *109*, 22767–22774.

[51] V. Moravetski, J.-R. Hill, U. Eichler, A. K. Cheetham, J. Sauer, *J.Am. Chem. Soc.* **1996**, *118*, 13015–13020.

[52] H. Cho, A. R. Felmy, R. Craciun, J. P. Keenum, N. Shah, D. A. Dixon, *J.Am. Chem. Soc.* **2006**, *128*, 2324–2335.

[53] R. F. Lobo, M. Pan, I. Chan, H.-X. Li, R. C. Medrud, S. I. Zones, P. A. Crozier, M. E. Davis, *Science* **1993**, *262*, 1543–1546.

[54] B. M. Lok, T. R. Cannan, C. A. Messina, *Zeolites* **1983**, *3*, 282 – 291.

[55] R. M. Barrer, P. J. Denny, *J. Chem. Soc.* **1961**, 971.

[56] C. Baerlocher, W. M. Meier, *Helv. Chim. Acta* **1969**, *52*, 1853–1860.

[57] G. T. Kerr, *Inorg. Chem.* **1966**, *5*, 1537.

[58] G. T. Kerr, *Science* **1963**, *140*, 1412.

[59] D. Mootz, R. Seidel, *J. Incl. Phenom.* **1990**, *8*, 139–157.

[60] M. Wiebcke, J. Emmer, J. Felsche, *J. Chem. Soc. Chem. Commun.* **1993**, 1604 – 1606.

[61] C. D. Chang, A. T. Bell, *Cat. Let.* **1991**, *8*, 305–316.

[62] S. L. Burkett, M. E. Davis, *J. Phys. Chem.* **1994**, *98*, 4647–4653.

[63] S. L. Burkett, M. E. Davis, *Chem. Mater.* **1995**, *7*, 1453–1463.

[64] P. A. Cox, J. L. Casci, A. P. Stevens, *Faraday Discussions* **1994**, *106*, 473–487.

[65] C. S. Brickenkamp, D. Panke, *J.Chem. Phys.* **1973**, *58*, 5284–5295.

[66] A. Moini, K. D. Schmitt, E. W. Valyocsik, R. F. Polomski, *Zeolites* **1994**, *14*, 504 – 511.

[67] A. P. Stevens, A. Gorman, C. P. Freeman, P. A. Cox, *J. Chem. Soc. Faraday Trans.* **1996**, *92*, 2065–2073.

[68] D. W. Lewis, D. J. Willock, C. R. A. Catlow, J. M. Thomas, G. J. Hutchings, *Nature* **1996**, *382*, 604–606.

[69] D. W. Lewis, G. Sankar, J. K. Wyles, J. M. Thomas, C. R. A. Catlow, D. J. Willock, *Angew. Chemie Int. Ed.* **1997**, *36*, 2675–2677.

[70] T. Verstraelen, B. M. Szyja, D. Lesthaeghe, R. Declerck, V. Van Speybroeck, M. Waroquier, A. P. J. Jansen, A. Aerts, L. R. A. Follens, J. A. Martens, C. E. A. Kirschhock, R. A. van Santen, *Angew. Chemie Int. Ed.* **2009**, *52*, 1261–1271.

[71] S. H. Garofalini, H. Melman, *Better Ceramics Through Chemistry II*, Elsevier Science Publishing Co.: New York, **1896**.

[72] B. P. Feuston, S. H. Garofalini, *J. Phys. Chem.* **1990**, *94*, 5351–5356.

[73] B. P. Feuston, S. H. Garofalini, *Chem. Phys. Let.* **1990**, *170*, 264 – 270.

[74] G. E. Martin, S. H. Garofalini, *J. Non-Cryst. Sol.* **1994**, *171*, 68 – 79.

[75] J. C. G. Pereira, C. R. A. Catlow, G. D. Price, *J. Phys. Chem. A* **2001**, *105*, 1909–1925.

[76] J. C. G. Pereira, C. R. A. Catlow, G. D. Price, *J. Phys. Chem. A* **2002**, *106*, 130–148.

[77] *Discover 96.0*, **1996**, Molecular Simulations Inc., San Diego, USA.

[78] W. Smith, *The DL POLY Molecular Simulation Package*, CSE Department, STFC Daresbury Laboratory.

[79] A. Lasaga, G. Gibbs, *Phys. Chem. Min.* **1987**, *14*, 107–117.

[80] A. Lasaga, G. Gibbs, *Phys. Chem. Min.* **1988**, *16*, 29–41.

[81] J. R. Hill, J. Sauer, *J. Phys. Chem.* **1994**, *98*, 1238–1244.

[82] I. Papai, A. Goursot, F. Fajula, J. Weber, *J. Phys. Chem.* **1994**, *98*, 4654–4659.

[83] J. Sauer, *Chem. Rev.* **1989**, *89*, 199–255.

[84] J. G. C. Pereira, C. R. A. Catlow, G. D. Price, *Chem. Comm.* **1998**, 1387–1388.

[85] J. C. G. Pereira, C. R. A. Catlow, G. D. Price, *J. Phys. Chem. A* **1999**, *103*, 3252–3267.

[86] J. C. G. Pereira, C. R. A. Catlow, G. D. Price, *J. Phys. Chem. A* **1999**, *103*, 3268–3284.

[87] C. L. Schaffer, K. T. Thomson, *J. Phys. Chem. C* **2008**, *112*, 12653–12662.

[88] D. B. Cook, *Handbook of Computational Quantum Chemistry*, Dover Publications, **2005**.

[89] F. Jensen, *Introduction to Computational Chemistry*, Wiley : Chichester, **2007**.

[90] A. Leach, *Molecular Modelling: Principles and Applications*, Prentice Hall, **2001**.

[91] D. J. Cole, M. C. Payne, G. Csányi, S. M. Spearing, L. C. Ciacchi, *J.Chem. Phys.* **2007**, *127*, 204704.

[92] K. D. Nielson, A. C. T. van Duin, J. Oxgaard, W.-Q. Deng, W. A. Goddard, *J.Phys. Chem. A* **2005**, *109*, 493–499.

[93] P. Atkins, R. Friedman, *Molecular Quantum Mechanics 4th ed.*, Dover Publications, **1996**.

[94] A. Szabo, N. Ostlund, *Modern Quantum Chemistry: Introduction to Advanced Electronic Structure Theory 2nd ed.*, Dover Publications, **1996**.

[95] C. Møller, M. S. Plesset, *Phys. Rev.* **1934**, *46*, 618–622.

[96] A. Leach, *Molecular Modelling Principles and Applications, 2nd Ed.*, Prentice Hall: Harlow, **2001**.

[97] R. Jones, *NIC Series* **2006**, *31*, 45–70.

[98] P. Hohenberg, W. Kohn, *Phys. Rev.* **1964**, *136*, B864–B871.

[99] W. Kohn, L. J. Sham, *Phys. Rev.* **1965**, *140*, A1133–A1138.

[100] D. Langreth, J. Perdew, *Sol. State Comm.* **1975**, *17*, 1425–1429.

[101] G. Ortiz, P. Ballone, *Phys. Rev. B* **1994**, *50*, 1391–1405.

[102] A. D. Becke, *Phys. Rev. A* **1988**, *38*, 3098–3100.

[103] C. Lee, W. Yang, R. G. Parr, *Phys. Rev. B* **1988**, *37*, 785–789.

[104] J. P. Perdew, K. Burke, M. Ernzerhof, *Phys. Rev. Lett.* **1996**, *77*, 3865–3868.

[105] A. D. Becke, *J.Chem. Phys.* **1993**, *98*, 5648–5652.

[106] C. Tuma, J. Sauer., *Phys. Chem. Chem. Phys.* **2006**, *8*, 3955–3965.

[107] E. Hult, H. Rydberg, B. I. Lundqvist, D. C. Langreth, *Phys. Rev. B* **1999**, *59*, 4708–4713.

[108] U. Zimmerli, M. Parrinello, P. Koumoutsakos, *J.Chem. Phys.* **2004**, *120*, 2693–2699.

[109] V. Polo, E. Kraka, D. Cremer, *Mol. Phys.* **2002**, *100*, 1771–1790.

[110] J. P. Perdew, A. Zunger, *Phys. Rev. B* **1981**, *23*, 5048–5079.

[111] J. A. Pople, G. A. Segal, *J.Chem. Phys.* **1965**, *43*, S136–S151.

[112] J. A. Pople, D. L. Beveridge, P. A. Dobosh, *J.Chem. Phys.* **1967**, *47*, 2026–2033.

[113] R. C. Bingham, M. J. S. Dewar, D. H. Lo, *J.Am. Chem. Soc.* **1975**, *97*, 1285–1293.

[114] M. J. S. Dewar, W. Thiel, *J.Am. Chem. Soc.* **1977**, *99*, 4899–4907.

[115] B. Meyer, *NIC Series* **2006**, *31*, 71–83.

[116] G. Lippert, J. Hutter, M. Parinello, *Mol. Phys.* **1997**, *92*, 477–488.

[117] P. Ewald, *Annal Phys.* **1921**, *369*, 253 – 287.

[118] F. A. Hamprecht, A. J. Cohen, D. J. Tozer, N. C. Handy, *J. Chem. Phys.* **1998**, *109*, 6264–6271.

[119] `http://openmopac.net/manual/index.html`.

[120] A. Dick, B. Overhauser, *Phys. Rev.* **1958**, *73*, 90–103.

[121] L. Verlet, *Phys. Rev.* **1967**, *159*, 98–103.

[122] H. J. C. Berendsen, J. P. M. Postma, W. F. van Gunsteren, A. DiNola, J. R. Haak, *J. Chem. Phys.* **1984**, *81*, 3684–3690.

[123] W. G. Hoover, *Phys. Rev. A* **1985**, *31*, 1695–1697.

[124] S. Nose, *Mol. Phys.* **1984**, *52*, 255–268(14).

[125] H. C. Andersen, *J. Chem. Phys.* **1980**, *72*, 2384–2393.

[126] D. Marx, *NIC Series* **2006**, *31*, 195–244.

[127] J. VandeVondele, M. K. F. Mohamed, M. Parrinello, T. Chassaing, J. Hutter, *Comp. Phys. Comm.* **2005**, *103*, 167–169.

[128] M. Born, *Z. Physics* **1920**, *1*, 45.

[129] L. Onsager, *J. Am. Chem. Soc.* **1936**, *58*, 1486–1493.

[130] E. Cancès, B. Mennucci, J. Tomasi, *J.Chem. Phys.* **1997**, *107*, 3032–3041.

[131] S. Miertus, E. Scrocco, J. Tomasi, *Chem. Phys.* **1981**, *55*, 117–129.

[132] V. Barone, M. Cossi, J. Tomasi, *J.Chem. Phys.* **1997**, *107*, 3210–3221.

[133] J. Tomasi, M. Persico, *Chem. Rev.* **1994**, *94*, 2027–2094.

[134] K. Kitaura, K. Morokuma, *Int. J. Quant. Chem.* **1976**, *10*, 325–340.

[135] C. J. F. Bottcher, P. Bordewijk, *Theory of Electronic Polarization*, Elisvier, **1973**.

[136] F. J. Luque, M. J. Negre, M. Orozco, *J.Phys. Chem.* **1993**, *97*, 4386–4391.

[137] R. Bonaccorsi, P. Palla, J. Tomasi, *J.Am. Chem. Soc.* **1984**, *106*, 1945–1950.

[138] M. Orozco, F. J. Luque, *Chem. Phys.* **1994**, *182*, 237.

[139] C. Curutchet, A. Bidon-Chanal, I. Soteras, M. Orozco, F. J. Luque, *J.Phys. Chem. B* **2005**, *109*, 3565–3574.

[140] R. A. Pierotti, *J.Phys. Chem.* **1963**, *67*, 1840–1845.

[141] P. Claverie, *Intermolecular Interactions: from Diatomics to Biomolecules*, J.Wiley, Chichester, **1978**.

[142] I.Ando, G. Webb, *Org. Mag. Res.* **1981**, *15*, 111–130.

[143] A. D. Buckingham, T. Schaefer, W. G. Schneider, *J.Chem. Phys.* **1960**, *32*, 1227–1233.

[144] D. Chesnut, B. Rusiloski, *J.Mol. Str. : THEOCHEM* **1994**, *314*, 19–30.

[145] H. A. Gremer, *Th. Chim. Acta* **1974**, *34*, 145–155.

[146] K. V. Mikkelsen, P. Jorgensen, K. Ruud, T. Helgaker, *J.Chem. Phys.* **1997**, *106*, 1170–1180.

[147] B. Mennucci, J. Martinez, J. Tomasi, *J.Phys. Chem. A* **2001**, *105*, 7287–7296.

[148] C.-G. Zhan, J. Bentley, D. M. Chipman, *J.Chem. Phys.* **1998**, *108*, 177–192.

[149] C.-G. Zhan, D. M. Chipman, *J.Chem. Phys.* **1999**, *110*, 1611–1622.

[150] D. M. Chipman, *J.Chem. Phys.* **2000**, *112*, 5558–5565.

[151] D. M. Chipman, *J.Chem. Phys.* **1996**, *104*, 3276–3289.

[152] A. Klamt, *J.Phys. Chem.* **1996**, *100*, 3349–3353.

[153] D.Cremer, L. Olsson, F. Reichel, E. Kraka, *Isr. J. Chem* **1993**, *33*, 396.

[154] G. Klopmann, *Chem. Phys. Let.* **1967**, *1*, 200–202.

[155] `http://www.chem.wisc.edu/~nbo5/web_nbo.HTM`.

[156] A. E. Reed, L. A. Curtiss, F. Weinhold, *Chem Rev.* **1988**, *88*, 899–926.

[157] F. Weinhold, C. Landis, *Valency and Bonding: A Natural Bond Orbital Donor-Acceptor Perspective*, Cambridge University Press, **2005**.

[158] J. A. Bohmann, F. Weinhold, T. C. Farrar, *J. Chem. Phys.* **1997**, *107*, 1173–1184.

[159] A. E. Hansen, T. D. Bouman, *J. Chem. Phys.* **1985**, *82*, 5035–5047.

[160] M. Schindler, W. Kutzelnigg, *J. Am. Chem. Soc.* **1983**, *105*, 1360–1370.

[161] J. Jeneer, B. Meier, P. Bachmann, R. Ernst, *J. Chem. Phys* **1979**, *71*, 4546–4553.

[162] B. Bussemer, K. Schrder, J. Sauer, *Sol. State NMR* **1997**, *9*, 155 – 164.

[163] L. M. Bull, B. Bussemer, T. Anupold, A. Reinhold, A. Samoson, J. Sauer, A. K. Cheetham, R. Dupree, *J. Am. Chem. Soc.* **2000**, *122*, 4948–4958.

[164] S. Krishnamurty, T. Heine, A. Goursot, *J.Phys. Chem. B* **2003**, *107*, 5728–5732.

[165] J. A. Tossell, *J. Phys. Chem. C* **2007**, *111*, 3584–3590.

[166] G. Engelhardt, H. Jancke, R. Radeglia, *Zeit. Chemie* **1977**, *17*, 376–376.

[167] G. Engelhart, R. Radeglia, H. Jancke, E. T. Lippmaa, M. Maegi, *Org. Magn. Reson.* **1973**, *5*, 561–566.

[168] E. T. Lippmaa, M. A. Alla, T. J. Pehk, G. Engelhardt, *J. Am. Chem. Soc.* **1978**, *100*, 1929–1931.

[169] G. Engelhardt, R. Radeglia, *Chem. Phys. Let.* **1984**, *108*, 271–274.

[170] A. Grimmer, R. Radeglia, *Chem. Phys. Let.* **1984**, *106*, 262–265.

[171] R. Radeglia, G. Engelhardt, *Chem. Phys. Let.* **1985**, *114*, 28–30.

[172] R. Radeglia, A. R. Z. Grimmer, *Phys. Chem.(Leipzig)* **1981**, *262*, 718–720.

[173] C. Creswell, R. Harris, P. Jageland, *Chem. Comm.* **1984**, 1261.

[174] D. Hoebbel, G. Engelhardt, *Chem. Comm.* **1984**, 514.

[175] S. D. Kinrade, T. W. Swaddle, *Inorg. Chem.* **1988**, *27*, 4253–4259.

[176] S. D. Kinrade, T. W. Swaddle, *Inorg. Chem.* **1988**, *27*, 4259–4264.

[177] R. K. Harris, C. T. G. Knight, *J.Mol. Str.* **1982**, *78*, 273 – 278.

[178] C. E. A. Kirschhock, V. Buschmann, S. Kremer, R. Ravishankar, C. J. Y. Houssin, B. L. Mojet, R. A. van Santen, P. J. Grobet, P. A. Jacobs, J. A. Martens, *Angew. Chem. Int. Ed.* **2001**, *40*, 2637.

[179] C. J. Y. Houssin, C. E. A. Kirschhock, P. C. M. M. Magnusin, B. L. Mojet, P. J. Grobet, P. A. Jacobs, J. A. Martens, R. A. van Santen, *Phys. Chem. Chem. Phys.* **2003**, *5*, 3518–3524.

[180] J. A. Bohmann, F. Weinhold, T. C. Farrar, *J.Chem. Phys.* **1997**, *107*, 1173–1184.

[181] Y. Liu, H. Nekvasil, J. A. Tossell, *J. Phys. Chem. A* **2005**, *109*, 3060–3066.

[182] P. W. G. J. Wijnen, T. P. M. Beelen, J. W. de Haan, C. P. J. Rummens, L. J. M. van de Ven, R. A. van Santen, *J. Non-Cryst. Sol.* **1989**, *109*, 85–94.

[183] M. J. Frisch, G. W. Trucks, H. B. Schlegel, G. E. Scuseria, M. A. Robb, J. R. Cheeseman, J. A. Montgomery, Jr., T. Vreven, K. N. Kudin, J. C. Burant, J. M. Millam, S. S. Iyengar, J. Tomasi, V. Barone, B. Mennucci, M. Cossi, G. Scalmani, N. Rega, G. A. Petersson, H. Nakatsuji, M. Hada, M. Ehara, K. Toyota, R. Fukuda, J. Hasegawa, M. Ishida, T. Nakajima, Y. Honda, O. Kitao, H. Nakai, M. Klene, X. Li, J. E. Knox, H. P. Hratchian, J. B. Cross, V. Bakken, C. Adamo, J. Jaramillo, R. Gomperts, R. E. Stratmann, O. Yazyev, A. J. Austin, R. Cammi, C. Pomelli, J. W. Ochterski, P. Y. Ayala, K. Morokuma, G. A. Voth, P. Salvador, J. J. Dannenberg, V. G. Zakrzewski, S. Dapprich, A. D. Daniels, M. C. Strain, O. Farkas, D. K. Malick, A. D. Rabuck, K. Raghavachari, J. B. Foresman, J. V. Ortiz, Q. Cui, A. G. Baboul, S. Clifford, J. Cioslowski, B. B. Stefanov, G. Liu, A. Liashenko, P. Piskorz, I. Komaromi, R. L. Martin, D. J. Fox, T. Keith, M. A. Al-Laham, C. Y. Peng, A. Nanayakkara, M. Challacombe, P. M. W. Gill, B. Johnson, W. Chen, M. W. Wong, C. Gonzalez, J. A. Pople, *Gaussian 03, Revision C.02*, Gaussian, Inc., Wallingford, CT, 2004.

[184] M. M. Francl, W. J. Pietro, W. J. Hehre, J. S. Binkley, M. S. Gordon, D. J. DeFrees, J. A. Pople, *J.Chem. Phys.* **1982**, *77*, 3654–3665.

[185] T. H. J. Dunning, *J.Chem. Phys.* **1989**, *90*, 1007–1023.

[186] J. Pople, *Discuss. Faraday Soc* **1962**, *34*, 7–15.

[187] A. Schäfer, H. Horn, R. Ahlrichs, *J. Chem. Phys.* **1992**, *97*, 2571–2577.

[188] A. Schäfer, C. Huber, R. Ahlrichs, *J. Chem. Phys.* **1994**, *100*, 5829–5835.

[189] J. Casanovas, F. Illas, G. Pacchioni, *Chem. Phys. Let.* **2000**, *326*, 523 – 529.

[190] J. Casanovas, G. Pacchioni, F. Illas, *Mater. Sci. Eng. B* **1999**, *68*, 16 – 21.

[191] D. Sykes, J. D. Kubicki, T. C. Farrar, *J. Phys. Chem. A* **1997**, *101*, 2715–2722.

[192] D. Hoebbel, G. Garzo, G. Engelhardt, H. Jancke, P. Franke, W. Wieker, *Z. Anorg. Allg. Chem.* **1976**, *15*, 424–428.

[193] S. D. Kinrade, T. W. Swaddle, *J.Am. Chem. Soc.* **1986**, *108*, 7159–7162.

[194] Y. Marcus, *Chem. Rev.* **2009**, *109*, 1346–1370.

[195] Y. Marcus, *J.Sol. Chem.* **1996**, *25*, 455–469.

[196] A. K. Soper, *Chem. Phys.* **2000**, *258*, 121 – 137.

[197] Y. Marcus, *J.Sol. Chem.* **1992**, *21*, 1217–1230.

[198] Y. Marcus, *The Properties of Solvents*, Wiley, Chichester, **1998**.

[199] U. Bergmann, A. D. Cicco, P. Wernet, E. Principi, P. Glatzel, A. Nilsson, *J. Chem. Phys.* **2007**, *127*, 174504.

[200] P. Wernet, D. Nordlund, U. Bergmann, M. Cavalleri, M. Odelius, H. Ogasawara, L. A. Naslund, T. Hirsch, L. Ojamae, L. M. Pettersson, A. Nilsson, *Science* **2004**, *304*, 995–998.

[201] D. Prendergast, G. Galli, *Phys. Rev. Let.* **2006**, *96*, 215502.

[202] D. Prendergast, J. C. Grossman, G. Galli, *J. Chem. Phys.* **2005**, *123*, 014501.

[203] D. Xenides, B. Randolf, B. Rode, *J. Mol. Liq.* **2006**, *123*, 61 – 67.

[204] R. Kumar, J. R. Schmidt, J. L. Skinner, *J. Chem. Phys.* **2007**, *126*, 204107.

[205] J. Enderby, G. Neilson, *Reports on Progress in Physics* **1981**, *44*, 593–655.

[206] J. Turner, A. K. Soper, J. L. Finney, *Mol. Phys.* **1990**, *70*, 679–700.

[207] W. J. McLean, G. A. Jeffrey, *J. Chem. Phys.* **1967**, *47*, 414–417.

[208] R. K. McMullan, T. C. W. Mak, G. A. Jeffrey, *J. Chem. Phys.* **1966**, *44*, 2338–2345.

[209] J. Turner, A. K. Soper, *J.Chem. Phys.* **1994**, *101*, 6116–6125.

[210] H. Kanno, K. Shimada, T. Katoh, *J. Phys. Chem.* **1989**, *93*, 4981–4985.

[211] J. L. Green, M. G. Sceats, A. R. Lacey, *J. Chem. Phys.* **1987**, *87*, 3603–3610.

[212] W. L. Jorgensen, J. Gao, C. Ravimohan, *J.Phys. Chem.* **1985**, *89*, 3470–3473.

[213] T. Lazaridis, M. E. Paulaitis, *J.Phys. Chem.* **1992**, *96*, 3847–3855.

[214] D. Feakins, F. Bates, W. Waghorne, K. Lawrence, *J. Chem. Soc. Faraday Trans.* **1993**, *89*, 3381–3388.

[215] K. Nishikawa, H. Hayashi, T. Iijima, *J. Phys. Chem.* **1989**, *93*, 6559–6565.

[216] B. Madan, K. Sharp, *Biophys. Chem.* **1999**, *78*, 33 – 41.

[217] W. L. Jorgensen, J. Chandrasekhar, J. D. Madura, R. W. Impey, M. L. Klein, *J.Chem. Phys.* **1983**, *79*, 926–935.

[218] H. Krienke, D. Opalka, *J.Phys. Chem. C* **2007**, *111*, 15935–15941.

[219] H. J. C. Berendsen, J. R. Grigera, T. P. Straatsma, *J.Phys. Chem.* **1987**, *91*, 6269–6271.

[220] S. Bradl, E. W. Lang, *J. Phys. Chem.* **1993**, *97*, 10463–10471.

[221] W. Gren, S. C. Parker, *Geochim. Cosmochim. Acta* **2008**, *72*, A328–A328.

[222] S. Caratzoulas, D. G. Vlachos, M. Tsapatsis, *J. Phys. Chem. B* **2005**, *109*, 10429–10434.

[223] S. Caratzoulas, D. G. Vlachos, M. Tsapatsis, *J. Am. Chem. Soc.* **2006**, *128*, 16138–16147.

[224] S. Caratzoulas, D. G. Vlachos, M. Tsapatsis, *J. Am. Chem. Soc.* **2006**, *128*, 596–606.

[225] `http://www.ucl.ac.uk/nanogrowth`.

[226] C. R. A. Catlow, J. M. Thomas, S. C. Parker, D. A. Jefferson, *Nature* **1982**, *295*, 658–662.

[227] S. C. Parker, C. R. A. Catlow, A. N. Cormack, *J. Chem. Soc.Chem. Commun.* **1983**, *17*, 936 – 938.

[228] S. C. Parker, C. R. A. Catlow, A. N. Cormack, *Acta. Cryst. Section B* **1984**, *40*, 200–208.

[229] M. A. Sanders, M. Leslie, C. R. A. Catlow, *J. Chem.Soc. Chem. Commun.* **1984**, 1271–1273.

[230] S. Tsuneyuki, M. Tsukada, H. Aoki, Y. Matsui, *Phys. Rev. Lett.* **1988**, *61*, 869–872.

[231] P. F. Mc Millan, A. C. Hess, *Phys. Chem. Min.* **1990**, *17*, 97–107.

[232] B. W. H. van Beest, G. J. Kramer, R. A. van Santen, *Phys. Rev. Lett.* **1990**, *64*, 1955–1958.

[233] J. Purton, R. Jones, C. R. A. Catlow, M. Leslie, *Phys. Chem. Min.* **1993**, *19*, 392–400.

[234] M. Sierka, J. Sauer, *Faraday Discuss.* **1997**, *106*, 41–62.

[235] G. J. Kramer, A. J. M. De Man, R. A. Van Santen, *J. Am. Chem. Soc.* **1991**, *113*, 6435–6441.

[236] J. Hill, J. Sauer, *J. Phys. Chem.* **1995**, *99*, 9536–9550.

[237] K. Schroder, J. Sauer, M. Leslie, C. R. A. Catlow, J. M. Thomas, *Chem. Phys. Let.* **1992**, *188*, 320 – 325.

[238] K. Schroder, J. Sauer, *The J.Phys. Chem.* **1996**, *100*, 11043–11049.

[239] A. Pedone, G. Malavasi, M. C. Menziani, U. Segre, F. Musso, M. Corno, B. Civalleri, P. Ugliengo, *Chem. Mater.* **2008**, *20*, 2522–2531.

[240] E. Demiralp, T. Çağin, W. A. Goddard, *Phys. Rev. Lett.* **1999**, *82*, 1708–1711.

[241] A. K. Rappe, W. A. Goddard, *J. Phys. Chem* **1991**, *95*, 3358–3363.

[242] N. T. Huff, E. Demiralp, , T. Çağin, W. A. Goddard, *J. Non-Cryst. Sol.* **1999**, *253*, 133 – 142.

[243] A. Takada, P. Richet, C. R. A. Catlow, G. D. Price, *J. Non-Cryst. Sol.* **2004**, *345-346*, 224 – 229.

[244] M. Wilson, P. A. Madden, M. Hemmati, C. A. Angell, *Phys. Rev. Lett.* **1996**, *77*, 4023–4026.

[245] J. D. Kubicki, A. C. Lasaga, *Am. Mineral.* **1988**, *65*, 941–955.

[246] L. V. Woodcock, C. A. Angell, P. Cheeseman, *J. Chem. Phys.* **1976**, *73*, 1565–1577.

[247] P. Tangney, S. Scandolo, *J. Chem. Phys.* **2002**, *117*, 8898–8904.

[248] A. C. T. van Duin, A. Strachan, S. Stewman, Q. Zhang, X. Xu, W. A. Goddard, *J. Phys. Chem. A* **2003**, *107*, 3803–3811.

[249] A. Palaria, G. Klimeck, A. Strachan, *Phys. Rev. B* **2008**, *78*, 205315.

[250] D. E. Yilmaz, C. Bulutay, T. Çağin, *Phys. Rev. B* **2008**, *77*, 155306.

[251] D. Raymand, A. van Duin, M. Baudin, K. Hermansson, *Surf. Sci.* **2008**, *602*, 1020 – 1031.

[252] *Materials Studio*, **2001**, Accelrys Software Inc.

[253] N. H. de Leeuw, S. C. Parker, *Phys. Rev. B* **1998**, *58*, 13901 – 13908.

[254] F. M. Higgins, N. H. de Leeuw, S. C. Parker, *J. Mater. Chem.* **2002**, *12*, 124–131.

[255] C. R. A. Catlow, *Proc. Royal Soc. London. A* **1977**, *353*, 533–561.

[256] M. J. Mora-Fonz, *PhD in Chemistry*, University College London, Christopher Inglod Laboratories, 20-22 Gordon Street, London WC1H 0AJ, U.K., **2006**.

[257] K. Eggers, T. Eichner, J. Woenckhaus, *Int. J. Mass Spec.* **2005**, *244*, 72 – 75.

[258] M. A. Zwijnenburg, F. Cora, R. G. Bell, *J. Phys. Chem. B* **2007**, *111*, 6156–6160.

[259] J. Sefcik, A. McCormick, *AICHE Journal* **1997**, *43*, 2773–2784.

[260] S. Svensson, S. Sjöberg, L.-O. Öhman, *J. Chem. Soc. Faraday Trans. 1* **1986**, *82*, 3635–3646.

[261] S. D. Kinrade, J. C. H. Donovan, A. S. Schach, C. T. G. Knight, *J.Chem.Soc. Dalton Trans.* **2002**, *7*, 1250–1252.

APPENDIX A

Calculated ^{29}Si NMR Chemical Shifts

This appendix presents the calculated chemical shifts of 59 species which have been calculated. All values are presented in ppm, relative to TMS. Where possible an experimentally assigned value is also presented, the experimental assignments are from references [5, 44, 52, 261]. As the experimental values in references [44] and [261] were given relaitve to the orthosilicic acid monomer;the shift of which was not presented, we have used our calculated value of this shift : -71.05 ppm as a reference.

	a
This Work	-71.05
Ref [5]	-71.75

	a
This Work	-78.04
Ref [26]	-79.91
Ref [5]	-80.17
Ref [125]	-81.5

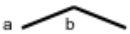

	a	b
This Work	-76.17	-84.76
Ref [26]	-79.41	-87.77
Ref [5]	-79.90	-88.50
Ref [125]	-81.1	-89.7

	a
This Work	-84.06
Ref [26]	-81.16
Ref [5]	-81.90
Ref [125]	-82.90

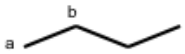

	a	b
This Work	-76.49	-83.08
Ref [26]	-79.41	-87.32
Ref [125]	-81.1	-89.3

	a
This Work	-88.83
Ref [26]	-87.09
Ref [5]	-87.84
Ref [125]	-89.0

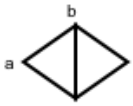

	a	b
This Work	-81.08	-85.91
Ref [125]	-81.02	-90.9

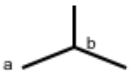

	a	b
This Work	-78.61	-95.00
Ref [125]	-80.7	-97.6

	a
This Work	-81.26
Ref [26]	-96.35
Ref [5]	-98.11

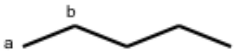

	a	b
This Work	-79.68	-88.44
Ref [125]	-81.2	-89.2

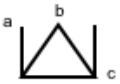

	a	b	c
This Work	-78.34	-81.92	-
Ref [26]	-79.07	-80.45	-89.28

	a	b	c
This Work	-76.14	-84.22	-100.28

	a	b	c	d
This Work	-75.23	-82.69	-85.35	-88.54
Ref [26]	-79.30	-80.93	-87.26	-88.91

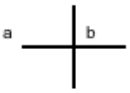

	a	b
This Work	-79.66	-100.28

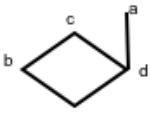

	a	b	c	d
This Work	-77.44	-84.40	-87.68	-93.98
Ref [26]	-78.90	-86.81	-87.23	-95.00

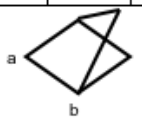

	a	b
This Work	-88.84	-97.79
Ref [26]	-85.19	-92.25
Ref [5]	-86.4	-94.1
Ref [125]	-87.0	-94.7

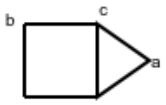

	a	b	c
This Work	-83.67	-90.21	-91.77
Ref [26]	-80.85	-87.35	-88.07
Ref [5]	-81.7	-88.3	-89.1
Ref [125]	-82.6	-89.4	-89.9

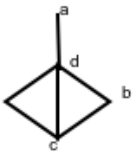

	a	b	c	d
This Work	-79.10	-80.55	-83.35	-92.95

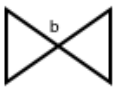

	a	b
This Work	-84.08	-97.53

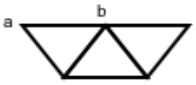

	a	b
This Work	-81.91	-78.54

	a	b	c
This Work	-76.92	-85.45	-107.17

	a	b
This Work	-89.83	-5.04

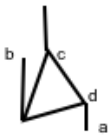

	a	b	c	d
This Work	-77.87	-78.53	-90.39	-89.31
Ref [26]	-79.29	-79.48	-88.98	-89.06

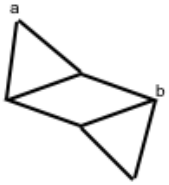

	a	b
This Work	-84.20	-89.54
Ref [26]	-81.69	-88.79
Ref [5]	-88.44	-89.08
Ref [125]	-83.4	-92.8

	a	b
This Work	-84.01	-92.06
Ref [26]	-81.43	-87.55
Ref [5]	-82.27	-88.66
Ref [125]	-83.2	-89.4

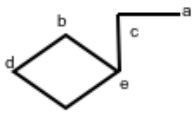

	a	b	c	d	e
This Work	-72.97	-81.66	-87.29	-86.29	-93.29
Ref [26]	-79.23	-86.76	-86.93	-87.23	-94.49

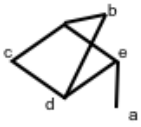

	a	b	c	d	e
This Work	-80.11	-84.58	-84.06	-94.46	-95.69
Ref [26]	-79.34	-85.26	-85.42	-92.79	-93.32

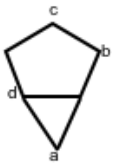

	a	b	c	d
This Work	-82.10	-89.34	-89.42	-92.20
Ref [26]	-79.98	-87.38	-87.59	-89.55

	a
This Work	-91.47
Ref [26]	-89.11
Ref [5]	-89.27
Ref [125]	-89.9

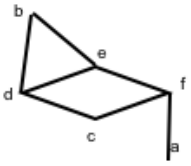

	a	b	c	d	e	f
This Work	-75.10	-84.73	-86.94	-90.66	-91.20	-89.69
Ref [26]	-78.96	-81.00	-86.79	-87.68	-87.97	-95.00

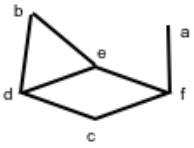

	a	b	c	d	e	f
This Work	-79.56	-84.00	-85.00	-90.44	-91.08	-94.85
Ref [26]	-78.88	-81.09	-87.03	-88.15	-88.25	-95.52

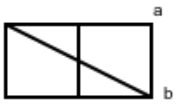

	a	b
This Work	-85.26	-93.63
Ref [26]	-85.49	-92.31

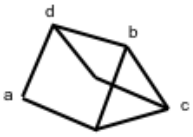

	a	b	c	d
This Work	-89.03	-89.51	-91.53	-99.16
Ref [26]	-87.05	-87.52	-88.38	-95.65

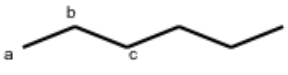

	a	b	c
This Work	-78.72	-87.41	-89.16

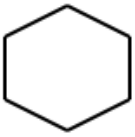

	a
This Work	-83.98

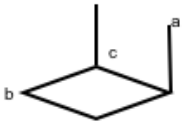

	a	b	c
This Work	-79.28	-84.48	-98.58

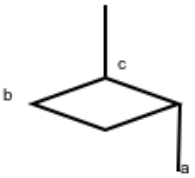

	a	b	c
This Work	-76.15	-82.66	-93.70

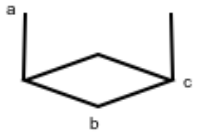

	a	b	c
This Work	-76.15	-82.66	-93.70

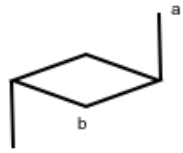

	a	b	c
This Work	-79.07	-87.16	-95.00

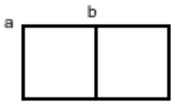

	a	b
This Work	-85.28	-97.90
Ref [26]	-87.06	-94.99
Ref [5]	-88.6	-96.4
Ref [125]	-89.3	-97.0

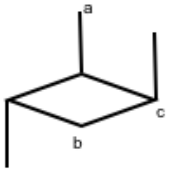

	a	b	c
This Work	-80.35	-85.94	-93.25

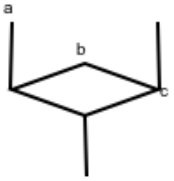

	a	b	c
This Work	-80.66	-86.66	-98.02

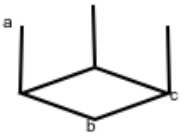

	a	b	c
This Work	-79.17	-83.65	-96.15

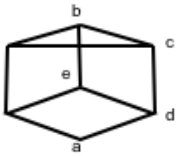

	a	b	c	d	e
This Work	-89.98	-90.47	-92.72	-98.34	-98.82
Ref [26]	-86.71	-87.46	-88.99	-95.77	-95.95

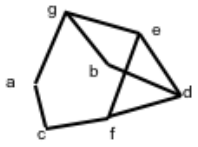

	a	b	c	d	e	f	g
This Work	-88.23	-84.59	-85.58	-90.18	-91.67	-91.85	-91.34
Ref [26]	-87.16	-87.52	-88.06	-88.17	-88.59	-90.18	-96.52

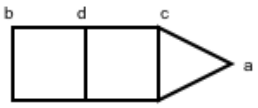

	a	b	c	d
This Work	-83.53	-87.04	-90.00	-94.77
Ref [26]	-81.24	-87.26	-87.59	-95.76

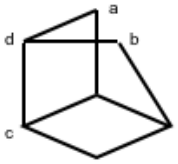

	a	b	c	d
This Work	-87.80	-89.53	-95.61	-98.83
Ref [26]	-86.53	-87.60	-94.87	-95.94

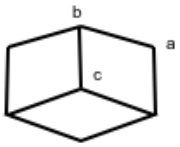

	a	b	c
This Work	-87.23	-95.88	-96.82
Ref [26]	-87.09	-95.52	-85.82

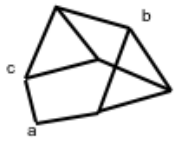

	a	b	c
This Work	-90.18	-92.26	-93.19
Ref [26]	-87.87	-88.79	-89.82

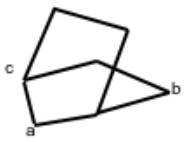

	a	b	c
This Work	-84.77	-88.05	-97.36

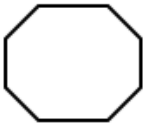

	a
This Work	-83.47

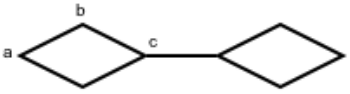

	a	b	c
This Work	-84.18	-85.46	-91.35

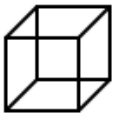

	a
This Work	-100.03
Ref [26]	-98.17
Ref [5]	-98.99

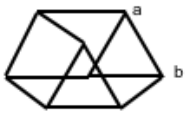

	a	b	c
This Work	-92.23	-93.79	-99.43
Ref [26]	-88.60	-91.38	-97.61
Ref [5]	-88.3	-88.7	-97.1

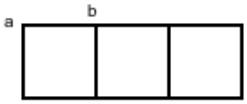

	a	b
This Work	-91.41	-99.10
Ref [5]	-87.8	-96.5

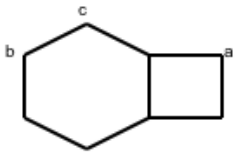

	a	b	c	d
This Work	-83.76	-84.38	-87.34	-92.40

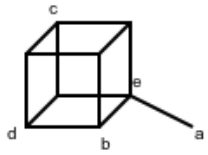

	a	b	c	d	e
This Work	-77.97	-98.76	-99.14	-99.13	-104.49
Ref [239]	-80.62	-98.06	-98.19	-98.37	-106.78

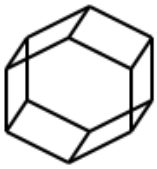

	a
This Work	-102.40

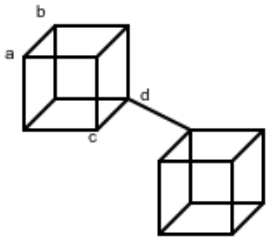

	a	b	c	d
This Work	-99.77	-99.01	-99.18	-105.14
Ref [239]	-98.06	-98.19	-98.37	-105.91

APPENDIX B

Ring Searching Algorithm

The ringsearching program comes together with an RDF analysis program for hydration layers in a single package, called Ringsearch.tar. The program can be complied and executed on any UNIX based platform. Compilation requires a FORTRAN 90 compiler. To run the program, first extract the package from the tar file. Next edit the file Make.sh, after "FC =" enter the name of your FORTRAN compiler. After "FFLAGS =" put any flags which you wish to include. The program runs with comparable efficiency using the commands ifort -fast and gfortran -O2. Once the Make.sh file is completed simply execute this file and the program should compile.

To run the program it is first necessary to select the type of analysis and set some parameters. These are set in a file named Input.txt, the options in this file are:

- CELL_DIMENSIONS this option requires three real numbers for the x,y and z cell vectors.
- NUMBER_ATOMS_IN_SOLUTE Requires an integer
- NUMBER_STEPS Requires an integer, the number of simulation steps to be analyzed
- HYDRATION_SPHERE Requires a real number, the radius of the hydration sphere from the centre of the solute, in Å.
- SOLUTE_RADIUS Requires a real number, the radius of the excluded volume of the solute, assuming spherical shape, in Å.
- RDF Requires either 1 or 0, 1 = Calculate RDFs, 0 = Do not calculate RDFs.

- NNN_SEARCH Requires either 1 or 0, do a search for the structural motif with topology NNN. 1 = Yes, 0 = No.

To read the MD trajectory the program reqires the trajectory in standard xyz format. Note: the solute coordinates must appear *at the top* of the list of coordinates at each step.

To perform the analysis simply type "./RunRings.sh SOLUTE", where SOLUTE should be replaced by the name of the trajectory files. For example to run the analysis on the TMA.xyz file in the *tests* directory, copy the file TMA.xyz to the directory containing the executables, then type "./RunRungs.sh TMA", note the .xyz extension is dropped for running.

The output is put into a directory called SOLUTE, in the example above it would be called TMA and consists of a number of files. The important output is now summarized.

- Table.dat

  This file contains a list of all of the steps and the number of 3 - 6 rings found at each point. This can then be copied into a spreadsheet for analysis. Note the sixth column (ENER) is only relevant to CP2K trajectories and is the potential energy of each step.

- Times_NR.dat

  This file contains the number of steps for which each ring of order N, found during the analysis, has lasted. Again this allows for analysis such as average ring lifetime.

- unique_Ns.dat

  Contains the indices of each of the unique rings of order N found at each step.

- look.xyz

  Contains the coordinates of the hydraion layer oxygens which were analyzed at each step, the indices correspond to unique_Ns.dat, and this geometry can be used to visualize the rings.

- connections_XX.dat

  This file contains information regarding the search for the topology XX in the hydration layer. At the bottom of the file is the number of times that structure has been found, and its average lifetime.

- Histogram.dat and RDF.dat

These files contain the output of the RDF analysis, in un-normalized (histogram) and normalized form. The program calculates OO, HH and OH histograms for the water in the hydration layer of the solute as defined in the Input.txt file.

In the "src" directory are the source files, they are:

- RDF.F The code for calculating RDFs.
- RING_COUNT.F The code for finding unique rings.
- CONN_RING_XX.F The codes for searching for different fragment topologies.
- LIFETIMES.F The code for calculating ring lifetimes.

For running the tests the parameters are as follows;
TMA:

- CELL_DIMENSIONS 10.452 10.452 10.452
- NUMBER_ATOMS_IN_SOLUTE 17
- NUMBER_STEPS 1
- HYDRATION_SPHERE 6.5
- SOLUTE_RADIUS 3.6
- RDF As desired.
- NNN_SEARCH As desired.

TEA_10000:

- CELL_DIMENSIONS 10.724 10.724 10.724
- NUMBER_ATOMS_IN_SOLUTE 29
- NUMBER_STEPS 10000
- HYDRATION_SPHERE 7
- SOLUTE_RADIUS 3.9
- RDF As desired.
- NNN_SEARCH As desired.

A full version of this code is also freely available from the Nanogrowth website at : http://www.ucl.ac.uk/nanogrowth/software.htm